Water Droplet Erosion Resistant Materials and Surface Treatments

Mohammad Sadegh Mahdipoor

A Thesis

In the Department

of

Mechanical and Industrial Engineering

Presented in Partial Fulfillment of the Requirements

For the Degree of Doctor of Philosophy (Mechanical and Industrial Engineering) at

Concordia University

Montreal, Quebec, Canada

February 2016

CONCORDIA UNIVERSITY
SCHOOL OF GRADUATE STUDIES

This is to certify that the thesis prepared

By: **Mohammad Sadegh Mahdipoor**

Entitled: **Water droplet erosion resistant materials and surface treatments**

and submitted in partial fulfillment of the requirements for the degree of

Doctor of Philosophy (Mechanical Engineering)

Complies with the regulations of the University and meets the accepted standards with respect to originality and quality.

Signed by final examining committee:

_____Chair
Dr. Amr Youssef

_____External Examiner
Dr. Mohammad Jahazi

_____External to Program
Dr. Michelle Nokken

_____Examiner
Dr. Martin Pugh

_____Examiner
Dr. Ramin Sedaghati

_____Thesis Supervisor
Dr. Mamoun Medraj

Approved by:

_____
Chair of Department or Graduate Program Director

_____2016 _____
Dean of Faculty

ABSTRACT

Water Droplet Erosion Resistant Materials and Surface Treatments

Mohammad Sadegh Mahdipoor
Concordia University, 2016

Water Droplet Erosion (WDE) is a mechanical degradation which is of great concern to power generation and aerospace industries, where water droplets interact with high-speed moving components. It is observed on multiple components of airplanes when flying in the rain, on steam turbine blades, and gas turbine compressor blades which is the focus of this study. Compressor blades in gas turbines suffer from WDE due to the recently implemented technology Inlet Fog Cooling. It is utilized to boost gas turbine efficiency in high ambient temperatures via the spraying of micro-sized water droplets into the intake air. Evaporation of water droplets cools the intake charge and increases the air density. The main drawback of inlet cooling is that part of the water droplets are carried into the compressor by intake air flow, which is called overspray. Repetitive impact between rotating blades and water droplets leads to WDE damage, which is a major problem.

This study attempted to improve WDE resistance of compressor blades made of Ti6Al4V. Two different approaches were considered: Studying WDE of TiAl alloy as a potential erosion resistant material for turbine blades and Surface engineering of Ti6Al4V via gas nitriding and HVOF spraying of WC-Co. To investigate WDE in this work, erosion experiments were carried out using the state-of-art WDE rig available at Thermodynamics of Materials Group (TMG), Concordia University. It enables control of erosion conditions such as impact velocity, impact angle, droplet size, and droplet impingement number.

In the first stage of this study, WDE of nearly fully lamellar TiAl alloy was directly compared to Ti6Al4V at relatively wide ranges of impact speed (i.e. 275m/s, 300m/s, 325m/s and 350m/s) and droplet size (i.e. 464μm and 603μm). TiAl demonstrated superior erosion performance (i.e. longer incubation period and slower material loss) compared with Ti6Al4V at all tested conditions. Herein, the relation of impact velocity and maximum erosion rates for TiAl and Ti6Al4V alloys was established and the damage threshold speeds of TiAl were determined. Afterwards, the erosion behaviour of TiAl was related to its mechanical properties and irregular

microstructure. Lastly, in-depth investigation was carried out to reveal erosion damage mechanism of TiAl at different stages including incubation, material loss initiation, maximum erosion rate, and advanced stages.

In the second stage of this study, the influence of gas nitriding on water droplet erosion behaviour of Ti6Al4V was investigated. Ti6Al4V coupons were nitrided at two different temperatures (i.e. 900 and 1050°C) for 5 and 10 hours and the nitrided coupons were characterized. Their erosion behaviour in comparison with as-received and annealed Ti6Al4V was examined at two impact speeds (i.e. 300m/s and 350m/s). Mechanical properties, erosion performance and damage mechanism of treated Ti6Al4V were significantly influenced by the nitriding temperature. Exploring the potential of HVOF spray WC-Co coating to combat WDE was the last part of this study. Erosion performance of two WC-Co coatings was examined at 250m/s, 300m/s and 350m/s impact speeds in comparison with Ti6Al4V. The as-sprayed coating did not show notable WDE protection; however, removing its top layers and smoothing its surface notably improved the erosion performance.

To my loving parents, **Pari Azizi** and **Saleh Mahdipoor**

And to my little but supportive sister, **Mahshid**

Who always help me to find my Smile

Without them I would never have finished this work

ACKNOWLEDGEMENTS

This research would not have been possible without constant guidance, support and advice of my supervisor, Professor Mamoun Medraj. He gave me a passion to learn more, freedom to find my path and instruction to stay in the right track. I am sincerely grateful to have this opportunity working under his supervision at TMG group, where I learned so many things.

I would like to thank Dr. Mohammad Jahazi, Dr. Michelle Nokken, Dr. Martin Pugh and Dr. Ali Dolatabadi for serving on my committee and providing guidance toward the completion of this degree.

I wish to thank Dr. Christian Moreau, Dr. Ali Dolatabadi, Dr. Martin Pugh, and Dr. Robin Drew for giving me permission to use the facilities in their laboratories. I am grateful to Dr. Dmytro Kevorkov and Dr. Pawel Jedrzejowski for their insightful comments and contributions in this work. I also like to thank Mr. Mazen Samara, who was always patient and helpful in the laboratories. Very warm thanks to all TMG members especially to: Hany Kirols, Dr. Ahmad Omar Mostafa, Jessie Yi, Guy Joel Rocher, Tian Wang, Benjamin Wallace, Bolarinwa Komolafe, Alex Chen, and Dina Ma. Thank you for the help with the experiments, the constructive discussions and the valuable suggestions. I wish to extend my thanks to Dr. Niloofar Kamkar from Ecole Technologie Superieure (ETS) for all the great helps during my PhD. I would like to also thank Dr. Fadhel Ben Ettouil, Dr. Fariba Tarasi and Dr. Samir Mourad for their helps through the experiments in Concordia and ETS Universities. I wish you all success in your endeavours.

This work was financially supported by Rolls-Royce Canada Ltd., the Consortium for Research and Innovation in Aerospace in Quebec (CRIAQ) under CRIAQ-MANU419 project and Natural Sciences and Engineering Research Council of Canada (NSERC). The financial support is acknowledged.

Friends, I wish to thank my amazing friends who were always there for me throughout the most challenging moments. My heartfelt thank goes to my lovely sister and wonderful friend, Mahshid, who always makes me smile regardless how much it was difficult time. I give my deepest appreciation to my uncles, Reza and Bahram, for their endless support, care and encouragement.

Though no amount of “Thank You” will suffice, I would like to wholeheartedly thank my parents, Pari and Saleh who are the foundation of my life. I am thankful for your boundless support

and unconditional love throughout my entire life. You have always inspired me to be a better person. Every day I have learned new things just by watching you. Watching and learning the real compassion, devotion and dedication. Without each of you, I would be nowhere near the person I am. Thank You.

Table of Contents

List of figures

List of tables

Chapter 1 : Introduction

1.1. Water droplet erosion

The word "erosion" is derived from the word “rodere”, which is a Latin verb and means “gnaw”. This word is widely used to describe wearing of rocks, sea shores, and soil by water and wind; however, in material science it is used to describe a mechanical damage caused by high speed impingements [1]. Erosion is the result of either solid/solid or liquid/solid interactions. Different types of erosion are known such as solid particle erosion, cavitation erosion, liquid impingement erosion, and slurry erosion. They are all associated with the cyclic loading and sharp pressure pulses [2-4]. Compared to solid particle erosion and cavitation erosion, liquid impingement erosion has not been well studied.

In the field of aerospace and power generation, water droplet erosion (WDE) refers to a progressive material loss caused by repetitive high speed impact of water droplets [2, 5]. WDE is a sub-category of liquid impingement erosion. It is widely observed in turbine blades, aircraft aerofoils, missiles, helicopter rotors, and the inner wall of certain steam pipes [2]. Also, it is a well-known damage for steam turbine blades, shown in Figure 1-1, and scientists have attempted to address this phenomenon since the beginning of 20^{th} century [6, 7]. When steam reaches to the last stages of turbine, because of low pressure and temperature small portion of steam goes below the saturation line and causes the formation of very small primary water droplets, which is called fog droplets. Such droplets coalesce and form a water film on the stationary blades. Accumulation of more water makes the water film unstable and leads to the formation of large droplets (more than 1mm). The large droplets are atomized and then brought with the steam flow to the plane of rotating blades [8]. The schematic of water droplet formation in steam turbines is demonstrated in Figure 1-1-a. The supersonic impingement of rotating blades and generated water droplets cause WDE, as shown in Figure 1-1-b. This type of erosion has also been observed on the blades of gas turbine compressor when fog cooling system is used [5, 9], shown in Figure 1-2. It is known that turbine efficiency decreases 0.3-0.5% by raising 1°F ambient temperature [10]. Fog cooling, spraying small water droplets to cool the intake air, is introduced as a practical approach to enhance the turbine efficiency through increasing air density. During fog cooling the sprayed water droplets partially evaporate; however, some of them remain and enter the compressor with the intake air, called overspray [5, 9, 11]. Successive high speed impingements between these droplets and

rotating blades result in water droplet erosion damage on their leading edge. This damage leads to material loss, distortion of the blades profile, and reduction of their aerodynamic performance. Moreover, weight loss of the blades may influence the balance of compressor and cause significant vibrations, which is a major issue for the engine. Hence, understanding water droplet erosion and reducing this damage is of high interest for power generation industries.

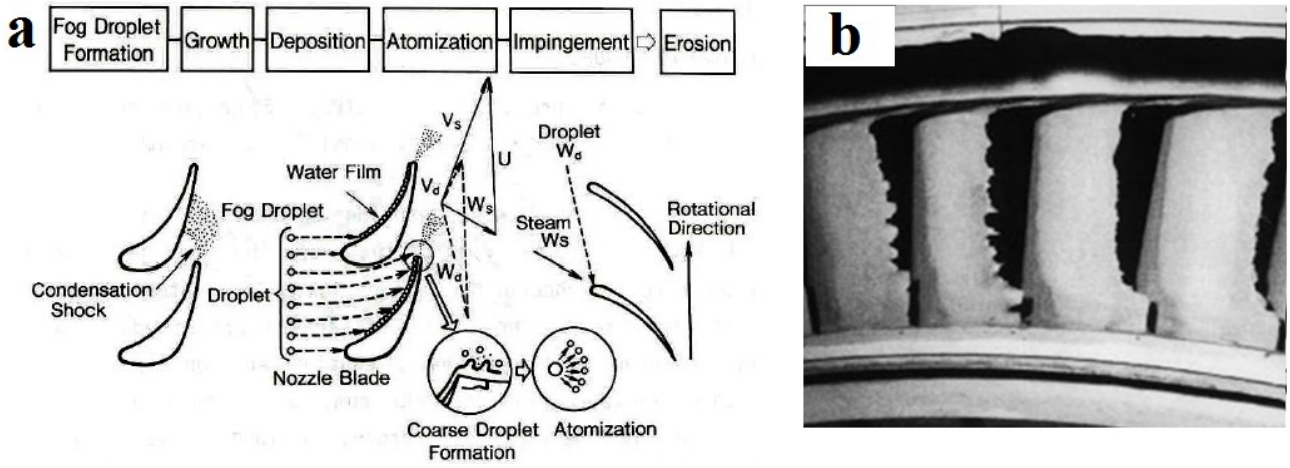

Figure 1-1: (a) Schematic of water droplet formation in the steam turbines [12], (b) severe water droplet erosion on suction side of steam turbine blades [13]

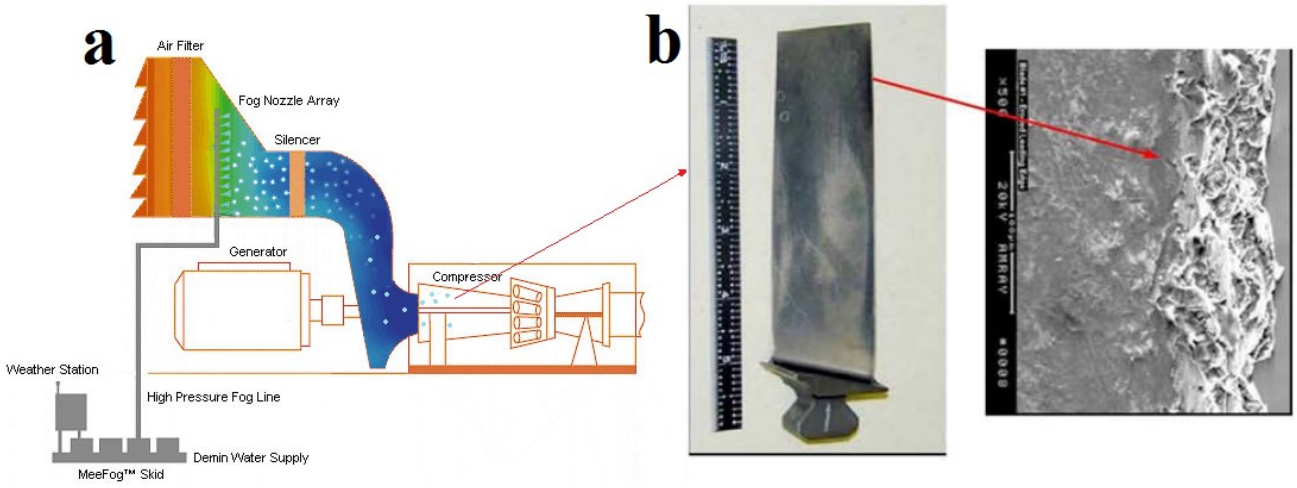

Figure 1-2: (a) Schematic of a gas turbine equipped with fog cooling system [14], (b)eroded blade of HP compressor in LM6000 turbine [15]

1.1.1. Physics of the water droplet impact on a solid surface

To explain the WDE, first the physics of a single liquid/solid impingement are reviewed. Upon impingement of single droplet onto a solid surface pressure pulses are generated and form a disturbed zone (shocked envelop) inside the liquid, close to liquid/solid interface [16], shown in Figure 1-3-a. After a few micro seconds, the compressed region of liquid breaks away. This moment, which is followed by the formation of lateral outflow jets, is commonly referred to as "stagnation moment". The generated jets travel across the surface with velocities up to 10 times the impact speed [3, 16, 19]. They are detrimental and play a notable role in initiating the erosion damage [2, 3, 20]. Once the disturbed region of water breaks away, the potential energy of compressed water transforms to kinetic and the impact pressure is released into the solid [21]. These pressures predominantly concentrate in the centre of contact area or its edges [21]. Lesser and Field [22] explained that pressure in the contact edge is higher than pressure at the centre (up to 3 times); however, these pressures last for very short duration of time and can be ignored for damage mechanism investigation [22]. Figure 1-3 demonstrates the schematic of a liquid droplet impact onto a solid surface at two different stages, before and after shock envelop detachment. The stress waves, high pressure locations, and the potential cracking sites are highlighted in this schematic.

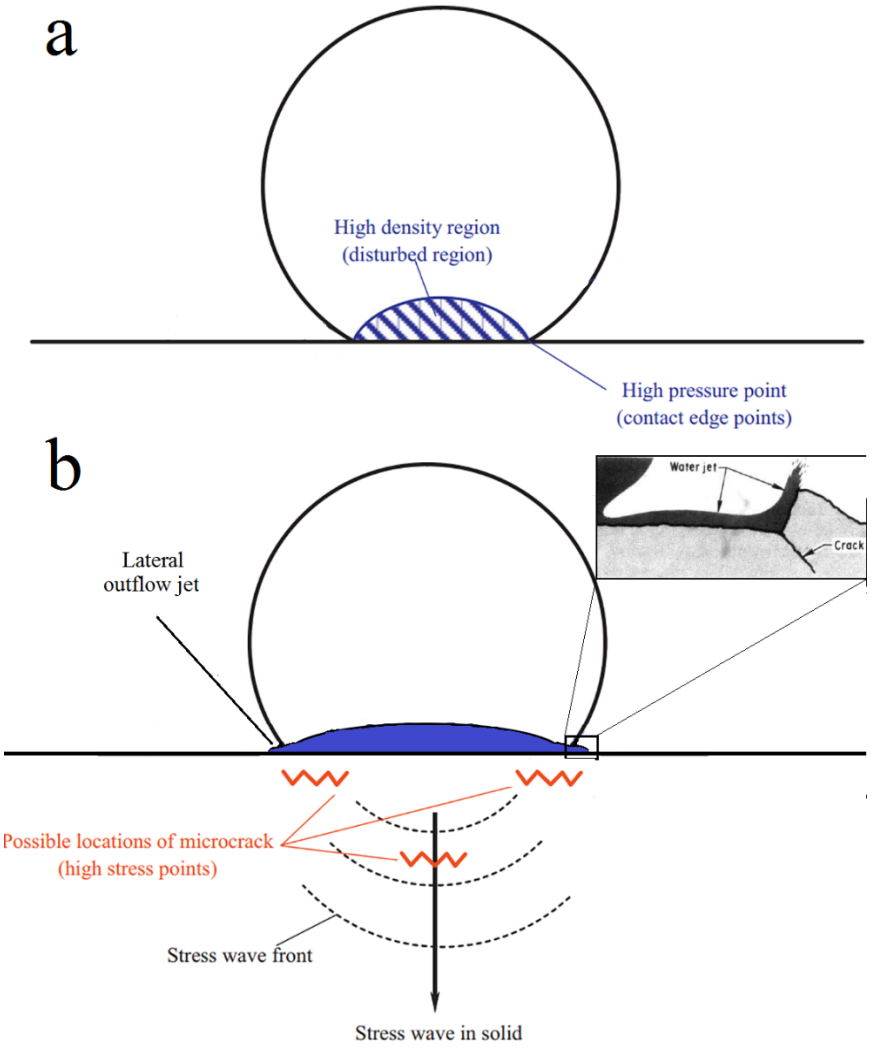

Figure 1-3: Schematic presentation of a water droplet impingement onto a solid surface: (a) upon impact and before the detachment of disturbed region, (b) after the detachment of disturbed region [3, 23]

In 1928, Cook [6] posited that the impingement of a liquid jet induces a constant pressure to a solid. He called this pressure "water hammer pressure" and proposed Equation 1-1 to calculate it.

$$P = \rho_0 C_0 V \qquad \textit{Equation 1-1}$$

where ρ_0 is the liquid density, C_0 is the speed of sound in the liquid and V is the impact speed. Equation 1-1 is not accurate to address the impact pressure because it was derived for simplified conditions. Indeed, the peak transient pressure is much higher than the proposed constant value by Cook. Later Heymann [24] analytically calculated and proposed another equation for the peak

transient pressure generated by the impingement of one droplet, Equation 1-2. It is used in this thesis to address the impact pressure.

$$P = \rho_0 C_0 V[2 + (2k - 1)\frac{V}{C_0}] \qquad \textit{Equation 1-2}$$

where k is liquid constant. In the case of water erosion, $k=2$, $\rho_0=1000kg/m^3$ and $C_0=1463m/s$. It is worthy to note that the impact pressure is approximately generated over a circle with radius of:

$$R = r\frac{V}{C_0} \qquad \textit{Equation 1-3}$$

where r is the radius of the droplet [18]. Due to the compressibility of fluid, the impact pressure in the liquid stay mainly at the centre of impact until the stagnation moment, when the release waves vacate the free surface and the lateral jetting initiates. This is called jetting time and Field [21] proposed Equation 1-4 to calculate it. He explained that time duration of an impact pressure pulse is around 3 times that of jetting time.

$$T_j = \frac{rV}{2C_0^2} \qquad \textit{Equation 1-4}$$

Upon water droplet impact, the disturbance transmits into the solid by the longitudinal (dilatational) and transverse (distortional) waves traveling at different speeds (C_1 and C_2). Rayleigh wave is also generated by the droplet impact and it travels on the solid surface with the speed of C_R, shown in Figure 1-4-a [16, 18]. Upon impingement the compressive longitudinal waves expand into the target. Thereby, they interact with microstructural discontinuities and rebound in the form of dilatational tensile waves [16, 18]. The interference of these released and reflective stress waves, shown in Figure 1-4-b, may cause considerable failure especially for a target with nonhomogeneous microstructure [25].

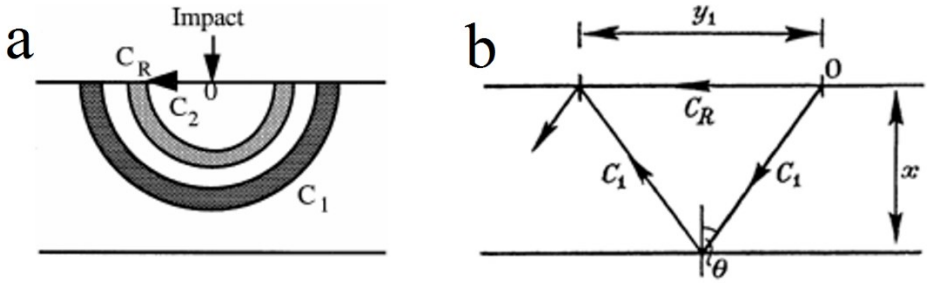

Figure 1-4: Schematic presentation of: (a) stress waves travelling in the target, (b) reflection and interference of longitudinal and Rayleigh waves [16, 18]

Exerted stresses on the solid during the water erosion can be classified into two main groups. The first group is associated with 'explosive' compressions, which influence the surface for very short time and are referred to as water hammering effect. The second group is a result of the erosive scouring action of the high speed radial outflow jetting [25]. Both groups contribute to the water droplet erosion damage. The physics of liquid/solid impingement becomes more complicated when the repetitive impacts are considered. In this case more parameters, e.g., surface roughness and absorbed energy, involve in the response of target to droplet impacts [26, 27]. Surface roughness varies during the impingements because of localized plastic deformation. Lesser and Field [22] highlighted that local plastic deformation of solid significantly influences liquid behaviour and its jetting time. Hence, the stress distribution and travelling shock waves differ with surface roughness variation. Once the droplet strikes any asperity on the surface, the high impact pressure coming from the compressed part of the liquid may not be generated. This is due to different deformation behaviour of the liquid. However, hitting a pit may cause even higher impact pressure due to shock wave collisions inside the pit [2]. In addition, the energy of each impingement is partially transferred to the solid surface. This energy may accumulate in the weak points of microstructure, such as grain boundaries, phase interfaces, cracks and porosities, as the vulnerable sites. Once the next droplet strikes these locations, a prompt failure may occur due to the interaction between the new incident impact waves with the reflected waves. This is not the case for the surface impacted by a single isolated droplet.

1.1.2. Damage mechanism of water droplet erosion

A considerable amount of research has been carried out over the last few decades seeking to understand the details of damage caused by water droplet erosion. It is well-known that the erosion damage mechanism is a function of target's mechanical properties and microstructure, as well as the solid surface conditions (i.e. roughness and presence of stress raisers) [2, 28-31]. To date, it is impossible to predict the water erosion behaviour of a certain material based on the knowledge of its mechanical and physical properties only. Therefore, the response of each material to water droplet impacts and the erosion damage mechanism need to be studied individually. However, some common erosion features found in the early and advanced stages of water droplet erosion are reviewed further.

1.1.2.1. Early stages of erosion

In 1985, Field *et al.* [16] shed light on the mechanism of erosion damage initiation for ductile targets. They proposed that the repetitive impacts of water droplet on a completely smooth surface cause development of damage in four stages, as demonstrated in Figure 1-5. After initial droplet impacts a shallow depression appears on the surface, shown in Figure 1-5-a. This depression becomes deeper with further impacts. Once the impacting droplet fills the generated depression, the water is thought to be compressed for a longer period of time. This results in greater impact pressure, Figure 1-5-b. The next droplet hitting the deformed location experiences different forms of disturbance, shown in Figure 1-5-c. Here, the angle between the water's free surface and the water/solid interface is important and if it goes beyond a critical angle, the shock envelope breaks away. The shock waves coming from the walls of deformed area compress the water and make a spear-like central jet [3]. The impact pressure and the strike of this central jet dig the base of depression and generate small central cavity, shown in Figure 1-5-d. This cavity becomes deeper until the air or water, which can be trapped in the pits, play some cushioning role and suppress further deepening [2].

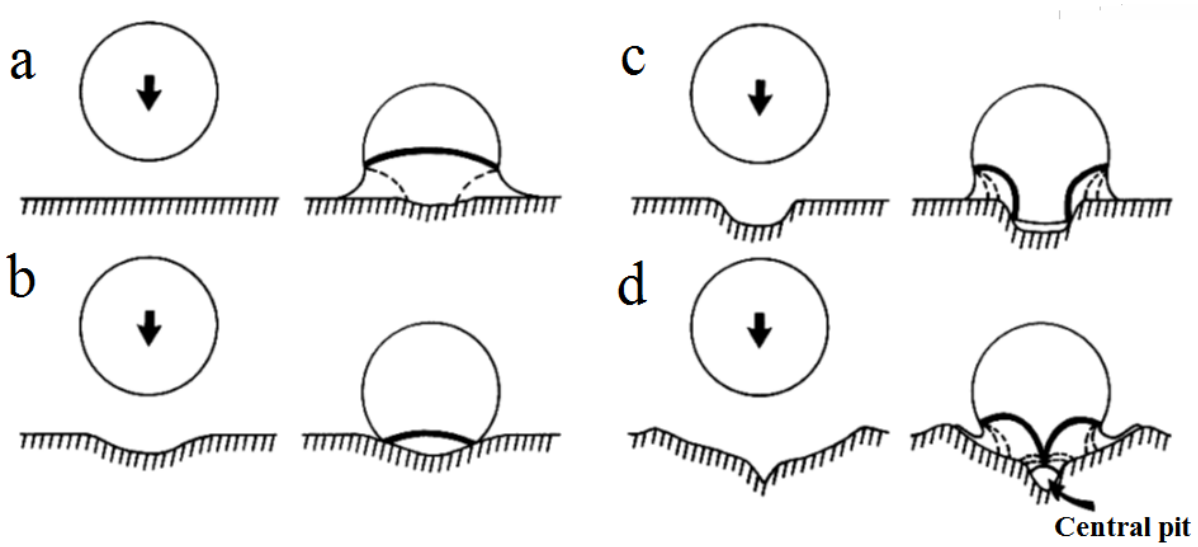

Figure 1-5: Schematic of erosion damage initiation on a ductile solid surface proposed by Field et al. [16]

Dimples and central depressions are common features reported for the erosion of ductile metals either in the laboratory or in service conditions of turbine blades [16, 32-34]. Other experimental studies have been carried out on a wide range of materials and their response to

droplet impacts were documented in the early stages of erosion [18, 25, 28-30, 35, 36]. Several features of erosion damage at early stages are listed below.

1. Circumferential surface fracture: upon collision the centre of impacted area is under compression. At the same time radial tensile stresses are exerted at the edges of impacted area for short durations. These stresses cause local fractures at the periphery of the droplet on hard and brittle targets, such as plexiglass, shown in Figure 1-6-a [25]. In some cases, an undamaged area in the centre of impact which is surrounded by ring fractures is observed, shown in Figure 1-6-b. Indeed, the fracture of central region is suppressed by induced compressive stresses and only elastic deformation may occur. For hard intermetallic alloys, material loss around the rim of the depression was posited to be the dominant phenomenon [25]; however, no experimental proof was provided.
2. Depression and localized material flow: the central compressive and subsequent shear stresses, caused by the water hammering, result in permanent local depression (saucer-shaped), shown in Figure 1-6-c. This is observed mainly for erosion of ductile metals [2, 25, 29, 30] once the dynamic exerted stresses exceed the dynamic yield strength of the solid. In addition to the local penetrations, large amount of micro-plasticity can be observed in the microstructure at high magnification. Slip lines, grain boundaries, and twin boundaries may appear on the surface of depressions [2, 25, 28]. Localized material flow needs to be studied in depth because it facilitates material loss in subsequent stages. Furthermore, the sub-surface flow and subsequent cracking are also observed once droplets impact the ductile targets [25]. In multiphase alloys, the softer phase predominantly shows micro-plasticity. This results in inhomogeneous localized deformation [2, 25, 35].
3. Micro-cracking due to local plastic deformation: surface and sub-surface cracks is often reported as the main erosion features [2, 25, 28-30]. In the case of ductile metals, they mainly initiate due to localized material flow [2, 28-30].
4. Grain boundaries failure: when the size of microstructure constituents is relatively small compared to droplet size, the impacting droplet considerably damage their boundaries. For instance, in erosion of metallic targets grain boundary damage is frequently observed [28, 29, 31, 35]. An eroded surface of aluminium with revealed grain boundaries is shown in Figure 1-6-c. Huang *et al.* [28] highlighted that the

rotating of small grains is the main reason for the grain boundary damage in erosion of Ti6Al4V. Different orientation of the grains and subsequent anisotropy were reported as another reason for the grain boundary damage [25].

5. Circumferential shear fractures: after a few microseconds of impingement and once the shocked envelop in the liquid breaks away, the lateral outflow jets form and hit any surface discontinuity with very high speed. This collision may lead to lateral material flow at the periphery of impacted area or localized fracture of surface asperities such as grinding tracks, elevated grain boundaries, or raised slip bands [25, 31], shown in Figure 1-6-b.
6. Micro-cracking due to stress waves: The travelling stress waves (mainly reflective tensile waves) may generate micro-flaws in the target. These waves interact with microstructural irregularities and initiate cracking [37]. Furthermore, the interference of Rayleigh waves with reflected tensile dilatational waves, shown in Figure 1-4, may cause circumferential fracture on the surface [18, 25, 38], shown in Figure 1-6. This was mainly observed in hard and brittle targets and could be more destructive compared to the other types of failure occurring over the attacked surface area [25].

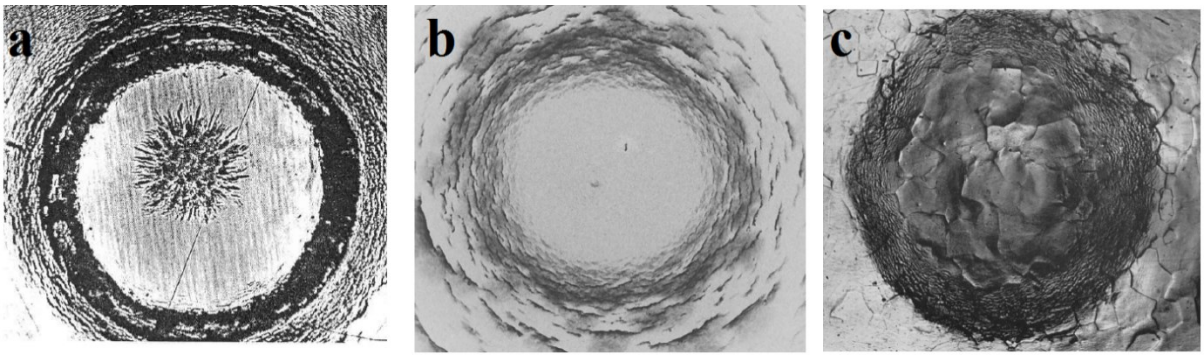

Figure 1-6: Eroded surface of: (a) polymethyl methacrylate showing ring fractures [25], (b) zinc sulphide showing an undamaged area surrounded by annular fractures [18], (c) aluminum showing the rim of depression and the revealed grain boundaries [25]

1.1.2.2. Advanced stages of erosion and material removal

Hancox and Brunton [39] investigated the response of copper to repetitive droplet impacts. They performed long erosion experiments using low impact speeds (<100m/s). After a few thousand impacts, large number of depressions on the surface of attacked copper were observed. Such localized material flow and surface roughening was put forth as the main cause of material loss initiation [39]. Indeed, peaks of asperities within the roughened surface are broken with the

impact of high speed jets flowing on the surface. Major portion of pitting on the surface of ductile copper was attributed to these impacts [39]. Huang *et al.* [28] reported that generation of crack networks and their coalescence is the dominant mechanism of material loss initiation for Ti6Al4V. They highlighted that droplet impacts slightly rotate the grains and cause intergranular cracking, and subsequent micro-pitting. Luiset *et al.* [30] reported the grain boundary damage in the initial stages of erosion of stainless steel. They explained that cracks development in the boundaries caused the detachment of grains and the generation of small pits. In several cases, the rupture of grains because of transgranular cracking was also observed. Triple splitting of grains is another mode of material loss which was documented by Kong *et al.* [36, 40]. The role of grain boundary as an important microstructural defect was elaborated by Hancox and Brunton [39]. They observed that a single crystal of copper shows fewer erosion pits and subsequent slower material loss compared to polycrystalline copper. Generally, erosion progress is associated with abundant cracking. Cracking behaviour is a function of target material properties and the fractography of eroded surface should be carried out for each specific material. However, intergranular cracking for damage initiation and transgranular cracking for the advanced stages were highlighted as the dominant behaviour for erosion of ductile metals [20, 28, 30, 40, 41].

Further droplet impacts on the generated small pits cause a phenomenon called “hydraulic penetration”, which was highlighted as one of the most damaging phenomena in the advanced phases of erosion [3, 20]. Hydraulic penetration was attributed to the formation of spear-like jets inside the cavities. These jets strike the floor of cavities with much larger force compared to the initial droplet impact and bore secondary pits inside the original cavity [3]. Hence, the cavities enlarge and merge together with further impingements. The coalescence of enlarged cavities causes detachment of large fragments and the generation of deep craters. In these stages water hammering, lateral jetting, and water penetration contribute to the erosion damage progress [2, 3, 20]. Droplet impacts on the deep craters result in inhomogeneous stress distribution and formation of different types of pits on the bottom and the sidewall of craters. For instance, generation of narrow and undercutting pits, called tunnels and sub-tunnels, were documented in the case of Ti6Al4V erosion [35]. Their generation roughens the surface along the edges of erosion craters. The vulnerable sites over the roughened surface will be broken with oncoming droplet impacts. Their fracture smooths the eroded surface, which was called water smoothing [41, 42].

1.1.3. Parameters affecting liquid droplet erosion

Liquid droplet erosion is a complex phenomenon which is a function of numerous parameters. They are classified into two main categories [2, 43]. The first group comprises liquid and solid properties including their densities, liquid viscoelasticity behaviour, and mechanical properties of solid target. The second group includes the impingement parameters such as impact speed, impact angle, droplet size, and its shape, which are mainly the interest of this thesis and thus reviewed further.

1.1.3.1. Impact speed

Water droplet erosion as repetitive impact wear is a function of impact speed because the induced pressure and kinetic energy of each impact are influenced by the velocity. Coulon [44] described that impact speed is significantly important since it changes the nature of damage (chemical or mechanical). Based on the impact speed, he divided the damage caused by liquid/solid interaction into four groups; corrosion, corrosion-erosion, erosion-corrosion, and erosion [44]. He explained that above a critical impact speed, no chemical degradation (corrosion) can be seen for liquid/solid interaction and there is only mechanical degradation (erosion). On the other hand, several experimental investigations showed that below a critical impact speed no mechanical degradation occurs [7, 45, 46]. However, Heymann [47] questioned this point and explained that mechanical damage happens at all speeds; however, it needs very long exposure to erosion. Furthermore, the relation between impact velocity and erosion rate, the most important indicator of erosion damage, was of great interest in previous works. Different functional forms were used to fit the experimental data for this relation [7, 8, 45-48] and they are reviewed in chapter 2.

1.1.3.2. Impact angle

In service conditions, blade twisting and air turbulence in the chamber result in different impact angles along the turbine blades. Therefore, the influence of impact angle on erosion behaviour was studied in the literature and it was mainly described by its effect on the impact speed [2, 32, 49]. Water erosion is a strong function of normal impact velocity and this velocity varies with changing the impact angle. The influence of impact angle was explored during the incubation period of erosion and before the formation of craters, because the crater formation leads

to lose of control of the impact angle [49]. Heymann [47] explained that even during the incubation period studying the influence of impact angle is challenging because of the surface roughness variation. This implies that the impact angle affects only very early stages of erosion and some researchers such as Lee *et al.* [49] claimed that this effect could be neglected. However, Ahmad [32] recently reported a notable influence of impact angle on water erosion, shown in Figure 1-7. The maximum erosion damage, cumulative volume loss after 50h, occurred at impact angle of 90° which is associated with the maximum normal component of impact velocity. In the case of solid particle erosion, the impact angle associated with the maximum damage depends on the target mechanical properties. It is 22.5° for ductile materials and 90° for brittle materials [50].

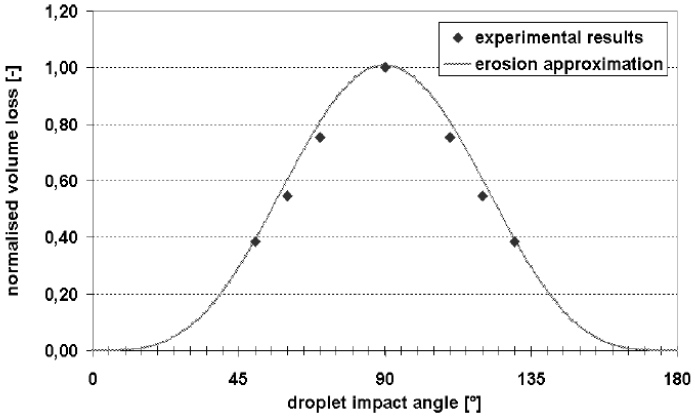

Figure 1-7: Normalized material loss of stainless steel eroded at different impact angles [32]

1.1.3.3. Droplet size

Another parameter affecting water erosion damage is the size of impacting droplets. The droplet size influences the area exposed to the impacts, time duration of each impact pulse, distribution of impact pressure, and the transferred kinetic energy [2, 49, 51]. The general trend is that increasing droplet size accelerates the erosion damage. Heymann [2] explained that using same volume of water, larger droplets cause more and faster damage. Although the target is impacted by greater number of smaller droplets, these impacts are not as destructive as large droplet impacts. This was explained by fatigue-like mechanism of erosion damage and detrimental kinetic energy of water droplets [2, 27]. Besides, it was claimed that the damage caused by water erosion is a function of droplet radius at the contact area and not its mass [19]. It denotes that the droplet shape also affects the erosion damage. Hence, the radius of flattened area must be taken as the influencing radii for a deformed droplet in the contact region. It has been argued that a small

flattened droplet behaves similar to a larger sphere droplet [18, 52]. This would be correct for the stress distribution; however, it can be questioned in term of transformed kinetic energy. This energy is a direct function of droplet mass/volume and the difference in amounts of kinetic energy for a small flattened droplet versus a large sphere droplet is significant.

1.1.4. Time dependence of water droplet erosion

Erosion is a progressive and time-dependent mechanical damage. As explained earlier, the localized plastic deformation, micro-cracking, and local fractures cause material removal during erosion. Time dependence of cumulative material loss has a non-linear nature, similar to what was observed for the cavitation erosion [53]. Figure 1-8 demonstrates different forms of erosion graphs, cumulative material loss versus cumulative exposure duration. Curve A is the typical S-shaped graph, which is seen for erosion of bulk materials. Curve B could be seen when the erosion conditions, i.e. impact speed and droplet size, are severe for the target. Curves C and D are anomalous for the erosion damage and therefore cannot be accepted. It is worthy to note that the erosion results of surface treated coupons do not necessarily fit in the aforementioned graphs and their behaviour depends on surface structure and microstructure.

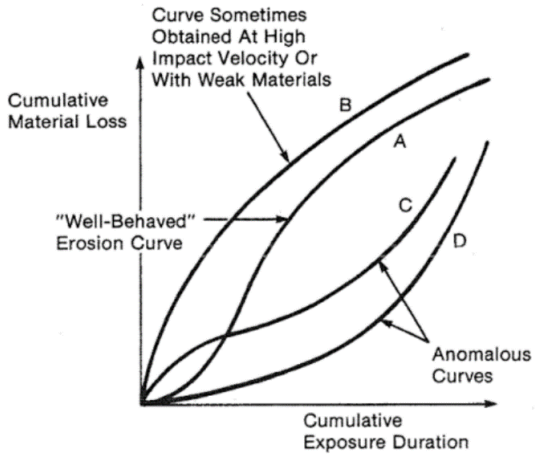

Figure 1-8: Different forms of erosion graphs [54]

Typical S-shaped erosion graph was divided by Heymann [2, 53] into five distinct stages, shown in Figure 1-9-a.

A. **Incubation stage:** At the beginning of erosion, droplet impacts mainly cause local material flow and micro-cracking; however, no material loss or a little can be detected, as can be seen in curve A of Fig 1-8. This stage may be very short and not observed in the case of

severe erosion conditions, when initial droplet impacts cause detectable material loss. This is demonstrated in curve B in Figure 1-8.

B. **Acceleration stage:** Immediately after the initiation of micro-pitting, greater material removals could be seen with further droplet impacts. In this stage, the erosion rate grows rapidly and reaches its maximum value, as shown in Figure 1-9. This period is associated with coalescence of the generated pits and noticeable increase in the size of the crater.

C. **Maximum erosion rate stage:** In this stage the material loss rate remains constant or nearly so, resembling the maximum erosion rate. The formed craters in this period of erosion become deeper and larger.

D. **Deceleration or attenuation stage:** Once erosion craters reach a certain depth, erosion rate decreases notably (25 to 50% of maximum erosion rate). It was attributed to the very high roughness of eroded surface (generated peaks and pits), which changes the stress distribution. Also, some water which is trapped in the crater may cushion the impact and decelerate the erosion damage.

E. **Terminal steady state stage:** This is the last stage of erosion evolution, when the material loss rate becomes again constant or nearly so. This stage was not captured in water droplet erosion of brittle materials.

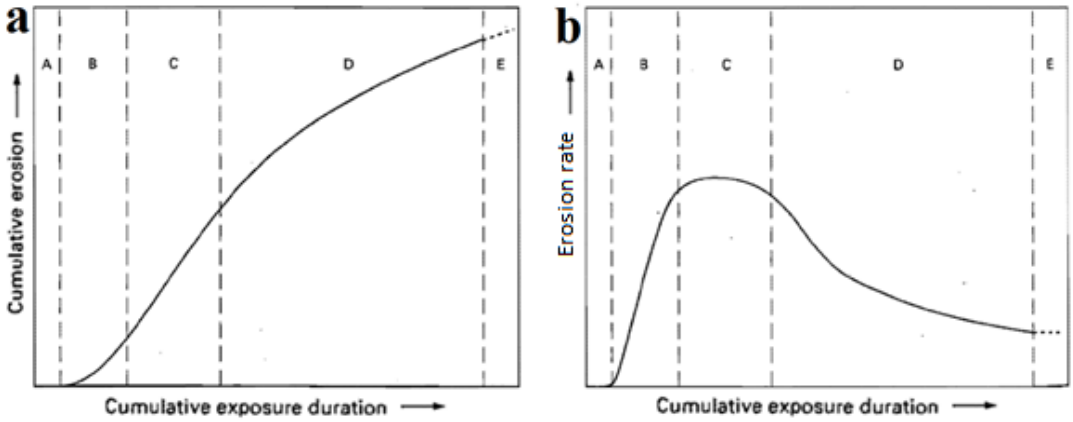

Figure 1-9: (a) Typical water droplet erosion and (b) erosion rate graphs showing five different stages [53]

1.1.5. Representation of water droplet erosion results

Erosion results are conventionally represented using the cumulative materials loss (vertical axis) as a function of cumulative erosion exposure duration (horizontal axis). They are referred to

as water droplet erosion graphs. In addition, erosion rate graphs are also considered in the literature, shown in Figure 1-9-b. They are beneficial to track down the erosion performance during the whole experiment. In open literature, erosion rate graphs are mainly plotted with the instantaneous erosion rates, which are the slopes of the lines connecting two consecutive points on the erosion graphs [2, 8, 46, 53, 55]. However, Rao & Young [56] proposed to use the cumulative erosion rates, which is the slope of the lines connecting the origin to each point on the erosion graphs, in order to diminish possible bios and noises. The cumulative erosion rate is not a popular idea in the literature; however, it was used by Ahmad *et al.* [8, 51] to find Cumulative Erosion Resistance (*CER*). *CER* is the reciprocal of cumulative erosion rate at the end of experiment.

The erosion graphs are represented in the literature with different parameters trying to capture the maximum amount of information in these graphs [2, 7, 8, 35, 41, 46, 48, 51, 57, 58]. For the vertical axis, either mass loss or volume loss were used [7, 8, 35, 41, 46, 58]. However, various parameters were used to represent the erosion exposure duration. Erosion time [8, 59-61], number of cycle [41, 51, 62], droplet/jet impact number [46, 63], droplet/jet energy [35] and volume of impacting droplets [53] were used to represent the erosion exposure. This makes comparison of the previous results impossible. ASTM standard G73 [54] describes the basic approach for erosion investigation and guidelines for results representation, which are used in this thesis.

In order to plot the erosion graphs, the experiments are interrupted at different time intervals to weigh the coupons and record the mass loss. This mass loss is converted to the volume loss knowing the density of tested coupons. Recording the cumulative mass loss at different time intervals reveals the points constructing the erosion graph, shown in Figure 1-10-a. ASTM standard G73 recommends to use volume loss (vertical axis) versus volume of water droplets impacting the surface (horizontal axis) for erosion graphs. This approach results in the dimensionless slope for the erosion graph, which would be necessary for the comparative studies. However, exact volume of impacting water was not known in most of the previous studies. Using the erosion graph, three important erosion indicators could be extracted, incubation period (H_0), maximum erosion rate (ER_{max}), and final erosion rate (ER_{final}), as shown in Figure 1-10-b [2, 54]. The first two can be found for all materials; however, the last one may not be revealed during the erosion of brittle materials [2]. Indeed, there is a relatively large variation for the final erosion rate

of such materials because of the brittle fractures leading to the detachment of relatively large fragments [25, 64]. In addition, very long experiments are required to reach the final steady state stage for the erosion resistant materials. In this thesis, incubation period (H_0) and maximum erosion rate (ER_{max}) are used to represent the erosion performances. ER_{max} is extracted by fitting the best line through the points in stage C, shown in Figure 1-10-a. The slope of this line is taken as ER_{max}. In addition, the intersection of this line with erosion exposure axis is taken as the incubation period (H_0), as shown in Figure 1-10-b [54]. Since the surface treated coupons do not usually show the typical S-shaped erosion graph, using the mentioned indicators for them is challenging. Therefore, cumulative erosion resistance (*CER*) are mainly used in this work for comparative investigations. *CER* is defined as the ratio of total volume of impacting water to total volume loss of the target. This indicator reflects the total resistance of the material to water droplet erosion. It is noteworthy that the erosion resistance, which is used further in the thesis, is inversely proportional to the erosion rate.

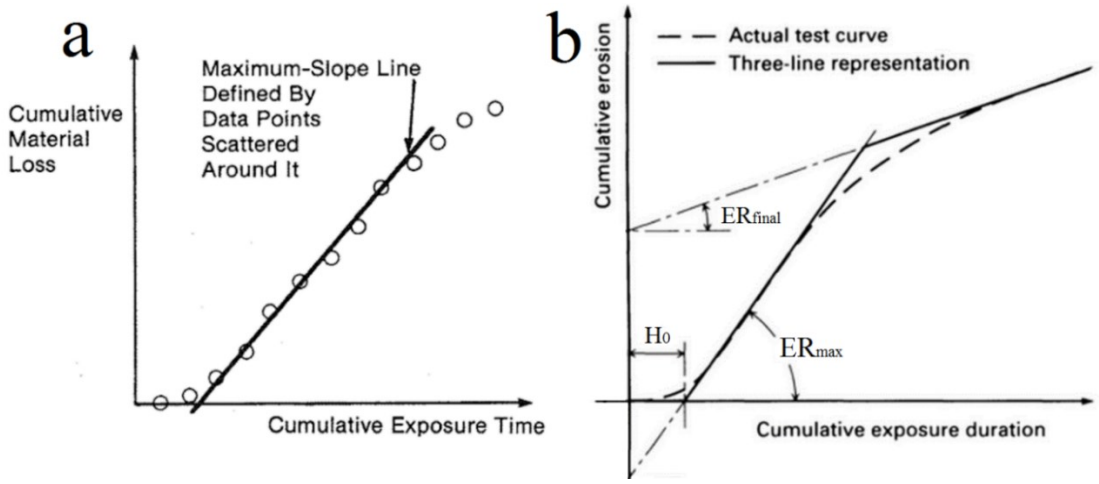

Figure 1-10: (a) Typical S-shaped erosion graph plotted through experimental points, (b) extracting the erosion indicators from material loss graphs [2, 54]

ASTM standard G73 describes a certain procedure to study the influence of impingement parameters (e.g., impact speed) on the erosion behaviour. Indeed, the results must be expressed using physically meaningful variables, which are dimensionless. Hence, the incubation period (H_0) is represented using specific number of impacts. Also, the rationalized erosion rates (*RER*) are used. These parameters are explained in detail in chapter 2. Furthermore, using a reference coupon in each erosion experiment is strongly recommended in ASTM standard G73. This approach allows to represent the erosion behaviour of each coupon with respect to that of the reference pair.

This is beneficial in order to detect small changes in water erosion performances. In this work, Ti6Al4V is used as the reference coupon in erosion experiments.

In summary, the erosion and erosion rate (instantaneous rate) graphs (Figure 1-9) are plotted as the basic erosion results. From these graphs, erosion indicators are extracted and the ones reported in this thesis are as follows: Incubation period in terms of either volume of impacting water or specific number of impacts (H_0); Maximum erosion rate (ER_{max} or RER_{max}); and Cumulative erosion resistance (*CER*) of each sample normalized to *CER* of Ti6Al4V pair. More details on erosion experiments could be found in Appendix.

1.2. Promising water droplet erosion resistant materials and surface treatments

Erosion resistance have been widely correlated to the mechanical properties of the target such as yield strength and hardness, ultimate resilience ($S_u/2E$, where S_u is ultimate strength and E is modulus of elasticity), true stress at fracture, strain energy to fracture, and work hardening rate [2, 8, 12, 65, 66]. Amongst these parameters, yield strength and modulus of elasticity were introduced as the most important ones by Heymann [66]. The material strength is the most corresponding index to erosion performance. Usually the higher the mechanical strength, the more the erosion resistance [66]. The mechanical strength is more important in the surface of target and it can be addressed by hardness. In order to enhance WDE of turbine blades, either a new stronger alloy should be used or the surface of currently used alloy (Ti6Al4V) must be hardened. Based on the high strength of TiAl alloy and its superior cavitation erosion resistance [67-69], it would be a promising water droplet erosion resistant material especially because it is even lighter than Ti alloys. Therefore, its WDE performance and damage mechanism are comprehensively investigated in chapters 2 and 3.

Surface of Ti6Al4V is being modified using different techniques. They can be classified into four main groups: thermal treatments; thermochemical treatments; deposition of thin films; and fabrication of thick coatings [70]. Surface treated samples using the mentioned techniques are schematically presented in Figure 1-11. Applying a thermal surface treatment such as laser hardening hardens the surface due to phase transformation and microstructure refinement. The main challenge for this process is controlling the formation of micro-cracks due to rapid solidification [71]. These micro-cracks would be detrimental in erosion applications. Thermochemical treatments harden the surface by making two main layers on the sample. The first

one is compound layer, which is hard and brittle ceramic film. The level of porosity and adhesion strength to the sample are the main parameters determining the mechanical stability of compound layer. Beneath this layer, there is a diffusion layer which is hardened by the formation of interstitial solid solutions [70, 72]. Solid solution strengthening increases the hardness without adding an interfaces, which is suitable for erosion applications. Thermochemical treatments require high temperature and it may change the microstructure of base material. To avoid this, hard and thin films at relatively low temperatures are fabricated on the substrate using vapour deposition methods such as Cathodic Arc Physical Vapor Deposition (CAPVD). The main issues for vapour deposited films are the formation of micro-cracks and micro-pores within the films, their residual stresses, and their adhesion to the substrate [70]. These films are vulnerable when they are subjected to the harsh mechanical loading. The last technique is thermal spray coating, which is used to fabricate thick layers on the surface by spraying various powders. [73]. The main issues for sprayed coatings are their porosity, adhesion of splat boundaries and the quality of coating/substrate interface [73]. Such microstructural defects would be detrimental for WDE application because they facilitate the cracking upon droplet impacts and stress wave propagation.

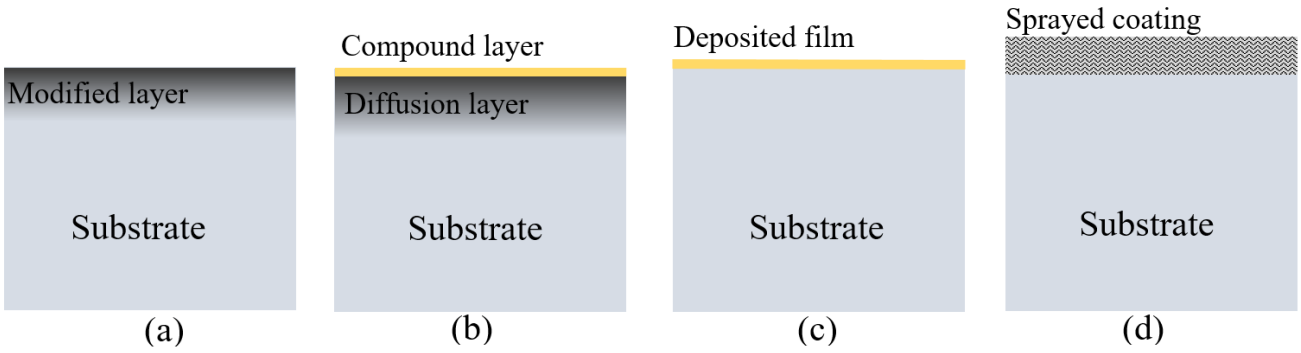

Figure 1-11: Different surface treatments of titanium alloys: (a) thermal treatments, (b) thermochemical treatments, (c) thin film deposition, (d) thermal spray coating

Water droplet erosion performance of surface treated Ti6Al4V have been rarely investigated. However, their cavitation erosion behaviour have been well studied in the literature [74-77]. The nature of cavitation erosion damage and water erosion damage is similar because in both cases hydrodynamic forces are exerted on the sample. Therefore, available literature for both cavitation and water erosion performance of surface treated Ti6Al4V and stainless steel are reviewed. Figure 1-12 demonstrates the erosion resistance of bulk TiAl and surface treated coupons normalized to their reference material (i.e. Ti6Al4V or stainless steel). Herein, the erosion

resistance were taken from different articles. In some of them, only the level of improvement at the end of experiment is given without clear definition for the considered erosion indicators [67, 74]. In the other ones, the erosion graphs are provided [76, 78-80]; however, there are different scales for the erosion graphs and no standard indicator is considered. In order to have relatively fair comparison, *CER* was derived from erosion graphs and then normalized by *CER* of reference material in that article. It is noteworthy that this graph is not a very accurate comparison because of different reference materials, different experimental setups, and different erosion conditions used in the previous studies. However, it provides general ideas about the potential of different surface engineering techniques or materials to combat erosion.

Nitriding is the most common thermochemical treatment applied on titanium alloys. Nitrided Ti6Al4V demonstrates superior erosion resistance almost at all of the previous studies, shown in the second column of Figure 1-12. Erosion performance of nitrided Ti6Al4V depends on the utilized nitriding parameters which are reviewed in chapter 4. Sprayed cermet coatings are found resistant to erosion; however, large variation can be seen for their performance [48, 62, 79]. In a few cases, they showed even worse performance compared to the substrate. The reasons for such variation are explained in chapter 5. Laser hardening enhanced the erosion resistance of Ti6Al4V and stainless steel in all previous investigations. Unlike laser hardened samples, vapour deposited hard films do not always show superior erosion resistance. The last column in Figure 1-12 indicates that the ratio of erosion resistance of coated sample to that of reference material is between 0.4 and 11. This ratio is highly dependent to the mechanical stability of deposited thin films, their thickness, and erosion severity. The more aggressive the erosion conditions, the less the erosion resistance of vapour deposited samples.

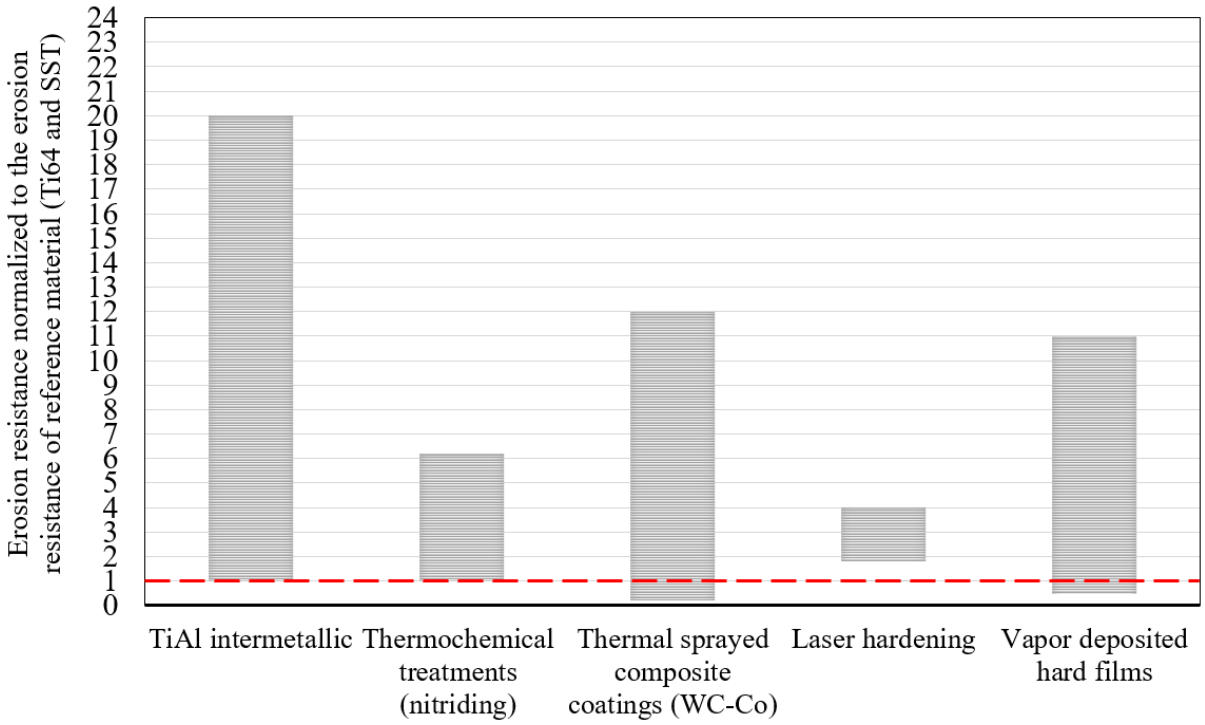

Figure 1-12: Cumulative erosion resistance of TiAl intermetallic and surface treated Ti6Al4V normalized to that of reference material [48, 61, 67, 68, 74-76, 78-81]

1.3. Objectives

The main objective of this research is to improve water droplet erosion resistance of gas turbine compressor blades. Two approaches are used to tackle this objective: (1) proposing an erosion resistant alloy which can be potentially used for the compressor blade; (2) enhancing the erosion resistance of Ti6Al4V using two different surface treatments. To achieve the main objective, the sub-objectives are defined as follow:

- Studying water droplet erosion of nearly fully lamellar TiAl alloy
    - Investigating erosion performance of TiAl compared with Ti6Al4V at different impact velocities and droplet sizes
    - Understanding the erosion damage mechanism of TiAl alloy at different phases of erosion including the incubation, material loss initiation and advanced stages
- Studying the influence of gas nitriding treatment on water droplet erosion behaviour of Ti6Al4V
    - Investigating the erosion performance of Ti6Al4V which are nitrided at different conditions in comparison with non-treated Ti6Al4V
    - Understanding the erosion damage mechanism of gas nitrided Ti6Al4V
- Exploring the potential of WC-Co coating sprayed by HVOF technique to combat water droplet erosion damage
    - Investigating the erosion performance of WC-Co coatings sprayed at different conditions in comparison with Ti6Al4V
    - Understanding the erosion damage mechanism of thermal sprayed WC-Co coating

1.4. Thesis layout

This section outlines the format of the current manuscript-based thesis. This document consists of six chapters. Chapter 1 gives an introduction about water droplet erosion. The physic of solid/liquid impact are briefly described, the erosion damage mechanism is reviewed, and the common methods to represent the erosion results are highlighted. Afterward, the objectives of this thesis are presented. In chapter 2, the erosion performance of TiAl is investigated compared with Ti6Al4V. The influences of impact velocity and droplet size are examined on the erosion behaviour of these structural alloys. In addition, the critical impact speed or damage threshold (V_C) for water droplet erosion of TiAl is determined. In this chapter, it is verified that water droplet erosion resistance of TiAl is superior to that of Ti6Al4V at all erosion conditions. Hence, chapter 3 presents in-depth investigation of WDE damage mechanism for nearly fully lamellar TiAl alloy. The eroded coupons at different phases: incubation, material loss initiation, maximum erosion rate and advanced stages of erosion are characterized. In order to address the second approach mentioned in the objectives, chapter 4 is dedicated to the influence of gas nitriding on water erosion behaviour of Ti6Al4V. Ti6Al4V specimens which were nitrided at two different temperatures (900 and 1050°C) for 5 and 10 hours are characterized. Their erosion behaviour in comparison with as-received and annealed Ti6Al4V are examined at two different impact speeds. Afterwards, erosion damage mechanism of the nitrided coupons is described. In chapter 5, potential of WC-Co thermal sprayed coatings are examined to combat water droplet erosion. Two different WC-Co powders were sprayed using HVOF technique, and two relatively thick cermet coatings with different microstructures were obtained. Their erosion performance in comparison with the as-received Ti6Al4V are explored at three different impact speeds (i.e. 250, 300, and 350m/s). Afterward, the erosion damage mechanism of coatings with splat microstructure are explained. Chapter 6 summarizes the findings in this research and presents the conclusions, contributions, and recommendations for future work. At the end of each manuscript, a short text is added to connect the chapters and ensure the coherency of the thesis.

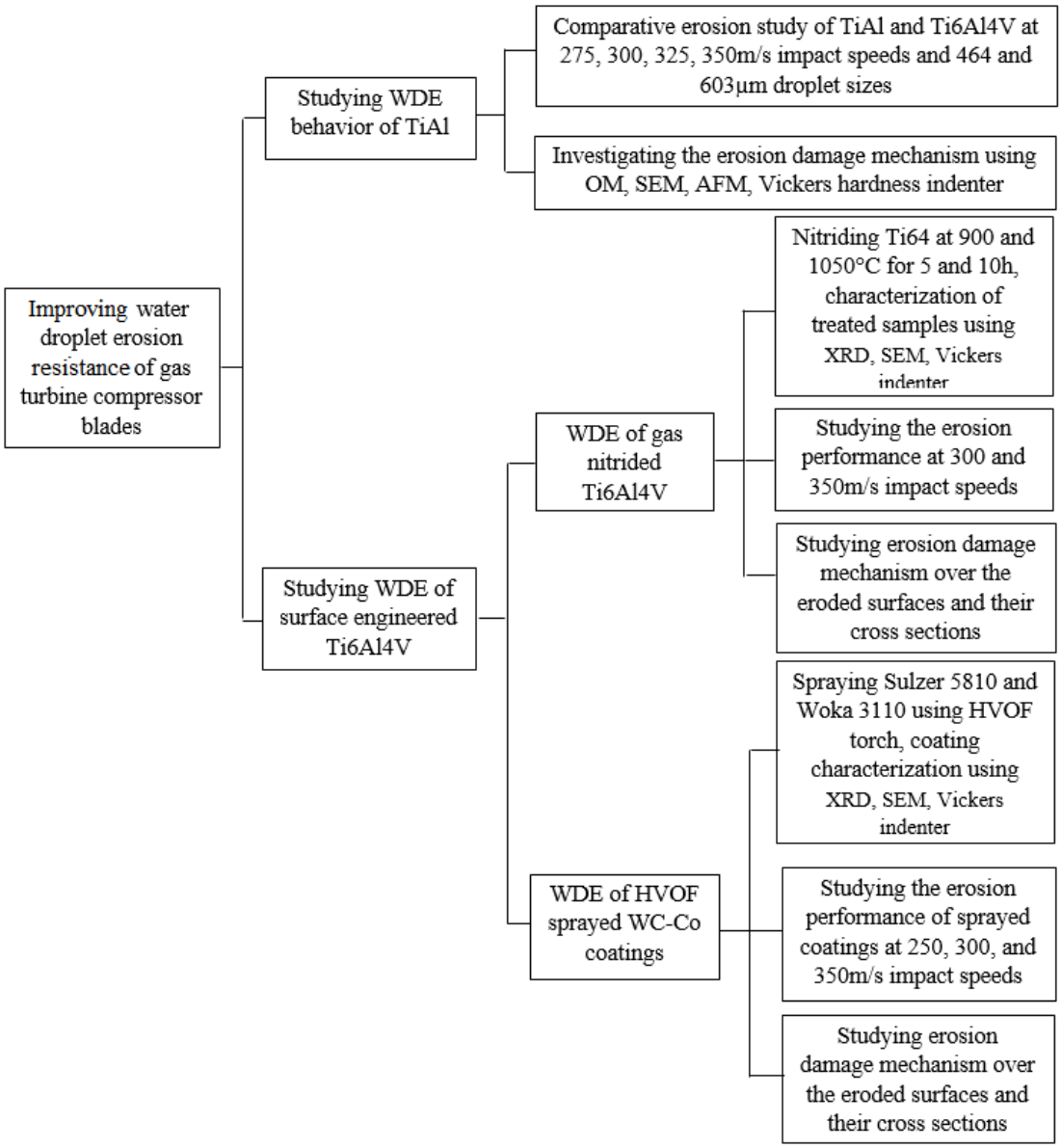

Figure 1-13: Flowchart of the thesis

Chapter 2 : Influence of impact speed on water droplet erosion of TiAl compared with Ti6Al4V

M.S. Mahdipoor[1], H.S. Kirols[1], D. Kevorkov[1], P. Jedrzejowski[2], M. Medraj[1,3]

[1] Department of Mechanical and Industrial Engineering, Concordia University, 1455 de Maisonneuve Boulevard West, QC, Montreal, Canada H3G 1M8

[2] Rolls-Royce Canada Ltd. Energy, 9545 Cote-de-Liesse, Dorval, QC, Canada H9P 1A5

[3] Department of Mechanical and Materials Engineering, Masdar Institute, Masdar City, Abu Dhabi, UAE, P.O. Box 54224

This article has been published in the *Journal of Scientific Reports,* 5 (2015), DOI: 10.1038/srep14182[1]

ABSTRACT

Water Droplet Erosion (WDE) as a material degradation phenomenon has been a concern in power generation industries for decades. Steam turbine blades and the compressor blades of gas turbines that use water injection usually suffer from WDE. The present work focuses on studying erosion resistance of TiAl as a potential alloy for turbine blades compared to Ti6Al4V, a frequently used blade alloy. Their erosion behaviour is investigated at different droplet impact speeds to determine the relation between erosion performance and impact speed. It is found that the relationship is governed by a power law Equation, $ER \sim V^n$, where the speed exponent is 7-9 for Ti6Al4V and 11-13 for TiAl. There is a contrast between the observed speed exponent in this work and the ones reported in the literature for Ti6Al4V. It is attributed to the different erosion setups and impingement conditions such as different droplet sizes. To verify this, the erosion experiments were performed at two different droplet sizes, 464 and 603μm. TiAl showed superior erosion resistance in all erosion conditions; however, its erosion performance exhibits higher sensitivity to the impact speed compared to Ti6Al4V. It means that aggressive erosion conditions decrease the WDE resistance superiority of TiAl.

[1] In this article, Mr. Kirols helped with the experiments. In addition, Dr. Kevorkov, as the Research Associate at TMG, and Dr. Jedrzejowski, as the industrial partner, helped in the interpretation of the results.

2.1. Introduction and literature review

Water droplet erosion (WDE) is a result of repetitive high-speed water droplet impacts on solid surfaces which generate impulsive pressures [2]. This impact wear phenomenon seen on high-speed moving components in environments containing water droplets has always been a challenge, as it may decrease their service life. For instance, water is sprayed to cool down the air intake to gas turbine compressors [9]. As a result, high speed impingements between the applied water droplets and the compressor's rotating blades cause WDE, especially for their leading edges. Moreover, the water droplets form at the low pressure stages of steam turbines due to steam condensation, which results in erosion of the blades [2, 11]. The erosion of these components reduces, to a great extent, the power generation efficiency of turbines [9, 11]. Water impingement erosion can also be observed in aircraft's aerofoils, missiles and helicopter rotors which is called rain erosion [2]. WDE is a complicated combination of several phenomena. The imposed normal pressure, the subsequent stress waves and the formed outflow jets are the main reasons for damage in the target material [2, 24]. The magnitude of impact pressure, area exposed to stresses and time duration of each impact pulse are functions of impingement conditions. Velocity of outflow jets and subsequent stresses also depend on the impact conditions [47]. Hence, determining theoretical and empirical relationships between the erosion rate or erosion resistance (reciprocal of material loss rate) and the WDE test parameters including impact speed and droplet size have been attempted by several scientists [24, 47, 57].

Theories based on the normal impact stresses (water hammering), stress waves, and energy transferred to the target were proposed in the literature for WDE [24, 47, 57]. The impact speed is the main parameter considered in all of them. It was also confirmed by experimental results [7, 8, 46, 48, 58] that the erosion performance and the damage mechanism change significantly at different impact speeds. Experimental data were fitted to different functional forms in order to find the relationship between the erosion performance (erosion rate) and the impact speed. The most important ones were summarized by Heymann [47] and are listed below:

$$ER = aV^n \qquad \textit{Equation 2-1}$$

$$ER = a(V - V_c)^n \qquad \textit{Equation 2-2}$$

$$ER = ae^{nV} \qquad \textit{Equation 2-3}$$

where ER is the erosion rate, V is the impact speed, V_C represents the threshold speed and a is a constant. The simple power relationship, Equation 2-1, is the most used form to correlate ER and V [46-48]. However, it implies that WDE takes place regardless how low the impact speed is. Whilst, the common thought is that there is a critical or threshold speed called V_C, below which erosion does not take place. Therefore, an erosion-impact speed relationship based on this concern was developed, Equation 2-2 [47], to fit the experimental data. Nevertheless, it was not as accurately representing the experimental results as Equation 2-1, in the usual range of impact speeds ($1.5<V/V_C<3$). Another relationship based on the analogy of fatigue is Equation 2-3; however, it was not referred to in the literature as much as the first two Equations [47, 66]. The speed exponent in Equations 2-1 and 2-2 is an important value in the erosion performance investigations. It was claimed that the erosion damage is proportional to V^2 for solid particle erosion [48]; however, it is not the case for water droplet erosion. A list of the reported speed exponent (n) values for different materials and their test conditions are summarized in Table 2-1. It is worth mentioning that the way of representing the ER_{max} is different in each case as explained in the table.

Table 2-1: The impact speed exponent in Equation 1-1 found in different water erosion investigations

Authors	Tested material	Range of impact speeds (m/s)	Impinging water conditions	ER representation	Speed exponent range (n)
Thiruvengadam *et al.* [46]	Al, Ni, 316 Stainless Steel, Ti6Al4V	90 - 250	800µm, water jet, rotating arm	Maximum material loss rate, $cc(hr)^{-1}$	5 - 7
Oka *et al.* [48]	Stainless steel, TiN coated steel, Sprayed cermet coating	60 - 300	45 to 130µm, water droplet, spraying water droplets on a stationary target	Erosion damage rate,$mm^3(kg)^{-1}$	3 - 5.5
Hackworth [58]	Zinc sulfide (for Infrared window application)	200 - 350	700 to 1800µm, water droplet (rain erosion), rotating arm	Transmittance loss* rate (not material loss), $\%\ loss\ (min)^{-1}$	9 - 14
Ahmad *et al.* [8]	Stainless steel, Ti6Al4V	350 - 580	100-350µm, spraying water droplet, rotating arm	Erosion resistance (reciprocal of average material loss rate) at 50 hours erosion, sm^{-1}	3.8 - 5.3
Tsubouchi *et al.* [82]	Stainless steel	450 - 630	50µm, water droplet, rotating arm	Average material loss rate at 30 hours erosion, $mm(h)^{-1}$	5

*Since the rain erosion of materials for infrared window application was studied, the transmittance loss with respect to the original transparency was considered.

Clearly, studying the influence of impact speed on water erosion was not carried out based on a standard method. Its influence has been studied using different erosion indicators. Some research groups [8, 58, 66, 82] compared the average erosion rate at a specific exposure time (e.g., 30 hours). This type of comparison can be questionable because after 30 hours different samples might be at different erosion stages when tested at different speeds. Studying the relationship between impact speed and maximum erosion rate, Thirwvengadam's work [46], eliminates this concern. Moreover, with the large number of available experimental data, it was concluded that

even the best proposed erosion rate-impact speed relationship would only fit the data over a limited speed range [47, 66]. Indeed, this relationship is a function of water droplet erosion conditions and target material properties. The observed speed exponents for erosion rate-impact speed relationship, which can be seen in Table 1, are different because of diverse erosion conditions. Considering all of these studies [7, 8, 46, 48, 58, 66, 82], it seems that using a standard method to find a dimensionless maximum erosion rate and determine its relationship with impact speed is necessary. This approach is proposed by ASTM G73 standard [54] and is used in this study to calculate dimensionless erosion rate, unlike the previous works [8, 46, 48, 58].

Droplet size and its shape also affect the erosion damage. Unlike impact speed, the magnitude of impact stress was defined as independent of the droplet size or shape [24, 47, 57]. However, their influence on the erosion damage was observed in several experimental studies [7, 51, 66, 83, 84]. Honegger [7] carried out erosion experiments using 500 and 1,500μm jets and they found significant difference in the erosion damage. The difference was function of the utilized impact speed. Indeed, at high impact speeds, the influence of water jet diameter on the erosion damage decreases. The erosion damage caused by six different jet diameters ranging from 1,000 to 2,500μm was compared in another work [66]. For the jet diameters less than 1,600μm, incubation period increased considerably by decreasing jet diameter. The influence of jet diameter on the incubation period was confirmed also by Hancox and Brunton for jets smaller than 1,000μm [39]. It was demonstrated [47] that threshold speed which corresponds to the erosion endurance was influenced by jet diameter based on the following relationship.

$$V_C^2 D = Critical - Velocity - Constant \qquad \textit{Equation 2-4}$$

Heymann suggested that Equation 2-4 can be generalized for water droplet erosion [47]; however, it was not verified experimentally. Decorso *et al.* [83] confirmed that the larger the water droplets, the lower the threshold speed. They concluded that for the equal volume of impacting water, droplet size considerably affects the erosion damage for impact speeds close to the threshold. However, it does not influence the erosion when erosion tests are carried out at the impact speeds well above V_C. In the case of small droplets, the higher V_C and longer incubation period were attributed to the attenuation of impact stresses, less energy transferred to the target and lower chance for large fragment detachment [47]. Despite the mentioned explanation, there is no complete agreement on the reasons for the influence of water droplet shape and diameter.

Recently, Hattori *et al.*[84] and Ahmad *et al.*[51] reported that the erosion rates of Al and Ti6Al4V are found to be proportional to the droplet diameter as, $ER \propto V^{4.7}$ for Al and $ER \propto V^{2.5}$ for Ti6Al4V. It is a notable dependency, which cannot be justified only by different duration of impact pulse or area exposed to the impacts. Therefore, more investigations need to be carried out in order to clarify the role of droplet size on the erosion damage.

Additionally, target material characteristics are effective parameters for water droplet erosion damage. Hardness, yield and ultimate strength, strain energy, modulus of resilience, hardenability, and crack-growth rate as a function of stress intensity (Paris law) are the mechanical properties of target material which were found to play roles in erosion damage [2, 39, 66]. None of these parameters has been accepted as the only index for erosion performance. Hardness is the most common property to which difference in erosion performance of materials relate. Heymann [66] reported that erosion resistance of metals is proportional to the target hardness as, $\propto HV^{2.5}$. He did not observe direct relationship between strain energy or modulus of resilience and erosion resistance. An empirical value, which is the product of strength squared and modulus of elasticity, $\sigma_u^2 E$, showed the best correlation with the WDE performance among the mentioned mechanical properties. Heymann [66] demonstrated that WDE resistance is proportional to $(\sigma_u^2 E)^{2/3}$. Hence, the higher the strength and modulus of elasticity, the higher the erosion resistance. Such values can be only assumed as primary indications for the erosion performance. However, to study the WDE behaviour measuring the erosion resistance by itself is essential.

Over the years, TiAl alloys have been considered as suitable materials for aeroengine applications, such as engine vanes or blades [85]. Their high specific strength, modulus of elasticity, hardness, fatigue strength, and hardenability make them potential candidates for wear and erosion applications. These alloys were investigated mostly for high temperature applications [85, 86]. However, some promising results about their cavitation erosion behaviour at room temperature were reported [68, 87]. Nakao *et al.* [87] investigated the cavitation erosion of different TiAl-based alloys compared to pure titanium and austenitic stainless steel. They reported that TiAl showed 20-30 times better cavitation erosion resistance than the other alloys. Howard and Ball [68] attributed the high cavitation erosion resistance of TiAl alloys to their initial high tensile strength and high work hardening rate, compared to 304 stainless steel and WC-Co. High strain hardening of TiAl works as a surface treatment and leads to hardness increases upon water

droplet impact, which is beneficial for erosion performance. They also proposed that the erosion mechanism is based on the "twinning deformation" that happened in this alloy. Twinning at the tip of large cracks impedes their propagation and causes the formation of micro-cracks instead [69]. Such behaviour results in the decrease of crack growth rate, and it was mentioned as another reason for superior cavitation erosion performance of TiAl alloy [68]. Thereby, if twinning occurs upon water droplet impact, a deceleration in crack growth rate is expected, which is beneficial for WDE performance. Despite the great potential of TiAl alloy to combat WDE, their water droplet erosion behaviour could not be found in the literature.

The main objective of this work is to study the WDE performance of TiAl compared with Ti6Al4V. This has been accomplished through the following sections. First, the erosion performance (incubation period and maximum erosion rate) of TiAl and Ti6Al4V alloys at different impingement conditions are compared and their differences based on the mechanical characteristics and microstructural changes are justified. Secondly, the erosion rate-impact speed relationships for TiAl and Ti6Al4V, which is also referred to as Ti64, are determined. Finally, the threshold speed or the erosion endurance of TiAl alloy for different droplets sizes is determined.

2.2. Materials and experimental procedures

2.2.1. Materials

An annealed Ti6Al4V sheet and a heat treated Ti45Al2Nb2Mn0.8TiB_2 (45-2-2XD) plate were received from Titanium Industries Inc. and Rolls-Royce Canada Ltd., respectively. They are referred to as Ti6Al4V and TiAl. Erosion specimens (23mm×8mm×3mm) were prepared from these two alloys. The target surfaces were ground using SiC grinding papers of 600 grit size. The surface roughness of erosion coupons was kept as similar as possible to minimize its influence on the erosion behaviours. The received Ti6Al4V contains α and β phases with a homogenized equiaxed microstructure as shown in Figure 2-1-a. The studied TiAl alloy was received as a plate undergone a special treatment (i.e. hot isostatic pressed and then heat treated). TiAl alloy has nearly fully lamellar microstructure composed of α_2 phase in γ phase matrix, as shown in the Figure 2-1-b. The density and mechanical properties of these alloys including their young's modulus, yield strength, and modulus of resilience are listed in Table 2-2. The young's modulus was taken from the literature [69, 88, 89]. The yield strengths values were inferred from the hardness measured in this work. They are approximately 1/3 times the Vickers hardness [90]. Modulus of resilience was

derived from the yield strength and Young's modulus. In this work, erosion performance are explained based on the mechanical properties and microstructures.

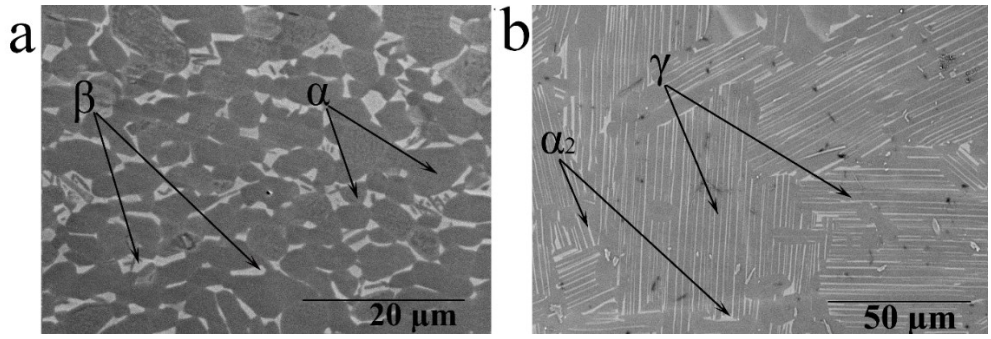

Figure 2-1: SEM micrographs of: (a) annealed Ti6Al4V, (b) HIP TiAl

Table 2-2: Mechanical properties of Ti6Al4V and TiAl [69, 86, 88-91]*

	Density (g/cm^3)	Young's Modulus (GPa)	Yield Strength (MPa)	Modulus of Resilience, $\sigma y^2/2E$ (kJ/m^3)
Ti6Al4V	4.42	113	993	4.36
TiAl	4.00	160	1120	3.92

* Mechanical properties of TiAl may vary with microstructure; however, the most corresponding ones are presented here.

2.2.2. Water droplet erosion test

Water droplet erosion tests were performed using a rotating disk erosion rig with controlled conditions. It was designed based on the ASTM G73 standard [54]. It provides simulated impingement conditions between high speed rotating blades and liquid droplets for erosion studies. A schematic of the erosion rig including water droplet generation system is presented in Figure 2-2. The rotating disk can reach a maximum linear speed of 500m/s. Erosion test coupons should be mounted on the disk and based on the desired impact speed, the rotation speed would be set. The coupons mounted on the rotating disk are subjected to the water droplets with an impact angle of 90°, as can be seen in Figure 2-2. In order to produce the water droplets, distilled water is pumped into the droplet generation system after passing through 5 micron filters.

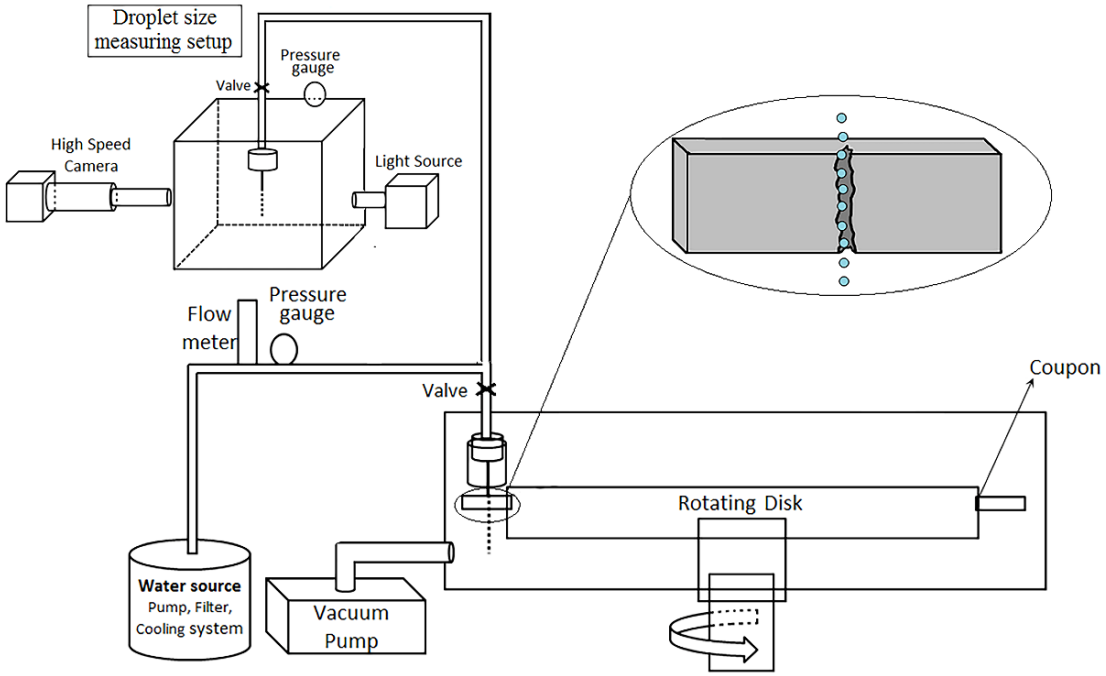

Figure 2-2: Schematic of the water droplet erosion rig and droplet size measuring setup

The water generation system includes a flow meter, a pressure gauge and a nozzle. The pressure of the pumped water and its flow were optimized to have water droplets in desired size and narrow size distribution. The nozzle is shielded against the turbulence occurring inside the chamber to ensure the straightness of water stream with minimum deviation and droplet distortion till impact. To acquire the droplet size distribution, a transparent box, shown in Figure 2-2, simulating the erosion chamber in terms of its pressure and the water droplets conditions was used. The water droplet diameters were measured in the box when the same water droplet generation system, nozzle, back pressure and flow rate were utilized. The falling droplets were monitored using a high speed camera and the diameters of 200 droplets were measured. The erosion test results are presented in the form of cumulative material loss versus cumulative exposure. Accordingly, the erosion tests were divided into several time intervals, in order to measure the mass loss per interval. After each interval, coupons were weighed five times. Their average weight was recorded and the difference from the initial mass is taken as the cumulative mass loss. The volumetric material loss was derived using the measured eroded mass and the density of the tested alloys. To make the erosion results consistent and following the ASTM standard, the obtained volume loss was normalized by the area exposed to droplet impacts. Such area was measured from the optical micrographs recorded at the beginning of the maximum erosion rate stage. Other

erosion characteristics were obtained from these water erosion graphs. Since all the erosion results are derived from mass loss, a high precision (0.1mg) balance was used. The maximum observed standard deviation was 0.2mg, which is less than 2% of the average measured mass loss after each interval.

The erosion curves were plotted according to the ASTM G73 standard [54]. The erosion performance variables, incubation period and maximum erosion rate, were determined from the graphs. Since quantitative comparison among different impingement conditions is one of the goals of this study, rationalized and dimensionless values for erosion rate and erosion time were utilized, based on the ASTM standard. Therefore, specific impact and rationalized erosion rate *(RER)* are defined [54] as:

$$Specific\ impat = \frac{Total\ number\ of\ impacts \times Area\ influenced\ by\ one\ droplet}{Total\ surface\ area\ exposed\ to\ erosion} \qquad \textit{Equation 2-5}$$

$$Impingement\ rate\ (U_i) = \frac{Volume\ of\ impacting\ water\ droplets}{Unit\ time \times Area\ influenced\ by\ one\ droplet} \qquad \textit{Equation 2-6}$$

$$Rationalized\ erosion\ rate\ (RER) = \frac{Volumetric\ erosion\ rate}{U_i \times Total\ surface\ area\ exposed\ to\ erosion} \qquad \textit{Equation 2-7}$$

According to the ASTM G73 standard [54], straight line best fit for the maximum slope points was plotted and its slope was considered as RER_{max}. The incubation period (H_0) was determined as the intersection of the fitted line with the X-axis.

As explained earlier, the threshold speed corresponds to the impact speed below which a very long incubation period can be seen. To determine the threshold, this long incubation needs to be defined. In this work, V_C corresponds to the speed at which one million droplets impacts per 1mm^2 do not cause measurable mass loss. It is noteworthy that 25m/s is the used interval in this work to study the influence of impact speed. Hence, the real critical impact speed would be between V_C (the speed at which one million droplets impacts per 1mm^2 do not cause measurable mass loss) and V_C+25 (the speed at which one million droplets impacts per 1mm^2 cause measurable mass loss). Here, V_C which is the minimum of this range is reported as the critical impact speed for safety measures.

An important aspect for experimental work is the repeatability of the tests. Therefore, the following experimental conditions were monitored and their repeatability was verified using sensors and gauges available on the test setup: stability of speed (rpm), stability of vacuum, and vibration. In order to ensure the repeatability and reliability of WDE test results, three specimens from annealed Ti6Al4V alloy were prepared. The material and its properties are assumed to be identical. Three erosion tests were performed at the same conditions, 350m/s impact speed and 464μm droplet size. The results are presented in Figure 2-3. They are consistent; however, some deviations can be seen. Similar deviations were reported in the literature [8]. The degree of deviation increases with the erosion time and higher deviation can be seen at the last stages. Erosion initiation and material loss is a function of coupon surface quality [2, 54]. There is less deviation at the initial stages because of the preparation of the coupons, which leads to similar surface conditions. It is not the case for the later stages, since the formation of craters change the surface topography with same degree of variability and lead to different hydrodynamic loadings and subsequently mass loss variation. The mass loss per interval was measured and the maximum standard deviation of mass loss in each interval was 1mg among the replicas, even at the later stages. The coupon resulting surface topography, impurities in the water, accuracy of the used balance and microstructural variations might be the reasons for such differences. In the current study, the influence of impingement speed on the erosion behaviour of Ti6Al4V and TiAl is studied. Four different impact speeds, 275, 300, 325, 350m/s, and two different droplet sizes are investigated as the erosion test conditions. Nozzle 1 and 2 were used to generate different droplet sizes of 464μm and 603μm, respectively.

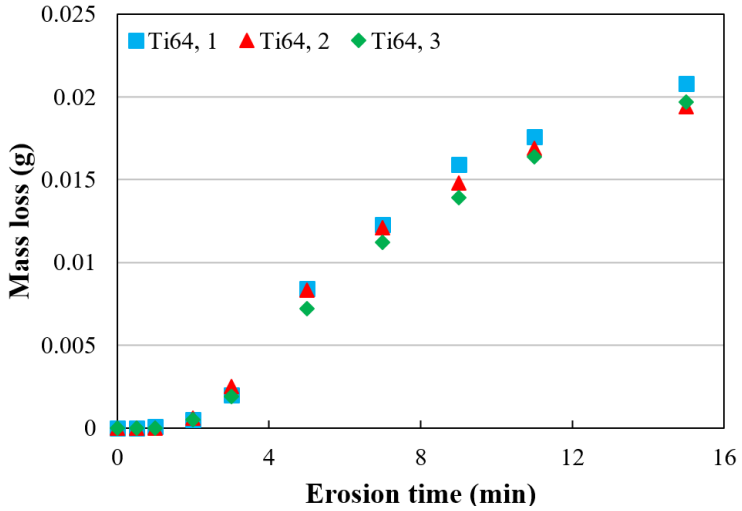

Figure 2-3: Erosion results of three Ti6Al4V coupons tested at 350m/s impact speed and 464µm droplet size showing repeatable experimental results

2.2.3. Imaging techniques

To document the microstructures of the as-received materials, a Hitachi S-3400N Scanning Electron Microscope (SEM) equipped with a backscattered electron detector was used. During the erosion experiment and after each time interval, the erosion craters were observed using an optical microscope MEIJI Techno IM7100 and their images were recorded. These optical images provide general idea of how erosion damage initiates, progresses and forms a complete erosion line.

2.2.4. Hardness measurements

Vickers hardness tester was used to measure the surface hardness of Ti6Al4V and TiAl specimens. Five indentations were performed (10kg load) at different positions on the test samples and their average value was taken as the hardness. In order to compare the mechanical behaviour of tested specimens, their yield strength values were inferred from their measured hardness.

2.3. Results

2.3.1. Surface hardness and roughness of erosion test coupons

The surface roughness and hardness of prepared coupons were measured after polishing. Respectively, 0.082±0.007 and 0.078±0.004µm are the surface roughness of Ti6Al4V and TiAl. Although they were polished using 600 grit SiC grinding papers, small variation are observed for the values of surface roughness. The hardness of Ti6Al4V and TiAl was found to be 284 and 338HV_{10}, these values are the averages of 5 readings. The hardness measurements were close and standard deviations were 12.5 and 9.1 for Ti6Al4V and TiAl, respectively.

2.3.2. Droplet size distributions

The diameters of 200 water droplets coming from each nozzle were measured using a high speed camera and their distributions are presented in Figures 2-4 and 2-5.

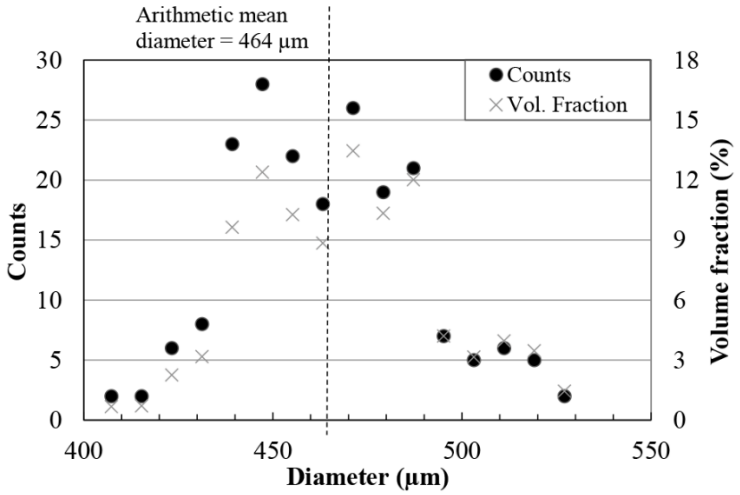

Figure 2-4: The number and volume droplet size distributions of 200 droplets generated using nozzle 1

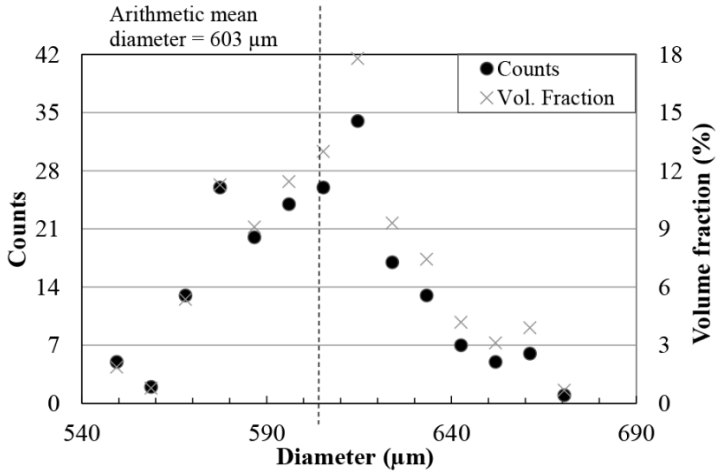

Figure 2-5: The number and volume droplet size distributions of 200 droplets generated using nozzle 2

Based on the droplet size distribution, the diameter of 78% of droplets range from 440 to 490µm in case of nozzle 1 and the diameter of over 80% of droplets range from 575 to 635µm for nozzle 2. Also, the presented volume fractions verify that a large volume of water (more than 75%) impacts the coupons as the droplets with diameter in the range of 430 to 490µm and 575 to 635µm. The arithmetic mean diameter based on the number of droplet counts was calculated as 464µm for droplets generated by nozzle 1 and 603µm for the ones generated by nozzle 2. To address droplet size further, these mean diameters are used.

2.3.3. Water droplet erosion performance of TiAl and Ti6Al4V alloys

2.3.3.1. Cumulative erosion, incubation period and maximum erosion rate

The erosion results are reported based on the cumulative material loss versus cumulative exposure. The cumulative material loss is defined as the difference in volume between the as-received specimen and the eroded specimen. The cumulative exposure can be represented using different parameters such as erosion time, number of impingements, and volume of water impacting the coupon [7, 8, 46, 48]. In this study, the cumulative volume of water impinging the surface was used to represent exposure, which results in a dimensionless erosion rate. It is noteworthy that in most of previous studies [8, 46, 58] either the number of rotations (in rotating arm designs) or exposure time (hours or minutes) were reported as the cumulative exposure parameter. These do not accurately describe WDE, since in most of these studies, the actual amount of water droplets impacting the samples was not known.

The erosion tests results of the current study are presented in Figures 2-6 and 2-7. They are plotted as the volume loss of material per unit area (mm^3/mm^2) versus the volume of impacting water droplets per unit area (mm^3/mm^2). In each figure, the erosion behaviour at constant droplet size but different velocities is demonstrated. Different stages of erosion damage can be easily identified in the plotted graphs of Ti6Al4V. However, this is not the case for TiAl alloy at low impact speeds and small droplets, where erosion did not reach the terminal stage as shown in Figure 2-7-a.

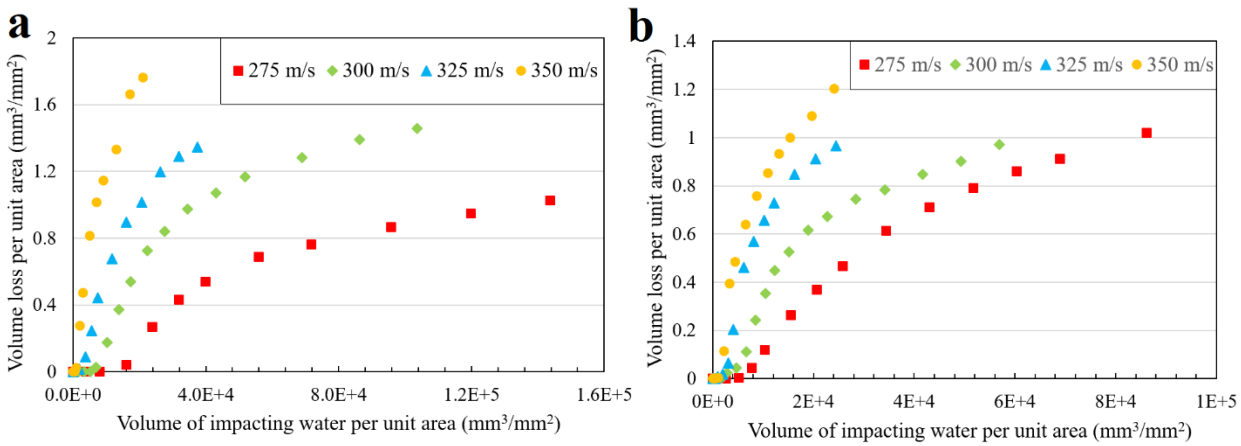

Figure 2-6: Water droplet erosion results, material loss versus volume of impinging water, for Ti6Al4V specimens tested at different impact speeds and droplet size of (a) 464µm, (b) 603µm

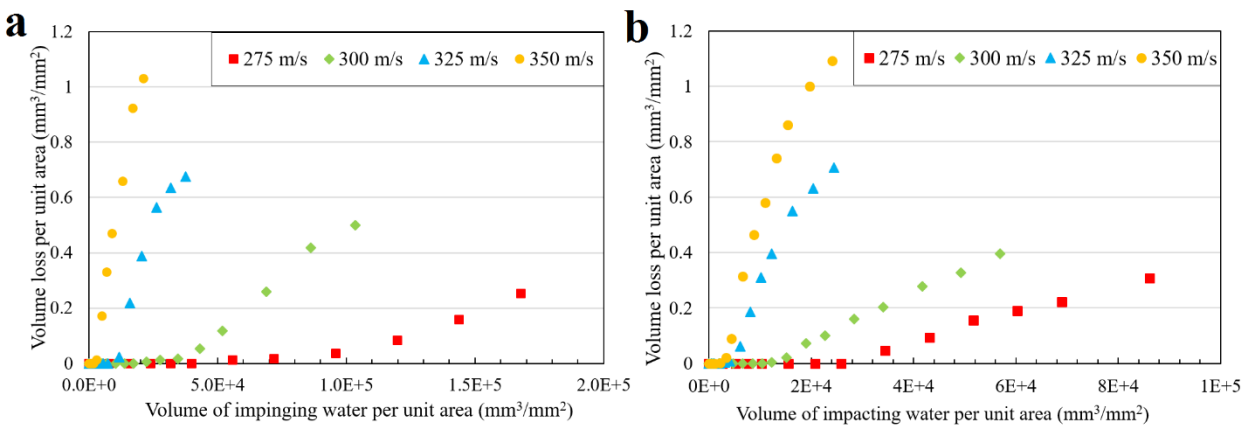

Figure 2-7: Water droplet erosion results, material loss versus volume of impinging water, for TiAl specimens tested at different impact speeds and droplet size of (a) 464µm, (b) 603µm

Different trends were observed for Ti6Al4V and TiAl alloys' erosion performance with changing the impact speed. The general propensity is that the higher the impact speed, the more the erosion damage. Furthermore, the larger the droplets size, the less the incubation period and the higher the maximum erosion rate. This is more evident for the erosion of Ti6Al4V. Here, erosion performance is represented by the incubation period (in terms of specific impacts), and the maximum erosion rate. These values were determined and plotted in Figures 2-8 and 2-9. TiAl shows 6 times lower RER_{max} than Ti6Al4V and more than 3 times longer incubation at the least severe erosion condition. In case of the most aggressive erosion condition, it exhibits 2.5 times lower RER_{max} than Ti6Al4V and only 2 times longer incubation period.

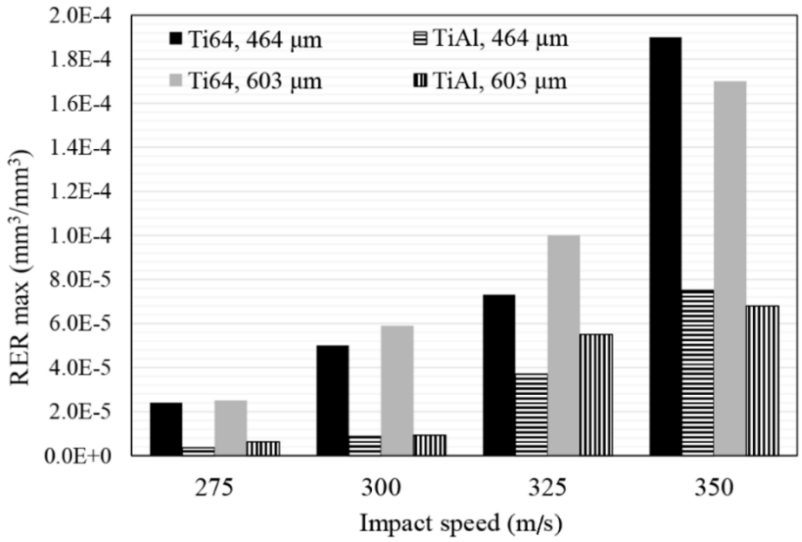

Figure 2-8: Maximum erosion rate of Ti6Al4V and TiAl alloys eroded by 464 and 603µm water droplets at four different impact speeds

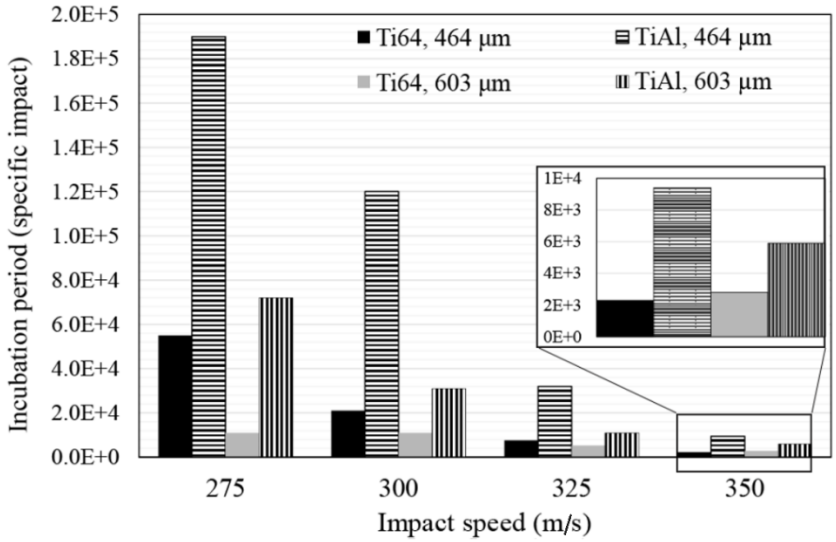

Figure 2-9: Incubation period of Ti6Al4V and TiAl alloys eroded by 464 and 603µm water droplets at four different impact speeds

2.3.3.2. Influence of impact speed on incubation period and erosion rate

Increasing the impact speed results in increasing the localized impulsive pressure on the target. The pressure resulting from liquid-solid impingement, known as the water hammer pressure, was firstly explained based on one-dimensional liquid-solid impact model [6].

$$P = \rho_0 C_0 V \qquad \textit{Equation 2-8}$$

where ρ_0 is the liquid density, C_0 represents the speed of sound in the liquid and V is the impact speed. It is a simplified condition which is not an accurate representation of reality. Heymann [24] theoretically analyzed and proposed a more accurate model to include the effect of shockwave formation.

$$P = \rho_0 C_0 V[2 + (2K - 1)\frac{V}{C_0}] \qquad \textit{Equation 2-9}$$

where k is an impinging liquid constant. The impact pressure is presented independent of the droplet size. In this study, Heymann's Equation is used to calculate the impact pressure corresponding to different erosion conditions. In the case of water droplet erosion k, ρ_0 and C_0 are 2, 1,000kg/m^3 and 1,463m/s [24], respectively.

In addition, the time duration of an impact pressure pulse was found to be a function of droplet diameter and Equation 2-10 was introduced by Bowden and Field [21, 38].

$$\Delta\tau = \frac{3rV}{2C_s^2} \qquad \textit{Equation 2-10}$$

where *r* represents the radius of the water droplet front curvature, and *Cs* is the shock wave velocity in the water droplet. Table 2-3 presents the impact pressure and duration of each impact pulse which help to explain different erosion performances.

Table 2-3: Impact pressure and time duration of one impact pulse calculated for different erosion conditions based on Equations 2-9 and 2-10

Impingement conditions		**Impact pressure (MPa)**	**Duration of the impact pulse (µs)**
Droplet size (µm)	**Impact speed (m/s)**		
464	275	1032	0.0234
	300	1148	0.0243
	325	1268	0.0251
	350	1392	0.0258
603	275	1032	0.0307
	300	1148	0.0319
	325	1268	0.0330
	350	1392	0.0339

Figures 2-10 and 2-11 show the relation between the incubation periods of Ti6Al4V and TiAl alloys and impact speeds/impact pressure. The plotted curves show similar behaviour to fatigue S-N curves. To find the erosion endurance of TiAl eroded by 464µm water droplets, the range of impact speeds was widened and erosion experiment was carried out at speed down to 250m/s. At this speed, no mass loss was observed after one million droplet impacts per 1mm^2 corresponding to 240,000 specific impacts. Hence, 250m/s was assigned as the threshold speed for TiAl when 464µm droplets were utilized, shown by arrow in Figure 2-10. Knowing *Vc* in case of 464µm water droplets and using Equation 2-4, the critical-velocity-constant of TiAl was calculated. Based on this constant and Equation 2-4, we should be able to estimate *Vc* in case of using any droplets size for TiAl. To prove that, the threshold speed for 603µm droplets were theoretically calculated and the corresponding experiment for that speed were carried out. The *Vc* for 603µm was calculated to be 202m/s. Then, the erosion experiment was carried out at 200m/s

impact speed. No erosion damage was detected after one million impacts per 1mm^2 (280,000 specific impacts), shown in Figure 2-11. Therefore, 200m/s was assigned as threshold speed of TiAl when eroded by 603µm water droplets. The experiment proved that Equation 2-4 is applicable to find the threshold speed for TiAl alloy when subjected to water droplet erosion.

In contrast to TiAl, the critical-velocity-constant could not be calculated for Ti6Al4V from the curve presented in Figure 2-10. Indeed, the critical-velocity-constant is a function of target material and its mechanical properties. Since Ti6Al4V shows lower erosion resistance compared to TiAl and presents much shorter incubation periods, additional experiments corresponding to the lower impact speeds are essential to determine threshold speed. Therefore, it will be the subject of a future study.

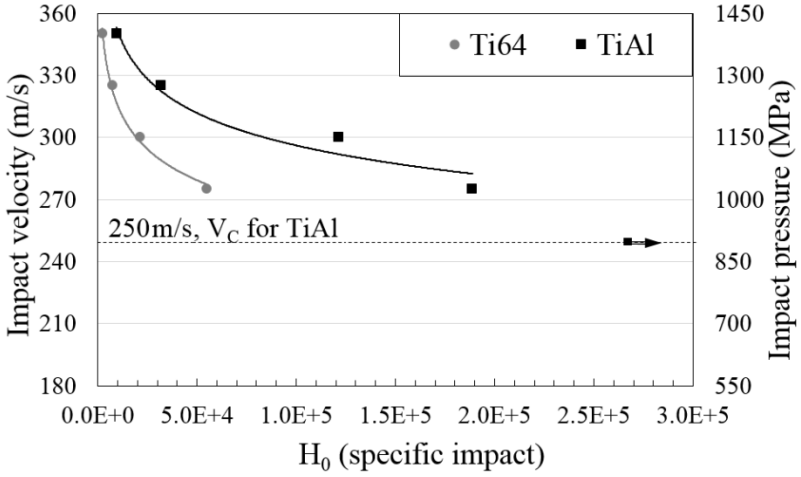

Figure 2-10: The dependency of Ti6Al4V and TiAl incubation period on the impact speeds when they are eroded by 464µm water droplets. The arrow indicates the test performed at 250m/s caused no measurable erosion after 10^6 impacts

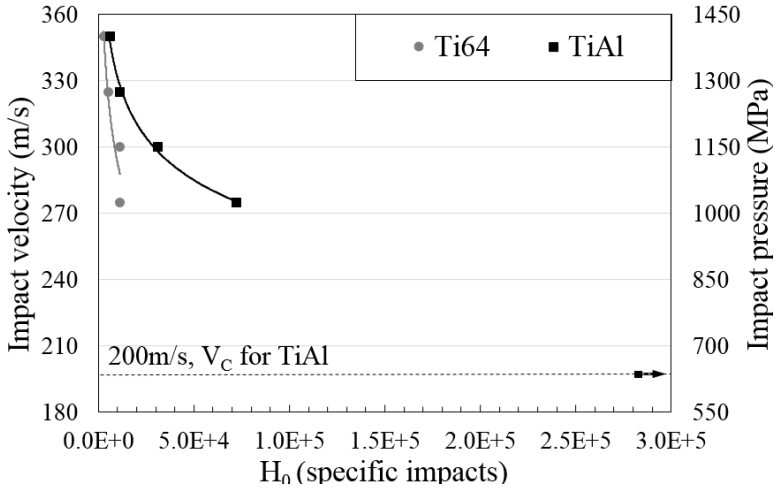

Figure 2-11: The dependency of Ti6Al4V and TiAl incubation period on the impact speeds when they are eroded by 603µm water droplets. The arrow indicates the test performed at 200m/s caused no measurable erosion after 10^6 impacts

The maximum erosion rate versus impact speed for Ti6Al4V and TiAl are presented in Figures 2-12 and 2-13. The experimental data are plotted in log-log graphs and fitted using a power law relationship. The slope of the fitting line is reported as the speed-dependency-exponent. In the case of the 464µm droplets, it was found that the ER_{max} is related to the impact speed with 8.9 and 12.5 exponents for Ti6Al4V and TiAl, respectively. However, for 603µm droplets, it was found to be 7.7 and 11.5, respectively. Ti6Al4V and TiAl are considered as erosion resistant alloys, but their material loss rates were increased notably with increasing the impact speed. TiAl erosion resistance drops significantly by increasing impact speed.

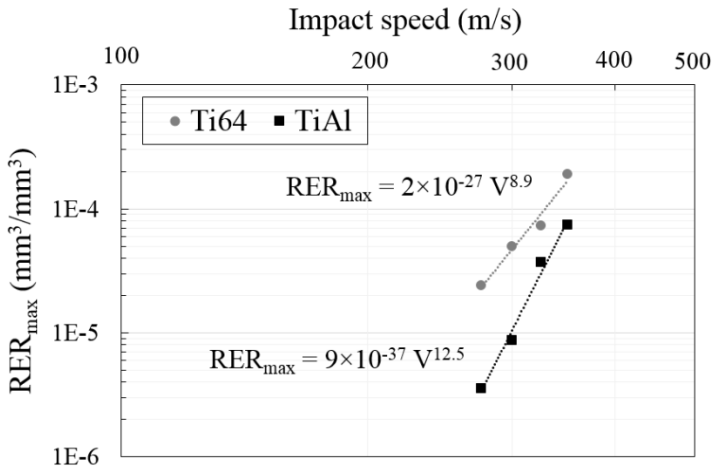

Figure 2-12: Dependency of maximum erosion rate on the impact speed for Ti6Al4V and TiAl alloys eroded by 464µm water droplets

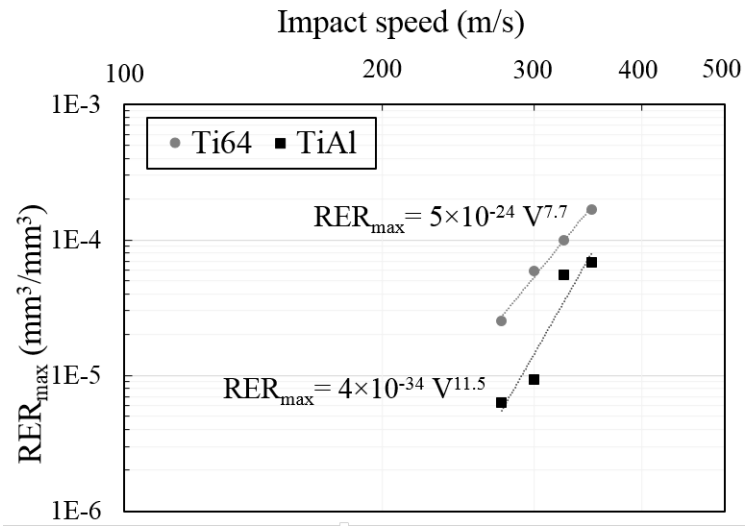

Figure 2-13: Dependency of maximum erosion rate on the impact speed for Ti6Al4V and TiAl alloys eroded by 603µm water droplets

2.3.3.3. Comparison between TiAl and Ti6Al4V WDE performances

In order to compare the response of TiAl with that of Ti6Al4V during the erosion test, the percentage of superiority at each interval versus volume of impinging water was plotted at different impact speeds. Figures 2-14 and 2-15 exhibit these graphs for 464µm and 603µm droplets.

$$Material\ loss\ superiority\ of\ TiAl = \frac{Volume\ loss\ of\ Ti6Al4V - Volume\ loss\ of\ TiAl}{Volume\ loss\ of\ Ti6Al4V} \times 100\ (\%) \qquad \textit{Equation 2-11}$$

TiAl shows superior erosion resistance in all WDE test conditions used in this study. In the case of low impact speeds or small droplets, higher superiority can be seen. However, difference in erosion performance becomes less significant at high impact speeds or large water droplets. Indeed, TiAl shows very high erosion resistance as the severity of the erosion conditions decreases. In order to understand these material loss superiority graphs, the curve corresponding to 325m/s impact speed and 464µm droplet size, shown by triangle markers in Figure 2-14, is explained here. At the beginning of the experiment and during the incubation of Ti6Al4V and TiAl, superiority is meaningless, zero divided by zero in the Equation 2-11, and it is not reported in the graph. Thereby, the curves do not start from zero, shown in the magnified parts of Figure 2-14. The beginning of the curve is once the material loss of Ti6Al4V initiates (point a). This point represent 100% superiority of TiAl since it did not lose any material yet, but Ti6Al4V did. The graph continues with 100% superiority until TiAl material loss initiates (point b). Further impacts lead to TiAl material loss and decrease in superiority from point b to point c. The reduction of erosion

superiority is attributed to the different erosion stages experienced by the specimens. For instance, when Ti6Al4V is undergoing a reduction in the erosion rate in the last stages of erosion (deceleration or terminal erosion rate), TiAl might still be in the second or third stages of erosion (acceleration or maximum erosion rate). The superiority curve keeps decreasing until it reaches a plateau (point d), when 30,000mm^3 of water impacted 1mm^2 of target surface. This plateau is detected because both specimens reach their terminal erosion stages.

It is expected to see such plateau of superiority for all conditions when both specimens reach their terminal erosion rate stage. This plateau was observed for some of the experiments performed mainly at severe conditions such as 48% for 464µm and 325m/s or 12% for 603µm and 350m/s. However, it was not revealed for the experiments performed at low impact speeds because the terminal stage of erosion for TiAl was not reached in these conditions. This type of representation is very helpful for the erosion comparison of two bulk materials especially their behavior at the later stages. The value of plateau can be reported as the superiority of TiAl at later stages of service compared to Ti6Al4V.

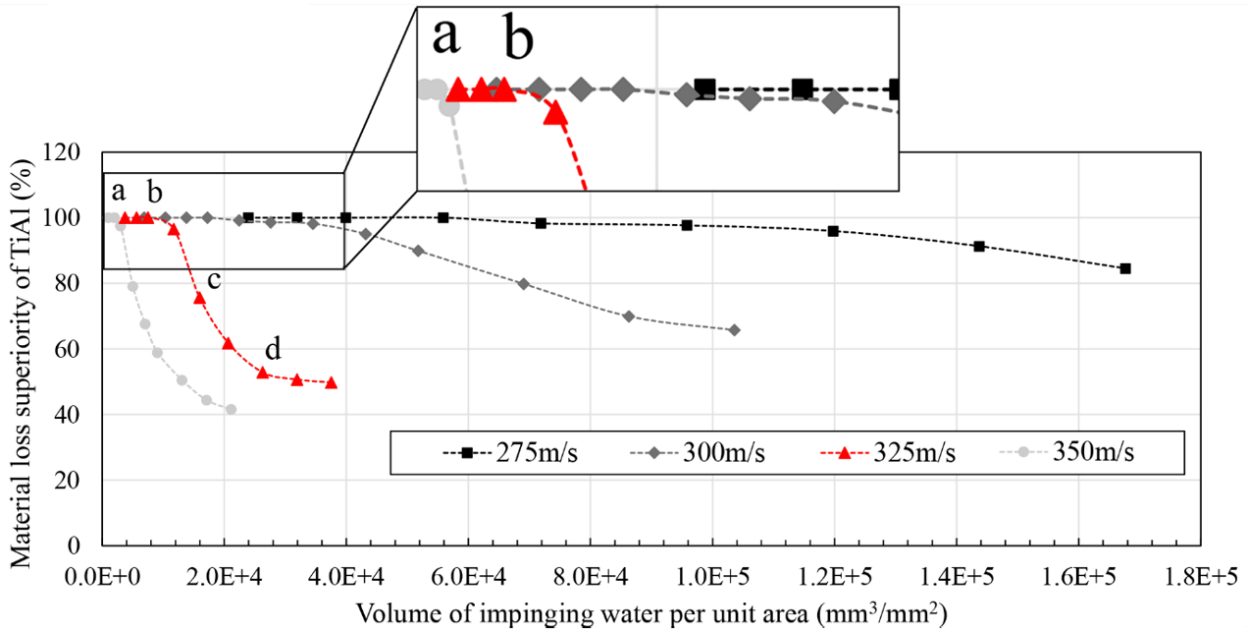

Figure 2-14: Material loss superiority of TiAl compared to Ti6Al4V during the WDE test performed using 464µm drops

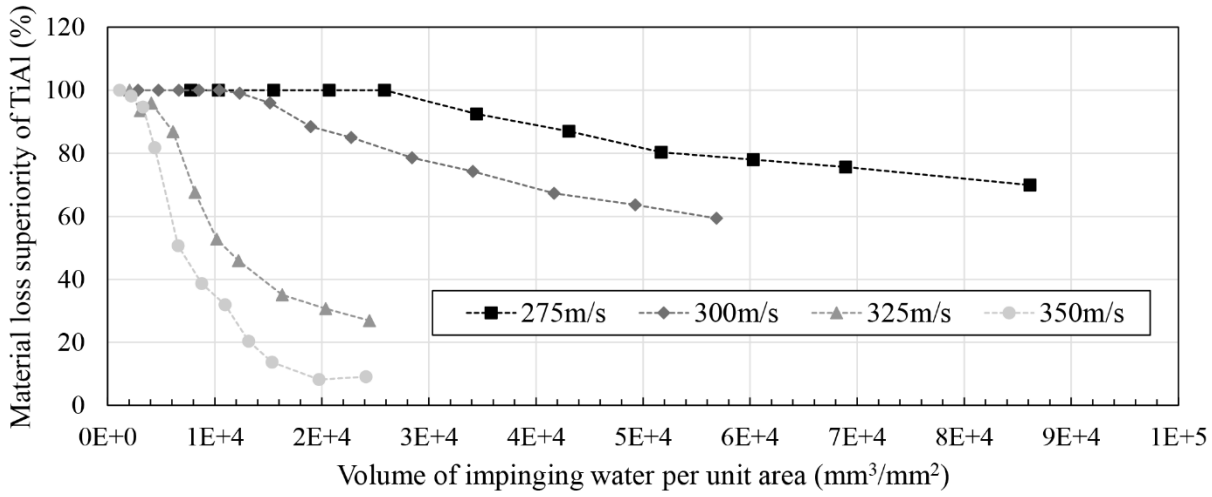

Figure 2-15: Material loss superiority of TiAl compared to Ti6Al4V during the WDE test performed using 603µm drops

2.3.3.4. Microscopic observation of erosion damage

As mentioned, the WDE tests were interrupted at different time intervals to weigh the coupons and record the material loss. Moreover, the areas exposed to the impacts were observed under an optical microscope to document the erosion features during the test. As a result, the pitting at different positions, the growth of eroded regions, their merging, formation of craters and grooves were recorded for the whole WDE test. For instance, the eroded Ti6Al4V and TiAl tested at impact speed of 325m/s and droplet size of 603µm are illustrated in Figure 2-16. Pitting and erosion damages can be seen on Ti6Al4V earlier than TiAl, which corresponds to the observed longer incubation for TiAl. The material loss rate for both alloys increased after the formation of initial pits. However, there is a considerable difference between Ti6Al4V and TiAl erosion progression. Ti6Al4V lost material from all area exposed to the erosion. The pits merged with one another and formed complete erosion crater after three minutes erosion. Nevertheless, in the case of TiAl instead of fast pits coalescence and having a complete erosion line, the initially damaged areas mostly got deeper and deeper by water droplet impacts. Then, as the formed pits enlarged by further impacts, they started to merge. The formation of deeper pits for TiAl compared to Ti6Al4V at early stages of erosion is shown in Figures 2-17-a and 2-17-c. They demonstrate the cross sections of typical pits formed during the erosion. Moreover, the cracking behaviours with respect to the local microstructures are presented in Figure 17-b and 17-d. In the case of Ti6Al4V,

relatively small intergranular and transgranular cracks can be seen. However, the trasngranular cracking (combination of interlamellar and translamellar cracks) are dominant in the case of TiAl.

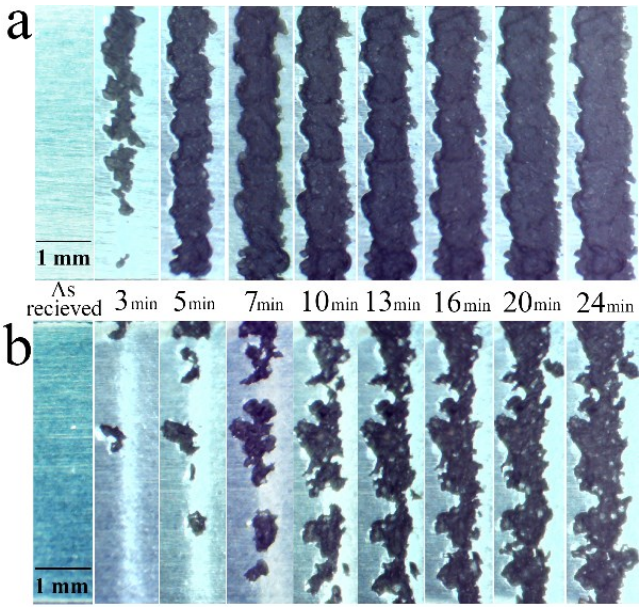

Figure 2-16: Micrographs of erosion craters at different time intervals (mentioned between two images) for the erosion experiments performed at 325m/s impact speeds and 603µm droplet size: (a) Ti6Al4V, (b) TiAl

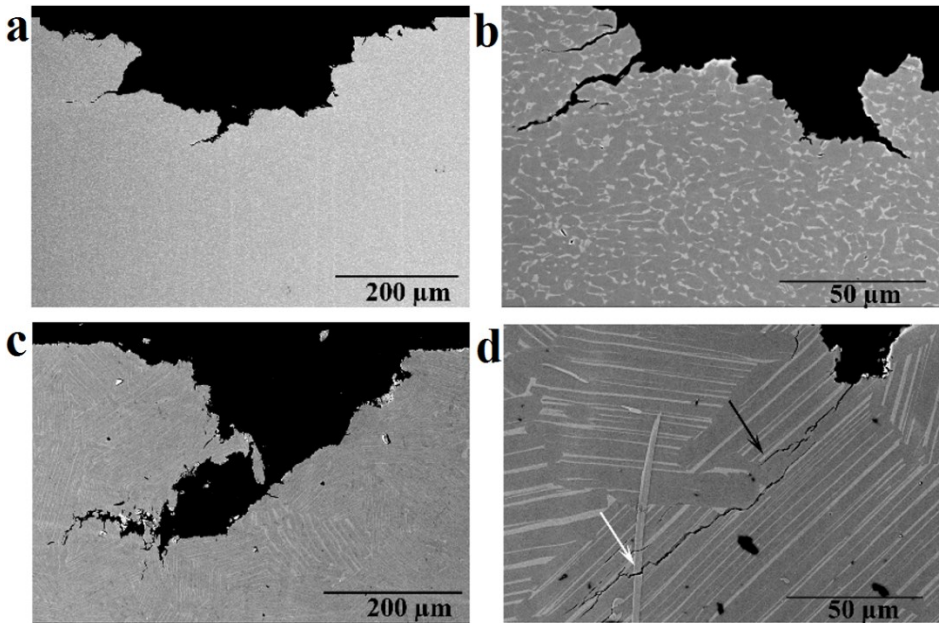

Figure 2-17: Cross sectional SEM micrographs of eroded (a and b) Ti6Al4V and (c and d) TiAl: (a and c) erosion pits at early stages, (b and d) edges of erosion crater showing the influence of local microstructure on cracking behavior

2.4. Discussion

The water droplet erosion performance strongly depends on the erosion conditions, and the tests need to be done in representative conditions. In order to understand the erosion behaviour of any material or in the case of comparing the performances of two different alloys, different erosion parameters need to be evaluated. In this study, the maximum erosion rate and incubation period of Ti6Al4V and TiAl alloys tested at different impact velocities and droplet sizes are compared. Furthermore, the erosion dependency of Ti6Al4V and TiAl alloys on the impact speed is compared. The obtained results are discussed below.

The erosion performance of TiAl is superior compared to Ti6Al4V. Figures 2-8 and 2-9 illustrating the maximum erosion rates and incubation periods confirm the lower ER_{max} and longer H_0 for TiAl. Higher erosion resistance can be explained by two parameters, mechanical properties and microstructure. The hardness, yield and ultimate strength, modulus of resilience and toughness are considered important mechanical properties that affect the erosion resistance. The hardness and strength of TiAl are higher than those of Ti6Al4V (up to 20%). Thus, they are in accordance with the WDE theories suggesting that these are key mechanical properties to study water droplet erosion. In terms of energy absorption, it was claimed that the higher the ability to absorb energy, the higher the resistance to erosion [24, 47]. Because the amount of energy transferred to the target from impacting water droplet was considered as an important cause of the erosion damage. Ti6Al4V can absorb more energy than TiAl during elastic deformation, since its modulus of resilience is higher than that of TiAl (shown in Table 2-2). But, Ti6Al4V showed worse erosion resistance compared to TiAl and it means high resilience does not indicate high erosion resistance. Since the energy exerted on the target material upon water droplet impact might exceed the elastic energy, it may appear more appropriate to consider total absorbed energy before fracture, which is the toughness [66]. Toughness is roughly approximated by the area under σ-ε curve of each material. It is 450,000kJ/m^3 for Ti6Al4V [88] and 420,000kJ/m^3 for TiAl [92] in the case of static compression condition. Although Ti6Al4V possess higher toughness than TiAl, its water erosion resistance is worse. Thereby, neither static resilience nor toughness can be assumed as a key mechanical property to address erosion behavior of Ti6Al4V and TiAl. Since there are high speed impacts and as a result high strain rates, the dynamic mechanical properties of TiAl and Ti6Al4V should also be considered. The higher the strain rate, the higher the strength and the energy required to fracture both alloys [91, 93]. However, in the case of TiAl with lamellar microstructure,

the influence of strain rate on the mechanical properties is significant [93]. Applying the load at a high strain rate results in much slower crack initiation and propagation rates [93, 94]. Accordingly, the lamellar TiAl alloy shows much higher strength under dynamic loading conditions than Ti6Al4V [91, 93]. They can be approximated around 1400MPa for Ti6Al4V and 2000MPa for TiAl. This justifies that TiAl outperformed Ti6Al4V.

Furthermore, the superior cavitation erosion resistance of TiAl was attributed to high strain hardenability of this alloy by Howard *et al.* [68]. Here, hardenability means that a higher value of stress would be required to cause deformation or failure after each collision. Similar condition might be experienced during water droplet erosion. To study the strain hardening of these alloys, their hardness were measured in 0.5min intervals during the incubation of water droplet erosion (i.e. 1.5min for Ti6Al4V and 2.5min for TiAl). Figure 2-18 shows that TiAl hardness increases by 11 and 17% after being subjected to repetitive water droplet impacts for 1.5 and 2.5min, respectively. However, Ti6Al4V hardness increases by 6% only after 1.5min. Such strain hardening observed for TiAl can be assumed as an important reason for its superior WDE resistance especially for its long incubation period and lower maximum erosion rate.

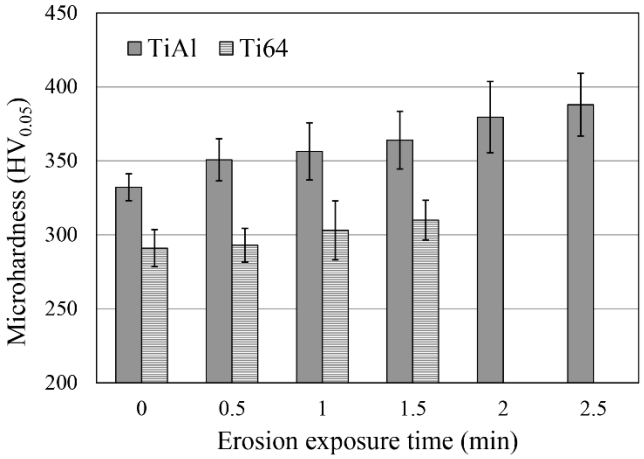

Figure 2-18: Surface hardness of TiAl and Ti6Al4V presented in 0.5min intervals during the incubation of erosion experiment performed at 350m/s using 464µm droplets

It was proposed by Heymann [66] that an empirical combination of strength and modulus of elasticity, $\sigma_u^2 E$, is the most corresponding mechanical property to the erosion performance. Thus

$$Erosion\ resistance \propto \sigma_u^2 E \qquad \textit{Equation 2-12}$$

In order to address the influence of strain hardening coefficient in Equation 2-12, we assume that there is a linear behaviour for the stress-strain relationship of materials up to yield point (Hooke's law). Also, it is supposed that their plastic deformation (from the onset of the plastic deformation to the tensile strength point) are governed by a power equation (Hollomon's law). By equating the stress-strain relationship for elastic and plastic regions at the yield point,

$$\sigma_y = E\varepsilon_y = K\varepsilon_y^n \qquad \textit{Equation 2-13}$$

the modulus of elasticity can be written as:

$$E = K\varepsilon_y^{(n-1)} \qquad \textit{Equation 2-14}$$

where K is material's constant, ε_y is the strain at the yield point and n is strain hardening coefficient. Therefore, Equation 2-12 can be written as

$$Erosion\ resistance \propto \sigma_u^2\ \varepsilon_y^{(n-1)} \qquad \textit{Equation 2-15}$$

TiAl possess higher values for σ_u and n than Ti6Al4V and it is in accordance with the water droplet erosion results, where TiAl outperformed Ti6Al4V. Hence, hardness, ultimate strength and strain hardening coefficient are confirmed to be the key mechanical properties influencing erosion performance.

According to the reported fatigue like mechanism of water droplet erosion [2, 57], the cracks' propagation rate and their preferred direction for the studied materials would be important parameters. Effect of the microstructure is a considerable factor, especially in the case of TiAl [69, 87, 95]. The near fully lamellar TiAl, used in this study, shows superior crack growth resistance compared to the other TiAl alloys with equiaxed or bimodal microstructure [69]. This was attributed to the beneficial shielding effects of crack blunting or deflection because of different colony orientations, shown by black arrow in Figure 2-17-d. Moreover, ligament bridging toughening is another reason for the high resistance of lamellar TiAl against crack growth [95]. This leads to crack growth deceleration and is shown by white arrow in Figure 2-17-d. Micro-cracking ahead of the tip of the main crack was also reported to delay the crack propagation especially in cyclic loading conditions [69]. Such micro-cracking ahead of one long crack can be seen in Figure 2-17-a. Although cracks deflection, bifurcation, and ligament bridging decelerate the cracks propagation within the lamellar microstructure, in few cases relatively large cracks are observed along the craters edges, Figure 2-17-d. Such cracking may cause slow and infrequent

detachment of relatively large portions of TiAl sample during the erosion. This is not the case for Ti6Al4V. Indeed, the local microstructure of Ti6Al4V with small and equiaxed α grains leads to faster cracks coalescence and subsequent material loss. Therefore, fast and frequent detachment of small fragments would be a dominant damage mechanism for Ti6Al4V. This corresponds to the lower erosion resistance of Ti6Al4V compared to TiAl.

Unlike Ti6Al4V alloy, the difference in RER_{max} of TiAl alloy between tests done at the impact speeds of 300m/s and 325m/s is considerably high, if compared to the RER_{max} differences for other speed intervals. It was more evident, when 603μm droplets were used in the test. In fact, RER_{max} increased more than 6 times when the impact speed increased from 300m/s to 325m/s. It can be attributed to a certain level of imposed stress causing significantly high crack propagation rates. Showing this type of critical stresses under dynamic loading is a known behaviour for intermetallics [69]. Furthermore, in most of WDE studies the water properties were assumed to be constant, neglecting its viscoelasticity. In light of the results in this paper and considering the high strain rate during the impact, a hypothesis can be made to explain the sudden increase in erosion rates for materials at some specific speeds, in terms of the viscoelastic properties of water and their dependency on impact speed. It is known that for viscoelastic liquids, the speed of impact can determine their response [22]. Thus, it can affect the amount of energy transferred to the material, and the amount causing the deformation of the water droplet itself. It was not proved experimentally; however, this point can be tackled in a future work.

In spite of different available Equations for erosion-impact speed relationship, the experimental data was fitted using Equation 2-1 as discussed in the results section. The speed exponent was mainly reported between 5 to 7 for metals [8, 46]; however, it was found to be more than 7 for Ti6Al4V in this study. In previous works similar inconsistency was observed, highlighted in Table 2-1. The main reasons for such a difference in values of the speed exponent, can be attributed to the different WDE rigs, different erosion test conditions and different erosion indicators on which the influence of impact velocity has been investigated. For instance, the influence of the impinging water characteristics (shape and size) on the speed dependency exponent were neglected in most of previous works since they generalized the speed dependency exponent [46, 48, 58]. The erosion severity including impact pressure and duration of each impact pulse is a function of both the speed and the water droplet size, Table 2-3. Hence, the speed

exponents acquired from the tests performed using different conditions for the impinging water droplets, are expected to have different values. Since there is no clear physical explanation for the observed trends and the determined speed exponents, the influence of the water droplet conditions on the erosion rate-impact speed relationship needs to be studied experimentally, while keeping other parameters constant. In the current study, the experiments were carried out using two different droplet sizes. The speed exponents were found to be 8.9 and 7.7 for Ti6Al4V in the case of 464 and 603μm droplets, respectively. This observed difference confirms that the speed exponent is function of droplet size, or generally speaking the "impact conditions". It verifies Heymann's conclusion that the presented erosion-speed relationship with certain exponent, Equation 2-1, would be valid over limited speed ranges [47].

Furthermore, the properties of target material affect these parameters. Higher speed exponent was reported for the erosion of ceramics compared to metals [47, 58]. Larger exponent would imply a higher tendency for brittle failure, and a higher transfer of impact energy through the interface between the droplet and the target material [96]. There is a notable difference between Ti6Al4V as a metal and TiAl as an intermetallic in terms of their erosion dependency on the impact speed. The erosion rate is linked to the crack propagation, and it is the main reason for material loss in terminal stages of the water droplet erosion damage. For intermetallics, especially TiAl, the crack propagation rate is extremely sensitive to the stress intensity. It was proved by having a large exponent in the Paris law [69], which is 5 to 10 times larger than typical values of metallic systems. Since TiAl tends to act in a more brittle manner due to its high sensitivity to speed increase, it has higher speed exponent than that of Ti6Al4V which is in accord with the current results.

As mentioned earlier, critical or threshold speeds for the erosion damage were estimated for TiAl. This approach was used by researchers in the field of cavitation erosion or water jet erosion [7, 45, 46]. The attempt was to relate the erosion endurance to the fatigue limit. Thirwvengadam [46] compared the water erosion endurance with the fatigue strength (obtained from magnetostriction oscillator setup for fatigue test) for stainless steel and Ti6Al4V. The erosion endurance was found to be half and one third of the fatigue strength. This considerable difference was correlated to the local fatigue failure caused by water erosion which could not be represented by the used fatigue setup. In fact, the considerable difference in endurance levels for materials subjected to conventional fatigue and WDE would confirm the divergence in material's strength

for both loading conditions, despite their similarity in terms of cyclic loading. The drawback of Thirwvengadam's work was neglecting the variation of the critical speed. This speed was found to be a function of droplet size based on Equation 2-4. The product of the droplet diameter and V_C^2 being critical-velocity-constant, was proposed and confirmed mainly for metals [47]. This work affirms the validity of this equation in representing erosion for TiAl alloy, seen in Figures 2-10 and 2-11. It is noteworthy that the droplet size distributions presented in section 3.2 confirm the accuracy of Equation 2-4 in the case of water droplet erosion damage. Here, the volume fraction distributions show that for both nozzles large volume of water (more than 75%) impinging the target are droplets that their diameter standard deviation from the mean value is less than 5%.

2.5. Conclusions

The present study makes several noteworthy contributions to our knowledge about the water droplet erosion behaviour of TiAl and Ti6Al4V alloys. The superior erosion resistance of nearly fully lamellar TiAl compared to Ti6Al4V is shown at all tested conditions. However, its superiority was found to be function of the impact speed and droplet size. The less the severity of erosion test, the higher the superiority of TiAl erosion resistance compared to Ti6Al4V. Such superiority could be attributed to the higher hardness, strength, modulus of elasticity, hardenability and lamellar microstructure. Indeed, the randomly oriented TiAl colonies with fine lamellar microstructure result in relatively low crack growth rate improving erosion resistance. Furthermore, the maximum erosion rate and impact speed relationship for both tested materials, a metallic and an intermetallic alloy, showed a linear trend on the logarithmic scale. For Ti6Al4V, the speed exponent was found to be 8.9 and 7.7 for 464 and 603μm droplets, respectively. In the case of TiAl alloy, it was found to be 12.5 and 11.5 for 464 and 603μm droplets, respectively. The observed exponents for Ti6Al4V are higher than the reported values in the literature, 5 to 7. This difference is attributed to the erosion test conditions and different approaches used to derive erosion rate. Finally, the threshold speed was found to be function of the impinging droplet diameter so that the product of the droplet diameter and V_C^2 is constant. Using such Equation, the threshold speeds for the TiAl alloy eroded by 464 and 603μm water droplets were determined as 250m/s and 200m/s, respectively.

Relating to the theme of thesis

In chapter 2, the erosion performance of TiAl was studied in relation to Ti6Al4V. Their behaviour differences within wide ranges of impact speeds and droplet sizes were quantified. Superior erosion performance of TiAl at all impingement conditions has been observed. This fulfils the first objective of this thesis which is proposing a water droplet erosion resistant alloy for turbine blades. Superior erosion performance of TiAl was attributed to its mechanical properties and microstructure. The influence of mechanical properties (i.e. hardness and hardenability) was explained. The chapter 3 presents the influence of TiAl microstructure on its erosion behaviour. In-depth analysis of TiAl response to water droplet impacts reveals the main reasons for its superior erosion behaviour.

Chapter 3 : Water droplet erosion mechanism of nearly fully-lamellar gamma TiAl alloy

M.S. Mahdipoor[1], D. Kevorkov[1], P. Jedrzejowski[2], M. Medraj[1,3]

[1] Department of Mechanical and Industrial Engineering, Concordia University, 1455 de Maisonneuve Boulevard West, QC, Montreal, Canada H3G 1M8

[2] Rolls-Royce Canada Ltd. Energy, 9545 Cote-de-Liesse, Dorval, QC, Canada H9P 1A5

[3] Department of Mechanical and Materials Engineering, Masdar Institute, Masdar City, Abu Dhabi, UAE, P.O. Box 54224

This article has been published in the *Journal of Materials & Design,* 89 (2016): 1095-1106, DOI: 10.1016/j.matdes.2015.10.077[2]

ABSTRACT

Water droplet erosion (WDE), is a known mechanical degradation and progressive damage for turbine blades in the power generation and aerospace industries. Hence, water droplet erosion study of TiAl as an important structural material in such industries would be very attractive. The current work is to investigate the erosion damage mechanism of nearly fully lamellar Ti45Al2Nb2Mn0.8TiB_2 (45-2-2XD) alloy. This alloy was subjected to water droplet erosion using 464μm droplets and 350m/s impact speed. In order to track the erosion damage, WDE test was interrupted at different stages; incubation, maximum erosion rate and final steady state stages. The eroded specimens were characterized using optical microscope (OM), scanning electron microscope (SEM) and atomic force microscope (AFM). The qualitative and quantitative study reveals that the erosion damage of TiAl initiates by inhomogeneous and localized material flow followed by crack network generation on the surface. Such cracks mainly nucleate on the interlamellar slip bands and cause delamination of lamellae. Further droplet impacts result in the cracks coalescence and subsequent micro-pitting within the colonies. In the advanced stages, the erosion damage was governed by periodic water roughening and water polishing, which were observed on the bottom and the sidewalls of deep erosion craters.

[2] In this article, Dr. Kevorkov, as the Research Associate at TMG, and Dr. Jedrzejowski, as the industrial partner, helped in the interpretation of the results.

3.1. Introduction and literature review

Liquid impingement erosion is the result of repetitive high-speed impacts of a liquid streak (jet or droplet) on a solid surface. It leads to a progressive material loss and the subsequent failure [2]. Water droplet erosion (WDE) is a practical problem in the power generation and aerospace industries where the droplets interact with the high-speed moving components. It has been known as a cause of blades degradation in the last stages of the low-pressure steam turbines [2, 57]. This type of erosion is also an issue for the compressor blades of gas turbine when fog cooling system is used [2, 11]. Furthermore, water droplet erosion is the main concept of plain water jet cutting process [40, 97]. It has been attractive mainly for cutting of the materials that have poor machinability such as TiAl alloys [40, 69].

Water droplet erosion has been studied over the past few decades and its damage mechanism, that is different from other types of erosion such as solid particle and cavitation erosions, was addressed [2, 39, 40, 57, 98, 99]. Water hammering, stress wave generation, radial jetting and hydraulic penetration are usually described as the most destructive phenomena during the water droplet erosion [39, 52]. Micro-cracking is one of the initial responses of the target and it has been argued to be a result of stress concentration around the slip steps, microstructural irregularities, and pre-existing flaws. In the case of homogenous bulk materials, localized plastic deformation and surface roughening, caused by water impacts, act as a trigger for the initiation of micro-cracks [31]. Interaction of stress waves with the microstructural irregularities and flaws, which causes stress concentration and may generate tensile stress, also contributes to micro-cracking [18]. Substantial influence of microstructural flaws on the cracking behavior and erosion performance was observed in the case of surface treated coupons such as laser nitrided Ti6Al4V [100, 101] or sprayed cermet coating [102].

Water droplet erosion of the current turbine blade alloys, martensitic stainless steels and Ti6Al4V, have been studied over the years [28, 30, 39, 41, 47, 103]. Luiset *et al.* [30] described the local plastic deformation, cracking and fatigue spalling as the WDE mechanism of stainless steels. After intergranular cracking on the surface, they observed that the cracks propagate thorough the grains and result in their pulling-out and ruptures. Similar behavior was observed for erosion damage initiation of Ti6Al4V by Huang *et al.* [28]. They elaborated the damage initiation mechanism and highlighted the shallow depression and grains tilting as the main erosion features

during the incubation of erosion. Afterwards, propagation and coalescence of these superficial cracks were reported to be the main cause for fatigue spalling and localized material loss [30, 103]. Recently Kamkar *et al.* [41] studied the WDE damage mechanism of Ti6Al4V at advanced stages and highlighted a periodic surface roughening and smoothing which were caused by water droplet impacts inside the erosion crater. However, such periodic roughening and smoothing were not elaborated. It is worth noting that the surface roughening by droplet impacts and formation of a jagged surface, observed for different target materials [8, 31, 104], was not clearly justified. In the case of TiAl alloys, the water droplet erosion damage has been rarely investigated. Kong *et al.* [40] studied the damage mechanism of γ-TiAl using plain water jet milling. They considered γ-TiAl as a semi-brittle material and presumed that the micro-plasticity governs its initial stage erosion. However, the micro-plastic deformation was not documented because they could not capture the early stage of erosion using water jet milling setup. Unlike the ductile metals which their damage initiation mechanism has been established [28, 30, 103], the erosion mechanism of TiAl intermetallic particularly two phase alloys ($\alpha_2+\gamma$) is unknown. Additionally, there is no information about the cracking behavior of these alloys during the water droplet erosion as the key contributor to the damage. It is noteworthy that the erosion damage has some similarities to the low cycle fatigue, especially, when it comes to the cracking behavior [39, 57, 105]. The fatigue behavior of TiAl alloys has been well studied and micro-cracking on the slip bands was highlighted as the main contributor to the damage [106-108].

Two-phase titanium aluminide alloys particularly the ones with lamellar microstructure show much better mechanical performances comparing to the alloys having monolithic microstructure of γ and α_2 constituents [69, 109]. Their mechanical characteristics significantly depend on the microstructure, colony size and lamellar spacing [107, 109, 110]. Polycrystalline lamellar TiAl alloys comprising randomly oriented colonies deform and fracture inhomogeneously [107, 111]. The deformation is mostly confined to the γ phase and not that much in α_2. In these alloys, the lamellae interfaces and colony boundaries act as obstacles for crack propagation and may blunt the cracks [108, 112-114]. Furthermore, the mechanical twining and the intersection of dislocations mainly at the interfaces and boundaries result in the anomalous high hardenability for these alloys [69, 107]. γ/γ domain boundaries were highlighted as the key contributor to the cyclic hardening because they are the main obstacles for the motion of dislocations in the γ lamellae [107, 115]. High cyclic hardening of TiAl alloys was reported as an important reason for their superior

cavitation erosion performance [68] and its contribution to water droplet erosion was documented in our previous work [64]. Therein, the water erosion behavior of TiAl was compared with that of Ti6Al4V at different impact speeds. TiAl outperformed Ti6Al4V, which was attributed to its higher strength and hardenability. Water erosion performance of these two materials was reported and compared in terms of, complete erosion curves, incubation period and erosion rate. Due to space limitation, the erosion damage mechanism was not discussed in our previous paper [64].

The present paper focuses on the water droplet erosion damage mechanism of Ti45Al2Nb2Mn0.8TiB_2 (45-2-2XD), referred to as TiAl, with nearly fully lamellar microstructure. The damage initiation of TiAl alloy is investigated in depth with respect to the local microstructure. The erosion evolution in the advanced stages is also discussed.

3.2. Material and experimental procedure

3.2.1. Material and preparation

A Ti45Al2Nb2Mn0.8TiB_2 (45-2-2XD) plate received from Rolls-Royce Canada Ltd has been investigated in this paper. The as-cast plate, was hot isostatically pressed (HIPped) at a pressure of 140MPa and then annealed. The applied post treatments resulted in nearly fully lamellar microstructure of γ/α_2 laths (TiAl and Ti_3Al phases) presented at Figure 3-1. Equi-axed γ grains among the randomly oriented lamellar colonies, which are the predominant constituents, can be seen in Figure 3-1-b. The mean size of colony and the mean lamellar spacing are 120μm and 4.1μm, respectively.

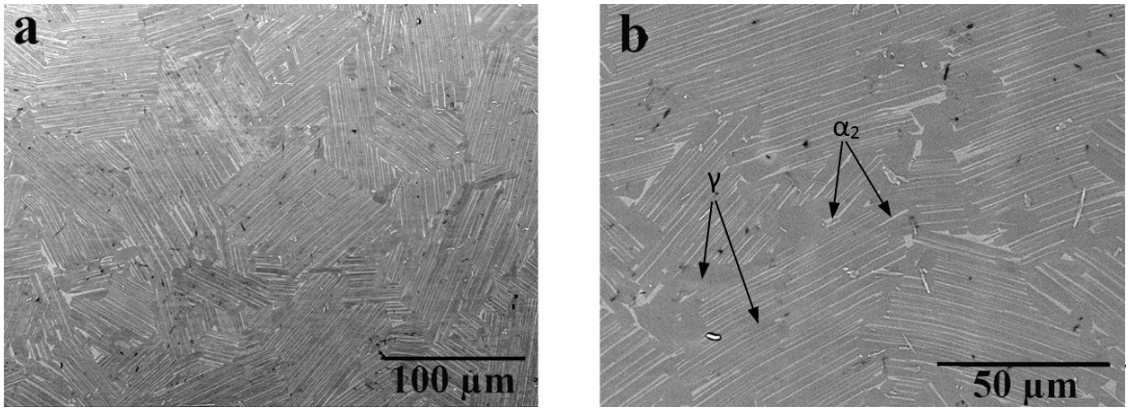

Figure 3-1: SEM micrographs of TiAl alloy: (a) low magnification showing the random oriented colonies, (b) high magnification showing the lamellar microstructure

TiAl plate was cut based on the required dimensions for the water droplet erosion test coupons. The specimen surface was grinded using SiC papers and polished by diamond vibromet polisher for 24 hours (surface roughness, Ra=0.038μm). Then, the polished surface was subjected to the water droplet erosion.

3.2.2. Water droplet erosion experiments

A testing rig with rotating disk, specifically designed for water droplet erosion according to the ASTM G73 standard [36], was used in this study. It works under pressure between 30 to 40 mbar. The erosion coupons of 23mm length, 8mm width and 3mm thickness were mounted on the disk and in each rotation they were subjected to the water droplet impacts. The impact angle is 90° relative to the target surface. The size distribution of generated droplets was measured using high speed camera for each nozzle. In addition, the number of droplet impacts was accurately monitored and measured in our group [26]. However, in the previous works mainly time of erosion [61] and number of impacts (rotation number) were used [41, 62]. More details on the erosion rig could be found in our previous works [26, 64]. In this study, the impact speed was set to 350m/s. The erosion experiments are interrupted at different time intervals to weigh the coupons and record cumulative mass loss. Knowing the mass loss and density of tested coupon its volume loss is calculated. Hence, the relation of cumulative material loss versus erosion exposure could be established. Typical WDE performance of TiAl at impact speed of 350m/s and droplet size of 464μm reported by Mahdipoor *et al.* [64] is shown in Figure 3-2-a along with a schematic of the water droplet erosion process in Figure 3-2-b. The current paper focuses on elucidating the water erosion damage mechanism of this material. Herein, incubation, maximum erosion rate and terminal steady state stage of erosion, shown by number 1, 2 and 3 in Figure 3-2-a, are studied. To explore the changes happening to the sample during the incubation stage, Figure 3-2-a (1), the samples were examined after 100,000 droplet impacts. To study the onset of material loss and the maximum erosion rate stage, Figure 3-2-a (2), the coupons eroded by 400,000 droplets were examined. The terminal stages of erosion, Figure 3-2-a (3), was investigated after 1,800,000 water droplet impacts. Although the mentioned stages were studied separately and sporadically for the erosion of other materials such as Ti6Al4V, stainless steel and WC-Co coating [8, 28, 30, 41, 79, 103, 116], a comprehensive study of water droplet erosion damage mechanism would be necessary for each material. Hence, the evolution of cracks and fractography of eroded TiAl specimens have been examined for both the impacted surface and cross sections in the proximity of erosion lines.

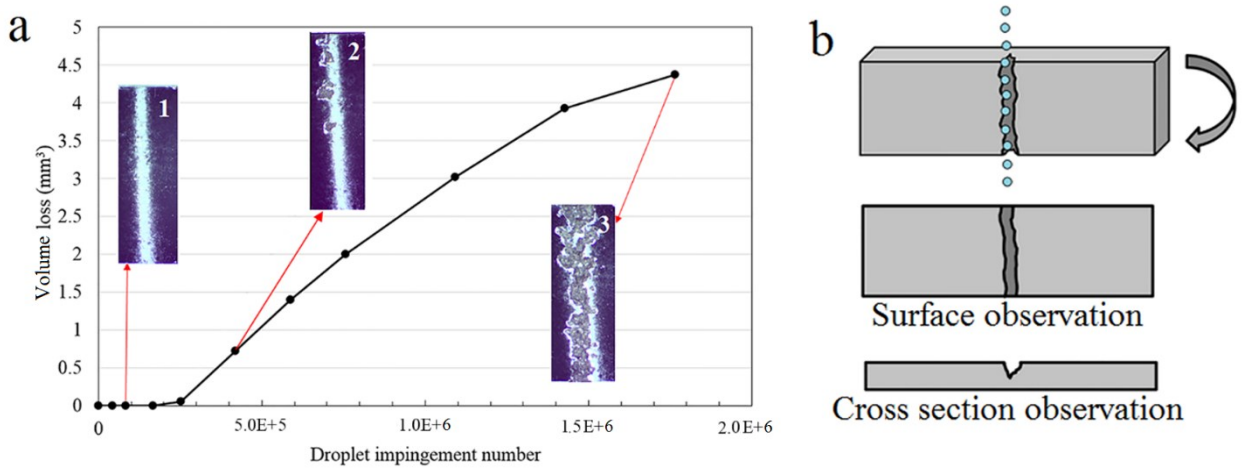

Figure 3-2: (a) WDE result (cumulative material loss) of TiAl and the appearance of erosion line at different stages [111]: (1) incubation stage, (2) maximum erosion rate stage, (3) terminal steady state stage, (b) Schematic of water droplet erosion investigation

3.2.3. Damage analysis

In order to document the erosion features, the area subjected to water droplet impacts was investigated on the surface and the cross sections (Figure 3-2-b). Scanning electron microscope (SEM) Hitachi S-3400N was used to study the fracture surfaces in the damaged region and monitor the cracks development. In addition, multimode atomic force microscope (AFM) was used to monitor the surface topography before and after droplet impacts (incubation stage) to document the local topography of the surface.

In order to capture sub-surface features, the cross section of eroded specimens was studied using SEM. The eroded coupons were cut using slow cutting machine with a diamond coated blade, then grinded and polished with diamond vibromet polisher. Then qualitative observation of erosion features as well as statistical analysis of cracking behavior through the cross sections of eroded coupons were performed.

3.3. Results and discussion

3.3.1. Systematic analysis of erosion damage at different stages

Water droplet erosion is a progressive and time dependent damage. Its mechanism varies at different stages of erosion. The target material response to the high speed droplet impacts and the damage mechanism at different stages are studied as following.

3.3.1.1. Incubation stage: microscopic observation

After 100,000 droplet impacts, the erosion experiment was stopped and the eroded coupon was explored using SEM. In the incubation period (stage 1), no clear damage or erosion features could be found macroscopically except for the change from a mirror-like to a non-reflective surface over the impacted area, as can be seen in Figure 3-2-a. In this stage, the erosion features were observed at high magnifications. Localized material flow can be clearly seen on the attacked surface, shown in Figure 3-3-a. It implies that the transition of high amounts of energy, caused by initial droplet impacts, is sufficient to activate slip systems in certain locations. It is clear that plastic deformation or material flow is notably influenced by the localized microstructure predominantly the orientation of lamella. The response of colony to mechanical loadings is known to be a strong function of its orientation with respect to the loading direction [108]. This dependency leads to anisotropic micro-plasticity, which contributes to damage initiation. Figures 3-3-b and 3-3-c, which show the plan-view of the impinged surface, demonstrate the material flow at higher magnification. Inhomogeneous micro-plasticity within the colonies is obvious in these micrographs. Here, water droplets perpendicularly impact the target surface. The colonies, based on their orientation with respect to the droplet impact direction, demonstrate distinct responses to the impingements. They are classified in three categories; A, B, and C, which are highlighted in Figure 3-3-b and schematically presented in Figure 3-4. Colony A shows soft mode response [108, 111] where the angle between loading direction and lamellar planes is 45° (ϕ=45) or nearly so. It is the most favorable orientation for slip activation and plastic deformation. Here, the slip and twinning occur on {111} planes of γ layers leading to material flow parallel to the lamella interfaces, interlamellar slips [108, 117]. In this orientation, the colonies do not show cyclic hardening because the γ/γ domain boundaries are not effective barriers for the motion of dislocations [69, 107]. Colony B which is oriented parallel to the loading direction (ϕ=0) exhibits hard mode response [108, 111]. In these colonies, the micro-slips and twins are mostly inclined to the lamella interfaces and the slips are called translamellar. Such colonies show strong cyclic hardening because both α_2/γ lamellar boundaries and γ/γ domain boundaries effectively prevent the motion of dislocations [69, 107, 108]. The third mode can be seen in colony C presenting hard and brittle behavior. There is no notable plastic deformation in this colony, as shown in Figure 3-3-b. Such colonies, whose lamella interfaces are almost perpendicular to the loading axis, exhibit very high yield strength [69, 112]. In this case, direct cracking before fracture is expected. These three modes will be referred to in the following explanations. Here, the observed slip bands are

not easily transmitted to the contiguous colonies and it is the main reason of heterogeneous plasticity. Indeed, the slip and plastic deformation are impeded by reaching the boundaries because the next colony is oriented differently, as shown in Figure 3-3-c. Other slip systems and potentially twins are activated in the next colonies. The features' contrast manifests that there are some extrusions mainly parallel to the lamella interfaces for the specific colonies. The extrusions are mostly the raised slip bands due to the shear deformations. It is noteworthy that the development of a severely deformed colony beside a non-deformed colony leads to local depressions and height variation near their boundaries, as shown in Figures 3-3-b and 3-3-c.

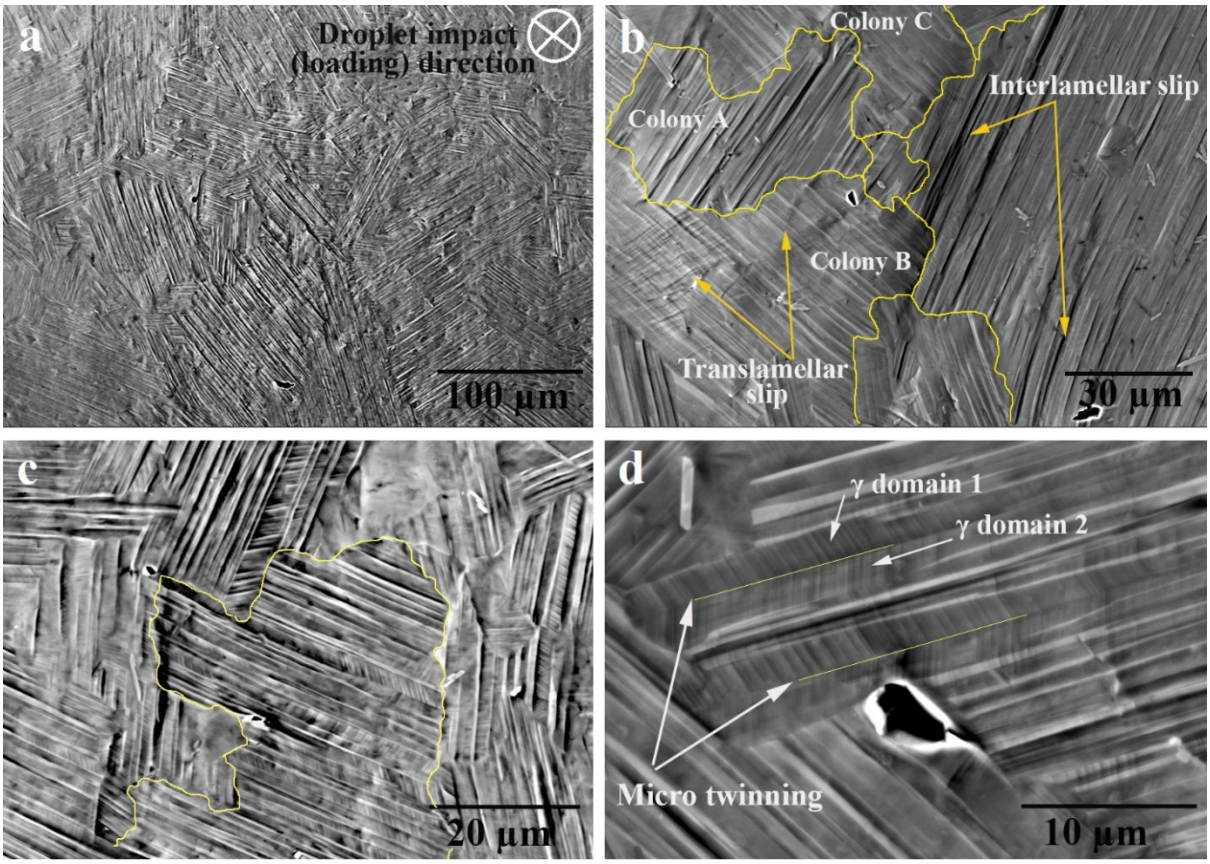

Figure 3-3: SEM micrographs of slightly eroded TiAl at incubation period showing: (a) localized material flow, (b) different responses of colonies to droplet impacts, (c) slip bands impeded by colony boundaries, (d) micro-twinning within the γ layers

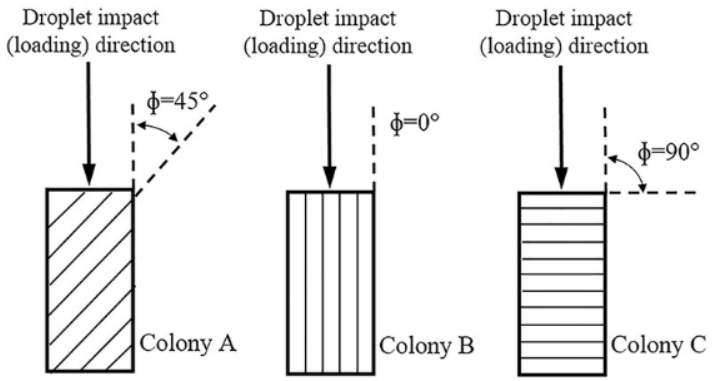

Figure 3-4: Schematic of different orientation of the colonies subjected to water droplet impacts

Micro-twinning is also observed on the surface of slightly eroded TiAl alloy, as shown in Figure 3-3-d. In fact, high level of exerted stresses (water hammering) leads to localized crystal reorientation and formation of twinning bands within the γ layers. This reduces the level of stress concentration and partially dissipates the transmitted impact energy to the material. Further impacts thicken and raise the level of generated twinning bands. Hence, they become the potential sites for crack initiation. The contribution of twinning bands to crack initiation during the cavitation erosion of TiAl was elaborated by Howard *et al.* [68]. However, their formation decelerate the crack propagation because of releasing some strain energy and stress intensity in the cracks wake.

Figure 3-5 depicts AFM images of original polished and slightly eroded surfaces (incubation stage). Although there is no detectable material loss in this stage, the surface topography is affected significantly by successive droplet impacts. The polished surface is relatively flat and no height variation, could be seen in the image. However, the water impinged surface exhibits perceptible contrast and height variation caused by local plastic deformations. Different levels of height variation for two adjacent colonies (A and B), shown in Figure 3-5-b, verifies the inhomogeneous micro-plasticity among the colonies. Moreover, the notable contrast on the boundary of colonies indicates the local depression at the interface between these two colonies. The droplet impacts during incubation stage increased the surface roughness (Ra=0.117μm) relative to the original polished surface (Ra=0.038μm). This surface roughening is responsible for the erosion damage initiation.

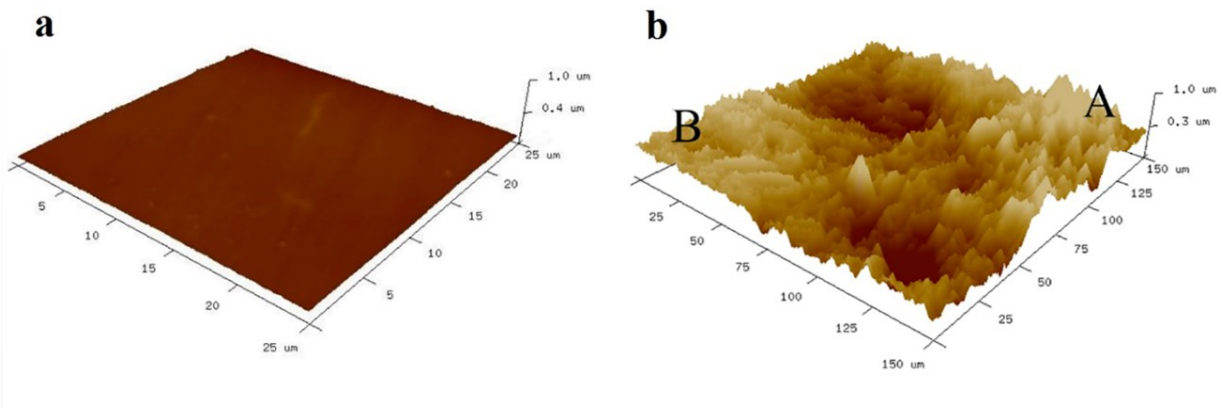

Figure 3-5: AFM images of: (a) original polished surface of TiAl (b) eroded surface of TiAl after 100,000 droplet impacts

AFM data was processed using Bruker Nano Scope Analysis 1.40 [118] to capture the magnitude of height variations. The height profiles across a deformed colony, in two different directions, has been extracted and plotted in Figure 3-6. Line 1 crosses the lamella interfaces and line 2 lies on a γ lamella and runs parallel to the interface. Thereby, the first line represents the height variation generated by interlamellar slips and the second line represents the height variation generated by translamellar slips. To elaborate the meaning of height variation along lines 1 and 2, lines 1′ and 2′ running through similar areas are demonstrated on the SEM micrograph shown in Figure 3-6-b. The significant height variation along line 1 indicates very high potential for cracks nucleation at the sharp notches. These stress raiser positions are mainly the α_2/γ interfaces, shown as points b_1 and d_1 in Figure 3-6-(1). The cracks nucleated at these notches are interlamellar cracks and are shown over line 1′ in Figure 3-6-b. Such cracks were often observed in type A colonies. It is worth noting that the colony boundaries indicated by points f_1 and e_2 in Figure 3-6, show relatively deep depressions. Such depressions are also shown by intense contrast of colony boundaries in Figures 3-5-b and 3-6-a. The formation of these deep intrusions is function of the adjacent colonies' micro-plasticity. For instance point f_1, which looks as a deep and sharp notch, is a boundary located between two A type colonies with high level of localized material flow and interlamellar slip. Such boundary may act as a stress raiser and by further droplet impacts cause intergranular cracking.

The surface roughening in the incubation of Ti6Al4V was attributed to the tilting of grains caused by high speed droplet impacts [28]. It cannot be the case for TiAl because of its large colonies (120µm) compared to the Ti6Al4V grains (30µm). Also, in the case of TiAl the

boundaries are often depressed all around the colonies, whilst grain tilting causes the formation of depression in one side and bump in the other side of grains [28]. Indeed, the local depression at the colony boundaries of TiAl could be attributed to the different levels of micro-plasticity for adjacent colonies.

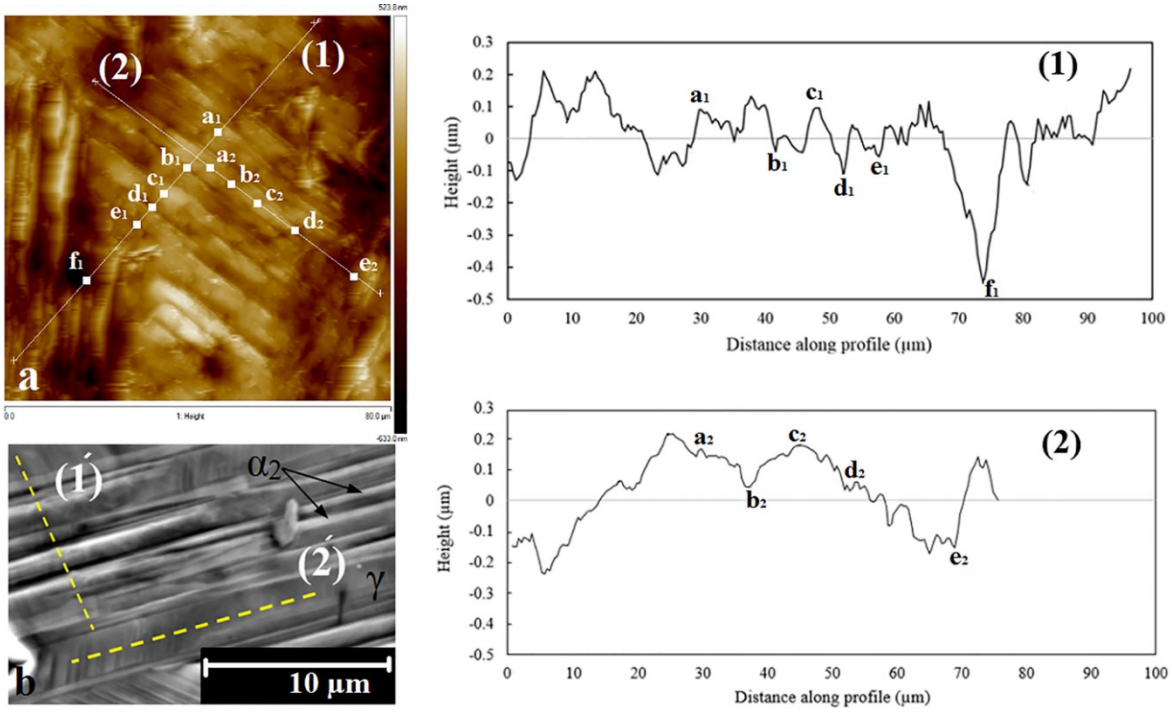

Figure 3-6: (a) AFM height image of a deformed colony and extracted average height profiles along two lines, (b) SEM micrograph of another deformed colony showing two lines with similar conditions

The presented height profiles correspond to the extrusion/intrusion pattern, which is a result of shear deformation in the γ lamellae across their interfaces (referring to the points between a_1 and e_1 in Figure 3-6) and parallel to their interface (raised steps between points a_2 and d_2 in Figure 3-6). Here, further droplet impacts lead to high stress concentration at the sharp positions and nucleation of micro-cracks along the slip bands (interlamellar). Delamination of two adjacent lamellae accelerates the interlamellar cracking, points b_1 and d_1. An interlamellar micro-crack just nucleated at the γ/α_2 interface is shown in Figure 3-7-a. The hindered plastic flow by the lamellae interfaces and γ domain boundaries expedites such crack initiation. Figure 3-7-b exhibits the interlamellar cracks near colony boundaries where high local micro-plasticity and depression are observed, corresponding to point f_1 in Figure 3-6-a. It is interesting to note that the points between a_2 and d_2 indicate the raised steps either by translamellar slips or micro-twinning. These features

are not as sharp as the interlamellar slip steps, which are shown by the points between a_1 and e_1. It indicates that this structure resists translamellar cracking more than interlamellar cracking.

In addition to surface cracking, a few sub-surface micro-cracks caused by stress wave propagation were observed over the weak sites of the microstructure. Figure 3-7-c shows an infrequent mixed translamellar/interlamellar sub-surface crack. During incubation stage, such cracks were seen mainly within the type C colonies, showing hard and brittle behavior.

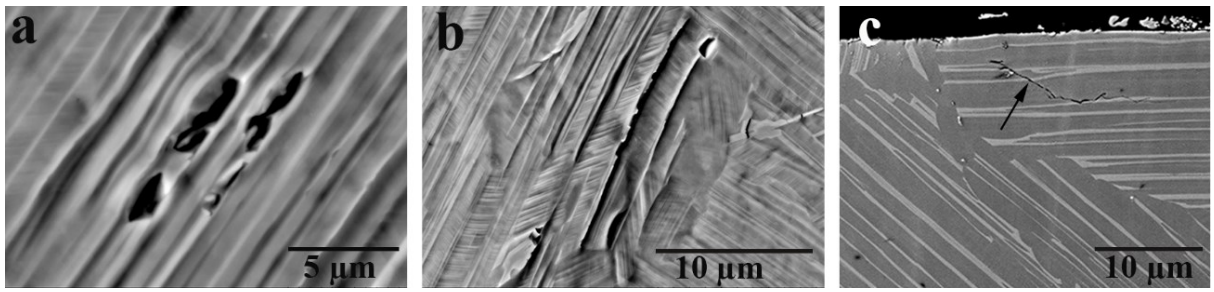

Figure 3-7: (a) SEM micrograph of eroded surface showing interlamlellar cracks nucleation, (b) SEM micrograph of eroded surface showing interlamellar cracking near colony boundaries, (c) cross sectional SEM micrograph of slightly eroded surface showing a sub-surface crack

3.3.1.2. Maximum erosion rate stage

3.3.1.2.1. Microscopic observation of eroded TiAl once material loss starts

After localized plastic deformation and cracks initiation, further droplet impacts result in cracks propagation, their merging and micro-voids formation. The mechanism of material loss initiation is a function of material response to the initial droplet impacts (incubation) and the erosion features generated on the surface. Upon the droplet impact, the hydrodynamic pressures (water hammering) cause local stress concentration and lead to the propagation of cracks. Further propagation results in cracks coalescence, detachment of small fragments and formation of micro-voids. This is demonstrated in Figure 3-8-a where two cracks running along both sides of a γ lamella at the interfaces. After reaching a certain length, they deviate into the γ lamella and meet each other leading to a local fracture and the formation of a micro-void. The micro-voids might also be generated by high speed collision of lateral outflow jets with the raised slip bands. The speed of these jets is up to 10 times of the original droplet impact speed and they are detrimental specially when flowing on the roughened surface [3]. This type of micro-pitting mainly occurred on the lamella interfaces near the boundary of colonies as demonstrated in Figure 3-8-b. It is due to the high level of micro-plasticity and local depressions in these regions, as can be seen in Figure

3-5-b. The high stress concentration on the rim of generated micro-voids results in delamination of the lamellae. These lamellae fracture easily by the following impacts. Furthermore, water hammering and hydraulic penetration lead to crack propagation inside these micro-voids, digging their bottoms and enlarging them. In some cases, the formation of micro-voids occurred at the colony boundaries, as shown in Figure 3-8-c. To give a quantitative insight, twenty micro-voids in the impacted regions were considered. Out of twenty, thirteen were created within the colony and 7 were formed at the boundaries. Even the generated micro-voids at the boundaries expand towards colony interiors because of the preferential crack propagation, as shown in Figures 3-8-c and 3-8-d. Several micro-pits are demonstrated close to each other in Figure 3-8-d. The micro-pit at the boundary of colonies is shown by white arrow and the ones near the colony boundaries are shown by black arrows. The successive droplet impacts result in the growth of these micro-pits and their coalescence forming relatively large and isolated crater, as presented in Figure 3-9.

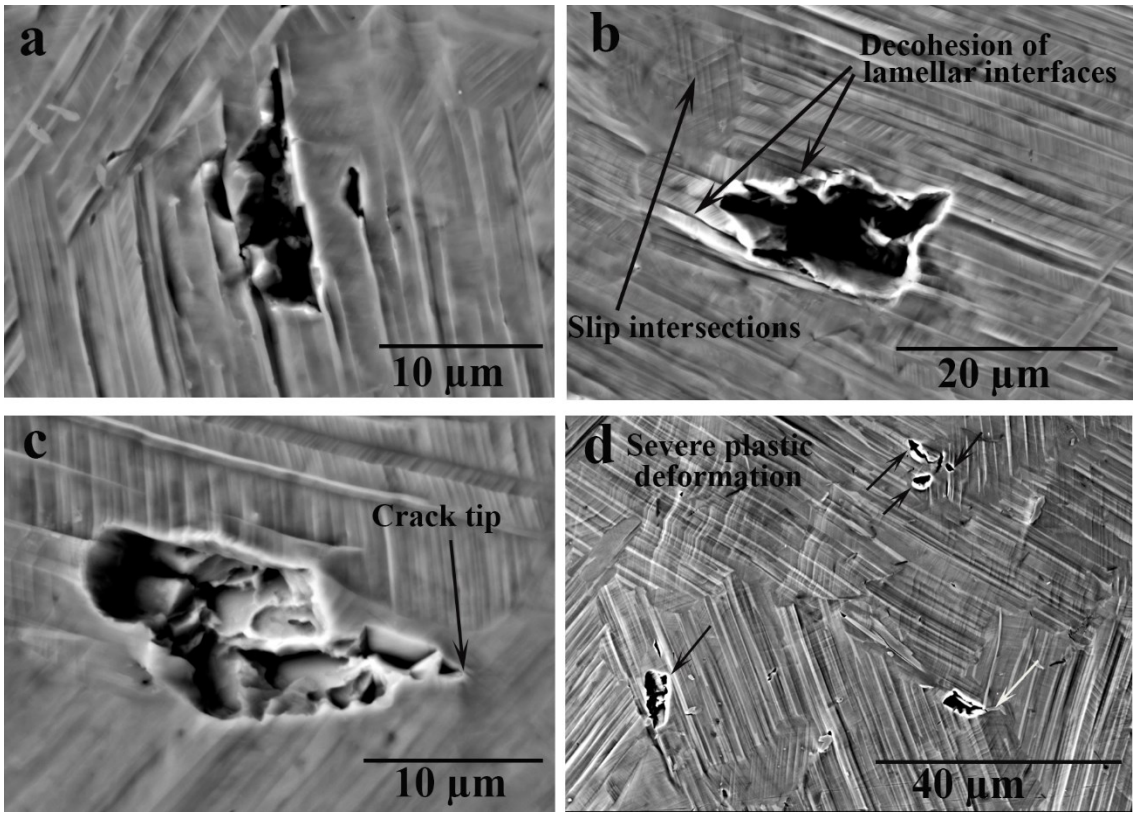

Figure 3-8: SEM micrograph from eroded surface of TiAl after 400,000 droplet impacts, demonstrating severe local plastic deformation, micro-cracking and micro-pitting

3.3.1.2.2. Microscopic observation of eroded TiAl at maximum erosion rate stage

Due to the severe plastic deformation as well as notable micro-pitting at the areas near to the colony boundaries, they become high potential sites for further damage and the formation of isolated erosion craters. Figure 3-9 exhibits one of these isolated craters, which is a common feature in the maximum erosion rate stage. The irregular edges of eroded regions indicate the preferential cracks propagation which is in accordance with the brittle nature of TiAl fracture. Successive droplet impacts cause the propagation of cracks, predominantly interlamellar, both at the rim and bottom of the pits. Initially, the small fragments are removed by delamination of lamellae and their fractures within one colony, highlighted in Figure 3-9. Then, water hammering and subsequent stresses cause development of opened micro-cracks. They run along the lamella interfaces in depth of the target, deviate into the lamella and continue propagating along the next interface. This track is found to be the typical cracking path and subsequent fracture among type A colonies. Another type of fracture, shown in the micrograph, is translamellar fracture. Higher level of stress intensity is required for crack propagation in this manner because the lamella interfaces blunt the propagating cracks. This type of cracking cannot only be attributed to water hammering stresses and the hydraulic penetration seems to be its main cause. Figure 3-10 demonstrates the hydraulic penetration phenomenon through the cross sections of erosion craters. After merging of the generated micro-voids, a relatively wide and shallow cavity was created, shown in Figure 3-10-a. Initially, small fragments of material were removed within one colony. They were associated mostly with interlamellar fractures, highlighted in Figures 3-9 and 3-10-a. Once further droplets impact directly on the cavity, water strikes its bottom in the form of spear-like central jet. This central jet forms because of shock waves coming from the sidewalls of cavity which compress the entering water and generate spear-like jet. It is the main reason of well-known phenomenon during WDE called hydraulic penetration [3], shown by arrow in Figure 3-10-a. The impinging droplets bore the crater and form a narrow pit at the bottom or an undercutting pit at the sidewalls of crater. An evolved tunnel is shown in Figure 3-10-b where the direction of water penetration is indicated by white arrows. Development of such tunnels results in the formation of undercutting pits which are significantly detrimental. The water penetration through these undercuts results in significant stress intensity, which is sufficient for translamellar fractures, highlighted in the micrograph. In this condition, the penetrated water can pull out a big chunk of material. Indeed, it results in high level of tensile stresses in the main crack wake, the direction of

which is shown by the black arrows in Figure 3-10-b. As a result, this crack may propagate upward along the shown dashed line to reach the surface. In the lamellar TiAl alloy, the multiple micro-cracking ahead of the main crack tip, seen in Figure 3-10-b, may decelerate the crack growth. However, the high level of exerted stresses overcome this toughening mechanism and cause fracture. Here, the detachment of large fragments leads to the enlargement of erosion craters. This is the main reason for the observation of maximum material loss rate (erosion rate) in this stage.

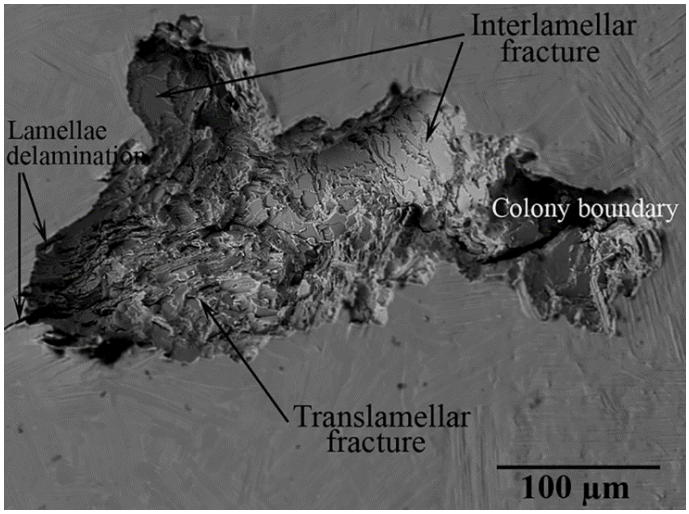

Figure 3-9: SEM micrograph of an isolated erosion crater forming during the maximum erosion rate stage

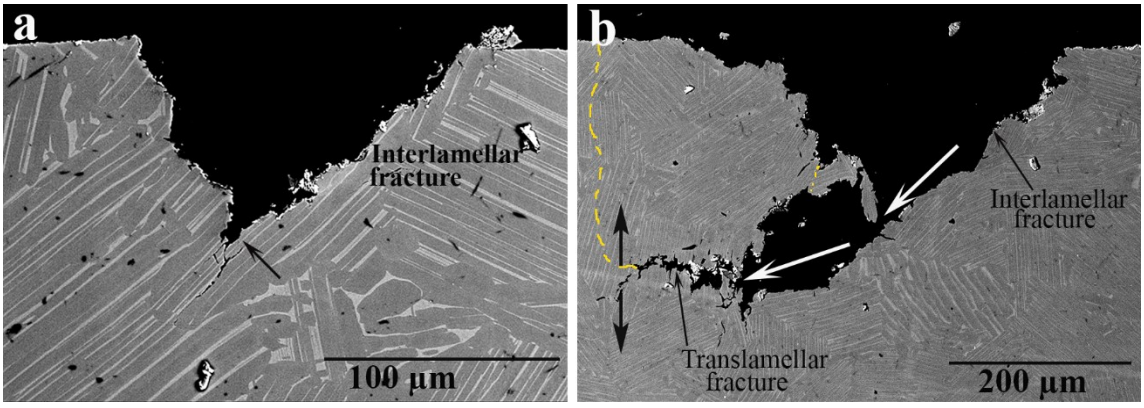

Figure 3-10: Cross sectional SEM micrographs of isolated erosion craters showing hydraulic penetration at: (a) Early stage, (b) evolved stage, leading to formation of an undercutting pit

3.3.1.3. Terminal stage

3.3.1.3.1. Characterization of erosion craters and damage progress

Successive water droplet impacts cause enlarging and merging of isolated erosion craters and lead to evolution of complete erosion line. Figure 3-11-a presents a typical erosion damage

along the impingement line during the terminal stage. The width of erosion crater is 1.08 ± 0.4mm. Unlike ductile metals which show mainly circular craters or voids [30, 41], erosion craters with irregular shapes and sharp edges were observed for TiAl. Figures 3-11-b to 3-11-e present four different cross sections of erosion line. It is clear that the depth of damage varies notably along the erosion line and it may reach 800µm. It is due to the significant inhomogeneous cracking behavior of TiAl alloy which is function of local stress state and localized microstructure including texture and morphology. The surface pattern of erosion crater is another parameter which varies in these micrographs. A wide and relatively shallow crater with smooth surface can be seen in Figure 3-11-b. Such smooth surface could be roughened by droplet impacts, and form a jagged surface such as that shown in Figure 3-11-c. Indeed, hydraulic penetration results in the formation of small and narrow pits on the floor of cavities, and roughens the surface of erosion crater. These features play critical role in controlling material loss. The formation of jagged surface means the creation of vulnerable sites for fracture and it expedites the material loss. In addition, it influences the impact energy transmitted to the target, which is responsible for erosion damage. Herein, the evolution of generated tunnels (narrow pits) causes the formation of some deep voids (sub-surface or undercutting voids) and their adjacent weak sites, shown in Figure 3-11-d. The fractures of these vulnerable sites, which are usually the peaks between two adjacent tunnels or narrow voids, result in smoothing the surface. Similar behavior was reported for the erosion of Ti6Al4V [41]. In general, the evolved erosion damage inside the crater can proceed from the bottom (deepening) and the sidewalls (widening). Their progress and mechanism are reviewed below.

3.3.1.3.1.1. Damage progress on the bottom of erosion crater

In the evolved stages, the water droplets can reach and impinge the bottom of the crater. In this condition, water hammering, water penetration and stress waves are the main damage causes. The exerted stresses by water hammering open the micro-cracks, developed in the previous stages, and cause small detachment of material. These areas are shown by BWH (Bottom Water Hammering) in Figures 3-11 and 3-12-c. Moreover, the hydraulic penetration, explained in section 3.3.1.2.2, damages the bottom of the crater. The induced stresses create a cracks network and subsequently generate tunnels, which result in water roughening. These areas are shown by BWP (Bottom Water Penetrating) in Figure 3-11. Another cause of erosion damage is the stress waves propagating into the depth of target material. It may cause sub-surface crack formation which is depicted in Figure 3-12-a.

3.3.1.3.1.2. Damage progress on the sidewalls of erosion crater

Damage may proceed also on the sidewalls of the erosion craters. Upon droplet impacts, the side jetting results in water penetration and stress wave propagation laterally into the target. They are the main reasons of erosion damage on the sidewalls. The water penetration caused by side jetting occurs mostly at the corners of the erosion crater and leads to the generation of undercutting narrow pits or sub-tunnels. Such features are indicated in Figure 3-11 by SWP (Sidewall Water Penetrating). Development of these pits will be followed by the removal of large fragments, shown in Figure 3-11-e. In addition, the successive jetting leads to stress wave propagation into the sidewalls. It results in high level of stress intensity and subsequent lateral sub-surface cracking. Despite the high level of required stress intensity for translamellar cracking, their formation near sidewalls can be observed in Figure 3-12-b.

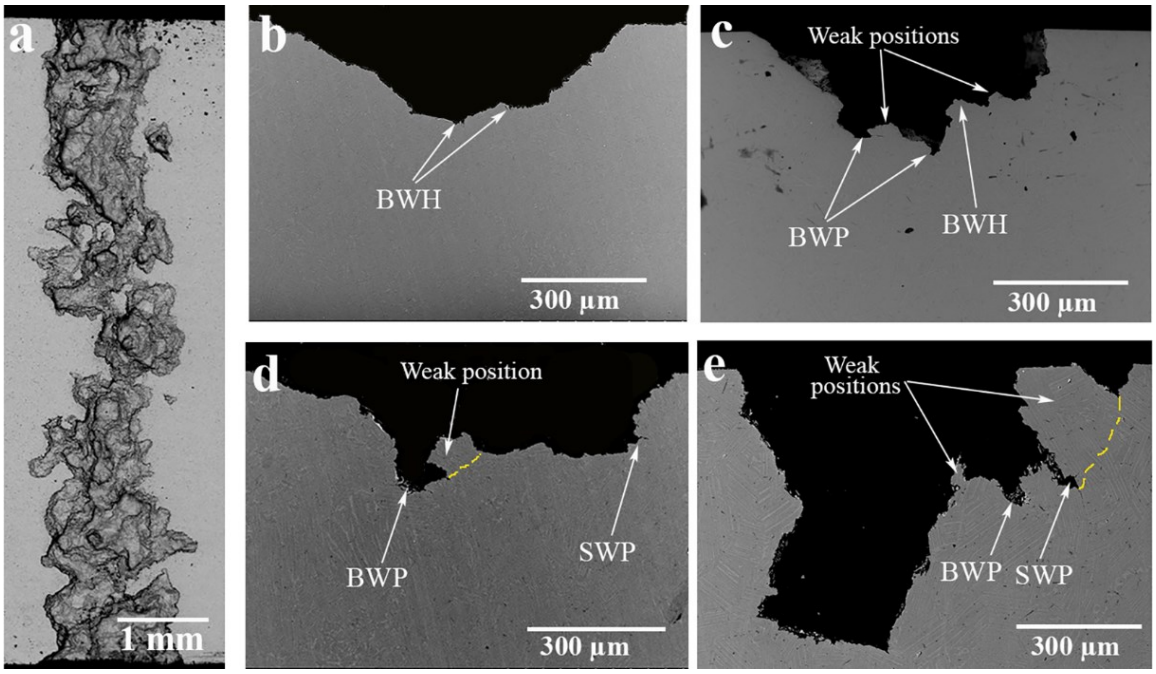

Figure 3-11: (a) SEM micrograph of complete erosion damage line, (b) cross section of eroded TiAl showing wide and shallow pit with relatively smooth surface, (c) cross section of eroded TiAl showing a jagged surface, (d) cross section of eroded TiAl showing formation of an undercutting void at the bottom of crater, (e) cross section of eroded TiAl showing sever damage

3.3.2. Micro-analysis and fractographic interpretation of eroded TiAl at terminal stage

Cracks development is the main contributor to water droplet erosion damage. A systematic study was performed on the cracking behavior using the cross sectional view of eroded specimens. Intergranular cracks, transgranular cracks including, interlamellar and translamellar cracks, and

mixed intergranular/transgranular cracks were documented and analyzed as shown in Figure 3-12. Surface and sub-surface cracks as well as crack networks can be seen over the cross sections. The interlamellar cracks were often observed and they nucleated predominantly through γ/α_2 interfaces, as shown in Figures 3-12-a and 3-12-b. After reaching a certain length these cracks deviated into the adjacent lamella, which is called ligament bridging. The interlamellar cracks and their bridging are shown, respectively, by white and black arrows in Figure 3-12-a. The sub-surface cracks are formed due to the stress waves propagation, either in bottom or sidewalls of erosion craters, as shown in Figure 3-12-b. Figure 3-12-c presents the micro-cracking and fracture caused by water hammering at the bottom of a crater. It results in the removal of small fragments and it is a typical damage in type A and type B colonies. The hydraulic penetration leading to formation of a crack network and subsequent tunnel (BWP) is presented in Figure 3-12-d. The interlamellar cracks are the main contributor in this network; however, the hydraulic penetration on the sidewalls (SWP) is usually associated with translamellar cracking. Figure 3-12-e shows a crack network caused by SWP and the subsequent undercutting pit (sub-tunnel) formation. In addition, the observed intergranular crack indicates the high level of stress intensity in that region. Moreover, very long mixed cracks (interlamellar/translamellar crack shown by black arrow and intergranular/transgranular crack shown by white arrow) were observed at the bottom of another erosion crater, as shown in Figure 3-12-f. Formation of these long cracks are not typical cracking behavior of lamellar TiAl alloys subjected to the cyclic loading [107, 108]. Besides, they were rarely seen in the case of water droplet erosion.

Cracks propagation is a function of local stress state, microstructure, and material properties [107, 119, 120]. For instance, the preferential cracking along the rolling direction was observed over the edges of erosion craters in case of Ti6Al4V, damaged by water droplets [41]. In the case of TiAl, no general trend can be seen for cracking direction. However, the lamellar microstructure and its orientation, which is locally different, control the cracking behavior. As mentioned earlier, the colony's orientation with respect to induced loading direction is critical parameter for the localized cracking. In the advanced erosion stages and inside the erosion crater, determining the loading direction with respect to the colony's orientation is not possible. Because when the droplets impact inside the erosion crater, the hydrodynamic stresses caused by water hammering, water penetration and stress waves propagation are quite inhomogeneous. Hence, the cracking behavior could not be easily analyzed based on this parameter. High speed droplet

impacts cause nucleation of different types of micro-cracks. Not all of them necessarily propagate and cause fracture, since the local stress intensity in the crack wake should be sufficient to cause propagation. For the lamellar TiAl alloys, crack propagation rate significantly depends on the local stress, shown by large exponent for the Paris law [69]. The cracks need to reach a critical stress intensity for propagation. The γ domain boundaries, lamellae interfaces, and colony boundaries are the potential obstacles for crack propagation. The interaction of cracks and these barriers changes in different local microstructures and morphologies. In order to provide quantitative insight on dependency of erosion damage on local microstructure, more than 300 cracks were systematically studied through the cross sectional micrographs. The number of counts for different types of observed cracks, interlamellar, translamellar, mixed interlamellar/translamellar, intergranular, mixed intergranular/transgranular, is shown in Figure 3-13. It is worth noting that all of the interlamellar, translamellar, and mixed interlamellar/translamellar could be assumed as the transgranular cracks.

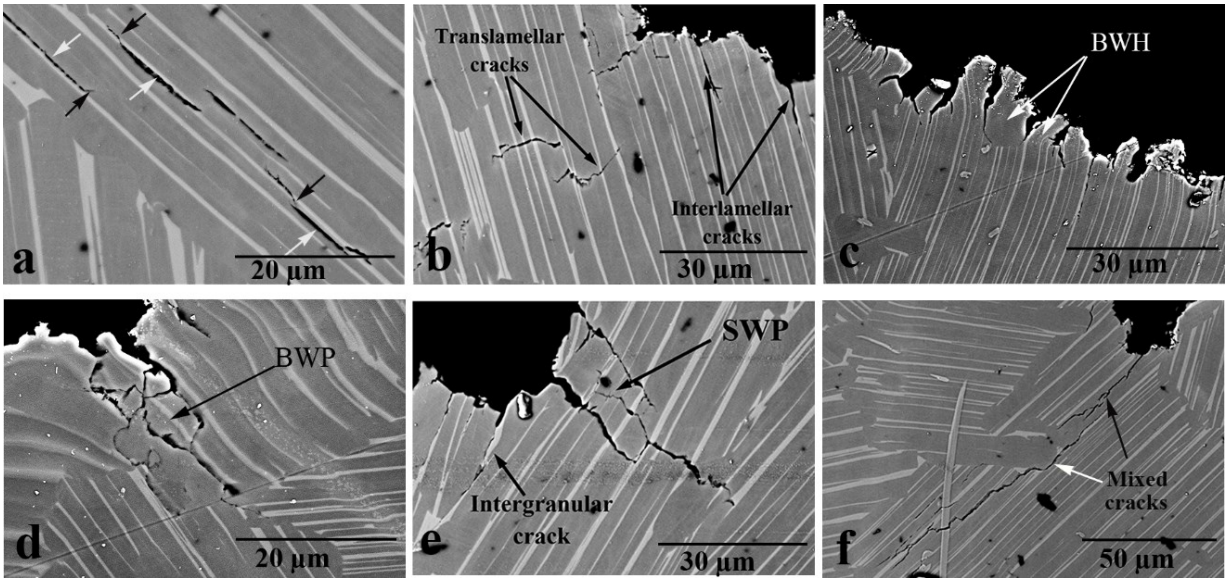

Figure 3-12: SEM micrographs from cross sections of eroded TiAl at terminal stage of erosion, illustrating initiation of different types of cracks as well as their propagation and coalescence

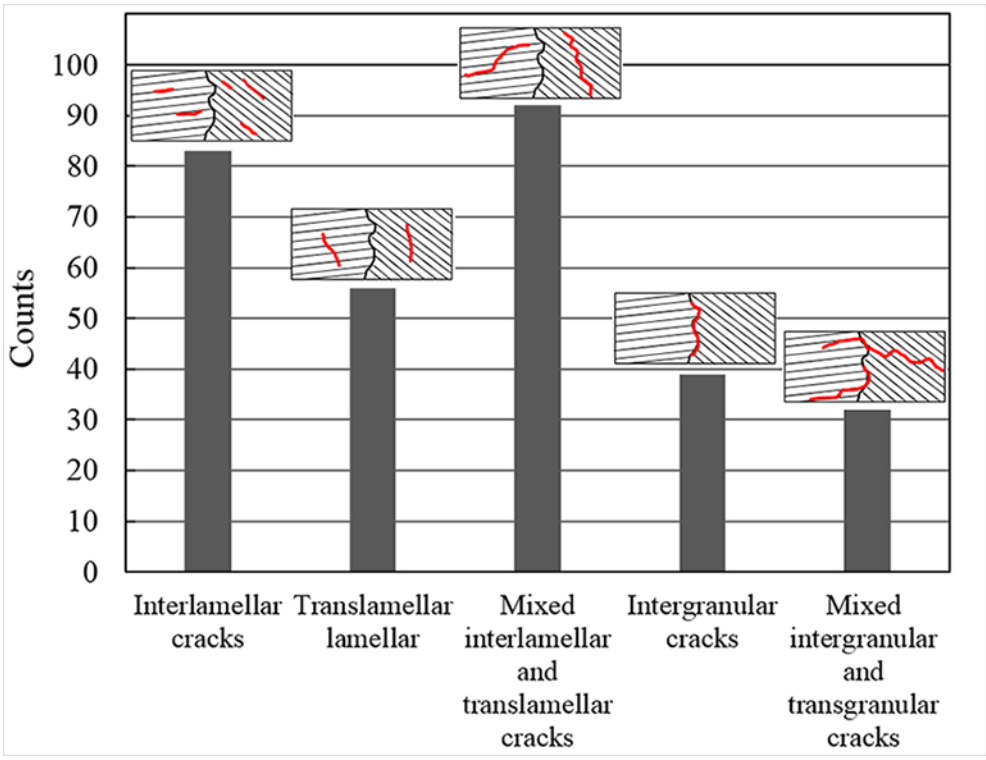

Figure 3-13: Distribution of different types of cracks observed on the edges of erosion craters

The large number of transgranular cracks (interlamellar, translamellar and their combination) indicates that they significantly contribute to the erosion damage. Here, the largest number of cracks is for the mixed interlamellar and translamellar which mainly cause fracture and material chipping off. The number of intergranular cracks is also notable and they need to be taken into account. In some cases, the cracks running along the colony boundaries (intergranular), deviated into the adjacent colony and generated mixed intergranular/transgranuar cracks. This combination was mainly detected at the bottom of erosion crater, as shown in Figure 3-12-f, where there would be the highest stress intensity. The mixed intergranular/transgranuar cracks may result in detachment of large fragments and contribute significantly to erosion damage.

Additionally, the length distribution of these cracks is presented in Figure 3-14. Using cross sectional micrographs, the length of fifty interlamellar, fifty translamellar, fifty mixed interlamellar/translamellar, thirty intergranular and thirty mixed intergranular/transgranular cracks were measured and their length distribution are presented. Almost 80% of interlamellar cracks are shorter than 10µm and the rest are shorter than 20µm. The wider range was observed for the translamellar cracks in which around 70% are longer than 10µm. The length distribution of mixed

cracks is the widest, from 10 to 70μm, and they are mainly (70%) between 10 and 30μm. These results suggest that the cracks predominantly nucleate at the lamella interfaces. Then, a crack running along the lamella interfaces deviates and bridges mainly into γ phase (translamellar) and forms a mixed crack. This bridging is known as one of the toughening mechanism of lamellar TiAl alloys [106, 107]. This is clearly observed here for the eroded TiAl, shown in Figure 3-12-a. The bridging may occur once the interlamellar cracks reach a critical length. This critical length might be different depending on the local stress state and colonies orientation. However, the critical length would be mostly less than 10μm, since almost 80% of interlamellar cracks are smaller than 10μm, as shown in Figure 3-14. This confirms that the larger cracks showed strong tendency to deviate into the adjacent lamellae, which generates interlamellar/translamellar cracks. On the other hand, the translamellar cracks nucleated across lamellae are normally longer than interlamellar cracks. It seems that they overcame several obstacles such as lamella interfaces to reach this length. The high level of local stress intensity is the reason for nucleation and propagation of such relatively long cracks. These cracks could either cause direct translamellar fracture or deviate into the lamella interface, form mixed and longer cracks and then fracture. Kong *et al.* [40] did fractography of the water jet eroded γ-TiAl alloy. They referred to the complex and heterogeneous conditions inside the erosion crater and claimed possibility of different types of fractures. However, they did not provide enough evidence to support their theories. Here, the transgranular (interlamellar and translamellar) cracks are found to be the main contributor to the fracture. Based on the number of counts for intergranular cracks and their length distribution, their contribution to the fracture and erosion damage should be notably lower. The mixed interlamellar/translamellar cracks also participate in fractures and subsequent material loss. These long mixed cracks show several ligaments in the region ahead of their tips. As a result, unstable crack growth and fracture would occur by breaking these ligaments, and lead to detachment of large fragments.

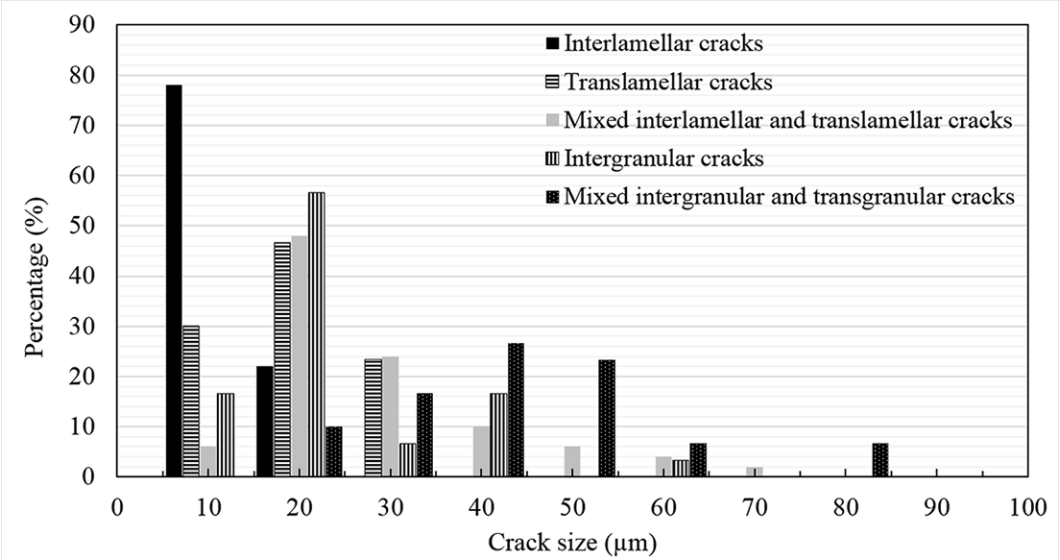

Figure 3-14: Length distribution of different types of cracks observed on the edges of erosion craters

Cracks propagation and their coalescence due to the successive impacts result in localized fracture. Fractography of eroded TiAl alloy in the advanced stages of erosion was performed on the eroded surface and on the cross section. Figure 3-15 illustrates cracks running along the colony boundaries which lead to intergranular fracture. Figure 3-15-a shows an eroded surface inside the erosion crater where the intergranular fracture surface is highlighted. Figure 3-15-b displays a crack propagating along the grain boundaries on a cross section micrograph. The observed cracks in this micrograph may merge and generate an intergranular fracture surface, shown by dashed line.

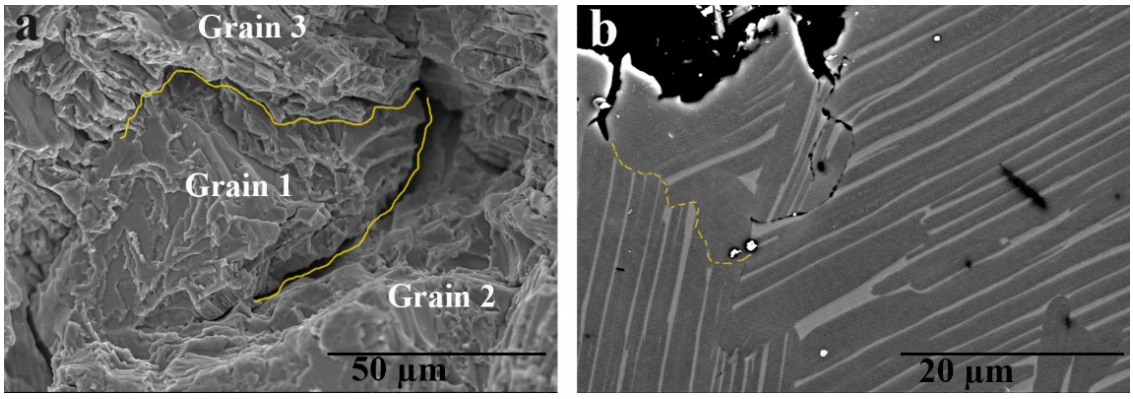

Figure 3-15: SEM micrographs of eroded TiAl at terminal stage of erosion: (a) fracture surface evolved by intergranullar cracks, (b) cross sectional view showing intergranullar cracks

Figure 3-16 presents two common fracture surfaces of eroded TiAl, the translamellar and interlamellar fractures. Translamellar fracture, which occurs across lamellae, was reported to occur

during the fatigue of the same alloy [121]. Rough surface of the observed translamellar fracture is attributed to the high levels of stress intensity. This causes the formation of secondary interlamellar cracks, shown by black arrows, and small steps along each lamellae, shown by a white arrow. There is very high possibility for material loss in the regions having the secondary cracks. The interlamellar fractures are shown in Figure 3-16-b with the revealed lamella surfaces. This kind of fracture was not as frequent as translamellar fracture on the eroded regions. In Figure 3-16-b the fracture surface shows several steps and they are attributed to the bridging of the cracks. It seems that the short interlamellar cracks rarely caused fracture. They often deviate into the lamellae and then continue propagating along the next lamella interface, resulting in mixed cracks. These micrographs suggest that predominantly the combination of interlamellar and translamellar cracks within a colony form the fracture surfaces. The large number of mixed interlamellar/translamellar cracks presented in Figure 3-13 is in accordance with the observed fracture surfaces. It is noteworthy that the striation marks observed on the eroded surface show the cyclic nature of water droplet erosion damage and reveal its fatigue like mechanism.

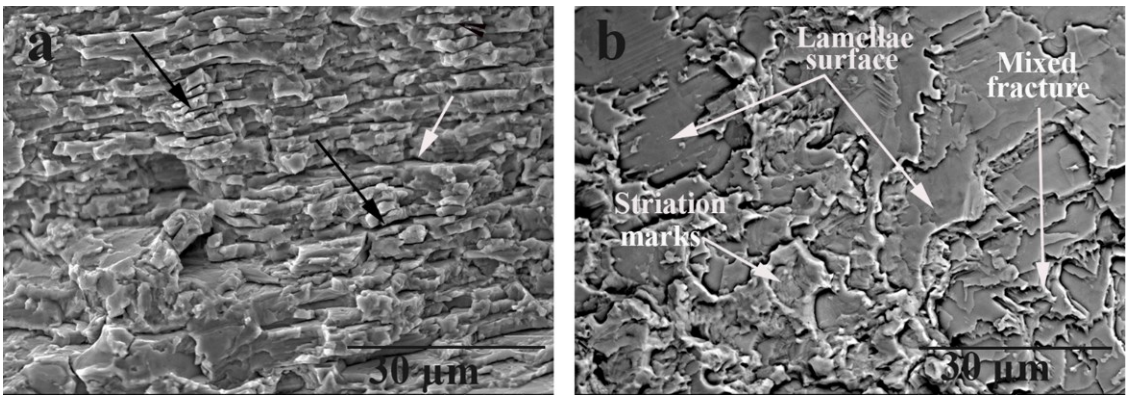

Figure 3-16: SEM micrographs from the surface of eroded TiAl at terminal stage (inside the erosion craters): (a) translamellar fracture surface, (b) interlamellar fracture surface and mixed fracture surface

3.4. Proposed water droplet erosion mechanism for nearly fully lamellar TiAl alloy

In the present study, WDE mechanism of TiAl was investigated at both initial and advanced erosion levels. Accordingly, the damage mechanism is described for different stages including incubation, onset of material loss, maximum erosion rate and terminal stages. Since most of the micro-scale erosion features are localized along the eroded line, the influence of local microstructure on damage mechanism is also addressed.

Microscopic observation of slightly eroded TiAl revealed the initial erosion damage features. Despite the brittle nature of intermetallics, heterogeneous micro-plasticity (slip and twinning) was observed during the incubation stage. Different responses of randomly oriented colonies (with respect to the loading direction) to the initial water droplets cause inhomogeneous plasticity, cracking, and fracture. Inhomogeneous micro-plastic deformation is a known behavior during the fatigue of binary TiAl alloys [107]. In this alloy, slip mainly occurs on {111} planes parallel to the interface of γ and α_2 phases [106]. Their activation by droplet impacts in either γ matrix or γ/α_2 interfaces caused the generation of interlamellar slip steps. Translamellar slips require higher critical resolved stress since they need to overcome more obstacles including closely spaced α_2 plates. Nevertheless, they were detected over the impinged areas. This indicates that the energy of droplet impact is larger than the energy required to create translamellar slips. These fine translamellar slip bands were observed in the high strain rate fracture of TiAl alloys [106, 108]. Indeed, the local transition of high amounts of energy to the target results in the activation of various slip systems in the preferential orientations. This energy could be released partially by the observed crystal reorientation and micro-twinning.

Development of micro-slip bands and micro-twins lead to creation of extrusion/intrusion patterns, shown in Figure 3-17-a, and followed by crack nucleation. This type of crack nucleation is called deformation-induced cracking [122] and was reported as the main contributor to crack development in lamellar TiAl alloys damaged by low cycle fatigue [107]. Herein, the generated intrusions become sharp and act as stress raisers. They result in the crack nucleation with further impacts. During the incubation of TiAl erosion, the cracks nucleated predominantly along the slip bands (intrusions), particularly interlamellar slip bands. This type of cracking was often observed in type A colonies representing soft mode. To provide a quantified insight 20 damaged colonies (within the incubation stage), which underwent slip band cracking and micro-void formation, were observed under microscope. Seventy percent of these colonies were type A showing soft mode. It proves that these colonies are more vulnerable compared to the other types and they notably contribute to the damage initiation. This vulnerability is due to their high level of experienced micro-plasticity. In type A colonies, the long and relatively easy motion of dislocations cause development of heavy extrusions and intrusions, shown in Figure 3-6. The micro-cracks observed along the lamella boundaries and interfaces in such colonies, as shown in Figure 3-6, support this theory. Crack propagation along the interfaces can cause delamination of two adjacent lamellae,

in cases of high local stress intensity. Such cracks may run at both sides of one lamella along the interfaces. After reaching a critical length, which was found around 10µm, they deviate into the lamella and meet each other. This leads to a localized fracture and micro-pitting. This type of pitting is often documented near the colony boundaries and is depicted in Figure 3-8. Unlike the large number of surface micro-cracks which significantly contribute to the damage initiation, sub-surface cracks were rarely observed. Only a few were documented within type C colonies, whose lamellae interfaces were almost perpendicular to the loading direction, demonstrated in Figure 3-b. They normally show high yield strength and very brittle behavior. In addition, the extrusions or raised slip steps, shown in Figure 3-6, also contribute to the damage initiation mechanism. Upon droplet impingement the lateral outflow jets strike the raised slips and twinning bands, causing cracks initiation, local fracture, and micro-void formation. The contribution of extrusions to damage initiation is also inhomogeneous due to different levels of height variation among the impinged colonies. A schematic of extrusion/intrusion pattern and potential sites for cracks nucleation (intrusions), redrawn from Polak's work [123], as well as the strike of lateral outflow jets to the extrusions, redrawn from Heymann's work [3], are presented in Figure 3-17.

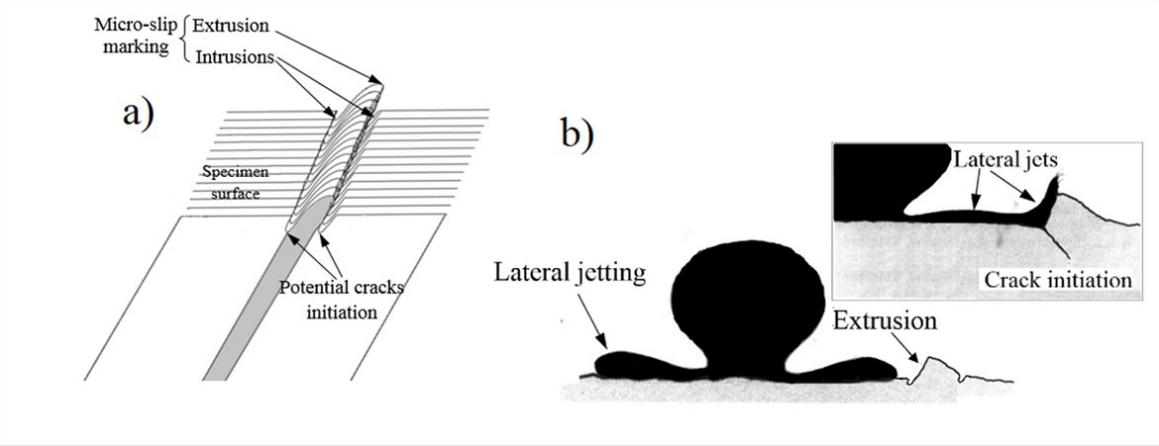

Figure 3-17: Schematic of: (a) extrusion/intrusion pattern and potential sites for cracks nucleation [120], (b) high speed strike of lateral jets to the exaggerated extrusion and subsequent cracks initiation [3]

It is noteworthy that the response of lamellar TiAl alloy to the initial droplet impacts is different from that observed for ductile metals mainly stainless steel and Ti6Al4V [28, 30, 31]. In the cases of ductile metals, droplet impacts predominantly cause local depressions and surface dimples. For Ti6Al4V, grain tilting, intergranular cracking and grain boundaries failure were

proposed as the dominant mechanism [28]. They were not the cases for water droplet erosion of TiAl alloy. No dimple-like deformation was seen on the impacted surface of TiAl. However, localized severe deformation of γ phase results in micro-cracking and initial pitting along the interlamellar slip bands within the colonies.

Further droplet impacts cause more cracking and pitting in the areas, which experienced severe plastic deformation, shown in Figure 3-8-d. Once erosion proceeds the generated micro-voids enlarge and coalesce causing the detachment of larger fragments and the formation of isolated craters scattered along the impingement area. The craters enlargement and their merging to each other correspond to the stage showing maximum erosion rate. These craters become deeper and wider with next droplet impacts. Deepening is due to water hammering and water penetration at the bottom of crater, Figure 3-10-a. Widening is due to the hydraulic penetration at the sidewalls and formation of sub-tunnels and undercutting pits, Figure 3-10-b. Once the relatively deep and complete erosion lines formed, the material loss rate decreases corresponding to the terminal stage of erosion. Herein, the inhomogeneous stress distribution inside the erosion crater results in preferential material loss, water roughening, and formation of jagged surfaces, shown in Figure 3-11-c. Water roughening is associated with the generation of narrow and small pits resulting from hydraulic penetration, which bore the bottom of formed voids and craters. The exerted hydraulic stresses cause the formation of crack networks (interlamellar and tarnslamellar) and their coalescence leads to tunnel formation, shown in Figure 3-12-d. In some cases, the tunnels enlarge and form an undercutting void in the range of colony's size, shown in Figure 3-11-d. Formation of these tunnels and voids cause the generation of a jagged surface and numerous vulnerable sites. Further droplet impacts lead to the fracture of vulnerable regions and smoothing of the surface, which is referred to as water polishing. The cycle of water roughening and water polishing may occur again, if there is sufficient local stress intensity for crack development on the freshly fractured surfaces. It is noteworthy that the attenuation of impact energy inside the deep craters and the subsequent lower local stress intensity, result in a notable decrease of crack development and material loss in the advanced stages of erosion. In addition, the trapped water inside the deep crater act as cushion and dissipate the impact energy. Also, the atomization of water droplet by hitting the sharp edges on the sidewalls of the crater may decrease the local concentration of impact energy and diminish the resulting damage or material loss. These points explain the reduction of material loss rate at the terminal stage of erosion.

3.5. Conclusions

Water droplet erosion damage mechanism of the nearly fully lamellar Ti45Al2Nb2Mn0.8TiB_2 (45-2-2XD) alloy was studied. The damage features at different stages of water droplet erosion were documented. Analysis of these features revealed the following conclusions.

1. Severe and localized micro-plasticity mainly in γ phase is the initial response of the two phase (γ/α_2) TiAl alloy to water droplet impacts. This localized material flow results in the deformation-induced cracking along the lamellae interfaces. Interlamellar cracking is the dominant mechanism of damage initiation.
2. The response of lamellar colonies to droplet impingements is significantly influenced by their orientation with respect to the droplet impact direction. The colonies, oriented with 45°, show the highest level of material flow. They are the most vulnerable colonies to droplet impacts, so that 70% of cracked colonies were oriented with 45° or nearly so.
3. Inhomogeneous plastic deformation of lamellar colonies results in local depressions in the areas near to their boundaries. Numerous local and brittle fractures in such areas lead to micro-pitting and commence material loss.
4. Water hammering, water penetration and stress waves propagation are the main reasons for erosion damage in the advanced stages. They cause a periodic water roughening and water polishing on the surface of erosion craters, which governs damage progress.
5. Fractography of the eroded surface reveals that transgranular fracture consisting of the interlamellar and translamellar cracks is the main contributor to the erosion damage.

Relating to the theme of thesis

In chapter 3, erosion damage mechanism of TiAl was investigated. Irregular erosion damage initiation of TiAl was observed and attributed to the anisotropic response of microstructural colonies to the droplet impingements. The lamellar microstructure of TiAl was found beneficial to suppress crack propagation. The influence of colonies orientation, with respect to the droplet impact direction, on their response to droplet impingements was determined. Based on these findings, the microstructure of TiAl alloys can be manipulated to enhance water droplet erosion resistance. It is aligned with the main objective of this thesis, which is proposing an erosion resistant material for turbine blade. In the next chapters, surface of Ti6Al4V is engineered by gas nitriding and thermal spraying of cermet coating. Influence of these surface treatments on water droplet erosion behavior is explored. At the end, the erosion resistance of surface treated Ti6Al4V and that of TiAl are compared.

Chapter 4 : Water droplet erosion behavior of gas nitrided Ti6Al4V

M.S. Mahdipoor[1], D. Kevorkov[1], P. Jedrzejowski[2], M. Medraj[1,3]

[1] Department of Mechanical and Industrial Engineering, Concordia University, 1455 de Maisonneuve Boulevard West, QC, Montreal, Canada H3G 1M8

[2] Siemens Canada Ltd. Energy, 9545 Cote-de-Liesse, Dorval, QC, Canada H9P 1A5

[3] Department of Mechanical and Materials Engineering, Masdar Institute, Masdar City, Abu Dhabi, UAE, P.O. Box 54224

This article has been submitted to the *Journal of Surface and Coating Technology,* December 2015[3]

ABSTRACT

Water droplet erosion (WDE) is a known cause of failure in the power generation and aerospace industries. It is due to the high speed impingements between water droplets and the target material, which is often seen on the blades of the steam turbines and gas turbines' compressor. Ti6Al4V is one of the most common materials for turbine blades and improving its water erosion resistance is of great interest. In this work gas nitriding was applied on Ti6Al4V and its influence on water droplet erosion performance was investigated. Nitriding was carried out at 900 and 1050°C temperatures using two different nitriding atmospheres, N_2 and N_2-4%H_2 for 5 and 10 hours. The microstructure of specimens was investigated using optical microscope (OM) and scanning electron microscope (SEM). The phases formed after nitriding treatments were analysed using X-ray Diffraction (XRD). Vickers indenter was used to carry out the surface and profile microhardness measurements. The erosion tests were performed using 464µm droplets impacting the samples at 300 and 350m/s speeds. The nitrided specimens at 900°C, which is below β-transus temperature of Ti6Al4V, displayed the best erosion resistance measured by their corresponding cumulative material loss, about two times higher than non-treated Ti6Al4V. The long exposure to nitriding was not beneficial for the erosion performance. The specimen nitrided in the N_2-4%H_2 atmosphere showed slightly higher resistance to erosion than those nitrided in N_2 atmosphere. The latter is due to the formation of a hard and dense compound layer that was deposited due, in part, to the presence of the reducing environment.

[3] In this article, Dr. Kevorkov, as the Research Associate at TMG, and Dr. Jedrzejowski, as the industrial partner, helped in the interpretation of the results.

4.1. Introduction and literature review

Titanium alloys and mostly Ti6Al4V, which has high specific in particular strength and toughness, display superior mechanical properties and corrosion resistance. They are extensively being used in aerospace, aviation, and marine industries [88, 124]. However, they suffer from some mechanical degradations in service conditions such as water droplet erosion, observed on the leading edges of turbine blades [2]. When inlet air cooling system for the gas turbine is in use, the compressors' blades are slowly eroded by the water droplet impingements [2, 11]. Few studies have been performed to explore the WDE mechanisms of Ti6Al4V, and surface and sub-surface cracking were highlighted as the main contributors for the erosion damage [28, 36, 125]. WDE initiation is mostly associated with the grain boundaries damage [28], whilst in the later stages the erosion damage is predominantly governed by transgranular cracking [36, 125].

Water droplet erosion is a progressive mechanical damage and a combination of several phenomena. It is caused by successive high speed impacts of small water droplets on a solid surface [2, 57]. The water hammering, stress wave generation, radial outflow jetting and hydraulic (water) penetration were usually described as the most destructive phenomena during the water droplet erosion [2, 39]. Increasing the hardness, while keeping the homogeneous microstructure on the surface, was found to be a promising approach to combat these destructive phenomena and improve erosion performances [2, 57, 70, 100, 126]. High tendency of titanium for chemical reactions at high temperatures provides large possibility of diffusion-based treatments to increase surface hardness [70, 127]. Nitriding treatments (gas, plasma, and laser based) have been applied to increase the surface hardness and their influence was studied on wear, fatigue and cavitation erosion behaviors of titanium alloys [74, 75, 100, 128-130]. However, it has rarely been investigated for water droplet erosion [100].

Gas nitriding is a practical and applicable technique to strengthen the surface of titanium alloys. The high solubility of nitrogen in α-titanium and its diffusion into this metal (activated by high temperature) results in hardening of the surface [72, 131, 132]. It is a cost-effective technique that is not sensitive to the specimen's geometry [70, 131]. However, the high temperature required for gas nitriding (more than 750°C) can be a major drawback, since it may influence the microstructure and properties of the core material [72, 127, 133]. Nevertheless, if this process is applied using heating techniques that generate localized heating at the surface, the impact on bulk

microstructures can be minimized. Cross sectional microstructure of nitrided Ti6Al4V shows surface compound and diffusion layers. The compound layer comprising of TiN, Ti_2N, Ti_3Al, and $TiAl_2N$ phases is hard and brittle. The mechanical stability of this surface layer which is influenced by its porosity, cracks, and adhesion strength plays a key role in its performance [72, 127, 132]. Despite using nitrogen with high purity for gas nitriding, the formation of oxide and oxynitride phases was found to be inevitable in high temperature nitriding [75, 126, 131]. Beneath the compound layer there is a homogeneous and relatively hard diffusion layer, which is caused by solid solution hardening. This layer is composed of mainly nitrogen enriched α grains, α-Ti(N), which play a key role in postponing the mechanical degradations such as wear and cavitation erosion [72, 75, 127, 134]. However, Mitchell and Brotherton [135] reported that the fatigue limit of Ti6Al4V was reduced by gas nitriding. Bell *et al.* [132] attributed this reduction to variation of the core metal microstructure and formation of brittle α case on the surface. Very high concentration of interstitial elements such as oxygen and nitrogen in α case led to detrimental brittleness of this layer for the low cycle fatigue performance. This high concentration was considered as a defect in some cases and called High Interstitial Defect (HID) [124].

Ti6Al4V subjected to the solution-based and overaged treatments with bimodal microstructure is typically used for engine blade and disk applications [124, 136]. The bimodal morphology is a combination of equiaxed and lamellar morphologies, two possible phase arrangements for α/β titanium alloys [88, 124]. β-annealing followed by slow cooling results in a lamellar or basket-wave microstructure; whereas, equiaxial microstructure is formed by recrystallization [88]. Strength and ductility of α-β titanium alloys considerably depend on the ratio of α to β phases and their morphology. However, lamellar microstructure is generally known for its higher fracture toughness [88, 124]. There is an ongoing debate about the fatigue behavior of these titanium alloys [88, 124, 136]; indeed, the lamellar microstructure is more resistant to crack propagation, yet the equiaxial microstructure is more resistant to crack initiation. Typical duplex microstructure, which benefits from the advantages of both morphologies, is more common in aerospace industries. Although there is a debate in the literature regarding considering water droplet erosion as a fatigue problem [46, 57], both involve cyclic loading conditions and are associated with surface cracking. Indeed, WDE was reported as having fatigue-like mechanism [2, 57]. Hence, nitriding at temperatures above β-transus may be beneficial for the erosion application since it results in a lamellar microstructure of the substrate, which may decelerate crack growth.

In this work, the influence of surface-nitrided layers and the variation of core material microstructure are considered to understand the resulting WDE performance. In addition, the effects of nitriding conditions including temperature, atmosphere and time are investigated on the erosion behavior of nitrided samples.

4.2. Material and experimental procedures

4.2.1. Material

Ti6Al4V sheet with a thickness of 3mm was received from Titanium industries Inc. It is an annealed Ti6Al4V (Grade 5) and its microstructure is composed of equiaxed α grains, retained β and small portion of the transformed β to co-orientated α plates. The α grains are significantly dominant constituent in this equiaxed microstructure, as shown in Figure 4-1, and their mean size is 11μm, which would be affected during the nitiding process.

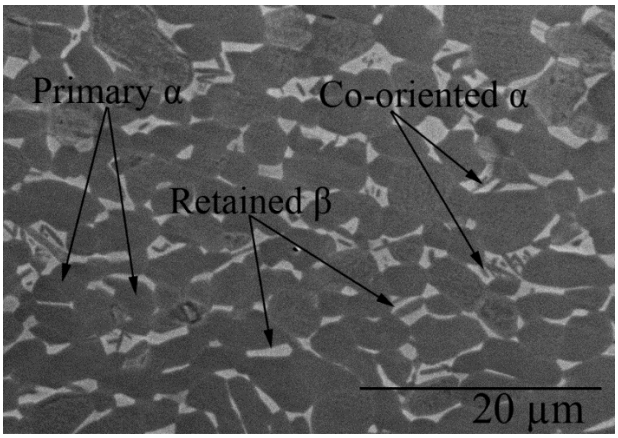

Figure 4-1: BSE-SEM micrographs of as-received Ti6Al4V

These sheets were cut in the dimensions required for the water droplet erosion experiment which is 23mm×8mm×3mm. Then, they were grinded using SiC papers to achieve a relatively smooth surface (R_a=0.06μm). All specimens were cleaned using acetone and then rinsed in distilled water before the nitriding treatment.

4.2.2. Gas nitriding treatment

Gas nitriding was performed using a furnace with controlled atmosphere. The prepared specimens were mounted inside the reaction chamber and it was pumped down to 2×10^{-3}Pa. Nitriding was performed under static atmospheres of N_2 and N_2–4%H_2 at temperatures of 900 and

1050°C. The dwell times were set 5 and 10h and then the specimens were cooled down in the furnace. The different steps of the nitriding process are demonstrated in Figure 4-2.

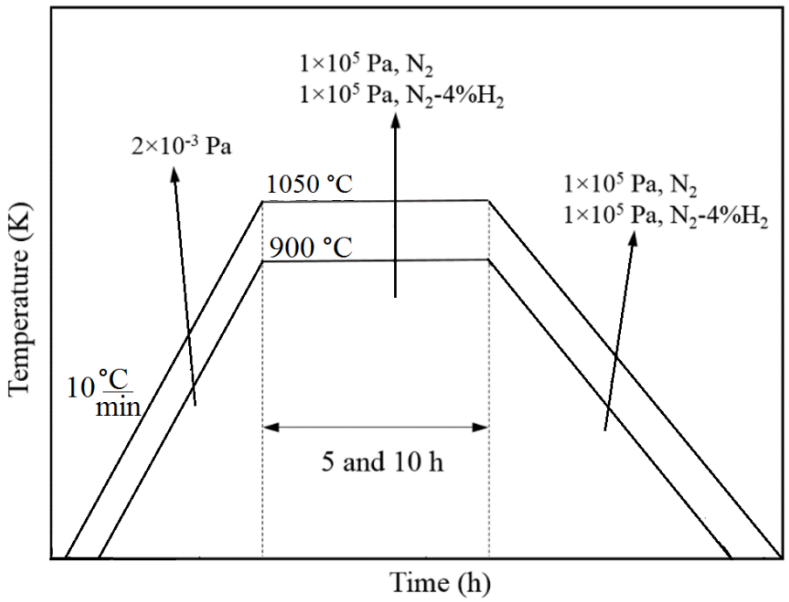

Figure 4-2: Different steps of nitriding process

The coupons nitrided with the above mentioned conditions are listed in Table 4-1. Further in the text, they will be referred to by their names that give clear indications of the different experimental conditions.

Table 4-1: Nitriding conditions of Ti6Al4V

Coupon number	Nitriding temperature (°C)	Nitriding atmosphere	Nitriding time (h)	Coupon name
1	900	100%N_2	5	900C-5h
2	900	100%N_2	10	900C-10h
3	1050	100%N_2	5	1050C-5h
4	1050	100%N_2	10	1050C-10h
5	900	96%N_2 + 4%H_2	5	H-900C-5h

4.2.3. Characterization of nitrided specimens

After the surface treatments, the phase constituents were investigated using X-ray diffraction (XRD) analysis. It was carried out using Cu-Kα radiation in a PANAnalytical X-ray

diffractometer. The surface and cross section of nitrided specimens, prepared by standard metallographic techniques, were explored using optical microscope (OM), and scanning electron microscope (SEM, Hitachi S-3400N). In order to reveal the microstructural features, cross section of nitrded coupons were etched using Kroll's Reagent etchant. Surface microhardness and microhardness profile of the specimens were measured using Vickers indenter at a load of 0.05kgf (0.5N) and 15s dwell. The measurements were carried out on cross sections taken from the surface to the middle of the specimens. At each depth, at least five measurements were performed and their average was recorded.

4.2.4. Water droplet erosion test

Water droplet erosion experiments were carried out using a rotating disk rig which was designed according to the ASTM G73 standard [54]. Figure 4-3 represents a schematic of the utilized erosion rig. Erosion test specimens are mounted on the disk and they are subjected to water droplet impacts during their high speed rotations. This rig enables accurate measurements of impingement speed and number of droplet impacts. More details on this rig can be found in our previous publications [26, 64]. In this study, droplet size of 464μm (average) and impact speeds of 300 and 350m/s were used for the erosion experiments. They were performed in pre-set time intervals to construct erosion graphs. After each interval, the eroded samples were studied including microscopic examinations and weight loss measurements. This routine allows to detect the damage level of various layers by examining the erosion features over the damaged area using an optical microscope. By measuring the weight loss after each interval and knowing the density of target, the cumulative volume loss curves are plotted versus the cumulative erosion exposure. The incubation period (H_0) and maximum erosion rate (ER_{max}), the typical erosion indicators, could be obtained from these graphs according to ASTM G73 standard [54]. The vertical axis of the erosion graphs is the volume loss and the horizontal axis is the volume of impacting water and both are normalized by the area exposed to water droplets. Hence, a dimensionless maximum erosion rate could be reported. The area exposed to water droplets was measured from the optical micrographs of the eroded specimen recorded at the beginning of the maximum erosion rate stage.

The instantaneous erosion rate graphs, which were derived from the slope between two consecutive points on the volume loss curves, are also presented. Since the mechanical properties and microstructure of several layers in depth of Ti6Al4V were influenced by nitriding, the

instantaneous erosion rate graphs are beneficial to track and associate the erosion behaviour and the damage mechanisms to the different layers.

In order to detect small changes in water erosion behaviour, it is important to always use an untreated Ti6Al4V sample as a reference coupon. This sample will counter balance the nitrided sample and will be used to gauge any improvement in water erosion performance. Thereby, the superiority graphs are presented minimize experimental errors, as detailed in our previous work [64]. During the erosion experiment the superiority of the nitrided coupon at each interval is defined according to Equation 4-1. Then they are used for the superiority graphs. In these graphs positive value for the superiority means that the nitrided Ti6Al4V lost less material than the as-received one and vice versa. It is notable that the aforementioned superiority equation is invalid within the incubation of reference Ti6Al4V when its volume loss is zero.

$$Superiority\ of\ nitrided\ Ti6Al4V(\%) = \frac{Volume\ loss\ of\ Ti64 - Volume\ loss\ of\ nitrided\ Ti64}{Volume\ loss\ of\ Ti64} \qquad \textit{Equation 4-1}$$

To consider the total erosion performance of specimens, their cumulative erosion resistance as the reciprocal of cumulative material loss rate [8] will also be reported according to the following equation:

$$CER = \frac{1}{ER_F} = \frac{Cumulative\ volume\ of\ impacted\ water}{Cumulative\ volume\ loss} \qquad \textit{Equation 4-2}$$

where ER_F is the cumulative material loss (erosion) rate at the end of erosion tests, which is slope of the line connecting the origin to the last point of erosion graph. The experiments were stopped when the last stage of erosion, terminal steady state stage, was reached. In cases of 350 and 300m/s impact speeds, the erosion tests were stopped after 15 and 60 minutes erosion, respectively. These time intervals correspond to 65 and 220ml of water which impinged the specimens.

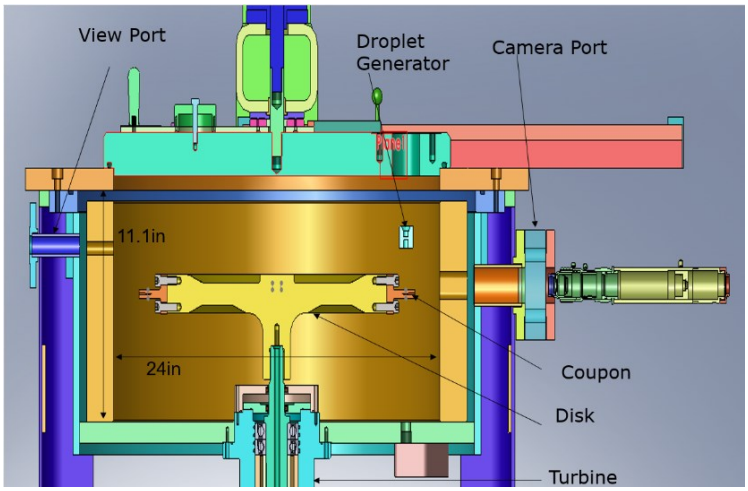

Figure 4-3: Schematic of the water droplet erosion rig

4.3. Results and discussion

4.3.1. Microstructural investigation

After nitriding, different colours were observed on the nitrided specimens. The coupons nitrided at 900°C were mainly golden or purple/golden which indicates the formation of titanium nitride phases, as shown in Figure 4-4. However, the samples nitrided at 1050°C for 5 and 10 hours became dark grey/black and light grey, respectively. It indicates the formation of other phases in addition to titanium nitrides, which were explored using the X-ray diffraction technique. The XRD patterns of as-received Ti6Al4V and nitrided specimens are presented in Figure 4-5. Strong α-Ti and weak β-Ti diffraction peaks were detected for the as-received Ti6Al4V. In the cases of nitrided specimens, α-Ti, TiN, TiNO, Ti_2N, $Ti_3AlO_{0.15}$ and TiO_2 peaks were revealed and there was no β-Ti peak. Ti6Al4V has considerable amount of aluminium and formation of relatively Al-rich phases such as Ti_2AlN and Ti_3Al was reported [72]. However, they were not detected in this work. Comparing the XRD spectrums of 900C-5h and H-900C-5h reveal that adding 4% hydrogen to the nitriding environment led to formation of more TiN compound on the surface, which have golden colour. In addition, α-Ti phase peaks display greater intensities for the coupons nitrided at higher temperatures. It is due to the higher diffusion of nitrogen in such specimens, stabilizing the α-Ti phase in the layers close to the surface. Despite the high purity of the nitrogen gas used for nitriding treatments, the oxide phases were observed for 900C-10h, 1050C-5h, and 1050C-10h coupons. In case of the sample nitrided at 900°C for 10h, the main peaks belong to titanium nitride phases. However, the rutile and titanium oxynitride phases are also detected. Relatively higher level of oxide phases can be seen in the specimens nitrided at 1050°C. It seems that there was a higher

chance for oxidation when nitriding was carried out at higher temperature, especially for longer time. This was also reported by others [75, 126, 131]. Titanium is very sensitive to oxygen particularly at temperature above 800°C [137]; however, oxides formation is usually suppressed by low partial pressure of oxygen in nitriding treatment. Using higher temperature for nitriding results in the partial displacement of nitrogen by oxygen and the formation of titanium oxides within the surface layers. Rutile is an undesired phase for the applied treatment and would be detrimental for the mechanical properties and erosion performance. This may not be the case for titanium oxynitride phase, since Pohrelyuk *et al.* [138] highlighted its superior microhardness compared to that of titanium nitride. Generation of rutile and titanium oxynitride phases for the coupons nitrided at 1050°C influences their surface microhardness, as will be discussed in section 3.2.

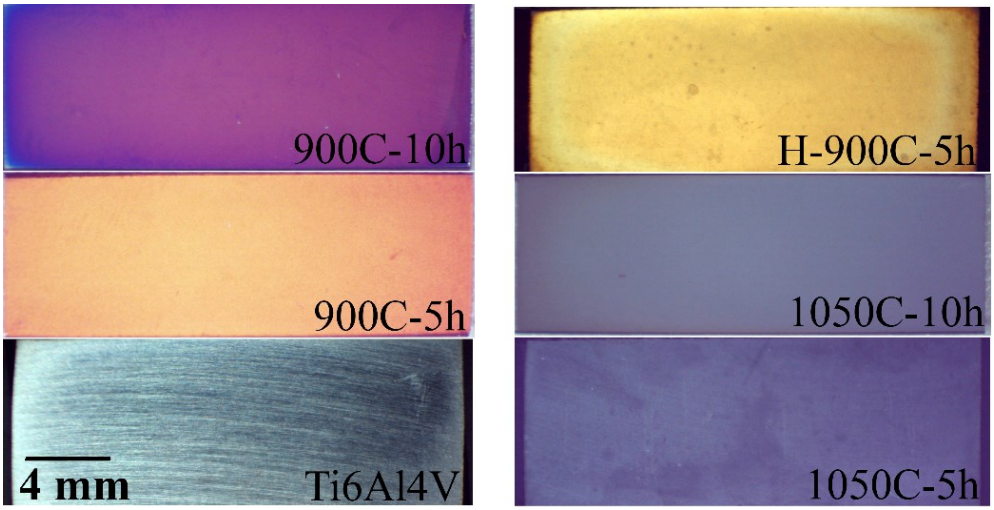

Figure 4-4: Appearance of as-received Ti6Al4V and nitrided Ti6Al4V coupons

Figure 4-6 demonstrates the surface morphology of Ti6Al4V nitrided at 900 and 1050°C temperatures for 5 hours. These morphologies are affected by nitriding temperature, formed phases, and the growth type of outermost layer. At 900°C, TiN compound with relatively fine and dense microstructure, composed of rounded agglomerates, were generated. However, TiO_2 compound with faceted structure predominantly form the outermost layer of nitrided Ti6Al4V at 1050°C. Titanium oxide is porous and relatively rough which is detrimental for erosion application.

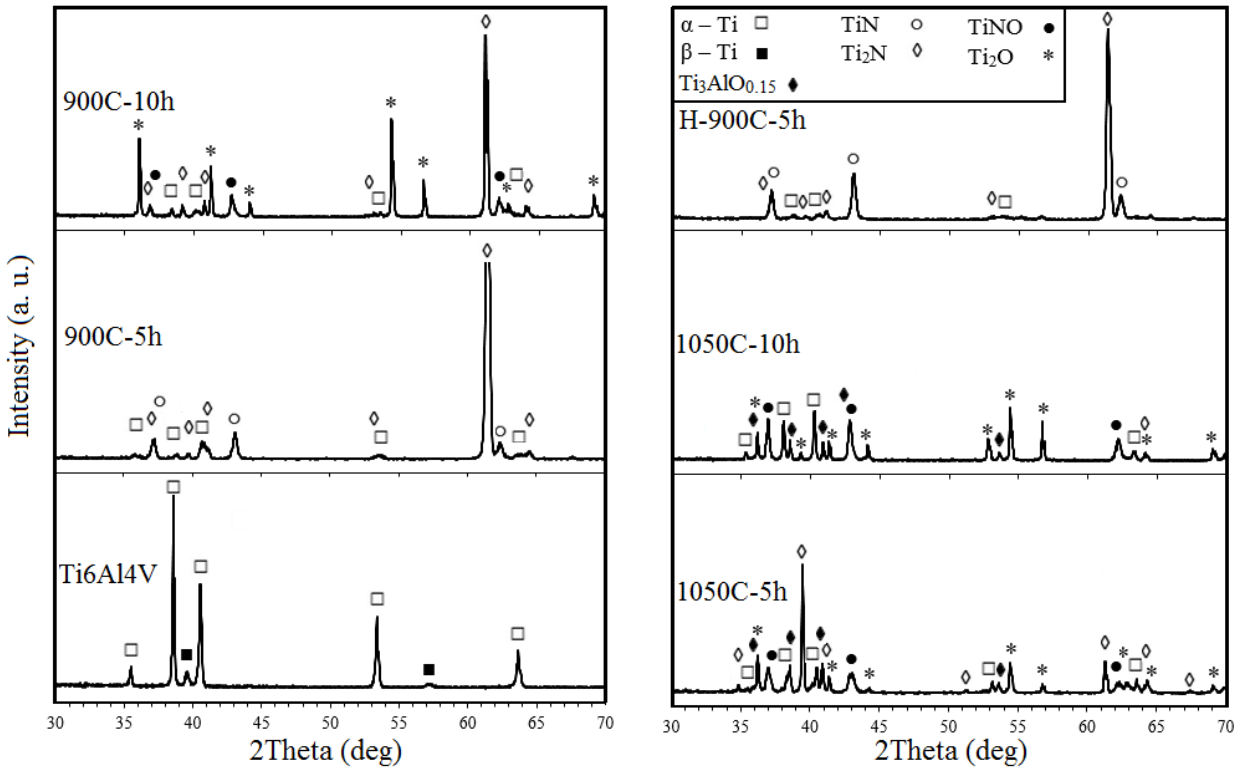

Figure 4-5: XRD patterns of as-received Ti6Al4V and nitrided coupons

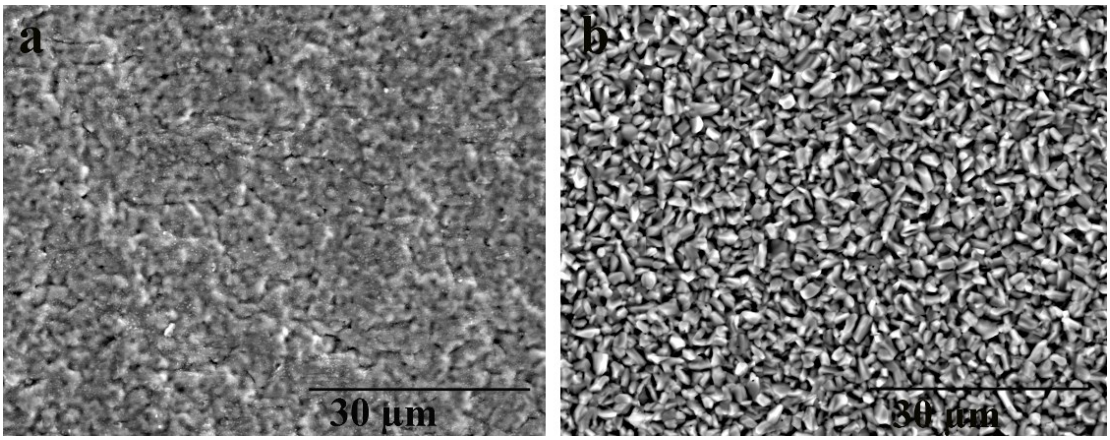

Figure 4-6: SE-SEM micrographs of the surface of nitrided Ti6Al4V: (a) 900C-5h, (b) 1050C-5h

Influence of nitriding temperature on the morphology and microstructure of nitrided layers are studied through the cross sectional micrographs using OM at low magnification and SEM at high magnification. Figure 4-7 shows these micrographs for the coupon nitrided at 900°C for 5 hour. Four different areas, A, B, C, and D can be observed in the OM micrograph. Area A depicts the compounds layers, TiN and Ti_2N, and their microstructure at higher magnification can be seen in SEM micrograph, shown in Figure 4-7-b. Relatively dense and thin TiN layer, 4µm thickness,

with crack-free interface is the outermost layer of the 900C-5h coupon. Within 5 to 15µm from the surface an intermediate layer composed of two phases, Ti_2N and α-Ti(N), can be seen. Beneath the compound layers, nitrogen diffusion areas are shown. Detecting nitrogen with EDS detector was not possible because it is a very light element and its peaks overlap with titanium. Therefore, diffusion areas were determined by considering the microstructure variation. Nitrogen is an α stabilizer element and its diffusion pushes down β phase. Hence, diffusion layers are roughly identified based on the amount of α phase, which was measured using ImageJ software [139]. Region B has more than 90% α phase. Here, there are nitrogen enriched α grains and some retained β phase in their boundaries. Below this area, region C can be seen which is composed of more than 70% primary globular α grains and less than 30% lamellar colonies. Going further in depth, region D having less than 70% globular α grains can be seen. The amount of globular α grains in the core material, which was not influenced by diffusion of nitrogen, were found 65±5%. Hence, region D is assumed as the part of coupon which was not influenced by nitrogen diffusion. However, the applied high temperature treatment changed the microstructure of this region where the average size of globular α grains slightly increased. During the dwell time some α grains transformed to β phase and they became small colonies with basket-weave microstructure during the cooling. These colonies have lamellar configuration which is composed of co-oriented α lamellae separated by ribs of retained β, shown in Figure 4-7-c. These lamellar colonies in the observed duplex microstructure may affect the cracking behaviour of nitrided coupons and subsequently their erosion performance.

Figure 4-8 demonstrates the cross sectional micrographs of Ti6Al4V nitrided at 1050°C for 5 hours. In this micrograph also four distinct regions, A, B, C, and D are distinguished. Region A indicates the compounds layers, which are also displayed in the magnified SEM micrograph. Unlike nitriding at 900°C, a relatively thick and porous TiO_2 layer formed at 1050°C at the top surface having large number of pores and cracks at its interface. This porous layer is not mechanically stable and is significantly vulnerable. Beneath this layer, a thin and dense film can be seen which might be a mixture of TiNO and Ti_2N phases. The last part of A region is a mixture of $Ti_3AlO_{0.15}$ compound and saturated α phase. In the case of sample 1050C-5h, there is a notable difference for the morphology of areas affected by nitrogen diffusion. A β-free layer consisting of large α grains is highlighted as B region. The formation of this relatively thick and highly saturated layer with nitrogen and oxygen is explained by the fact that 1050°C is above β-transus temperature.

Heating up to this temperature leads to the transformation of α to β phase. Nitrogen diffuses faster in bcc β phase due to its lower packing density compared to hcp α phase [70, 88]. Its diffusion caused phase transformation from β to α in the dwelling stage of nitriding treatment [132]. In the cooling stage, the remained saturated β phase completely transforms to α phase at the area close to the surface and generates β-free region B. Below region B, a duplex microstructure including large and irregular α needles and large lamellar colonies can be seen as region C. Last region in this micrograph, D, is the part which was not affected by nitrogen diffusion. However, its microstructure was completely affected by the high temperature of applied treatment. Generation of such coarse and lamellar microstructure is due to the temperature of nitriding (above β-transus) followed by furnace cooling. At this temperature, the initial equiaxed α grains were dissolved and transformed to β phase. Then subsequent slow cooling from this temperature caused recrystallization and the generation of very large lamellar colonies consisting of co-oriented α plates separated by retained β. It is noteworthy that the large and irregular α needles observed in the closer areas to the surface, region C, are basically α plates which are enlarged in their preferred orientation due to the nitrogen diffusion.

The mechanism and kinetic of nitrogen diffusion at these two temperatures are different which lead to different phases, morphology and thickness of the surface layers. In the case of compounds layers, competition between the formation of nitrirde and oxide phases needs to be highlighted. Nitriding at high temperature caused the formation of porous titanium oxide layer which plays a key role in erosion damage initiation, as will be explained in section 3.3.2. In the case of nitrogen diffusion areas not only their morphology, but also their mechanical properties (microhardness) were influenced by nitriding temperature. The nitrogen diffusion increases the hardness and plotting the microhardness profile over the cross section of nitrided coupons was conventionally used to reveal the thickness of diffusion layers. However, determining the depth of diffusion layers through the microstructure only is tricky because some of the observed differences can be results of particles segregation or phase transformations during the cooling. Hence, the microhardness profile measurements are explained in the following section.

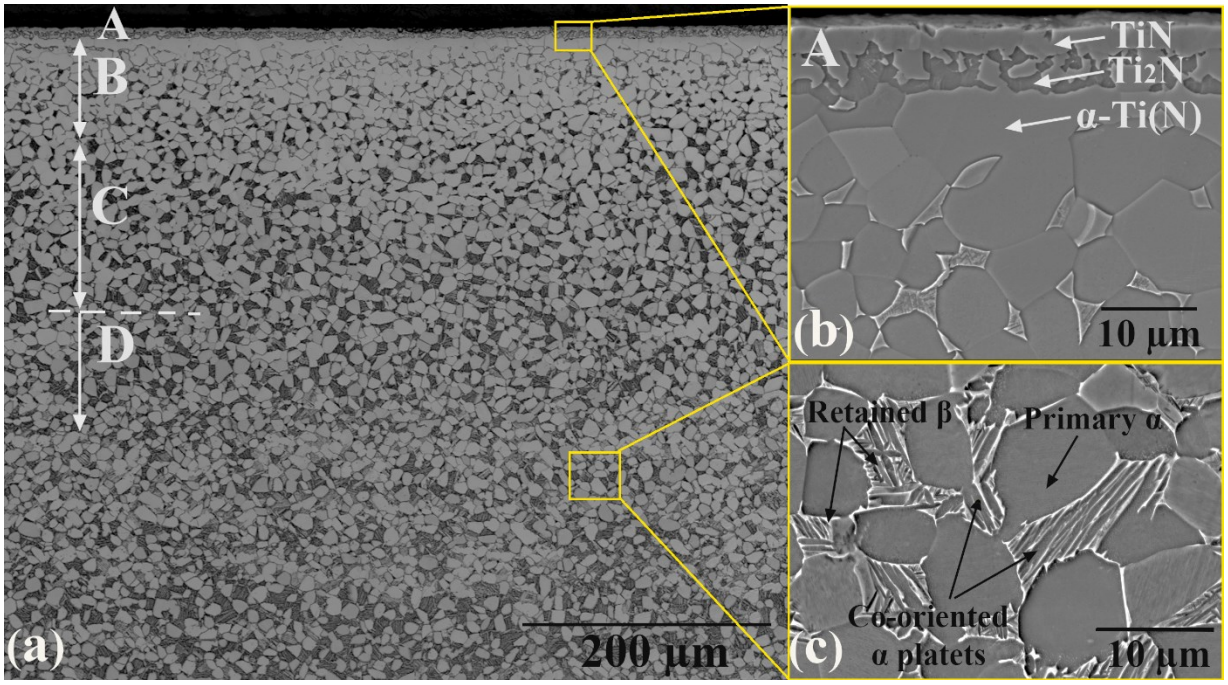

Figure 4-7: (a) OM and (b,c) BSE-SEM cross sectional micrographs of Ti6Al4V nitrided at 900℃ for 5 hours

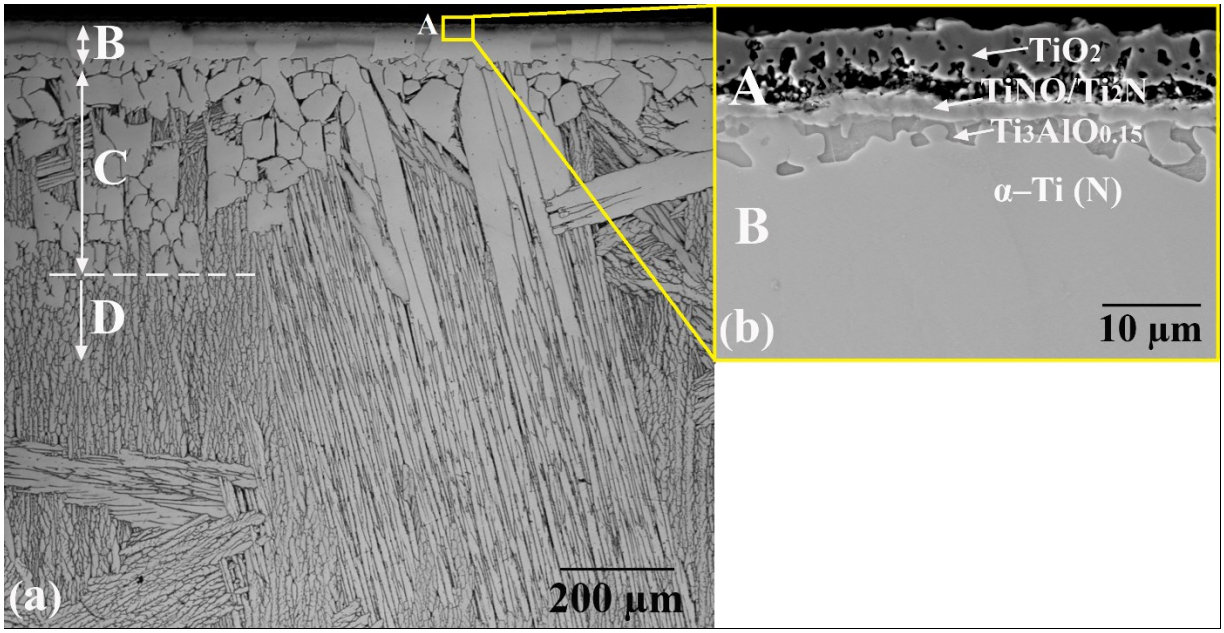

Figure 4-8: (a) OM and (b) BSE-SEM cross sectional micrographs of Ti6Al4V nitrided at 1050℃ for 5 hours

4.3.2. Microhardness of nitrided specimens

Microhardness profiles in depth of the coupons nitrided at 900°C are presented in Figure 4-9. The first point in these graphs was measured on the surface and corresponds to hardness of layer A (compound layer). The second to fifth points in the hardness profile of sample 900C-5h

correspond to layer B (diffusion layer). In this layer notable increase in hardness compared to region D can be seen. Also, it is up to $675HV_{0.05}$ which is two times the hardness of as-received Ti6Al4V. In the deeper parts which correspond to layer C no increase in hardness is observed. The higher amount of α phase in layer C compared to layer D was attributed to the nitrogen diffusion as described in section 3.1. Indeed, there is a slight diffusion which varies microstructure, but does not increase the hardness. Here, the highest surface hardness is observed for the sample nitrided at low temperature in the presences of hydrogen, H-900C-5h. It is due to formation of a dense compound layer consisting of titanium nitride compounds in this condition. Lower surface hardness for the sample nitrided for the longer time can be seen in this figure. It is attributed to the formation of some oxide phases within the compound layer of 900C-10h coupon. Nitriding time and the presence of H_2 do not affect the hardness of diffusion layer in the areas close to the surface (second point on the graphs); however, going deeper some variation can be seen. Thicker diffusion layer is detected for the sample nitrided for longer time, 900C-10h. While hardness profile of 900C-5h coupon reaches the hardness of core material at 90μm distance from the surface, it reaches base hardness at 200μm for 900C-10h coupon. Furthermore, the presence of hydrogen in the nitriding environment does not influence the hardness of diffusion layer considerably. In spite of some fluctuations, similar trend can be seen for the hardness profile of 900C-5h and H-900C-5h coupons.

Figure 4-10 shows the microhardness profiles over cross section of the coupons nitrided at 1050°C for 5 and 10 hours. The different layers (A, B, C, and D) observed in the micrographs of the sample nitrided at 1050C for 5h and discussed in section 3.1 are shown on this figure. Hardness of layer A or the compound layer is $988HV_{0.05}$ which was measured on the surface. The hardness within layer B was measured over the β-free layer, shown in Figure 4-8. Its gradient indicates the change in the concentration of nitrogen in diffusion layer. Unlike 900C-5h coupon, layers C and D of sample nitrided at 1050°C is harder than as-received Ti6Al4V. In layer C, it is due to the formation of large α needles which was attributed to the slight diffusion of nitrogen at this temperature. It is noteworthy that the hardness of these layers is similar to the hardness of annealed Ti6Al4V at 1050°C for 5h. Hence, the higher hardness cannot be easily correlated to nitrogen diffusion. Indeed, the lamellar-based morphology of these layers also contributes to the hardness increase. Furthermore, surface hardness of sample nitrided for 5 hours is slightly higher than that of sample nitrided for 10 hours. Similar hardness can be seen in depth of 1050C-5h and 1050C-

10h samples (their diffusion layers). It seems that nitriding time does not notably affect the concentration of diffused nitrogen in layers B and C. This can be explained by the formation of thick compounds layers in high temperature nitriding which may impede further nitrogen diffusion at long nitriding treatments.

Comparing the hardness profiles in Figures 4-9 and 4-10 show the significant influence of nitriding temperature on the hardness of nitrided coupons. Surface hardness of sample nitrided at 900°C for 5h is 1134$HV_{0.05}$ which is higher than that of sample nitrided at 1050°C for 5h, 988$HV_{0.05}$. It is attributed to the nitrided compounds in the surface layer of 900C-5h coupon which are harder than porous oxide compounds layer of 1050C-5h coupon. Nitridng temperature also affects the hardness of diffusion layers. Diffusion layer of sample nitrided at 1050°C (layer B) is approximately 100HV harder than that of sample nitrided at 900°C. It is explained by higher concentration of nitrogen and oxygen in the interstitial sites of titanium as a result of higher diffusion coefficient at this temperature. It is noteworthy that higher diffusion of nitrogen at 1050°C is mitigated notably by the formation of thick compound layer in the later stages of long nitriding treatments. Another difference between samples nitrided above and below β-transus temperature is the hardness of their core material. The hardness of 900C-5h sample at 300μm distance from the surface is 305$HV_{0.05}$, which is slightly higher (is considered within the error bars) than that of as-received Ti6Al4V (292$HV_{0.05}$). However, it is 364 for the 1050C-5h coupon, which is 74HV higher than that of as-received Ti6Al4V.

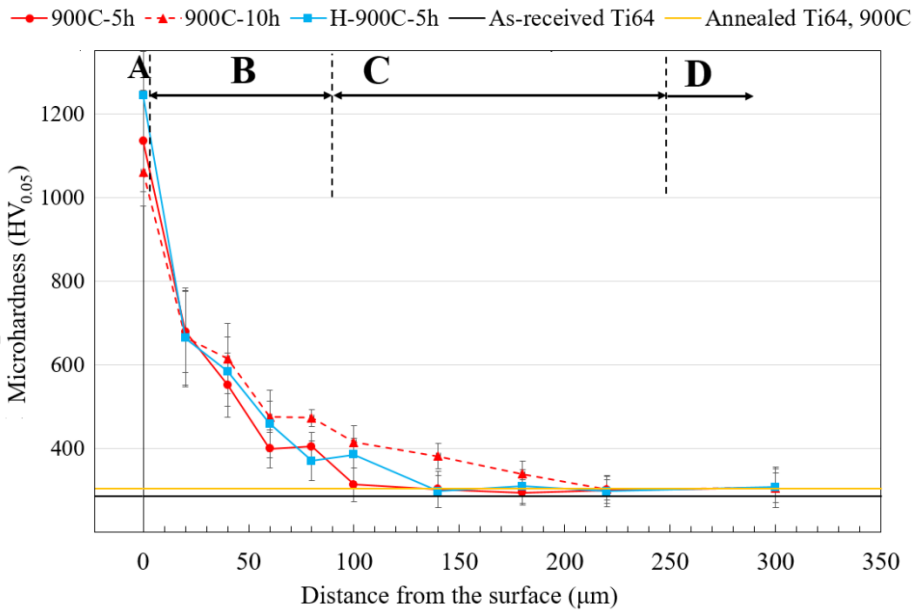

Figure 4-9: Microhardness profiles of nitrided Ti6Al4V at 900℃

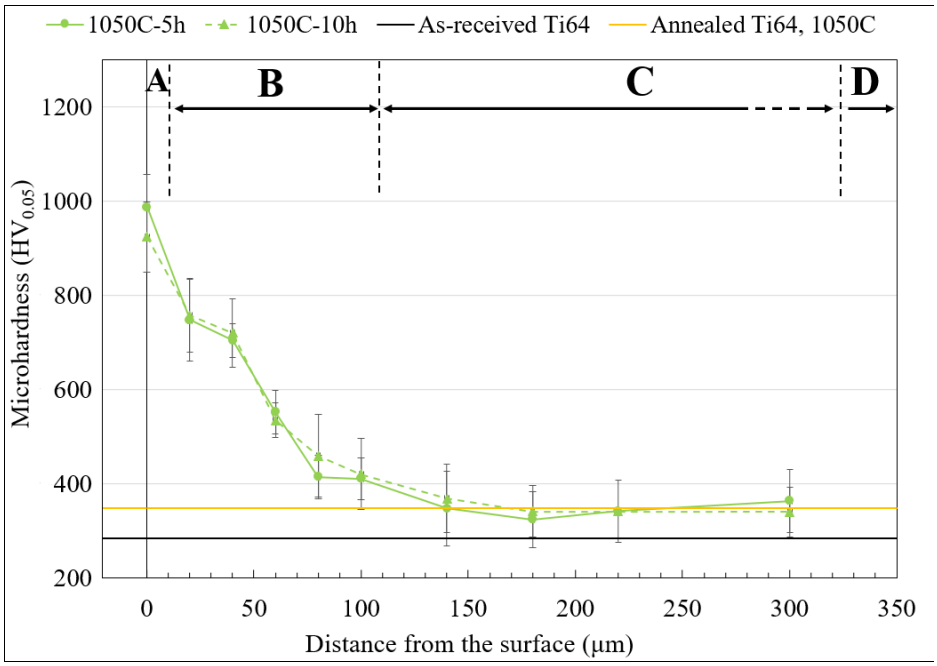

Figure 4-10: Microhardness profiles of nitrided Ti6Al4V at 1050℃

4.3.3. Water droplet erosion

4.3.3.1. Water droplet erosion performance

Erosion behaviour of as-received, annealed and nitrided Ti6Al4V is presented in Figures 4-11 to 4-14. Multi-layered nature of nitrided Ti6Al4V results in a non-uniform response to droplet

impacts, unlike the non-treated Ti6Al4V. In our previous works erosion behaviour was found to be a function of the surface history, mechanical properties and local microstructure [26, 36, 42, 64, 102]. Figures 4-7 and 4-8 display that local microstructures vary with depth for the nitrided specimens. Thereby, erosion damage at different layers is investigated using the instantaneous erosion rate graphs. All nitrided samples showed either negligible or a shorter incubation period compared to the as-received Ti6Al4V. The first two points in the erosion graphs correspond mainly to the compounds layer performance and the next four mainly to the diffusion layers performance. Notable differences between the samples' erosion resistance are detected. These differences gradually decrease and eventually disappear and similar behaviour can be seen for all samples in the advanced stages of erosion, as shown in erosion rate graphs of Figures 4-11 to 4-14.

4.3.3.1.1. Water droplet erosion performance at impact speed of 350m/s

Figure 4-11 demonstrates the material loss and erosion rate graphs of the samples treated at 900°C using impact speed of 350m/s. Nitrided samples at this temperature for 5 and 10h show more resistance compared to as-received Ti6Al4V. They demonstrate superior performance within the first six intervals. Their lower erosion rates in initial stages are attributed to the hard and dense nitrided layers which combat erosion damage. However, the compounds layer is relatively vulnerable and was partially damaged even in the first interval. The influence of nitrided layers particularly the diffusion layers to combat erosion damage can be verified by the lower erosion rates of the sample nitrided at 900°C for 5h compared to those of the Ti6Al4V annealed at the same condition. Although longer nitriding slightly increases the depth of diffusion layer, sample 900C-10h shows more material loss compared to the sample nitrided for 5 hours. It is attributed to its oxide compound layer which is mechanically unstable. Such layer is removed from larger area on the surface and leaves a cracked surface subjected to the next droplet impacts. This is detrimental for the performance of diffusion layers and is discussed further in section 3.3.2. After six intervals all nitrided layers were removed and water droplets impacted the samples at depths that were not influenced by nitrogen diffusion, region D shown in Figure 4-7. Therein, the difference of erosion behaviour is attributed to the different local microstructure. It seems that duplex microstructure, displayed in region D, is more resistant to erosion compared to the equiaxial microstructure of the as-received Ti6Al4V. This can be verified by lower erosion rates of annealed Ti6Al4V, which has duplex microstructure.

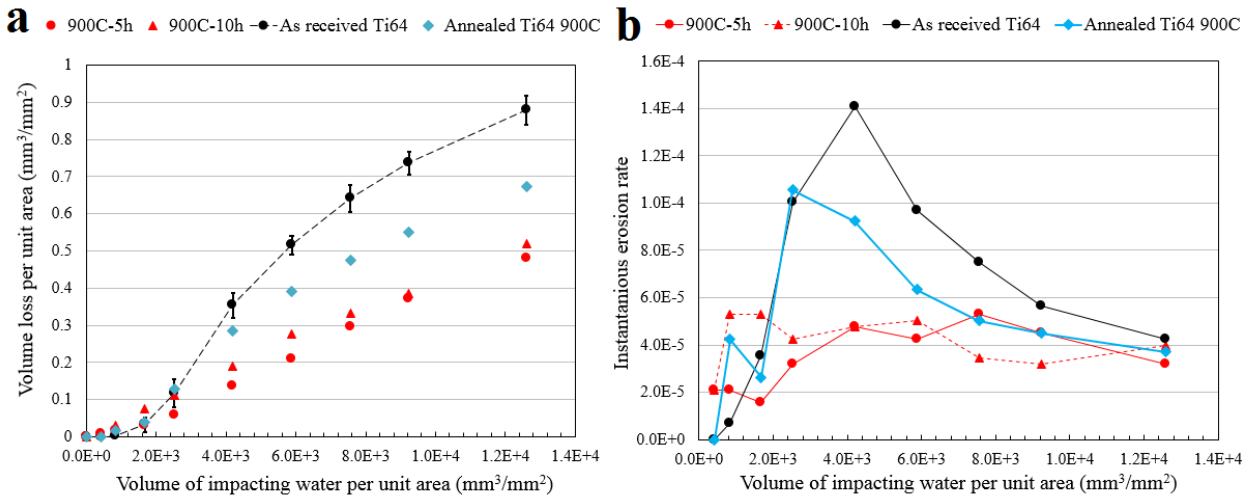

Figure 4-11: WDE results of the samples treated at 900°C using impact speed of 350m/s: (a) normalized material loss versus volume of impinging water, (b) the instantaneous erosion rate at different intervals

Figure 4-12 demonstrates the material loss and erosion rate graphs of the samples treated at 1050°C using impact speed of 350m/s. There is no improvement in erosion resistance of Ti6Al4V nitrided at 1050°C. They show no incubation period, which is associated with complete detachment of the compounds layers in the first two intervals. These layers were removed from large area on the surface, which are demonstrated in section 3.3.2. Despite the higher hardness of diffusion layer of nitrided samples at 1050°C, they do not show notable resistance to water droplet impacts. This can be realized from the high erosion rates of nitrided samples at initial intervals. Poor resistance of nitrided coupons at 1050°C can be explained by the early detachment of their porous compounds layers. Their detachment leaves a relatively rough surface, which is full of initiated cracks. These cracks can easily propagate with the induced stresses by further impacts and cause more material loss. This mechanism was documented and is explained in section 3.3.2. Nitriding samples for longer time was not beneficial for erosion performance which can be attributed to the formation of thicker vulnerable compounds layers. In addition to the compound layer issues, very high concentration of interstitial elements (oxygen and nitrogen) in diffusion layer may lead to detrimental brittleness (HID defect) and contribute to the poor erosion resistance. Such defect in α case was highlighted as a potential reason for the lower fatigue limit of gas nitrided Ti6Al4V [132]. Superior erosion resistance of the annealed Ti6Al4V at 1050°C for 5h compared to the nitrided sample at the same conditions indicates the detrimental role of porous and brittle nitrided layers to combat erosion damage. It is noteworthy that the sample annealed at 1050°C for

5h, shows superior erosion resistance compared to the as-received Ti6Al4V. In water droplet erosion, the damage and material removal are governed by cracking. Hence, the crack growth rate which is function of local microstructure plays a key role to control material loss. The higher erosion resistance of β-annealed Ti6Al4V is attributed to the lower crack growth rate of its lamellar microstructure [88, 136].

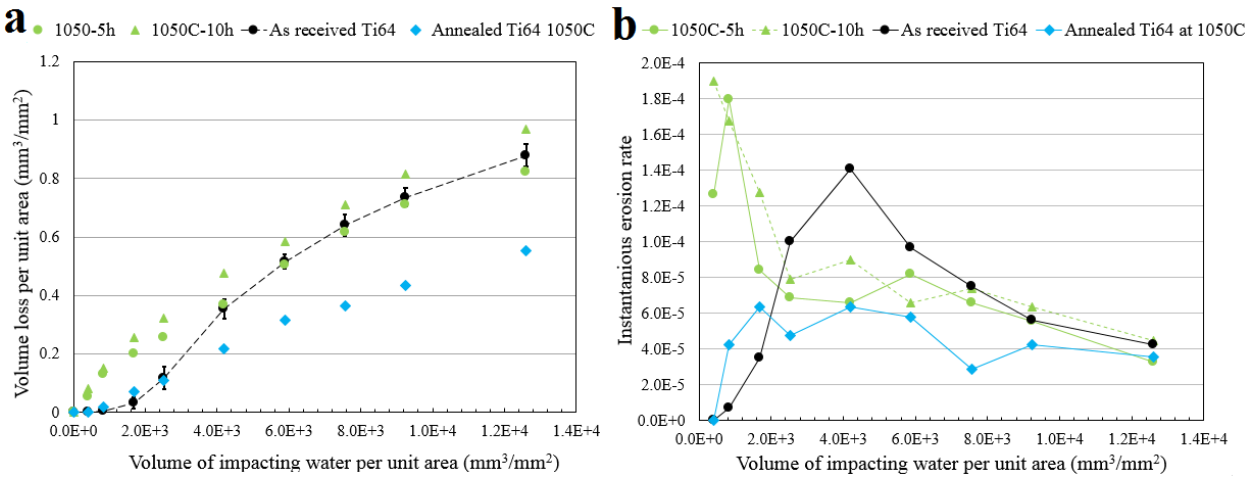

Figure 4-12: WDE results of the samples treated at 1050°C using impact speed of 350m/s: (a) normalized material loss versus volume of impinging water, (b) the instantaneous erosion rate at different intervals

4.3.3.1.2. Water droplet erosion performance at impact speed of 300m/s

Figure 4-13 presents the material loss and erosion rate graphs for the samples treated at 900°C using impact speed of 300m/s. The coupons nitrided at 900°C for 5 and 10h show considerably less erosion damage compared to the as-received and annealed Ti6Al4V. Nitrided layers in the initial stages, within the first six intervals, combat erosion damage and decelerate the material loss. In addition, the duplex microstructure of base material in nitrided coupons is slightly more erosion resistant compared to the equixial microstructure of the as-received Ti6Al4V. It can be verified by the lower erosion rates of annealed Ti6Al4V at 900°C for 5h, which is attributed to the cracking behaviour influenced by local microstructure. The longer nitriding treatment at this temperature is not beneficial for the erosion resistance and results in a slight increase in the erosion rate during the advanced stages. This could be attributed to the larger globular α grains observed in the sample nitrided for 10h; these larger grains may facilitate the detachment of large fragments and increase the erosion rate.

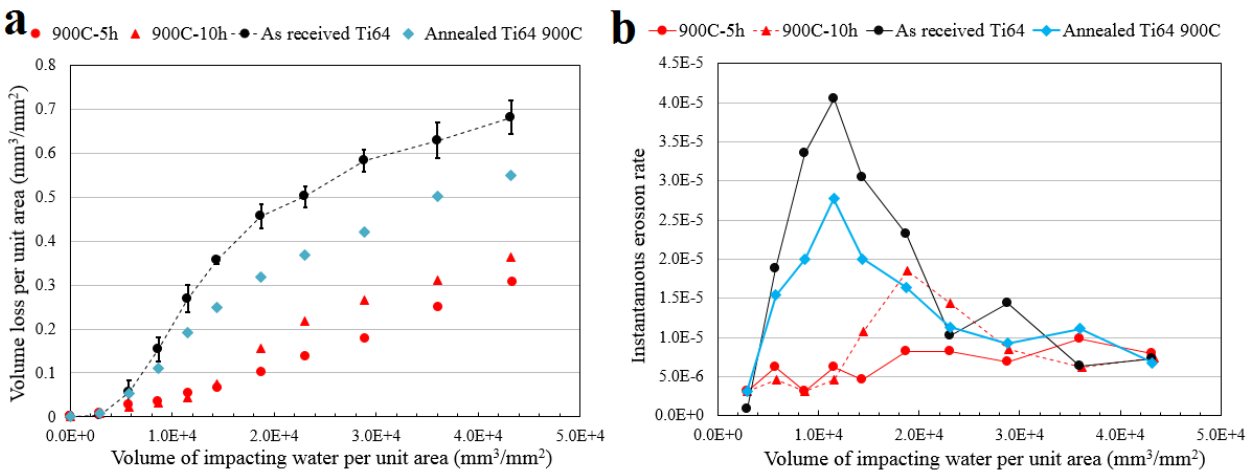

Figure 4-13: WDE results of the samples treated at 900°C using impact speed of 300m/s: (a) normalized material loss versus volume of impinging water, (b) the instantaneous erosion rate at different intervals

Figure 4-14 presents the material loss and erosion rate graphs for the samples treated at 1050°C using impact speed of 300m/s. At this speed, nitrided Ti6Al4V show more erosion resistance compared to the as-received Ti6Al4V than the high speed experiments. The influence of impact speed on the erosion performance of sample nitrided at high temperature can be attributed to the different levels of stresses induced to the target, 1392 and 1148MPa, by one droplet impact at 350 and 300m/s speeds [64]. It seems that at higher speed there is sufficiently high exerted stresses to damage the micro-cracked surface left after the detachment of the compound layer. However, the imposed stresses and stress intensities at impact speed of 300m/s would not be sufficient to propagate the cracks remained after the detachment of compounds layer. Hence, diffusion layer of the samples nitrided at 1050°C could combat droplet impacts and demonstrate lower erosion rates than as-received Ti6Al4V, as shown in Figure 4-14-b. Nitrided and annealed Ti6Al4V at 1050°C show similar behaviour in the advanced stages; however, there are some differences in the initial stages which indicate the role of nitrided layers. Nitrided coupons lost their compounds layer and showed high erosion rates in the first interval; however, annealed Ti6Al4V showed no material loss. In the next three intervals their diffusion layer decelerated the material loss; however, the annealed Ti6Al4V lost more material.

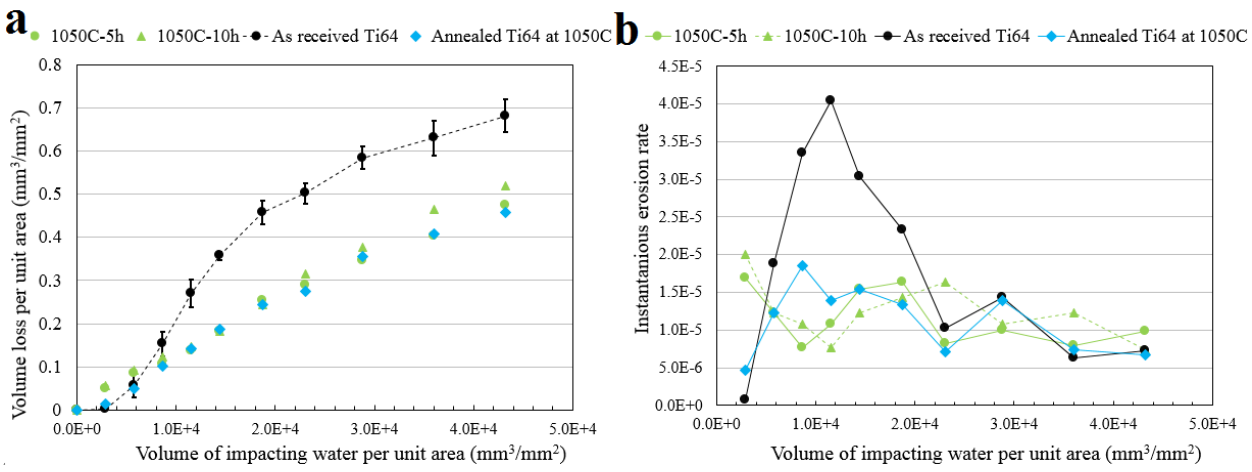

Figure 4-14: WDE results of the samples treated at 1050°C using impact speed of 300m/s: (a) normalized material loss versus volume of impinging water, (b) the instantaneous erosion rate at different intervals

4.3.3.1.3. Influence of nitriding atmosphere on the erosion performance

The influence of adding 4% H_2 to the nitriding environment on the erosion behaviour of the samples nitrided at 900°C for 5h was studied. Figures 4-15-a and 4-16-a show the erosion results of 900C-5h coupon, nitrided with N_2, and H-900C-5h coupon, nitrided with N_2-4%H_2. There are small differences between the erosion graphs of these coupons, but the appearance of their eroded surface (within the first three intervals) showed notable difference. Hence, the superiority graphs are presented to study the performances of nitrided coupons with respect to their reference Ti6Al4V pair and detect small differences. In case of the experiments performed at 350m/s, coupon H-900C-5h displays more superiority than coupon 900C-5h in the first three points, as shown in Figure 4-15-b, where the compound layer plays the most important role. The results of erosion experiments performed at 300m/s depict similar trend, which are presented in Figure 4-16-b. In the first two points, higher superiority can be observed for coupon H-900C-5h. This is due to the dense and crack free-compound layer consisting of titanium nitride compounds. These erosion results are consistent with the highest observed surface hardness for coupon H-900C-5h, shown in Figure 4-9. The erosion superiority of these samples at later stages of erosion for both impact speeds, 300 and 350m/s, are similar. This is expected because of the similar microhardness and microstructures beneath the nitrided layers for both coupons.

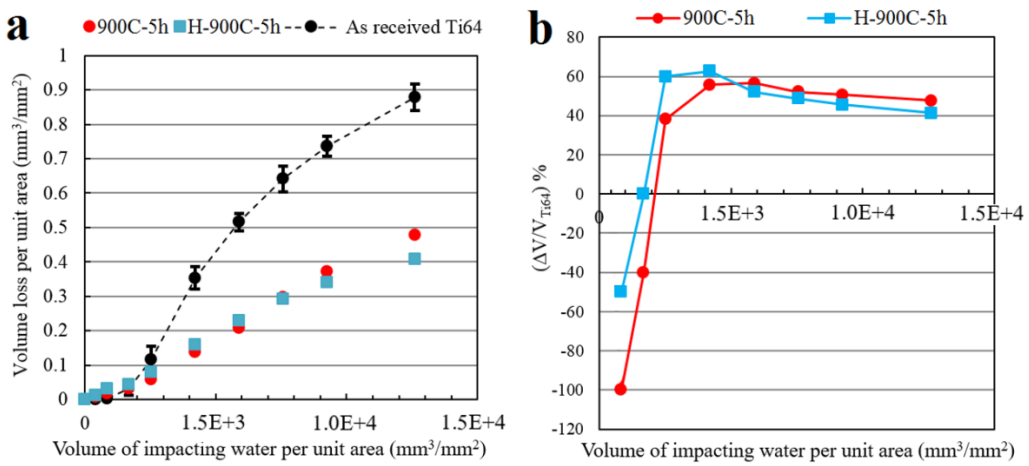

Figure 4-15: Water droplet erosion results of nitrided Ti6Al4V at N_2 and N_2-4%H_2 environments using impact speed of 350m/s: (a) erosion graph, (b) material loss superiority of nitrided Ti6Al4V compared to Ti6Al4V during the WDE test

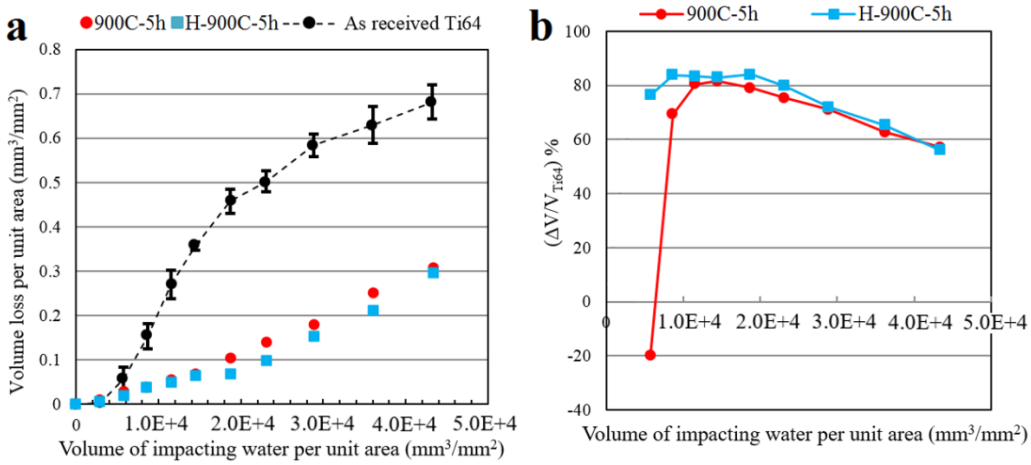

Figure 4-16: Water droplet erosion results of nitrided Ti6Al4V at N_2 and N_2-4%H_2 environments using impact speed of 300m/s: (a) erosion graph, (b) material loss superiority of nitrided Ti6Al4V compared to Ti6Al4V during the WDE test

4.3.3.1.4. Cumulative erosion resistance

Cumulative erosion resistances of the samples, derived using Equation 4-2, are presented in Table 4-2. These numbers represent the influence of both nitrided layers and the local microstructure of core material on the erosion behaviour. In addition, the microhardness values of surface and diffusion layers (50µm from the surface) are listed in Table 4-2. It is clear that nitriding at 900°C for 5 hours provides the best erosion performances. Coupons 900C-5h and H-900C-5h show the highest erosion resistance at 350 and 300m/s impact speeds, respectively. For these coupons, the mechanical support of hard diffusion layer from the hard and dense compound layers

results in their highest overall erosion resistance. Such mechanical support influences the failure mechanism of thin and hard compound layer. Lee *et al.* [140] highlighted that during the water droplet erosion of 12Cr steel coated by TiN films, the local depressions of ductile substrate is the main cause of hard film failure which leads to the circumferential cracking and fractures. In this case, a relatively hard diffusion layer beneath such hard and thin films diminish substrate deformations. Indeed, the diffusion layer may act as an intermediate layer and remove the large hardness mismatch within the interface between the hard film and ductile substrate. The beneficial role of diffusion layer to support top hard film, which leads to higher scratch or wear resistances, was reported in the literature [134, 141, 142]. In case of specimens 1050C-5h and 1050C-10h the impact speed considerably influences their erosion performances. For the aggressive erosion, carried out at higher impact speed, specimen 1050C-5h demonstrates similar erosion resistance to the as-received Ti6Al4V; however, it showes 44% higher erosion resistance at impact speed of 300m/s. The influence of impact speed is more obvious in the case of specimen 1050C-10h. It showed 9% less erosion resistance than Ti6Al4V at impact speed of 350m/s. However, reducing the impact speed to 300m/s leads to a 31% higher resistance.

It is worthy to note that the annealed Ti6Al4V samples at both 900 and 1050°C temperatures show higher cumulative erosion resistance compared to as-received Ti6Al4V. It is due to the different local microstructure of these samples. The slower crack propagation of lamellar colonies [136] is the main reason of such differences. It seems that lamellar microstructure is more resistant to erosion than duplex microstructure, and duplex microstructure is more resistant than equiaxial microstructure. This characteristic played a role mainly at the intermediate stages of erosion and ceased to have an influence at the advanced stages. Since the influence of nitrided or annealed Ti6Al4V microstructure on water droplet erosion performance is not the focus of this study, a future comprehensive study in this regard is recommended.

Table 4-2: Microhardness and erosion performance of as-received, annealed and nitrided Ti6Al4V

Coupons	Surface Microhardness	Microhardness of diffusion layer (50µm from the surface)	Erosion resistance at 350m/s, $CER/CER_{Ti6Al4V}$	Erosion resistance at 300m/s, $CER/CER_{Ti6Al4V}$
900C-5h	1134	510	1.83	2.24
900C-10h	1060	570	1.69	1.87

1050C-5h	1035	641	1.07	1.44
1050C-10h	939	653	0.91	1.31
H900C-5h	1243	551	1.74	2.34
As-received Ti6Al4V	292	292	1	1
Annealed Ti6Al4V at 900°C	308	308	1.3	1.24
Annealed Ti6Al4V at 1050°C	348	348	1.59	1.49

*Calculated based on equation 4-2

4.3.3.2. Characterization of erosion damage

Figure 4-17 shows the plan-view of progressive damage during the erosion experiments. It is clear that the damage initiation is different for the samples nitrided for 5 hours and as-received Ti6Al4V. These images indicate the high mechanical stability of compound layers and their resistance to droplet impacts for 900C-5h and H-900C-5h coupons, which were nitrided at low temperature. After 8 minutes, which corresponds to the second interval in Figures 4-13 and 4-14, relatively large and scattered pits appeared on the surface of Ti6Al4V and led to detectable material loss. In this stage, 900C-5h coupon lost its compound layer over the area impacted by water droplets. Also, a few small pits can be seen which indicate the local damage of diffusion layer. Further droplets caused the enlargement of these pits and their coalescence which led to the removal of diffusion layer. The erosion surfaces of 900C-5h coupon and the as-received Ti6Al4V, Figures 4-17-a and 4-17-d, indicate that the damage level observed after 12 min for as-received Ti6Al4V is similar to the one observed after 50 min for 900C-5h coupon.

The sample nitrided at 1050°C for 5h was seen very vulnerable to the initial droplet impacts and its compounds layer was removed from a larger area on the surface, shown in Figure 4-17-b. This detachment results in a notable peak at the beginning of the erosion rate graph, shown in Figure 4-14-b. The erosion damage surfaces in the later intervals indicate the beneficial role of diffusion layer of 1050C-5h coupon to combat water droplet erosion. This layer decelerated pitting and formation of deep craters for this sample compared to as-received Ti6Al4V, shown in Figures 4-17-b and 4-17-d.

Losing the compound layer was also seen for the coupon nitrided at 900°C and in the presence of hydrogen. However, it is from smaller surface area compared to the other nitrided samples, shown in Figure 4-17. It indicates the higher mechanical stability of the compounds layer

formed in the reducing environment and confirms the superior performance of H-900C-5h coupon compared to 900C-5h coupon in the initial intervals, which was presented in Figure 4-16-b.

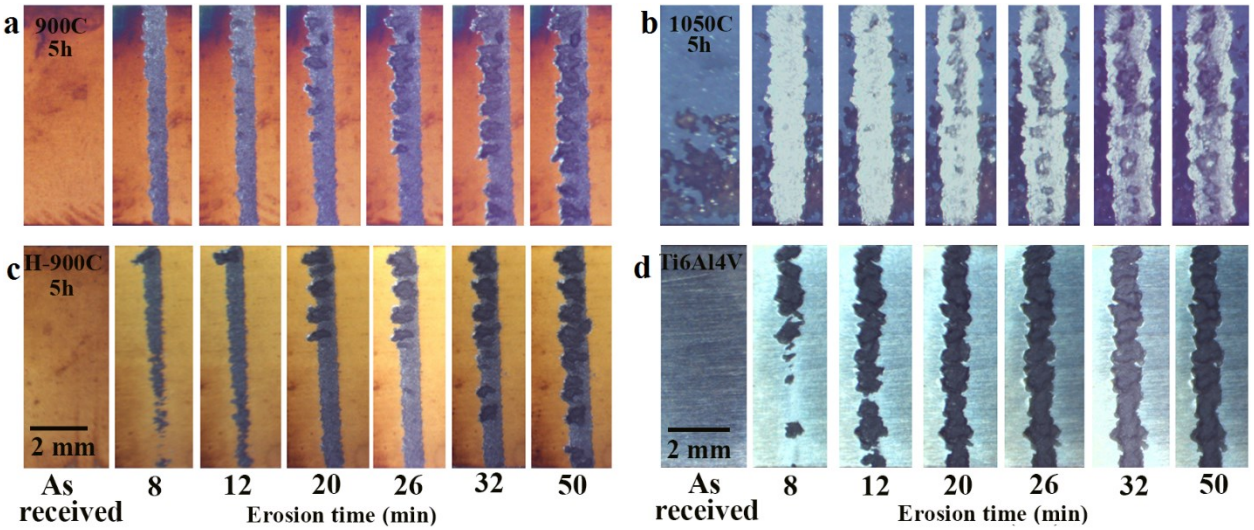

Figure 4-17: Optical micrographs of erosion craters at different time intervals of the erosion experiments carried out at 300m/s impact speed: (a) 900C-5h, (b) 1050C-5h, (c) H-900C-5h, (d) as-received Ti6Al4V

Figure 4-18 indicates the surface SEM micrographs of the sample nitrided at 900°C for 5h after it was eroded at the impact speed of 350m/s. Deep erosion craters at the advanced stage can be seen in Figure 4-18-a. It is clear that the erosion crater depth and width are not uniform along the area exposed to the droplet impacts. Severe damage and scattered deep pits can be seen over this area; however, some regions are not damaged significantly. The erosion damage initiation and its microstructural evolution can be seen in Figures 4-18-b to 4-18-e. The initial impacts cause the formation of crack networks and localized brittle fractures on the compound layer, shown in Figure 4-18-b. The detachment of compounds layers results in the formation of relatively rough surface with a large number of nucleated cracks. These faceted cracks with a cleavage appearance are highlighted by arrows in Figures 4-18-b, 4-18-c, and 4-18-d. Such cracked surface, which is basically the diffusion layer beneath the compounds layer, is prone to erosion upon further droplet impacts. According to the erosion results, diffusion layer plays an important role to combat water droplet erosion. This layer is supposed to impede cracking; however, numerous cracks which nucleated upon the compounds layer detachment, shown in Figure 4-18-d, influence its performance. Indeed, the resistance of this layer to crack propagation controls its failure. Further impacts damage the diffusion layer by imposing local stresses leading to crack development, shown in Figure 4-18-d. Water hammering and stress waves propagation caused by repetitive

droplet impacts are the main reasons for further cracking. The formation of striation marks on the eroded surface mainly over the facet of several grains, shown by white arrows in Figure 4-18-d, indicates the cyclic growth of the cracks during erosion. It is worthy to note that the lateral jetting upon droplet impacts damages the surface asperities and initiates more cracks. More droplet impacts remove the nitrogen enriched α grains and the core material would be subjected to the droplet impacts. Once the nitrided layers are gone, the large and deep pits can be formed along the erosion crater. The scattering of these deep pits along the erosion line, shown in Figure 4-18-a, could be attributed to the notable role of diffusion layer to combat erosion. When the diffusion layer was removed from a certain area, erosion damage quickly progressed in that area and deep pits were formed. Inhomogeneous loading inside the deep craters results in local damage and different types of cracking and fractures. The intergranular and transgranular cracks are highlighted by white and black arrows, respectively, in Figure 4-18-e. Such cracks and fractures can be seen in the cross sectional micrographs discussed later in the text.

The mechanical stability of compounds layer has been considered as an influencing parameter on the erosion performance of diffusion layer. Surface intergranular crack, shown by black arrows in Figure 4-18-c, indicates how the response of the compound layer affects the cracking behaviour of the diffusion layer. Here, a micro-crack initiated on the surface of brittle compound layer and the further droplet impacts made it to propagate into the diffusion layer. Hence, the hard diffusion layer cannot endure droplet impacts and would fracture faster leading to more material loss. In the case of sample nitriding at 1050°C, propagation of surface cracks into the diffusion layer and deteriorating the erosion resistance of this relatively brittle layer is the main reason for the poor erosion performance. The coupons eroded at 350m/s suffered more from this type of cracking, since higher local stresses were induced at this speed. Figure 4-19-a shows the slightly eroded surface of coupon 1050C-5h at this impact speed. Detachment of compound layer left numerous cracks on the surface of diffusion layer. Diffusion layer is hard and relatively brittle and nucleated cracks make it vulnerable upon further impacts. These cracks can be seen mainly along the boundaries of the large and enriched α grains, as shown by arrows in Figure 4-19-a. These grains with similar sizes are demonstrated within α case of 1050C-5h coupon, as shown in Figure 4-19-b. Such intergranular cracking into diffusion layer leads to its fast removal.

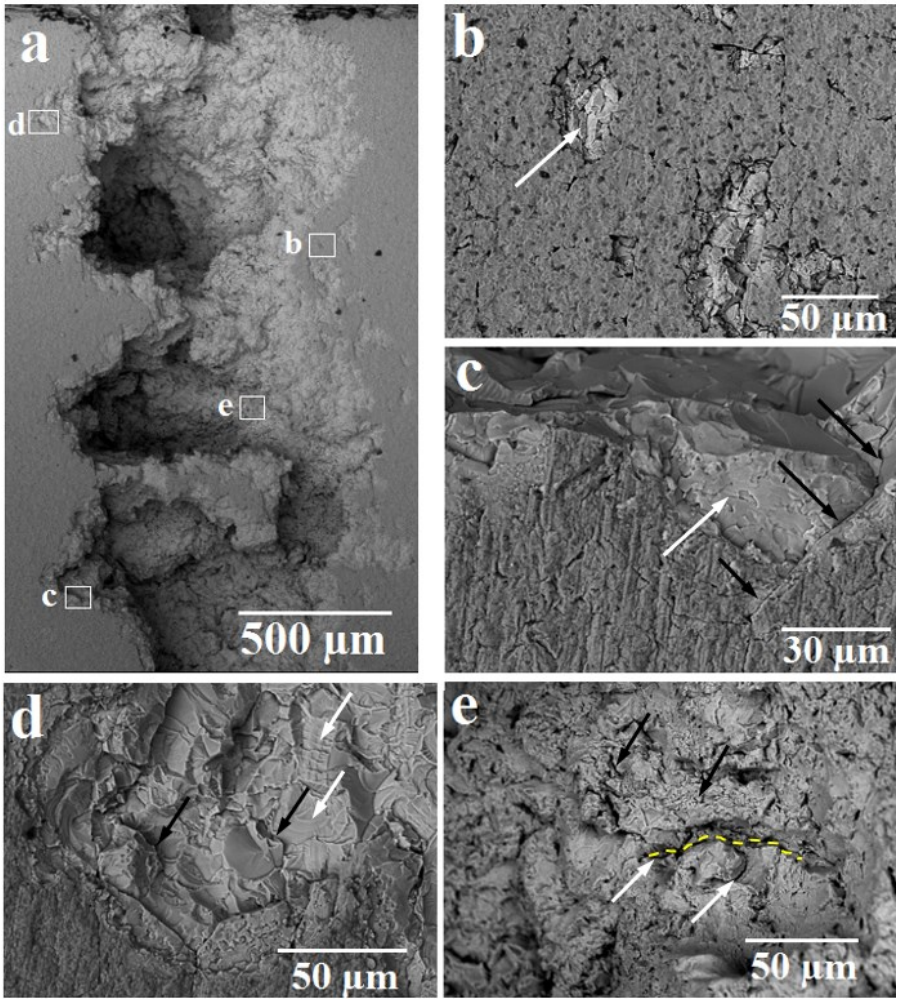

Figure 4-18: Surface BSE-SEM micrographs of nitrided Ti6Al4V (900C-5h) after erosion test: (a) erosion crater and deep pitting, (b) damage initiation on the compound layer, (c) top layers detachment at the edge of erosion crater, (d) erosion damage on diffusion layer, (e) eroded surface inside the erosion crater

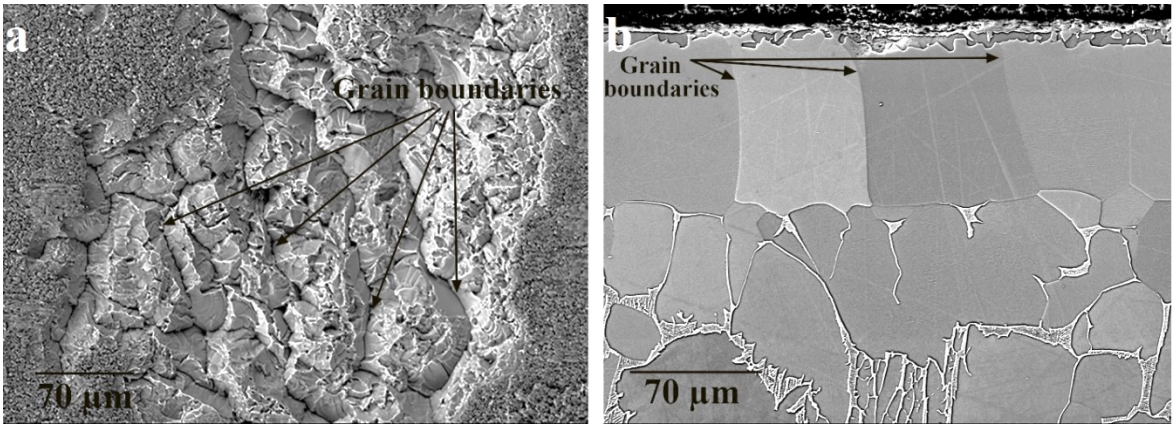

Figure 4-19: (a) Surface BSE-SEM micrograph of slightly eroded 1050C-5h sample, (b) cross section of 1050C-5h sample (non-eroded) showing diffusion layer

Figures 4-20 and 4-21 demonstrate the cross sections of eroded samples nitrided for 5h at 900 and 1050°C. Figure 20-a shows the cross section of coupon 900C-5h at the initial erosion stage. Several surface cracks, which are mainly developed due to water hammering, are highlighted by arrows. These cracks nucleate from either the compounds layer or the remaining surface after the detachment of the compound layer. Then, they propagate into the diffusion layer. No sub-surface crack, which is a known erosion damage feature in the early stages [42], could be detected over the cross section of eroded coupon 900C-5h. It is due to the homogeneous microstructure of diffusion layer. A similar behaviour is observed for the sample nitrided at 1050°C, shown in Figure 4-20-a, although it eroded faster than the sample nitrided at 900°C. Here, the localized intergranular and transgranular cracks are indicated by black and white arrows in Figures 4-20-a and 4-21-a, which are consistent with the observed cracks on the surface.

Cross section of eroded coupons in the advanced stages are also presented. The depth of erosion crater is around 310µm for coupon 900C-5h, shown in Figure 4-20-b, and 390µm for coupon 1050C-5h, shown in Figure 4-21-b. It is noteworthy that this depth varies along the erosion line, which was initially shown in Figure 4-18-a. For both specimens, the material affected by nitrogen diffusion was removed completely. Here, the local microstructure of core material controls the progress of the damage. Coupon 900C-5h, which was nitrided at 900°C below β-transus temperature, shows the duplex microstructure of equiaxed α grains and small lamellar colonies. However, the Ti6Al4V nitrided at high temperature was treated above β-transus temperature, and during the cooling large colonies with co-oriented α lamellae within prior β grains were formed. This fully lamellar microstructure shows higher crack growth resistance compared to the equiaxal microstructure. It is due to the larger degree of cracks deflection, bifurcation and secondary cracks formation, which were reported as the toughening mechanism in lamellar microstructures [69, 88, 136]. The slower crack growth of lamellar microstructures leads to the superior erosion performance of annealed Ti6Al4V compared to the as-received one.

In addition to the water hammering and travelling stress wave into the target, hydraulic penetration is an important reason for crack propagation and fracture. Water hammering and initial fractures firstly cause the formations of relatively small cavities. Further droplets and subsequent hydraulic penetration dig the bottom of the small cavities and generate either deep and elliptical or narrow and undercutting pits. Figures 4-20-c shows the formation of deep and elliptical pits at

the bottom of erosion crater within duplex microstructure. Figure 4-21-c demonstrates the narrow and undercutting pits within the lamellar microstructure. The observed erosion features along with the instantaneous erosion rate graphs reveal two different erosion mechanisms for these microstructures. Indeed, the small grain size of duplex microstructure results in the acceleration of cracks coalescence and subsequent material loss. Hence, fast and frequent detachment of small fragments is the dominant mechanism for the erosion of bimodal microstructure. In contrast, the cracks deflection and bifurcation decelerate the cracks propagation within the lamellar microstructure. Thereby, slow and infrequent detachment of relatively large portions could be mentioned as the dominant material loss mechanism for this microstructure.

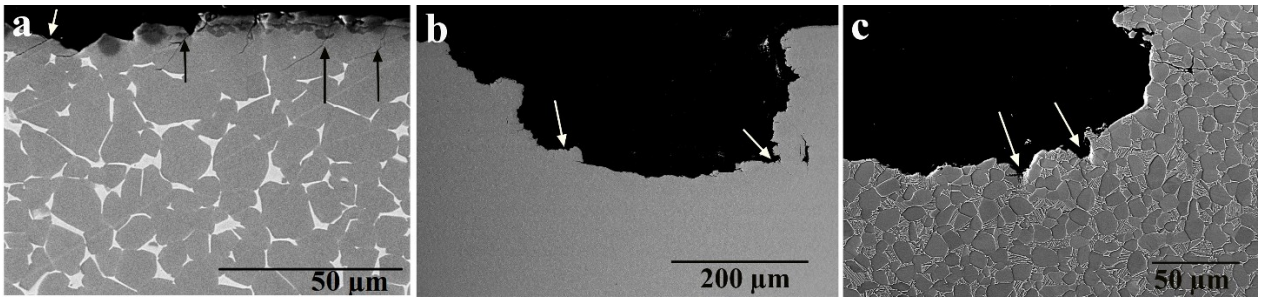

Figure 4-20: Cross sectional BSE-SEM micrographs of nitrided Ti6Al4V at 900°C after erosion test showing: (a) erosion damage of nitrided layers, (b) main erosion crater at low magnifications, (c) cracks propagation and hydraulic penetration

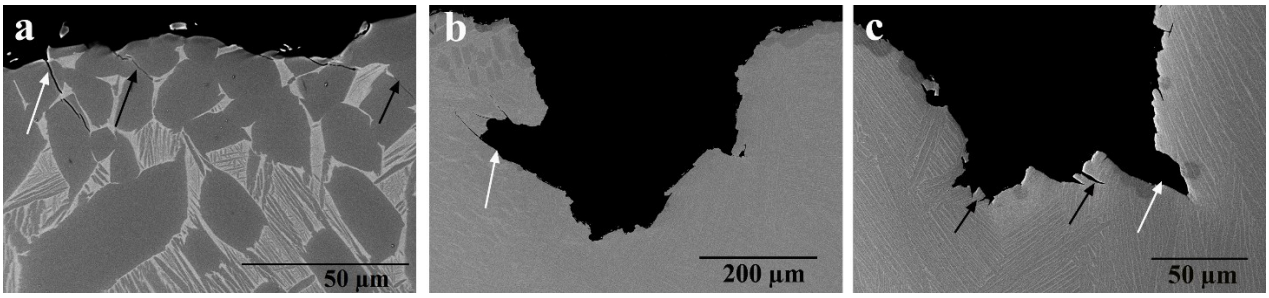

Figure 4-21: Cross sectional BSE-SEM micrographs of nitrided Ti6Al4V at 1050°C after erosion test showing: (a) erosion damage of nitrided layers, (b) main erosion crater at low magnifications, (c) cracks propagation and hydraulic penetration

4.4. Conclusions

Water droplet erosion performance of nitrided Ti6Al4V at different conditions were studied. Different erosion indicators were considered to track the erosion damage during the whole test. In addition, the microstructural investigation on the surface and cross section of eroded coupons revealed the erosion mechanisms. The following conclusions can be drawn:

1. Gas nitriding generated a very hard and brittle compounds layer and a relatively hard and homogeneous diffusion layer in Ti6Al4V. Nitriding conditions particularly the temperature altered the resulting layers as well as the core material microstructure which influenced the cracking behavior and subsequently the erosion performance.

2. The Ti6Al4V nitrided at 900°C showed the best erosion resistance, which is measured by their corresponding cumulative material loss and is 70% to 125% higher than the as-received Ti6Al4V. Hard and dense compounds layer which is mechanically supported by the homogeneous diffusion layer led to the superior erosion performance of these nitrided coupons. Longer nitriding was not beneficial for the erosion resistance.

3. Erosion performance of Ti6Al4V nitrided at 1050°C was notably sensitive to the impact velocity. At 350m/s, the nitrided coupon showed either a worse or similar performance to the as-received Ti6Al4V. However, they displayed up to 44% higher resistance than the as-received Ti6Al4V when the impact speed was decreased to 300m/s. This superior performance was attributed to the relatively hard diffusion layer and the lamellar microstructure of core material.

4. Nitriding in the presence of hydrogen enhanced the hardness of compounds layer and led to its higher mechanical stability. Ti6Al4V nitrided in the presence of hydrogen displayed slightly higher resistance during the initial stages of water droplet erosion.

Relating to the theme of thesis

The gas nitrided Ti6Al4V showed up to 2.2 times higher cumulative erosion resistance (*CER*) compared with Ti6Al4V. Nitrided layers showed lower instantaneous erosion rates mainly in the intermediate stages, which correspond to the acceleration and maximum erosion rate stages of bulk Ti6Al4V erosion. Theses layers did not remain on the surface for long time and as a result could not provide overall significant protection. Indeed, high speed droplet impingements and their destructive consequences (i.e. stress waves propagation) influence the relatively large volume of surface. Therefore, large depth of treatments on the target (i.e. not thin layers) would be required for more protection. In the next chapter, erosion behaviour of the thick WC-Co layer (more than 400μm thickness) sprayed with HVOF torch on Ti6Al4V is evaluated.

Chapter 5 : HVOF sprayed coatings of nano-agglomerated tungsten-carbide/cobalt powders for water droplet erosion application

M.S. Mahdipoor[1], F. Tarasi[1], C. Moreau[1], A. Dolatabadi[1], M. Medraj[1,2]

[1]Department of Mechanical Engineering, Concordia University, 1455 De Maisonneuve Blvd. West, Montreal, QC, Canada H3G 1M8

[2]Department of Mechanical and Materials Engineering, Masdar Institute, Masdar City, Abu Dhabi, UAE, P.O. Box 54224

This article has been published to the *Journal of Wear,* 330 (2015):338-347, DOI: 10.1016/j.wear.2015.02.034[4]

ABSTRACT

Water droplet erosion damage is due to the high speed impingement of several hundred micron-sized water droplets on solid surface. Thermal sprayed tungsten carbide based coatings show potential to combat such erosion problems. However, there are a considerable discrepancies about their erosion performances in the literature. In the present work, the composition and mechanical properties (microhardness and fracture toughness) of WC-Co coatings are studied in relation to their water droplet erosion performance. Coatings were deposited by high velocity oxygen fuel (HVOF) process and they were tested as-sprayed in WDE erosion system. The nano-agglomerated WC-Co powders are in either sintered or non-sintered conditions. The WDE tests were performed using 464μm water droplets at 250, 300 and 350m/s impact velocities. The coating with homogeneous microstructure shows up to 7 times less erosion rate than Ti6Al4V, while the coating with heterogeneous microstructure shows worse erosion rate compared to Ti6Al4V.

[4] In this article, Dr. Tarasi helped with spraying the coating and their characterization. In addition, Dr. Moreau and Dr. Dolatabadi from Thermal Spray Group helped in the interpretation of final properties for the sprayed coatings.

5.1. Introduction and literature review

Liquid erosion, often reported as a source of part failure in the power generation plants is a material damage caused by repeated impacts of a water droplets at high relative velocities [2, 11, 79]. In the case of water as the impinging fluid, the solid surface encounters hydrodynamic forces resulting from the impingement of water droplets of several hundred-micron sized at hundreds of meters per second relative velocities [2].

Different approaches have been studied to combat water droplet erosion (WDE) such as laser surface treatments or thermal spray coatings [8, 79, 80]. Cermet coatings consisting of a ductile metallic binder and a hard phase (e.g. carbide, boride, nitride) are among the promising solutions to this problem [48, 80]. Tungsten carbide cobalt (WC-Co) cermet spray coatings are widely used for different applications which require abrasion, sliding, fretting and erosion resistance [48, 62, 80, 143]. In this composite structure, the hard carbide particles cause high hardness, while the metallic binder provides the coating toughness. The mechanical properties of these coatings are greatly affected by the processing parameters and final microstructure [143].

WC-Co coatings are mainly fabricated by thermal spraying techniques where the feed powder particles are injected into a hot flame generated by a heat source. They are next propelled at high velocities toward the substrate to form splats that stack on each other and generate the coatings. Thermal spray processes involve high-turbulence flow of material (gases, molten, semi-molten and/or solid particles) and high cooling rates [144]. Therefore, they often suffer from some common flaws in the resulting microstructures such as porosity, crack, low inter-splat adhesion and unstable interface between the matrix and hard reinforcement [144, 145]. Numerous studies have been done to improve coatings' properties by the choice of process, optimization of the process parameters and modifying the feedstock [143-145].

In addition to microstructural flaws, undesirable chemical and metallurgical reactions leading to the phase transformations are other major issues in thermal spray coating of these cermets. During spraying WC-Co powder, the agglomerated particles are heated at high temperature by the flame, the Co melts and dissolves a part of WC. The rapid cooling of the molten particles upon deposition causes the formation of regions of amorphous phases due to the short time for crystallization of the multicomponent phase (Co-C-W-O) [146-148]. The W_2C phase can precipitate around the original WC grains and, in case of severe oxidation and decarburization, W

precipitates close to the interface of splats [147]. The impact of these particles on the substrate makes them to be flattened and cements them in the cobalt binder splats. WC surrounded by molten cobalt can be well bonded in the middle of the splats due to appropriate wetting by the binder. It is noteworthy that oxidized carbide grains have lower wettability for Co binder and can result in weak bonding between the two components [147, 148]. Moreover, oxidized particle prevents the strong inter-splat bonding [148]. These chemical and metallurgical reactions strongly depend on the velocity and temperature of the spray particles [144, 149]. They can impair the mechanical properties specially the fracture toughness which is an important parameter for wear and erosion resistance [150].

High Velocity Oxygen Fuel (HVOF) spray process has been widely used to deposit WC-Co coatings. In this process, the fuel (in the form of gas or liquid) and oxygen are injected into a combustion chamber where they ignite and generate the heat for melting and the momentum to propel the particles toward the substrate. Moderate process temperature (up to 2800°C) and high particle velocity (up to 800m/s) in HVOF result in desired properties for these coatings [73, 144, 145]. High density, strong adhesion between coatings and substrates, high inter-splat adhesion, limited chemical reactions during the coating process, and compressive residual stresses are the main advantages supplied by HVOF [73, 145]. It is noteworthy that the compressive residual stresses would be beneficial for the applications which experience dynamic loading such as water droplet erosion [80].

Four primary damage modes have been proposed for WDE including plastic deformation and asperities formation, stress wave propagation, lateral outflow jetting and hydraulic penetration [2, 3, 79]. The impact pressure and subsequent imposed stresses result in shock waves which travel through the material. This sudden shock waves can cause initiation of micro-cracks, or further development of the pre-existing internal flaws such as cracks and porosities [2, 79]. The cracks merge together and result in material removal. Plastic deformation and stress wave propagation mainly cause surface and sub-surface cracking; and lateral outflow jetting and hydraulic penetration mainly cause development of the existing cracks [2, 57]. Hardness, ductility, fracture toughness and fatigue limit have been mentioned as the main material properties influencing WDE performance. However, there is no complete agreement on their influence [2, 46, 57]. Among these properties, hardness of target material plays relatively more significant role by delaying the

deformation. Ductility is another criterion leading to accommodation of localized stress concentration [57, 62]. A suitable combination of hardness and ductility can manifest itself in the fracture toughness which is the most relevant mechanical property to erosion resistance of spray coatings [48, 143].

Lima *et al.* [143] reported that the fracture toughness is the most relevant material property corresponding to the erosion resistance of WC-Co spray coatings; and the hardness would be a less important parameter. Lathabai *et al.* [151] mentioned that solid particle erosion of cermet coatings is not a function of their hardness. They found that coatings with low porosity, fine grain or splat size, absence of cracks and good inter-splat bonding show high erosion resistance. Oka *et al.* [48] investigated the water droplet erosion behaviour of different ceramics, cermet spray coating and martensitic stainless steel. They reported much less erosion rate and much longer incubation period for WC-20Cr_3C_2-7Ni coating compared to stainless steel. Mann *et al.* [80] studied the water droplet erosion of HVOF sprayed WC-Co coatings in comparison with Ti6Al4V and stainless steel at low impact speeds. They observed excellent erosion resistance for the WC-Co when they used a modified coating process. It was mainly attributed to the compressive residual stress introduced into the coating as well as its high hardness and toughness. It is noteworthy that their erosion tests were carried out at 150m/s impact speed which is not severe condition. Shipway *et al.* [79] also studied the water droplet erosion of WC-Co coatings sprayed by HVOF in comparison with Ti6Al4V. They used water jet cutting equipment to perform erosion experiments. The erosion test condition was very aggressive and the impact speed could reach 830m/s. In this case, the WC-Co coating did not show superior erosion resistance. They did not show any incubation period and they lost material faster than Ti6Al4V. The poor erosion resistance was attributed to the very aggressive erosion conditions and high impact speed. Water droplet erosion of WC-Co coatings was studied at either low impact speeds (150m/s) or very high impact speeds (830m/s). To the knowledge of the authors, there is no information related to their erosion performances for impact speeds within this range.

In the current study, water droplet erosion resistance of WC-12wt% Co coatings is investigated. The utilised feedstock results in two different microstructure with same chemical composition for the final coatings. The impact speeds studied in the current work (250, 300, 350m/s) are closer to the condition of water droplet erosion encountered in the compressor of gas

turbine. The erosion behaviour of coatings is discussed related to their microstructure and mechanical properties in order to understand the considerable difference for the erosion performance of WC-Co coating observed in the literature [48, 79, 80]. The erosion experiments were performed at three different droplet impingement speeds to explore the influence of this parameter on the erosion performance. The coatings' erosion behaviour are compared with that of Ti6Al4V which is currently used as a compressor blade material and known to exhibit high resistance to water droplet erosion.

5.2. Materials and experimental procedure

5.2.1. Materials

Commercially available WC–Co powders Sulzer 5810 and Woka 3110, both from (Sulzer Metco Canada Inc. Fort Saskatchewan, AB) were used as the feedstock. Both feedstock are agglomerated powders and the major difference between the two is that only Woka 3110 powder is sintered following agglomeration. The chemical composition and particle size of the powders are summarized in Table 5-1. To avoid confusion, WC grains are referred to as "grains" and the agglomerates are referred to as "particles", in the rest of the paper. Coatings were sprayed on Ti6Al4V substrates that were pre-cleaned in acetone and then blasted with 60 mesh alumina grits.

Table 5-1: Chemical composition of the feedstock used in the experiments

Materials	Shape	Particle size (diameter) distribution (μm)	Chemical composition
Sulzer 5810	Spherical (Agglomerated)	-63 +11	WC, 12 wt% Co
Woka 3110	Spheroidal (Agglomerated, sintered)	-25 +5	WC, 11-13 wt% Co

5.2.2. HVOF coating process

The feedstock of Sulzer 5810 and Woka 3110, were deposited using DJ 2600 HVOF gun (Sulzer-Metco). The Sulzer 5810 powder was sprayed at five different conditions and the best one in term of coating hardness and density was selected and presented in this article. The in-flight particle temperature and velocity were measured as 1860°C temperature and 660m/s at 200, 350 and 560 SLM oxygen, air and hydrogen flow rates, respectively. In the case of Woka 3110, it was sprayed using the flow rates of 230, 370 and 680 SLM for oxygen, air and hydrogen, respectively.

Woka 3110 spraying conditions (i.e. in-flight powder temperature and velocity) were optimised in order to obtain dense and homogeneous coatings [18]. The temperature and velocity of in-flight particles were 1986°C and 730m/s. Since, linking the erosion behaviour of coating to its microstructure is among the objectives of this study, Woka 3110 and Sulzer 5810 coatings will be compared further. In this paper Woka 3110 coating is called SD and Sulzer 5810 coating is called SP.

5.2.3. Coating characterization

To evaluate the coating porosity, SEM images of coating cross section taken at low magnification, were analysed using Scion Image software (Version 4.0.3.2). The cross section of cermet coatings were observed under scanning electron microscope (SEM Hitachi S-3400N) to confirm their thickness and study their morphology and microstructure. The mean surface roughness (R_a) values of as-sprayed coatings was measured using surface roughness tester (Mitutoyo SJ-210). The phase constituents of the coatings were analysed using an X-ray diffraction (XRD). The microhardness was measured on coating cross sections using a Vickers microhardness tester with a diamond Vickers indenter under 500 g load. The reported microhardness values are the mean value of 5 measurements. Moreover, fracture toughness measurements were performed using Vickers hardness tester at 10 kg load. In order to find the fracture toughness from the indents dimension, Equation 5-1 was utilized [152].

$$K_{IC} = 0.0193 H_V D \left(\frac{E}{HV}\right)^{0.4} a^{-0.5} \qquad \textit{Equation 5-1}$$

where *HV* is the Vickers hardness, *E* the Young's modulus, *D* the half-diagonal of the Vickers indentation, and *a* the indentation crack length.

5.2.4. Water droplet erosion test

An erosion rig specially designed for WDE testing, which provides simulated impingement conditions of high speed rotating blades was used in this study. Figure 5-1 illustrates a simplified schematic of this erosion rig. The erosion test coupons are mounted on the rotating disk and pass in front of the flow of water droplets emerging from a nozzle of specified size. The rotating coupons are impinged normally by the falling water droplets and experience water droplet erosion. The rotating disk can reach a maximum speed of 20,000 rpm, which corresponds to a linear impact speed of 500m/s for the impingement of the water droplet on the specimen. The erosion tests are

performed in vacuum pressure between 30 and 50 mbar for all experiments in order to balance friction and water droplet evaporation issues. To provide the desired impacting droplet sizes different nozzle sizes can be mounted on the system; and rotation speed is set based on the desired impact velocity.

To present the erosion results, the cumulative material loss curves were plotted versus cumulative erosion exposure. Also, the maximum erosion rate (ER_{max}) of coatings and Ti6Al4V were determined according to the ASTM G73 standard [54]. A straight line is drawn using the maximum slope points from which the maximum erosion rate (ER_{max}) is calculated. In this article, the vertical access of erosion graphs is the volume loss normalized by the area exposed to water droplets which roughly corresponds to the mean depth of erosion. The horizontal access or erosion exposure was presented using the normalized volume of impacting water by the area exposed to water droplets. Such area was measured from the optical micrographs of eroded specimen recorded at the beginning of the maximum erosion rate stage. Here, the maximum erosion rate or mean depth of erosion rate is dimensionless.

The erosion tests were performed on the as-sprayed coatings without prior surface polishing or grinding. The incubation stage in erosion curve is a function of surface roughness and since the surface roughness is different for the coatings and Ti6Al4V bulk material, the incubation stage characteristics are not compared in this study. Here, the maximum erosion rate is reported as the main criterion for the erosion resistance.

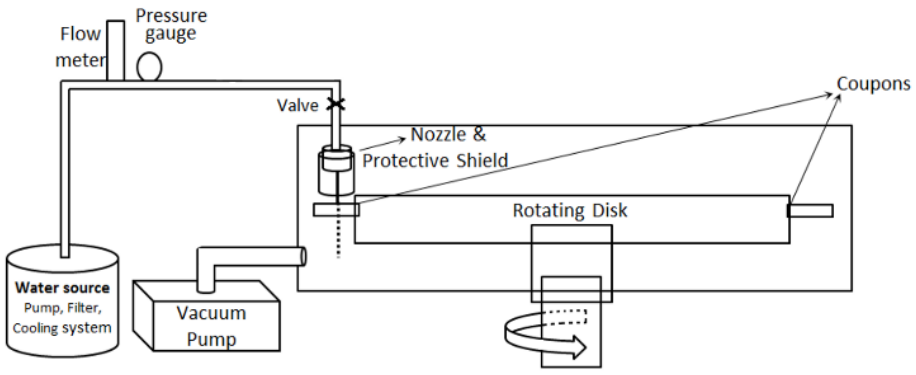

Figure 5-1: Schematic of the water droplet erosion rig

The cross section of eroded coatings were prepared for metallography along the erosion craters. From each cross section, more than thirty SEM images were taken at different

magnifications along the edge of the erosion lines. Hence, erosion features could be studied systematically.

5.3. Results

5.3.1. As-sprayed coatings characterization

Figure 5-2 shows the XRD spectra of the cermet feedstock and coatings deposited by HVOF. The as-received Sulzer 5810 and Woka 3110 powders are composed of WC and Co phases. The XRD patterns of the coatings show the presence of other phases which were formed in the spraying process. The SP coating contains W_2C and small amount of W, however the Co peaks are no more visible. Formation of W_2C and W confirms that the WC phase is decomposed and decarburized during HVOF process of Sulzer 5810 feedstock. The initial free Co could not be detected in the coating probably because it has reacted with carbon and tungsten during the coating process and formed nano-crystalline $Co_xW_yC_z$ phases as well as amorphous Co (W,C). This was also reported by others [147, 153]. $Co_xW_yC_z$ phases were not detected by XRD because of their relatively small quantities. In the case of SD coating, it is also composed of WC, W_2C, W and some amorphous phases. However, there is a higher level of decomposition and decarburization. This is shown by the higher peak intensity ratio of W_2C/WC in the pattern as well as larger amorphous hump observed between 35 and 45 degrees representing greater amorphous content. Formation of W phase in the coating also confirms the higher degree of decarburization. These indicate higher melting proportion of the agglomerated and sintered Woka 3110 particles than that of Sulzer 5810 (which is only agglomerated) during deposition. It is in accordance with the higher measured temperature for in-flight Woka powders during the spraying process. High temperature would enhance the coating density; however, it would be detrimental for final mechanical properties, especially for its toughness. Marple and Lima [153] introduced an optimized in-flight powder temperature range, 1750 to 1950°C, for different WC-Co feedstock sprayed by HVOF. The temperatures of in-flight powder sprayed in the current work are in this optimized range.

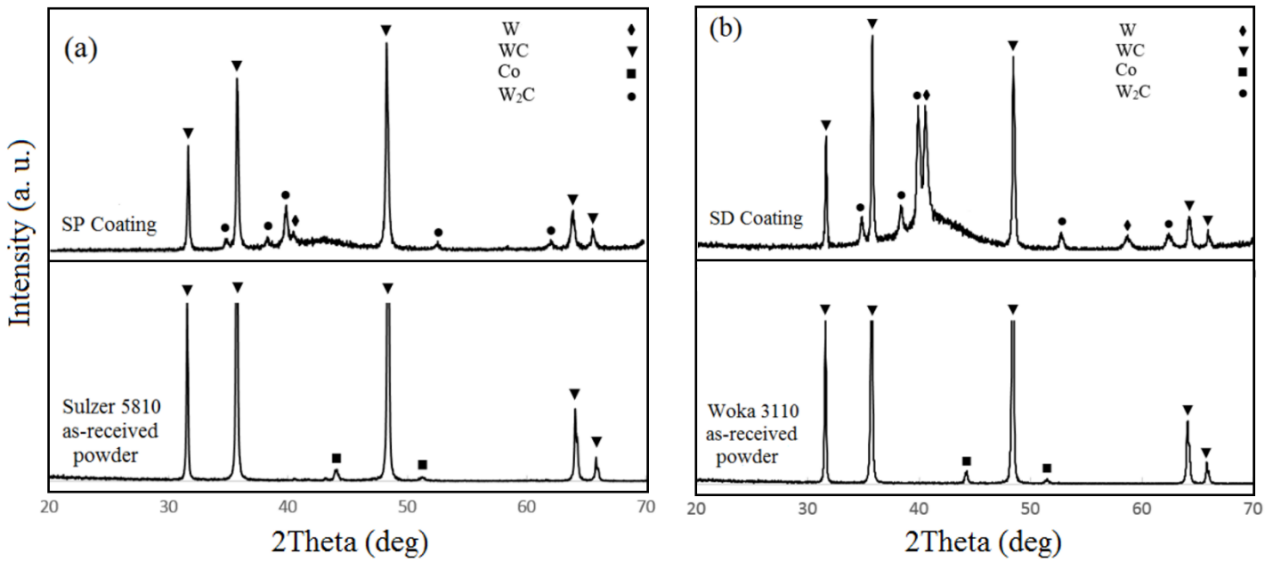

Figure 5-2: XRD patterns of (a) Sulzer 5810 powder and SP coating, (b) Woka 3110 powder and SD coating

Figure 5-3 presents SEM micrographs of polished cross sections of spray coatings. The porosity percentage, thickness and surface roughness of the coatings are presented in Table 5-2. The porosity and some microstructural-flaws mentioned as important parameters for mechanical properties can be seen in Figure 5-3. It is evident that there is much less porosity in SD coating, which can be assumed as the first structural indicator for good erosion behaviour. The surface roughness of the target material is another important parameter in erosion studies as it influences the initial stages of erosion significantly. The different roughness of the coatings and the bulk Ti6Al4V sample are mentioned in Table 5-2. Rougher surface of SP coating would be detrimental for its erosion behaviour.

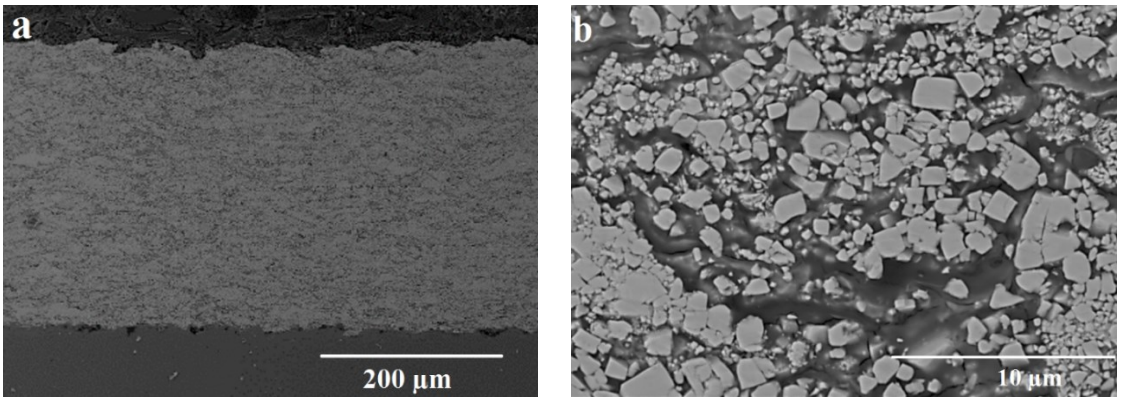

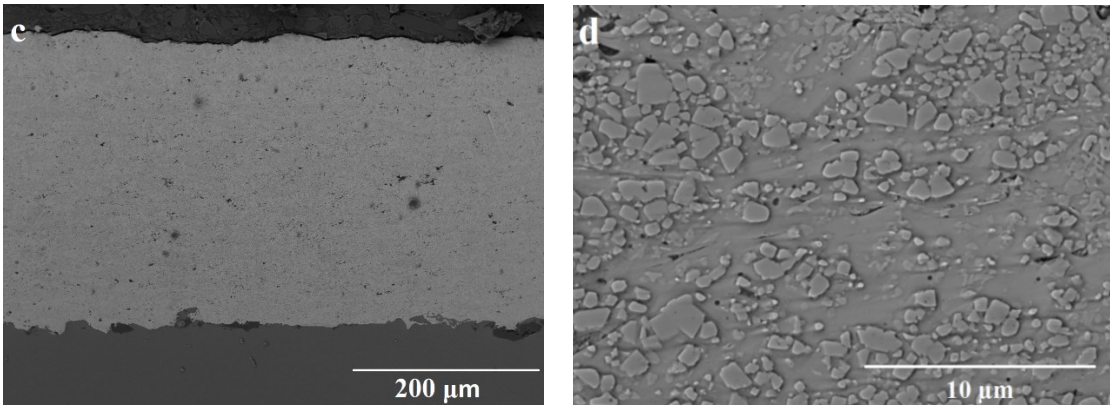

Figure 5-3: SEM micrographs showing cross sections of as-sprayed: (a) SP coating at low magnification, (b) SP coating at high magnification, (c) SD coating at low magnification, (d) SD coating at high magnification

Mechanical properties of the coatings as well as Ti6Al4V are listed in Table 5-2. The SP coating shows much lower hardness compared to the SD coating. It is attributed to the larger variations in its microstructure and lower inter-splat adhesion which will be discussed further. Fracture toughness could not be measured for SP coating since the cracks run along the edge of indents instead of radial cracking. This indicates the low tensile strength of this coating [148] which is in accordance with its heterogeneous microstructure (Figure 5-2-b) and low microhardness. This was not the case for SD coating and its fracture toughness was measured. The relatively high observed fracture toughness (8.2MPa.$m^{1/2}$) is in accordance with the dense and homogeneous microstructure of SD coating. However, high decarburization degree and formation of brittle and amorphous phases in this coating would cause reduction of fracture toughness.

Table 5-2: The characteristics of as-sprayed coatings

Specimens	Porosity percentage (%)	Thickness (µm)	Surface roughness, R_a (µm)	Microhardness ($HV_{0.5}$)	Fracture toughness (MPa.$m^{1/2}$)
SP Coating	2.9	360	3.62	874 ± 30	-
SD Coating	1.4	330	2.03	1232 ± 14	8.2
Ti6Al4V	-	-	0.08	298 ± 26	60-100

5.3.2. Water droplet erosion results

The erosion behaviour of the coatings and Ti6Al4V using 250, 300 and 350m/s droplet impact speeds are presented in Figures 5-4 to 5-6, respectively. Based on the ASTM standard, the

maximum erosion rates were calculated from the erosion curves and they are listed in Table 5-3 at different erosion conditions. In addition, cumulative erosion resistance (*CER*) of coatings normalized to those of Ti6Al4V are presented.

Figure 5-4 shows the erosion test results at 250m/s impingement speed. It exhibits significant differences between the erosion behaviour of the coatings and Ti6Al4V. The SP coating shows the highest erosion rate which is 3.7 times higher than that of Ti6Al4V. The SD coating demonstrated the best erosion performance in this condition since its erosion rate is 6.7 times lower than that of Ti6Al4V.

The erosion results for the impact speed of 300m/s are shown in Figure 5-5. There is a remarkable difference between the erosion behaviour of the coatings at this speed and that at 250m/s impact speed. No incubation period was observed for the coatings at 300m/s. This can be attributed to the higher impact pressure and subsequent stresses generated at 300m/s that are sufficiently high to commence material loss with initial droplet impacts. In term of erosion rate, the ER_{max} of SP coating is close to Ti6Al4V, i.e. 7×10^{-5} and 5.2×10^{-5}, respectively. However, SD coating shows significantly lower erosion rate, which is 1.9×10^{-4} (Table 5-3). It is 2.6 and 3.5 times less than the erosion rates of Ti6Al4V and SP coating, respectively.

Figure 5-6 shows the results for the most aggressive erosion conditions that is 350m/s impact speed. The erosion curves are closer to each other at this speed. The maximum erosion rates ER_{max} are 1.9×10^{-4}, 2.51×10^{-4}, and 1.17×10^{-4} for Ti6Al4V, SP and SD coatings, respectively. The erosion rate for the SP coating is higher than that of Ti6Al4V; however, SD coating again exhibits a lower erosion rate.

It is evident that SD coating shows the least ER_{max} in all erosion conditions. Although the coatings were deposited from feedstock with identical chemical compositions, the erosion resistance of SP coating is much less than that of SD coating. Explaining this significant difference in coating erosion behaviour which is also reported in the literature [79, 80] is one of the objectives in this study. To this end, microstructural characteristics and erosion mechanism investigation are presented.

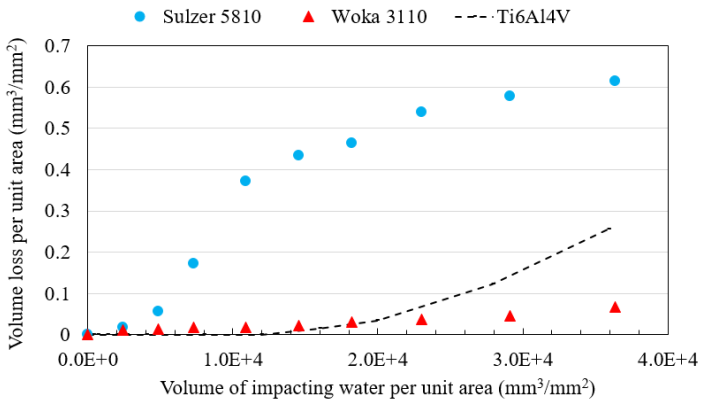

Figure 5-4: Cumulative volume loss per unit area vs. cumulative volume of water impacting unit area at the impingement speed of 250m/s

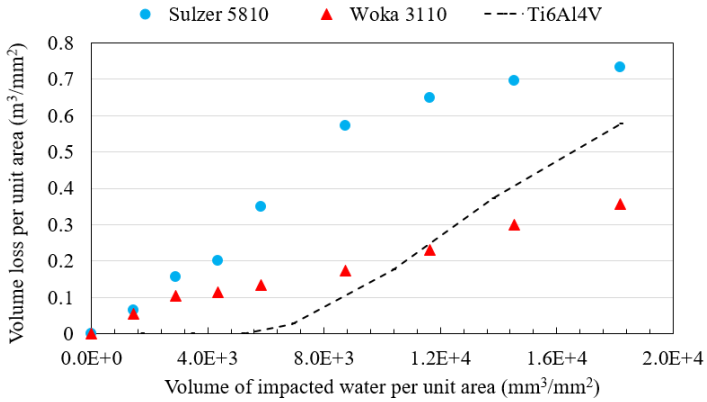

Figure 5-5: Cumulative volume loss per unit area vs. cumulative volume of water impacting unit area at the impingement speed of 300m/s

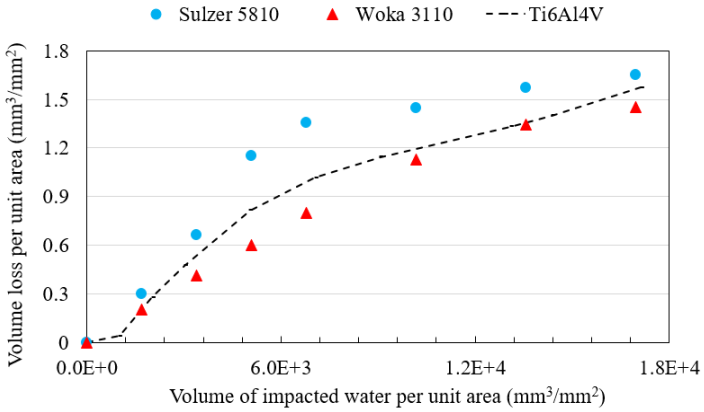

Figure 5-6: Cumulative volume loss per unit area vs. cumulative volume of water impacting unit area at the impingement speed of 350m/s

Table 5-3: Maximum erosion rate (ER_{max}) and cumulative erosion resistance (CER) of the coatings and Ti6Al4V

	ER $_{max,}$ V=250m/s	Erosion resistance at 250m/s, CER/CER $_{Ti6Al4V}$	ER $_{max,}$ V=300m/s	Erosion resistance at 300m/s, CER / CER $_{Ti6Al4V}$	ER $_{max,}$ V=350m/s	Erosion resistance at 350m/s, CER / CER $_{Ti6Al4V}$
SP Coating	5.2×10^{-5}	0.42	7×10^{-5}	0.79	2.51×10^{-4}	0.73
SD Coating	2.1×10^{-6}	3.8	1.9×10^{-5}	1.64	1.17×10^{-4}	1.07
Ti6Al4V	1.4×10^{-5}	1	5.2×10^{-5}	1	1.9×10^{-4}	1

5.3.3. Microstructural characteristics of eroded coatings

To reveal the influence of the coating's morphology and microstructure on the processes leading to material removal scanning electron microscope was utilized. Figure 5-7 shows the cross sectional view of the complete erosion crater. The width of the erosion line was roughly measured and the approximate width average was found to be 1.18mm for SP coating and 0.94mm for SD coating. These widths are more than two times the droplet diameter of 464µm. The smooth surface of the coating erosion craters is a notable feature which could not be seen on the edges of Ti6Al4V erosion crater. The topography of the eroded surface can play a vital role in the progress of the erosion damage and the processes causing erosion saturation [8]. During the erosion test a thin film of water would cover the eroded areas and acts as a cushion, leading to a decrease of the imposed impact pressure [2, 8]. The erosion crater texture influences the water film formation and its cushion role. In addition, it influences the deformation of water droplets upon impact and subsequently changes the stress distribution. Therefore, surface texture should be considered.

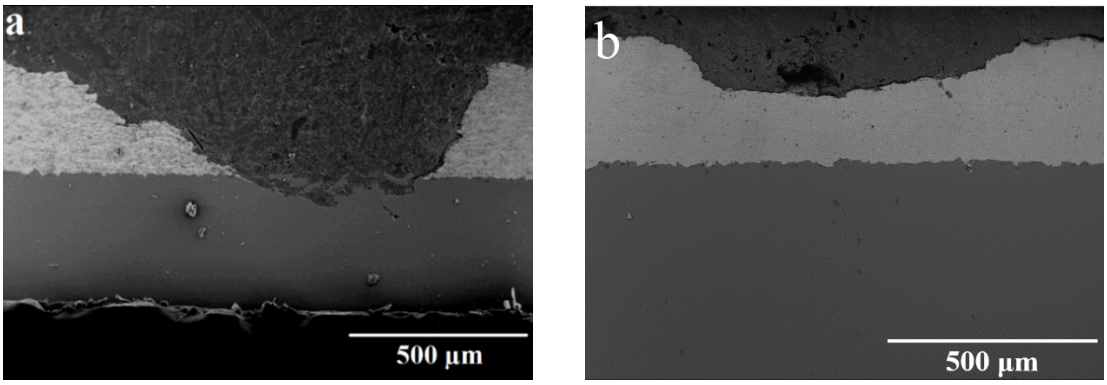

Figure 5-7: Cross sectional SEM images showing the depth and texture of the erosion craters at impact speed of 250m/s: (a) SP coating, (b) SD coating

Figure 5-8 presents the SEM images of erosion crater along its edges for SP coating. The splat microstructure and high density internal flaws close to the erosion line can be identified in

Figures 5-8-a and 5-8-b. The surface and sub-surface cracks, which are known mechanisms for WDE damage [79, 154], were observed (indicated by arrows). There are several cracks, as shown in Figure 5-8-d, which are very small relative to the other surrounding microstructural features. They are considered as nucleated cracks formed mainly at interface between the hard reinforcement WC grains and the Co binder (black arrows, 5-8-d) or at the interface between different splats (black arrow, 5-8-c). Figure 5-8-b shows a network of sub-surface cracks on the edge of the erosion crater. These cracks may nucleate due to the fracture of WC particles and their coalescence leads to detachment of large fragments of the coating. The cracks mainly initiated between the splats and some un-molten particles. As mentioned, SP coating does not show a homogenous microstructure; and low adhesion at the splat interfaces has left numerous internal flaws. These flaws, such as pre-existing cracks, grow significantly when receiving stress waves upon water droplet impingement. In addition, the detachment of WC grains from the cobalt binder and also their cracking are observed along the erosion line edge as shown in Figure 5-8-d.

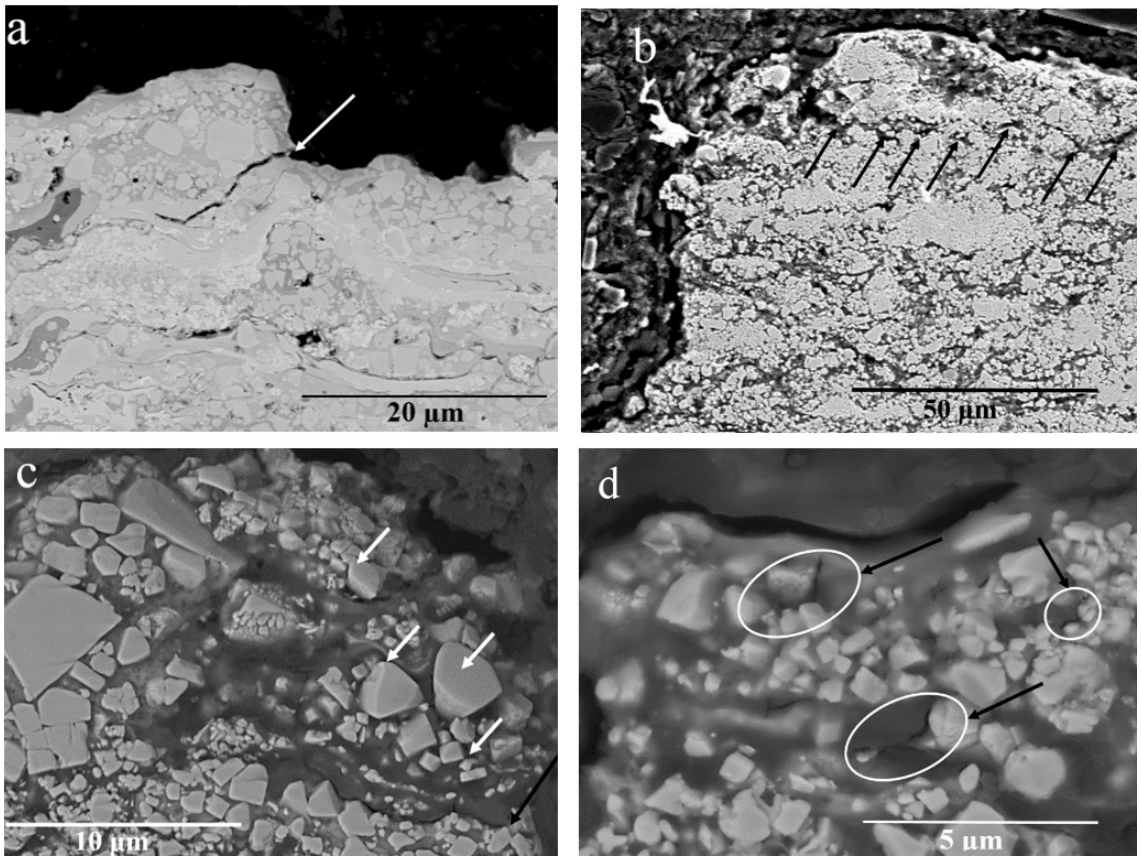

Figure 5-8: Cross sectional SEM images of eroded SP coating along the edges of erosion crater, WDE conditions: 464µm droplet size and 300m/s impact speed

Figure 5-9 shows cross sectional images of SD coating following WDE. The coating splat structure beside the damaged areas can hardly be identified because the microstructure is much more homogenous. Because of intense pressure of each water droplet impingement and subsequent stress wave propagation, the surface (white arrows) and sub-surface (black arrows) micro-cracks are formed as illustrated in Figures 5-9-a and 5-9-b. They propagate and merge together and form large sub-surface cracks which result in detachment of large lumps of the coating as shown in Figure 5-9-b. The sub-surface lateral cracking was observed during the solid particle erosion of brittle materials and highlighted as one of the dominant fracture mechanisms leading to material loss [154]. Moreover, a network of cracks can be seen in Figure 5-9-c. There is a very high chance for detachment of materials from this kind of crack networks by the repeated impingements. Figure 5-9-d shows cracking from pre-existing pores due to the high stress concentration around these defects in the coating microstructure. One can discern the WC–Co structure in the middle of the splats and note the excellent cohesion between the WC grains and binder. Here, the amorphous binder at the periphery of the splats is detrimental for their adhesion. The micrograph shows presence of cracks mainly between splats.

Clearly, density of internal flaws in SP coating is larger than that of SD coating. Also, the amount of nano-pores and micro-pores in the former coating is much higher. Low coating hardness is usually attributed to high porosity. However, the porosity reported in Table 5-2, corresponds only to micro-porosity and is too low to account for the low hardness of SP coating. In this coating, the low cohesion of WC/Co bonds causes the formation of high density zones of nano-pores around the WC grains. They were not considered in the porosity values listed in Table 5-2, but they contribute to the low observed hardness and result in worse erosion performance.

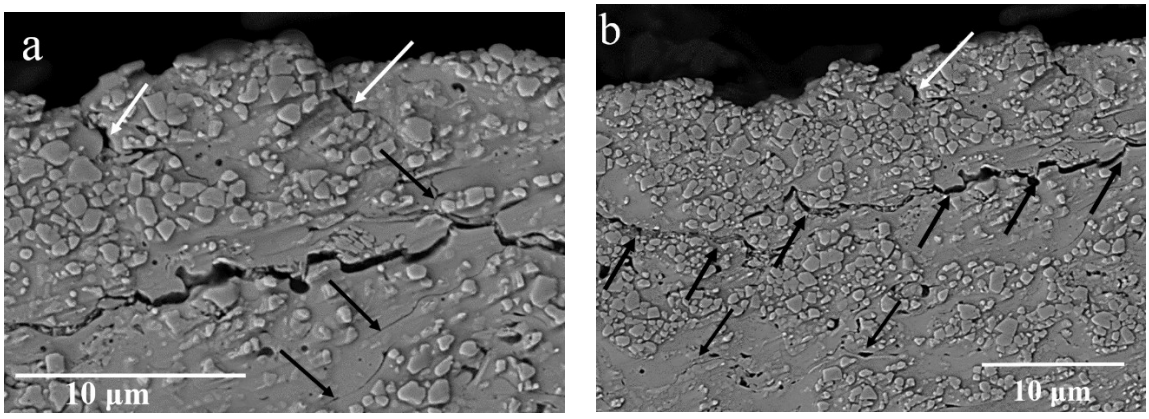

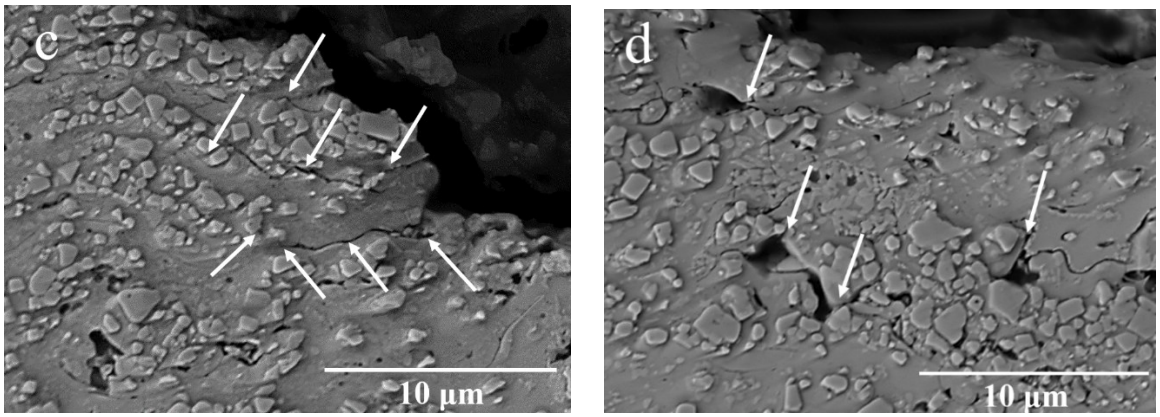

Figure 5-9: Cross sectional SEM images of eroded SD coating along the edges of erosion crater, erosion conditions: 464µm droplet size, 300m/s impact speed

5.4. Discussion

5.4.1. Water droplet erosion damage at different impact speeds

The water droplet impacts with high relative velocity cause damage to all materials. Different mechanisms for WDE have been found and described. They depend on the target material properties and water droplet impact conditions [2, 57, 79]. The magnitude of impact pressure and subsequent stress waves propagating through the material is a function of impact speed which is summarized in the following well-known Equation [6]:

$$P = \rho_0 C_0 V \qquad \textit{Equation 5-2}$$

where ρ_0 is the liquid density, C_0 is the speed of sound in the liquid and V is the impact speed. The accuracy of Equation 5-2 is limited due to the applied simplifications. Heymann [24] did some modifications and proposed Equation 5-3 which is used in the current study.

$$P = \rho_0 C_0 V[2 + (2K - 1)\frac{V}{C_0}] \qquad \textit{Equation 5-3}$$

where k is liquid constant. In the case of water erosion, $k=2$, $\rho_0=1000kg/m^3$ and $C_0=1463m/s$. Therefore, the impact speeds of 250, 300, and 350m/s correspond to impact pressures of 919, 1147, and 1391MPa, respectively.

The remarkable influence of impact pressure on the erosion behaviour of coatings manifests in the erosion curves, Figures 5-4 to 5-6. Figure 5-4 illustrates the erosion behaviour of the coatings and the Ti6Al4V bulk material at 250m/s. It can be seen that impact pressure of 919MPa could not impose sufficient stresses on SD coating to cause notable material removal.

Cracking in this condition was very slow and required a large number of impingements to propagate. In contrast, shorter incubation period in erosion of SP coating confirms that the shock pressure caused faster cracking and material loss in the microstructure of this coating.

At higher droplet impact speed, i.e. 300m/s that translates to impact pressure of 1147MPa, the stress was enough to cause material removal from early stages for both coatings. However, they did not show the same material removal rate. SD coating exhibits lower erosion rate due to its denser and more homogenous microstructure as shown in Figure 5-9. In this coating, crack development among the well bonded splat boundaries required higher stress and was slow. However, the cracking at the weak interfaces of SP coating microstructure was faster and require lower energy.

When erosion experiments were performed at 350m/s impact speed, the impact pressure and subsequent stresses induced brittle and catastrophic damage on both coatings. It seems that 1391MPa impact pressure was quite high enough for cracking in either the interface of WC/Co or splat boundaries leading to large fragments material loss. Also, it could enlarge the pre-existing cracks easily in both coatings. In the case of spray coatings, the adhesion strength among the interfaces would determine the required stresses for crack propagation. Indeed, the interaction between these required stresses and the stress waves resulted from droplet impacts causes the observed material loss. Hence, the different erosion testing conditions have a large influence on the variability of the reported erosion behaviours of WC-Co coatings in the literature [48, 79, 80].

It is known that the erosion resistance when plotted as material removal versus the impact speed, resembles an S-N curve for fatigue from which the fatigue limit is defined. Such a concept in erosion behaviour of materials could be called as erosion limit [46]. It means that there is a threshold velocity below which the induced pressures cannot cause material loss within a certain time limit. In the current work, it seems that 919MPa is close to the erosion limit of SD coating because of its relatively low material loss after more than 3 million droplet impacts. However, testing at lower impact speeds needs to be carried out to find the potential erosion limit of SP coating. Since both coatings have same chemical composition and grain size, it can be inferred that the coating microstructure determines its tolerable stress and erosion limit. Indeed, the microstructure is a function of utilised feedstock as well as coating process parameters and they should be optimized to achieve WDE resistant coating.

5.4.2. Erosion mechanism of spray coatings

In general, the WDE resistance of a target material has been related to its mechanical properties including resilience, hardness, toughness, elastic modulus, or ultimate tensile strength [2]. Erosion behaviour of bulk alloys can be classified into two main groups: materials which fail in a brittle manner and those which deform plastically. The erosion resistance of bulk materials such as titanium alloys was mainly related to their respective hardness [82]. Unlike titanium alloys, the erosion resistance of spray coatings was roughly related to their fracture toughness [48, 143]. However, both hardness and fracture toughness apart from the chemistry of the material, significantly depend on the coating morphology and microstructure. Hence, the coating microstructure has to be assessed in detail to identify the erosion mechanism, especially because the coating mechanical properties are normally reported from specific locations in the material; while the erosion phenomenon involves the entire coating and can find the regions of weakness in the microstructure to initiate material removal.

Figures 5-3-a and 5-3-b show the microstructures of the as-sprayed SP coating having a heterogeneous microstructure with high density of pores. The carbide grains distribution is not uniform and their large accumulation can be seen in the coating. The XRD results show the low degree of decarburization for SP coating. This is confirmed also by the angular shape of WC grains which indicates regions stayed solid throughout the coating process. The partial melting of particles can be attributed to the low density of 5810 powders and their low thermal conductivity. Indeed, the temperature of in-flight particles at the center is lower than at the surface and as a result some parts may not be molten. This has led to the heterogeneous microstructure of SP coating. Low level of carbon and tungsten dissolution in the cobalt decreases the amount of inter-diffusion of cobalt into WC grains and vice versa resulting in reduced wetting between the WC grains and the binder. The low adhesion of WC grains and cobalt binder forms a large number of micro and nano-pores (Figure 5-8-d). The high level of internal defects are consistent with the measured microhardness for SP coating. As mentioned, fracture toughness of this coating could not be measured since the cracking happened along the edges and not at the corners of the indent. This type of cracking contributed to the low tensile strength and accelerated crack growth [148]. The higher crack growth rate explains the poor erosion behaviour. Upon water droplet impacts, the stress waves propagate through the coating and they interact with microstructural flaws such as pre-existing cracks. These interactions lead to crack growth acceleration and increase the material

loss rate. The incubation period and the accelerated erosion rate depend strongly on the presence of internal defects. According to SP coating microstructure, the micro-pores, micro-cracks, low adhesion of WC grains and cobalt, and the weak splat boundaries are flaws present in this coating. Once the stress waves propagate through the coating, the present cracks in the splat boundaries grow and cause material detachment (Figure 5-8-a). The poor bonding of WC and Co and resulting built-in pores cause the formation of many micro-cracks. The micro-cracks next form a crack network that results in material removal (Figure 5-8-b). Moreover, the micro-cracking around the large WC grains would cause their direct detachment from the cobalt binder (Figure 5-8-c). In addition to individual detachment of carbide grains, because of the large accumulation of WC particles seen in this microstructure and their poor bonding with the Co binder, cracking occurs around these agglomerations and cause their group removal. The fracture of large WC particles as observed in the results expedites the material loss.

In the case of SD coating, there is a compact microstructure of well bonded WC grains into the binder which contributes to the higher hardness. The WC grains distribution is uniform and there is much less porosity leading to high fracture toughness. The optimized temperature and high velocity of in-flight powders result in relatively low porosity of this coating. Unlike SP coating, the adhesion of WC and Co is not the challenge for the erosion of this coating; but the inter-splat boundaries are the main issue. The higher in-flight powder temperature and uniform heat transformation among these sintered particles result in higher decarburization level which is confirmed by XRD results. Higher temperature also leads to enhanced wetting and adhesion between WC and Co. However, the higher the degree of decarburization, the lower the adhesion between the splats. This is due to the extra formation of undesired amorphous and brittle phases at the interfaces. They are clearly detrimental for fracture toughness and consequently for erosion resistance [148, 149]. Accordingly, the main weaknesses point in this microstructure are the splat boundaries. During the WDE test, the pre-existing cracks in the splat interfaces propagate and open their way toward the other weak point of the structure i.e. inter-splat interfaces. There they develop much more rapidly and cause detachment of large fragments or the whole of the splats as shown in Figures 5-9-a and 5-9-b. This phenomenon causes the detachment of complete or part of splats in the form of splat lifting. Although, recognizing different splats is difficult in the microstructure, the waviness of the observed cracks is a good way to verify the crack growth along the splat interfaces.

As in other thermal spray coatings, the role of the pores in this SD coating should not be ignored. Micro-pores are another internal flaw which causes cracking under hydrodynamic loading of erosion. Figure 5-9-d illustrates the crack initiation from the pores, which are already present in the microstructure. It was found that these cracks behave like a network and merge together with consecutive impingements.

In advanced stage of erosion, the lateral outflow jetting and hydraulic penetration participate in the erosion damage more than the initial stages. When a part of the coating is removed, the texture of the eroded surface becomes very important for the progress of erosion. In the case of rough surface, the droplet impacts are more detrimental. For the splat microstructure of spray coatings, the interfaces exposed to water impact are the main damage initiation points. Figure 5-10 illustrates a simple schematic representation of water droplet impingement on a spray coating with its splat microstructure. Upon water droplet impact onto the surface, lateral water jet forms and travels on the surface with very high speed. The water jet strikes any kind of irregularities on the surface such as raised splats and causes cracking. In Figure 5-10-b, water jet strikes the splat A and a micro-crack initiates at the interface of splat A and B. In advanced stages, when part of the coating was removed, a larger number of splat interfaces encounter the impacting water droplets. In this step, stress wave propagation, outflow jetting and hydraulic penetration contribute to erosion damage in parallel. There would be a high chance for sub-surface cracking by stress waves at positions such as number 6 which are beneath the centre of impact and experience the maximum impact pressure. Number 1 and 5 zones which are close to the circumference of the impact area would be damaged by the formed lateral outflow jets. The splat interfaces would be opened up and it causes lifting of splats. In number 2, 3, and 4 areas, the hydraulic penetration would be dominant process for cracking and subsequent digging.

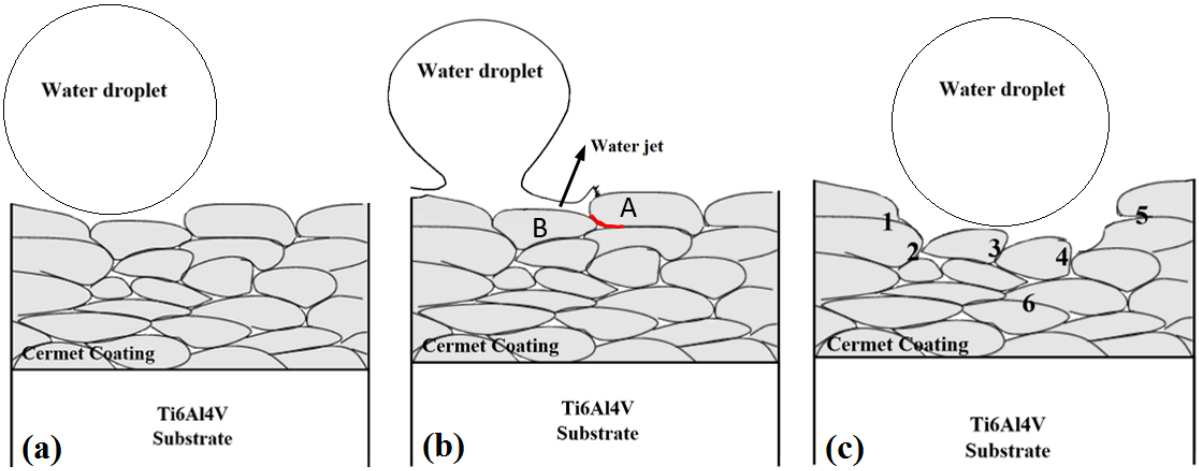

Figure 5-10: Schematic of water impact on a cermet coating with its typical splat microstructure: (a) as-sprayed cermet coating before water impact, (b) upon impact and formation of water jet, (c) Eroded cermet coating exposed to water droplet impingement in advanced

It was determined that the erosion damage of carbide cermet coatings is dominated by cracking. The erosion rate is controlled by cracks initiation and growth rate. Crack initiation is found to depend strongly on internal flaws (i.e. pores and crack in the interfaces). The droplet impact may cause carbide particle breaking, detachment of WC grains from the binder and lifting of splats. Indeed, the inter-splat adhesion strength plays a significant role on the crack growth rate and as a result the erosion rate.

It is noteworthy that WDE behaviour considerably depends on the surface roughness. Also, top layers of spray coating close to the surface show higher level of porosity compared to the underneath layers. Therefore, WDE performance of ground and polished SD coating will be compared with as-sprayed in a future publication.

5.5. Conclusions

In this study, the water droplet erosion behaviour of WC-12Co sprayed coatings having two different microstructures was evaluated. To gain insight into the importance of erosion test parameters, WDE experiments were performed at three impact speeds. The erosion mechanism of the coatings was also investigated. The following conclusions can be drawn:

- Spraying commercial Woka 3110 powder and Sulzer 5810 powder resulted in two different microstructure for WC-12Co coatings. SD coating showed superior erosion performance compared to Ti6Al4V; however, SP showed less erosion resistance. Despite their identical

chemical composition, the results show that the coating microstructure has a strong influence of WDE resistance and must be controlled carefully during spraying. In an optimum coating, the density of pores should be reduced, inter-splat adhesion and coating toughness should be maximised by limiting carbide degradation during spraying. They can be achieved by selecting appropriate feedstock and proper control of their temperature and velocity during spraying process.

- The spray cermet coating was eroded by different mechanisms depending on their microstructure and internal flaws. The main damage evolution process was cracking (surface and sub-surface) which was related to the coating fracture toughness. It involved carbide particles breaking, detachment of WC grains from the binder and lifting of the splats.

- The erosion damage of SD coating was governed mainly by splats lifting. The cracks propagation in the inter-splat boundaries followed by detachment of splats is the main phenomenon resulting in material loss. It is due to the stress wave propagation through the material. However, lateral outflow jetting and hydraulic penetration would accelerate this process in the later erosion stages.

- In the case of SP coating and its heterogeneous microstructure, erosion damage was operated by carbide particles breaking, detachment of WC grains from the binder and lifting of the splats in parallel and it was not possible to identify a dominant erosion mechanism.

- The water droplet impingement speed was found to have significant influence on the WDE performance of WC-Co spray coatings. The erosion rate of SP coating increased more than 100 time by increasing impact speed from 250m/s to 350m/s. In the case of SD coating, the potential erosion endurance limit in terms of impact speed should be located between 200 and 250m/s.

Relating to the theme of thesis

In chapter 5, erosion performance of sprayed WC-Co coatings was compared with that of Ti6Al4V. Significant influence of coating microstructure on its erosion performance was observed. As-sprayed WC-Co coating with homogeneous microstructure showed up to 3.8 times higher erosion resistance compared with Ti6Al4V. Its erosion resistance can be enhanced by optimizing the coating process parameters to reduce oxidation of inflight particles. In addition, removing top layers of sprayed coating and smoothing its surface lead to considerably high erosion resistance. This is aligned with the main objective of this research which is enhancing water droplet erosion performance of Ti64 alloy.

Chapter 6 : Concluding remarks

Experimental investigations were carried out for finding potential solutions to combat the water droplet erosion damage observed on the leading edges of turbine blades. Two approaches were used to reach this goal. First, examining the erosion behaviour of TiAl as a potential alloy for turbine blades. Second, studying the influence of two surface treatments on water droplet erosion of Ti6Al4V which is a currently used alloy for compressor blades.

In this thesis, the erosion performance of all specimens were examined at least using two different impact speeds, 350 and 300m/s which are close to what is experienced by the compressor blades of gas turbines. Erosion results with different indicators derived from the erosion graphs, which are incubation period (H_0) and maximum erosion rates (ER_{max}), were presented in the previous chapters; however, the cumulative erosion resistance (*CER*) of all specimens, treated and non-treated, can be seen in Figures 6-1 and 6-2 for impact speeds of 300m/s and 350m/s, respectively. *CER* has been defined as the ratio of total volume of impacting water to total volume loss of the target. In Figures 6-1 and 6-2 *CER* of tested coupons is normalized by that of Ti6Al4V as the reference material.

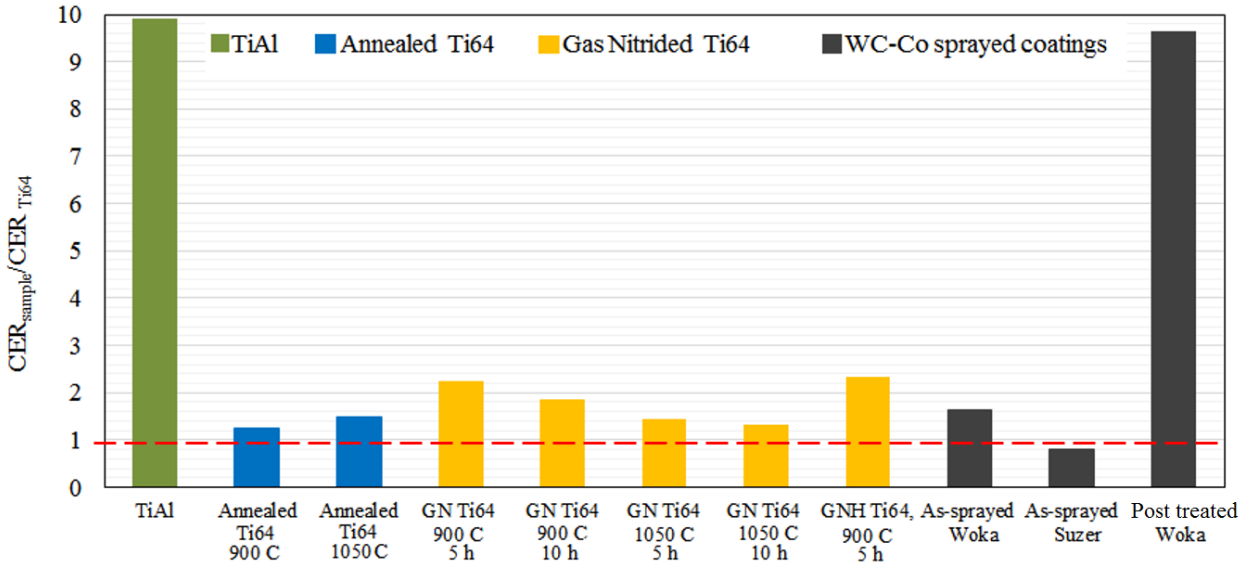

Figure 6-1: Normalized cumulative erosion resistance of all tested coupons at 300m/s

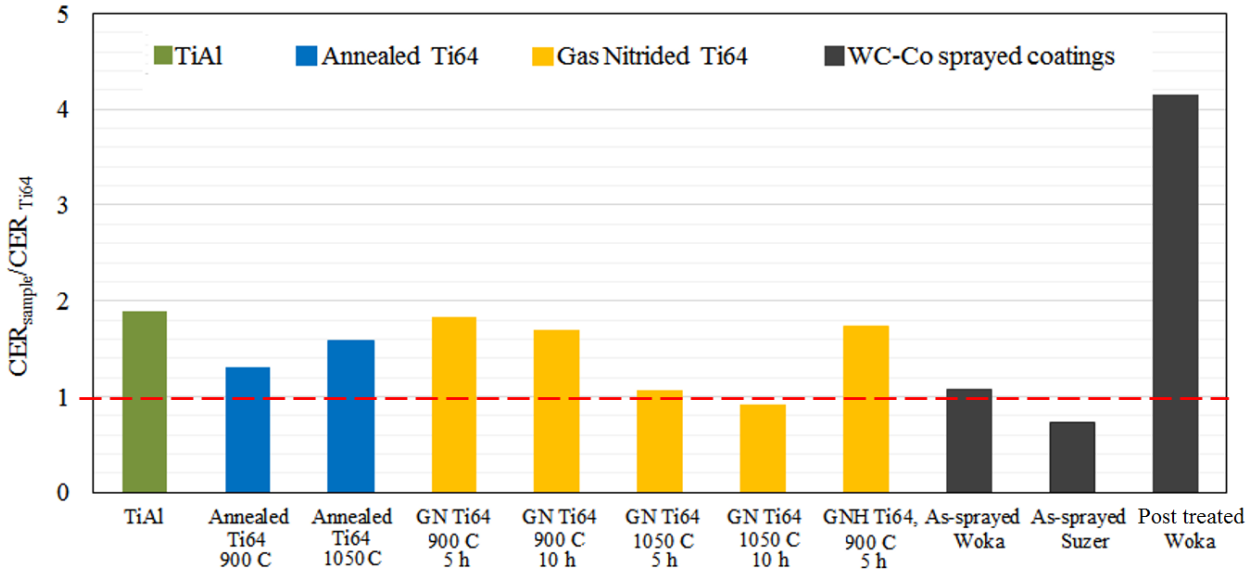

Figure 6-2: Normalized cumulative erosion resistance of all tested coupons at 350m/s

6.1. Conclusions

Nearly fully lamellar TiAl is proposed as a water droplet erosion resistant alloy for turbine blades. It showed superior erosion performance (i.e. longer incubation and slower material loss) compared to Ti6Al4V at all tested conditions. Direct comparison of TiAl and Ti6Al4V erosion performance at different impingement conditions, i.e. impact speeds and droplet sizes, displayed that TiAl superiority is a function of the erosion conditions. It is supported with the large value of speed exponent of the $ER \propto V^n$ relation. The value of n was 12.5 and 11.5 when the coupons were eroded by 464µm and 603µm droplets, respectively. They showed that TiAl erosion resistance, which is inversely proportional to the erosion rate, is highly dependent on impact velocity and reduces significantly at severe erosion conditions. Furthermore, the damage threshold speeds (V_C) of TiAl were specified. The value of V_C was determined between 250m/s and 275m/s when 464µm droplets impacted TiAl and 200m/s and 225m/s when 603µm droplets impacted its surface. These results indicate that the damage threshold speed is a function of impacting droplet size, and therefore only one speed cannot be reported for a certain material.

Superior erosion behaviour of TiAl was attributed to its higher hardness, strength, modulus of elasticity, and particularly hardenability. TiAl showed 11 to 17% hardness increase during the incubation period compared to only 6% increase for Ti6Al4V. Initial droplet impingements made TiAl harder which led to its longer incubation period. In addition, nearly fully lamellar

microstructure of TiAl showed high resistance to crack propagation and contributed to its superior erosion resistance. In this microstructure, numerous γ/γ domain boundaries, α_2/γ lamellae interfaces and colony boundaries decelerated the crack propagation.

Water droplet erosion of TiAl initiated with severe local micro-plasticity. The localized material flow was attributed to the formation of slip bands predominantly interlamellar slips. The large number of slip and twinning bands resulted in localized height variations and acted as stress raisers. The nucleation of initial cracks along the interlamellar slip bands was systematically observed. It showed that the transgranular cracking (within the colonies) is the main contributor to erosion damage during the incubation and acceleration stages. Anisotropic response and plastic deformation of TiAl lamellar colonies, based on their orientation with respect to the droplet impact direction, caused local depressions in the areas near to the colony boundaries. Numerous local and brittle fractures in such areas led to micro-pitting and commenced material loss. The colonies oriented with 45° or nearly so were vulnerable upon droplet impingements and demonstrated the largest number of pitting. Water hammering, outflow lateral jetting, and hydraulic penetration were the main reasons for the erosion damage in the advanced stages. They caused periodic processes of water roughening then water polishing of the TiAl erosion crater surfaces, which governed the damage progress. Fractography of the eroded surface in these stages revealed that transgranular fracture consisting of the interlamellar and translamellar cracks is the main contributor to the erosion damage.

The microstructure of Ti6Al4V considerably influenced its erosion performance. Annealed Ti6Al4V above β-transus temperature (1050°C) with fully lamellar microstructure showed up to 59% higher cumulative erosion resistance compared with as-received Ti6Al4V with equiaxial microstructure. In addition, annealed Ti6Al4V at 900°C with duplex microstructure (equiaxed α grains and small lamellar colonies) showed up to 30% higher erosion resistance compared to as-received Ti6Al4V. They revealed the significant role of lamellar microstructure to decelerate crack propagation and subsequently WDE damage. This is consistent with the proposed reasons for the superior erosion resistance of TiAl, which has nearly fully lamellar microstructure. This interesting finding about the role of lamellar microstructure in erosion behavior of Ti6Al4V was observed during the WDE investigation of gas nitrided Ti6Al4V. It was found that the nitriding temperature significantly affects both the quality of surface layers and the local microstructure of core material.

Gas nitriding of Ti6Al4V hardened the surface with forming a thin and hard compound layer and a relatively hard and homogeneous diffusion layer on the surface. Nitriding of Ti6Al4V enhanced the cumulative erosion resistance up to 134%. This is attributed to the hard nitrided layers on the surface and the formation of lamellar colonies in the core of the material. In water droplet erosion of nitrided Ti6Al4V, mechanical stability of compound layer (outermost layer) played a key role to combat erosion. Its failure left numerous cracks on the surface and accelerated material loss over diffusion layer. Ti6Al4V nitrided at 900°C showed the best cumulative erosion resistance, which is 70 to 134% higher than as-received Ti6Al4V. Hard and dense compound layer which was mechanically supported by the homogeneous diffusion layer resulted in the superior erosion performance of the nitrided coupon. Lower instantaneous erosion rates of nitrided coupon in the advanced stages of erosion was attributed to slower crack propagation in the duplex microstructure of core material, which was not influenced by nitrogen diffusion. Erosion performance of Ti6Al4V nitrided at 1050°C was notably sensitive to the impact speed. Nitriding at 1050°C could not provide erosion protection at impact speed of 350m/s. However, it enhanced the cumulative erosion resistance of Ti6Al4V up to 44% at impact of 300m/s. This superior performance was due to the resistance of diffusion layer against crack propagation upon impact at this speed. Formation of fully lamellar microstructure in the core material of Ti6Al4V nitrdied at 1050°C also contributed to its higher cumulative erosion resistance.

Spraying WC-Co powder using HVOF technique fabricated a thick and hard cermet coating on Ti6Al4V coupons. Microstructure homogeneity of these coatings influenced their hardness, fracture toughness and erosion behavior. Wettability of WC particles in cobalt binder, the strength of inter-splat boundaries, and the porosity of the coatings were specified as the critical microstructural features that affect erosion behavior. Woka 3110 coating (SD coating) with relatively dense and homogeneous microstructure showed high fracture toughness and superior erosion performance compared to Ti6Al4V. This coating demonstrated 7, 65 and 280% higher cumulative erosion resistance than Ti6Al4V when attacked by water droplets at 350, 300 and 250m/s impact speeds, respectively. However, Sulzer 5810 coating (SP coating) with same chemical composition but nonhomogeneous microstructure showed worse erosion performance compared to Ti6Al4V at all impact speeds. Erosion evolution of WC-Co coating was governed by cracks (surface and sub-surface) development. As-received Ti6Al4V showed no preferred direction in cracking. Unlike Ti6Al4V, crack propagation through the splat boundaries of sprayed

coating, almost parallel to the surface, was the main contributor to materials removal. Indeed, splat lifting was often observed in erosion of these coatings. Detachment of WC grains was also documented over the eroded surface particularly for the coating with low wettability between WC grains and Co binder.

Erosion behaviour of surface treated Ti6Al4V were strongly dependent on the performance of their outermost layers. The presence of a porous oxide layer on the surface of nitrided coupon was found considerably destructive for its erosion behaviour. In the case of WC-Co coatings, the applied post treatment increased their cumulative erosion resistance (*CER*) up to 7 times when impacted by 460μm droplets at 300m/s and 350m/s speeds. Indeed, the post treated coating showed uniform and slow material loss during erosion, which was not the case for erosion of as-sprayed coating.

In summary, TiAl alloy displayed longer incubation and lower erosion rates compared with Ti6Al4V. The surface treated Ti6Al4V (i.e. gas nitrided and WC-Co coating) start to lose material faster than the non-treated Ti6Al4V. However, their erosion was followed by lower instantaneous material loss rates compared to those of non-treated Ti6Al4V at the acceleration and maximum erosion rate stages. Indeed, the considered surface treatments particularly WC-Co coating would not be the best choice for the applications in which the damage initiation is the main concern. Furthermore, comparing the cumulative erosion resistance (*CER*) of all coupons reveals that TiAl and grinded WC-Co coating showed notably higher *CER* compared with gas nitrided Ti6Al4V. It is believed that to combat erosion damage large depth of treatments on the target (i.e. not thin layers) is required. Although nitrided layers showed lower instantaneous erosion rates in the intermediate stages of erosion, they did not remain on the surface for long time. Therefore, fabrication of thicker nitrided layers is more efficient to combat water droplet erosion damage.

6.2. Contributions

This study has enhanced the understanding of water droplet erosion process at different stages. A key strength of this study is using one of the most advanced water droplet erosion rigs which enables accurate control of erosion parameters, and produces representative results. The erosion rig provides a physical simulation of the water droplet erosion process that is experienced

by turbine blades in service conditions. Specific contributions stemming from this research project are listed below.

- For the first time, water droplet erosion behaviour of lamellar TiAl, potential alloy for turbine blades, has been studied experimentally. The study provides a comprehensive comparison with the erosion behaviour of current blade alloy, Ti6Al4V. Remarkable water droplet erosion resistance of nearly fully lamellar TiAl was determined in this research. It highlights this alloy as a very promising material to combat erosion damage of turbine blades. The notable dependency of TiAl erosion behaviour to impact speed, found in this research, provides a guideline for designing of turbine blades using this alloy. Furthermore, the findings about the influence of target hardenability on water droplet erosion performance contributes to the current knowledge on erosion prediction models which rely on the mechanical properties of the solid surface.

- The water droplet erosion damage mechanism of TiAl has been investigated both qualitatively and quantitatively at different phases of erosion including: incubation, material loss initiation and advanced stages. The response of TiAl alloy to the initial high speed droplet impacts were described. Its difference from the behaviour of ductile metals such as Ti6Al4V has been revealed. Fractography of TiAl eroded surfaces and the investigation of cracking behaviour in relation to the microstructure provide a framework for further investigation to manipulate the microstructure of this alloys and obtain a superior water droplet erosion performance.

- For the first time the influence of gas nitriding on water droplet erosion behaviour of Ti6Al4V has been experimentally studied to provide accurate evaluation of its effectiveness to combat this degradation. The findings extend the current knowledge about the erosion behaviour of target with multilayered surface. It is the typical configuration for the thermochemically treated titanium alloys. In addition, the notable influence of microstructure variation of nitrided, annealed and as-received Ti6Al4V on erosion behaviour was highlighted. This could be used to design the microstructure of Ti6Al4V to enhance its water erosion resistance.

- Water droplet erosion of WC-Co coatings sprayed by HVOF technique were accurately examined. Their performance was compared with that of Ti6Al4V using 250, 300, 350m/s impact speeds, for the first time. The findings make several contributions to understand the remarkable influence of impingement conditions (e.g., impact speed) as well as the coating microstructure on erosion behaviour. This research can be served as a base for future studies on using cermet sprayed coating as a water droplet erosion resistant material.

In addition to the four journal publications used in the body of this thesis, the following publications have been accomplished during the course of the current work:

Journal publications:

1. **M.S. Mahdipoor**, M. Medraj "Comparative study of different surface treatments influence on water droplet erosion behaviour of Ti6Al4V", (In preparation).

2. F. Tarasi, **M.S. Mahdipoor**, A. Dolatabadi, M. Medraj, C. Moreau "HVOF and HVAF Coatings of Nano-Agglomerated Tungsten Carbide-Cobalt Powders for Water Droplet Erosion Application", Submitted to *Journal of Thermal Spray Technology*, (2015).

6.3. Recommendations for future works

Combating the water droplet erosion damage of turbine blades is an urgent issue in aerospace and power generation industries and this thesis contributes to the ongoing efforts of finding solutions for this problem. In order to approach a comprehensive framework to address this issue, some suggestions for future works are summarized as following.

- Water droplet erosion behaviour was highly dependent on the impingement conditions (i.e. impact speed and droplet size). In this thesis they are similar to what is experienced by the gas turbine compressor blades in service. Water droplet erosion could be also seen on the steam turbine blades that undergo different impingement conditions. It is recommended to extend the studied impingement conditions encountered in other applications such as steam turbines and aerospace applications.

- In this thesis, water droplet erosion performance of flat coupons was examined. However, in service it is the leading edge of blades that are the most affected by water droplet erosion.

Depending on the used blade type, the leading edge would have a specific curvature. Future work should assess the erosion behaviour of TiAl alloy and the surface treated Ti6Al4V using coupons with geometries that simulate real blades.

- In this study, the erosion experiments were carried out via specific nozzles generating only one water stream. However, there are complex interactions between large number of droplets in the compressor, impacting the rotating blades. Further researches using shower nozzles, which produce several water streams, can contribute to the knowledge of water droplet erosion damage in turbine industries.

- The erosion damage mechanism of gas nitrided Ti6Al4V revealed that the nitrided layers do not remain on the surface for long time. The compound layer of such coupons needs to be mechanically stable on the surface and their diffusion layer needs to be thicker and harder. To achieve these conditions, using plasma nitriding treatment would be a fruitful area for further work.

- Considerable influence of microstructure variation on the erosion performance of Ti6Al4V was highlighted in the annealed and nitrided Ti6Al4V. It was stated that Ti6Al4V with lamellar microstructure is more resistant to crack propagation, which results in the higher erosion resistance. Therefore, comprehensive investigation of crack development during erosion of Ti6Al4V with equiaxial, lamellar, and duplex microstructure would be a very interesting subject to pursue.

- Thermal sprayed WC-Co coating followed by grinding process was found to be a promising surface treatment to reduce water droplet erosion damage. Considerably more experimental work needs to be done to accurately evaluate the efficiency of such coatings to combat erosion damage at different industrial situations. It is recommended that further research be undertaken in the following areas: the influence of chemical composition of spraying feedstock (WC-Co based); the effect of the temperature and velocity of in-flight powders; and the role of post-treatments such as polishing on water droplet erosion performance of sprayed cermet coatings.

References

[1] C. M. Preece and N. H. Macmillan. Erosion. *Annual Review of Materials Science*, 7 (1977) 95-121.

[2] F. J. Heymann, *Liquid impingement erosion*, Wear, ASM Handbook, Materials Park, OH, USA, 18 (1992) 221-223.

[3] F. J. Heymann, Erosion by liquids (Metals erosion by cavitation and liquid impingement, discussing test methods and resistance prediction), *Machine Design*, 42 (1970) 118-124.

[4] I. Kleis and P. Kulu. *Solid particle erosion, Occurrence Prediction and Control*, Springer Science & Business Media, Berlin, Germany, 2007.

[5] H. D. Chiang, P. Wang and B. Tsai. Gas turbine power augmentation by overspray inlet fogging, *Journal of Energy Engineering*, 133 (2007) 224-235.

[6] S. C. Cook. Erosion by water-hammer. *In Proceedings of the Royal Society of London. Series A, Containing Papers of a Mathematical and Physical Character*, 119.783 (1928) 481-488.

[7] E. Honegger. Tests on erosion caused by jets. *Brow Boveri Review*, 14 (1927) 95.

[8] M. Ahmad, M. Casey and N. Sürken. Experimental assessment of droplet impact erosion resistance of steam turbine blade materials, *Wear*, 267 (2009) 1605-1618.

[9] R. K. Bhargava, C. Meher-Homji, M. A. Chaker, M. Bianchi, F. Melino, A. Peretto and S. Ingistov. Gas turbine fogging technology: A state-of-the-art review-part I: Inlet evaporative fogging-analytical and experimental aspects, *Journal of Engineering for Gas Turbines and Power*, 129 (2007) 443-453.

[10] C. B. Meher-Homji and T. R. Mee. Gas turbine power augmentation by fogging of inlet air. *In Proceedings of the 28th Turbomachinery Symposium*, College Station, TX, USA (1999) 93-114.

[11] R. K. Bhargava, C. Meher-Homji, M. A. Chaker, M. Bianchi, F. Melino, A. Peretto and S. Ingistov. Gas turbine fogging technology: A state-of-the-art review-part II: Overspray fogging-analytical and experimental aspects, *Journal of Engineering for Gas Turbines and Power*, 129 (2007) 454-460.

[12] N. Yasugahira, K. Namura, R. Kaneko and T. Satoh. Erosion resistance of titanium alloys for steam turbine blades as measured by water droplet impingement. *Titanium Steam Turbine Blading*, (1988) 385-401.

[13] A. Martínez, F. Martínez, M. Velázquez, F. Silva, I. Mariscal and J. Francis. The density and momentum distributions of 2-dimensional transonic flow in an LP-steam turbine. *Energy and Power Engineering*, 4 (2012).

[14] Available online at: http://www.power-technology.com/contractors/powerplantequip/meeindustries/meeindustries3.html.

[15] V. Swaminathan. Investigation of high-pressure compressor blade failures in LM6000 sprint engines. *In Western Turbine Users and Combustion Turbine Operators Task Force Conferences*, (2004).

[16] J. E. Field, M. B. Lesser and J. P. Dear. Studies of two-dimensional liquid-wedge impact and their relevance to liquid-drop impact problems. *In Proceedings of the Royal Society of London A: Mathematical, Physical and Engineering Sciences*, 401.1821 (1985) 225-249.

[17] M. B. Lesser. Analytic solutions of liquid-drop impact problems. *In Proceedings of the Royal Society of London A: Mathematical, Physical Engineering Sciences*, 377.1770 (1981) 289-308.

[18] J. E. Field. ELSI conference: Invited lecture. Liquid impact: Theory, experiment, applications, *Wear*, 233 (1999) 1-12.

[19] W. F. Adler. Water drop impact modeling. *Wear*, 186-187 (1995) 341-351.

[20] W. F. Adler, The mechanics of liquid impact, *Academic Press, Treatise on Materials Science and Technology*, 16 (1979) 127-183.

[21] J. E. Field. The physics of liquid impact, shock wave interactions with cavities, and the implications to shock wave lithotripsy. *Physics in Medicine and Biology*, 36.11 (1991) 1475.

[22] M. B. Lesser and J. E. Field. The impact of compressible liquids, *Annual Review of Fluid Mechanics*, 15.1 (1983) 97-122.

[23] N. Li, Q. Zhou, X. Chen, T. Xu, S. Hui and D. Zhang. Liquid drop impact on solid surface with application to water drop erosion on turbine blades. Part I. nonlinear wave model and solution of one-dimensional impact. *International Journal of Mechanical Sciences*, 50.10-11 (2008) 1526-1542.

[24] F. J. Heymann. On the shock wave velocity and impact pressure in high- speed liquid-solid impact. *Transactions of the ASME. Series D, Journal of Basic Engineering*, 90.3 (1968) 400-402.

[25] J. H. Brunton. High speed liquid impact. *Philosophical Transactions of the Royal Society of London A: Mathematical, Physical and Engineering Sciences*, 260 (1966) 79-85.

[26] H. S. Kirols, D. Kevorkov, A. Uihlein and M. Medraj. The effect of initial surface roughness on water droplet erosion behaviour, *Wear*, 342-343 (2015) 198-209.

[27] H. S. Kirols, M. S. Mahdipoor, D. Kevorkov, A. Uihlein and M. Medraj, Energy based approach for understanding water droplet erosion. *In preparation*.

[28] L. Huang, J. Folkes, P. Kinnell and P. H. Shipway. Mechanisms of damage initiation in a titanium alloy subjected to water droplet impact during ultra-high pressure plain waterjet erosion. *Journal of Materials Processing Technology*, 212.9 (2012) 1906-1915.

[29] V. N. Varavka and O. V. Kudryakov, Regularities of steel wear under the impact of discrete water-droplet stream. Part II: Stage of the developed droplet-impingement erosion, *Journal of Friction and Wear*, 36 (2015) 153-162.

[30] B. Luiset, F. Sanchette, A. Billard and D. Schuster. Mechanisms of stainless steels erosion by water droplets, *Wear*, 303 (2013) 459-464.

[31] G. P. Thomas and J. H. Brunton. Drop impingement erosion of metals. *In Proceedings of the Royal Society of London A: Mathematical, Physical and Engineering Sciences*, 314.1519 (1970) 549-565.

[32] M. Ahmad, Experimental assessment of droplet impact erosion of low-pressure steam turbine blades, PhD thesis, Institut für Thermische Strömungsmaschinen und Maschinenlaboratorium der Universität Stuttgart, Stuttgart (Germany) 2009.

[33] M. Haag, Untersuchungen zur Schädigungsentwicklung an Dampfturbinenwerkstoffen infolge von Wassertropfenerosion, PhD thesis, Technische Universität Kaiserslautern, Kaiserslautern (Germany) 2012.

[34] V. A. Ryzhenkov, A. I. Lebedeva and A. F. Mednikov. Erosion wear of the blades of wet-steam turbine stages: Present state of the problem and methods for solving it. *Thermal Engineering*, 58.9 (2011) 713-718.

[35] A. Momber and R. Kovacevic. Fracture of brittle multiphase materials by high energy water jets. *Journal of Materials Science*, 31.4 (1996) 1081-1085.

[36] D. Ma, A. Mostafa, D. Kevorkov, P. Jedrzejowski, M. Pugh and M. Medraj, Water impingement erosion of deep-rolled Ti64, *Metals*, 5 (2015) 1462-1486.

[37] W. F. Adler. Analysis of particulate erosion. *Wear*, 37.2 (1976) 345-352.

[38] F. P. Bowden and J. E. Field. The brittle fracture of solids by liquid impact, by solid impact and by shock. *In Proceedings of the Royal Society of London A: Mathematical, Physical and Engineering Sciences*, 282.1390 (1964) 331-352.

[39] N. L. Hancox and J. H. Brunton, The erosion of solids by the repeated impact of liquid drops, *Philosophical Transactions of the Royal Society of London A: Mathematical, Physical and Engineering Sciences*, 260.1110 (1966) 121-139.

[40] M. C. Kong, D. Axinte and W. Voice. Aspects of material removal mechanism in plain waterjet milling on gamma titanium aluminide. *Journal of Materials Processing Technology*, 210.3 (2010) 573-584.

[41] N. Kamkar, F. Bridier, P. Bocher and P. Jedrzejowski. Water droplet erosion mechanisms in rolled Ti-6Al-4V. *Wear*, 301 (2013) 442-448.

[42] M. S. Mahdipoor, D. Kevorkov, P. Jedrzejowski and M. Medraj, Water droplet erosion mechanism of nearly fully-lamellar gamma TiAl alloy, *Materials & Design*, 89 (2016) 1095-1106.

[43] F. G. Hammitt, Y. Huang, C. L. Kling, T. M. Mitchell and L. P. Salomon. A statistically verified model for correlating volume loss due to cavitation or liquid impingement. Characterization and Determination of Erosion Resistance, *ASTM Special Technical Publication*, 474 (1970) 288-322.

[44] P. A. Coulon. Erosion-corrosion in steam turbines. Part II: A problem largely resolved. *Lubrication Engineering*, 42.6 (1986) 357-362.

[45] C. F. Kennedy and J. E. Field. Damage threshold velocities for liquid impact. *Journal of Materials Science*, 35.21 (2000) 5331-5339.

[46] A. Thiruvengadam, S. L. Rudy and M. Gunasekaran. Experimental and analytical investigations on liquid impact erosion. Characterization and Determination of Erosion Resistance, *ASTM Special Technical Publication*, 474 (1970) 249-287.

[47] F. J. Heymann, Survey of clues to the relationship between erosion rate and impact conditions, *In Second Meersburg Conference on Rain Erosion and Allied Phenomena*, Bondensee, Fedreal German Republic (1967).

[48] Y. I. Oka and H. Miyata. Erosion behaviour of ceramic bulk and coating materials caused by water droplet impingement. *Wear*, 267.11 (2009) 1804-1810.

[49] B. Lee, K. Riu, S. Shin and S. Kwon. Development of a water droplet erosion model for large steam turbine blades. *KSME International Journal*, 17.1 (2003) 114-121.

[50] K. Haugen, O. Kvernvold, A. Ronold and R. Sandberg. Sand erosion of wear-resistant materials: Erosion in choke valves. *Wear*, 186 (1995) 179-188.

[51] M. Ahmad, M. Schatz and M. V. Casey. Experimental investigation of droplet size influence on low pressure steam turbine blade erosion. *Wear*, 303 (2013) 83-86.

[52] W. F. Adler. Particulate impact damage predictions. *Wear*, 186 (1995) 35-44.

[53] F. J. Heymann. On the time dependence of the rate of erosion due to impingement or cavitation. *ASTM Special Technical Publication*, 408 (1967) 70-100.

[54] ASTM G73-10, *Standard test method for liquid impingement erosion using rotating apparatus*: ASTM International, West Conshohocken, PA, USA, 2010.

[55] S. Yerramareddy and S. Bahadur. Effect of operational variables, microstructure and mechanical properties on the erosion of Ti-6Al-4V. *Wear*, 142.2 (1991) 253-263.

[56] P. Rao and S. G. Young, Eds., Universal Approach to Analysis of Cavitation and Liquid-Impingement Erosion. *National Aeronautics and Space Administration. Scientific and Technical Information Branch*, (1982) 38.

[57] G. S. Springer, *Liquid Droplet Erosion*. John Wiley & Sons, New York, USA, 1976.

[58] J. V. Hackworth. Damage of infrared-transparent materials exposed to rain environments at high velocities. *In proceeding of 26th International Society for Optics and Photonics*, San Diego, USA, 362 (1983).

[59] R. H. Richman and W. P. McNaughton. A metallurgical approach to improved cavitation-erosion resistance. *Journal of Materials Engineering and Performance*, 6.5 (1997) 633-641.

[60] E. F. Tobin, T. M. Young, D. Raps and O. Rohr. Comparison of liquid impingement results from whirling arm and water-jet rain erosion test facilities. *Wear*, 271 (2011) 2625-2631.

[61] J. M. Robinson and R. C. Reed. Water droplet erosion of laser surface treated Ti-6Al-4V. *Wear*, 186-187 (1995) 360-367.

[62] B. S. Mann and V. Arya. HVOF coating and surface treatment for enhancing droplet erosion resistance of steam turbine blades. *Wear*, 254 (2003) 652-667.

[63] G. F. Schmitt Jr. Liquid and solid particle impact erosion, *Air Force Materials Lab Wright-Patterson, AFML-TR-4122* (1979).

[64] M. S. Mahdipoor, H. S. Kirols, D. Kevorkov, P. Jedrzejowski and M. Medraj. Influence of impact speed on water droplet erosion of TiAl compared with Ti6Al4V. *Scientific Reports*, 5 (2015).

[65] B. S. Mann and V. Arya. An experimental study to correlate water jet impingement erosion resistance and properties of metallic materials and coatings. *Wear*, 253 (2002) 650-661.

[66] F. J. Heymann. Toward quantitative prediction of liquid impact erosion. *ASTM Special Technical Publication*, 474 (1970) 212.

[67] R. L. Howard and A. Ball. The solid particle and cavitation erosion of titanium aluminide intermetallic alloys. *Wear*, 186 (1995) 123-128.

[68] R. L. Howard and A. Ball. Mechanisms of cavitation erosion of TiAl-based titanium aluminide intermetallic alloys. *Acta Materialia*, 44.8 (1996) 3157-3168.

[69] F. Appel, J. Paul and M. Oehring. *Gamma Titanium Aluminide Alloys: Science and Technology*, John Wiley & Sons, New York, 2011.

[70] H. Dong (Eds.), *Surface Engineering of Light Alloys: Aluminium, Magnesium and Titanium Alloys*, Woodhead Publishing, Cambridge, 2010.

[71] J. R. Lawrence and D. Waugh. (Eds.), *Laser Surface Engineering: Processes and Applications*, Woodhead Publishing, Cambridge, 2014.

[72] H. Spies. Surface engineering of aluminium and titanium alloys: An overview. *Surface Engineering*, 26 (2010) 126-134.

[73] J. V. Heberlein, P. Fauchais and M. Boulos. *Thermal Spray Fundamentals: From Powder to Part*, Springer, New York, 2014.

[74] K. Zhou and H. Herman. Cavitation erosion of titanium and Ti-6A1-4V: Effects of nitriding. *Wear*, 80.1 (1982) 101-113.

[75] H. Li, Z. Cui, Z. Li, S. Zhu and X. Yang. Effect of gas nitriding treatment on cavitation erosion behavior of commercially pure Ti and Ti− 6Al− 4V alloy. *Surface and Coatings Technology*, 221 (2013) 29-36.

[76] C. P. Qin, Y. G. Zheng and R. Wei. Cavitation erosion behavior of nanocomposite Ti–Si–C–N and ti/Ti–Si–C–N coatings deposited on 2Cr13 stainless steel using a plasma enhanced magnetron sputtering process. *Surface and Coatings Technology*, 204.21 (2010) 3530-3538.

[77] M. Duraiselvam, R. Galun, V. Wesling, B. L. Mordike, R. Reiter, J. Oligmuller and G. Buvanashekaran. Improvement of the cavitation erosion resistance of Ti-6Al-4V through laser alloying titanium aluminide based intermetallic matrix composites. *Lasers Engineering*, 16.5 (2006) 423.

[78] B. S. Mann, V. Arya and B. K. Pant. Influence of laser power on the hardening of Ti6Al4V low-pressure steam turbine blade material for enhancing water droplet erosion resistance. *Journal of Materials Engineering and Performance*, 20.2 (2011) 213-218.

[79] P. Shipway and K. Gupta. The potential of WC-co hardmetals and HVOF sprayed coatings to combat water-droplet erosion. *Wear*, 271.9 (2011) 1418-1425.

[80] B. S. Mann, V. Arya and P. Joshi. Advanced high-velocity oxygen-fuel coating and candidate materials for protecting LP steam turbine blades against droplet erosion. *Journal of materials engineering and performance*, 14.4 (2005) 487-494.

[81] B. K. Pant, V. Arya and B. S. Mann. Enhanced droplet erosion resistance of laser treated nano structured TWAS and plasma ion nitro-carburized coatings for high rating steam turbine components. *Journal of Thermal Spray Technology*, 19.5 (2010) 884-892.

[82] K. Tsubouchi, N. Yasugahira, S. Yoshida, R. Kaneko and T. Sato. Evaluation of water droplet erosion for advanced large steam turbine. *Pressurized Water Chambers: Advances in Steam Turbine Technology for Power Generation*, 10 (1990): 245-251.

[83] S. M. DeCorso. Erosion tests of steam turbine blade materials. *Proceeding of ASTM*, 64 (1964) 782-796.

[84] S. Hattori and G. Lin. Effect of droplet diameter on liquid impingement erosion. In Proceeding of 7th International Symposium on Measurement Technique for Multiphase Flows, Tianjin, China, 1428 (2012).

[85] W. Voice. The future use of gamma titanium aluminides by Rolls-Royce. *Aircraft Engineering and Aerospace Technology*, 71.4 (1999) 337-340.

[86] D. M. Dimiduk. Gamma titanium aluminide alloys - an assessment within the competition of aerospace structural materials. *Materials Science and Engineering: A*, 263.2 (1999) 281-288.

[87] E. Nakao, S. Hattori and T. Okada. Cavitation erosion of Ti-Al based intermetallic compounds. *Nippon Kikai Gakkai Ronbunshu, A Hen/Transactions of the Japan Society of Mechanical Engineers, Part A*, 62 (1996) 2130-2136.

[88] C. Leyens and M. Peters (Eds.), *Titanium and Titanium Alloys*, John Wiley & Sons, New York, 2003.

[89] X. Wu. Review of alloy and process development of TiAl alloys. *Intermetallics*, 14.10 (2006) 1114-1122.

[90] A. Hirano, M. Sakane and N. Hamada. Relationship between vickers hardness and inelastic material constants. *Journal of the Society of Materials Science*, 56.5 (2007) 445-452.

[91] R. Liu, S. Hui, W. Ye, C. Li, Y. Fu, Y. Yu and X. Song. Dynamic stress–strain properties of Ti–Al–V titanium alloys with various element contents. *Rare Metals*, 32.6 (2013) 555-559.

[92] R. Cao, L. Li, J. H. Chen and J. Zhang. Study on compression deformation, damage and fracture behavior of TiAl alloys: Part II. Fracture behavior. *Materials Science and Engineering: A*, 527.10 (2010) 2468-2477.

[93] A. Bartels, H. Clemens, G. Dehm, E. Lach and W. Schillinger. Strain rate dependence of the deformation mechanisms in a fully lamellar γ-TiAl-based alloy: Dedicated to professor dr. mont. karl leopold maurer on the occasion of his 75th birthday. *Zeitschrift Für Metallkunde*, 93.3 (2002) 180-185.

[94] J. Millett, N. K. Bourne, G. T. Gray and I. P. Jones. The response of TiAl based alloys to one-dimensional shock loading. *Acta Materialia*, 50.19 (2002) 4801-4811.

[95] K. S. Chan, J. Onstott and K. S. Kumar. The fracture resistance of a binary TiAl alloy. *Metallurgical and Materials Transactions A*, 31.1 (2000) 71-80.

[96] Y. I. Oka, S. Mihara and H. Miyata. Effective parameters for erosion caused by water droplet impingement and applications to surface treatment technology. *Wear*, 263 (2007) 386-94.

[97] M. Hashish. An investigation of milling with abrasive-waterjets. *Journal of Manufacturing Science and Engineering*, 111.2 (1989) 158-166.

[98] Y. Zhou, Z. Lu and M. Zhan. An investigation of the erosion–corrosion characteristics of ductile cast iron. *Materials & Design*, 28.1 (2007) 260-265.

[99] A. P. Harsha and D. K. Bhaskar. Solid particle erosion behaviour of ferrous and non-ferrous materials and correlation of erosion data with erosion models. *Materials & Design,* 29.9 (2008) 1745-1754.

[100] C. Gerdes, A. Karimi and H. W. Bieler. Water droplet erosion and microstructure of laser-nitrided Ti-6Al-4V. *Wear*, 186-187 (1995) 368-374.

[101] Z. D. Liu, X. C. Zhang, F. Z. Xuan, Z. D. Wang and S. T. Tu. In situ synthesis of TiN/Ti_3Al intermetallic matrix composite coatings on Ti6Al4V alloy. *Materials & Design*, 37 (2012) 268-273.

[102] M. S. Mahdipoor, F. Tarasi, C. Moreau, A. Dolatabadi and M. Medraj. HVOF sprayed coatings of nano-agglomerated tungsten-carbide/cobalt powders for water droplet erosion application. *Wear*, 330 (2015) 338-347.

[103] C. R. F. Azevedo and A. Sinátora. Erosion-fatigue of steam turbine blades. *Engineering Failure Analysis*, 16.7 (2009) 2290-2303.

[104] F. G. Hammitt and F. J. Heymann. *Liquid-erosion failures*. ASM Handbook, Materials Park, OH, USA, 11 (1986) 163-171.

[105] H. Medekshas and V. Balina. Assessment of low cycle fatigue strength of notched components. *Materials & Design*, 27.2 (2006) 132-140.

[106] K. S. Chan and Y. W. Kim. Relationships of slip morphology, microcracking, and fracture resistance in a lamellar TiAl-alloy. *Metallurgical and Materials Transactions A*, 25.6 (1994) 1217-1228.

[107] K. S. Chan and D. S. Shih. Fundamental aspects of fatigue and fracture in a TiAl sheet alloy. *Metallurgical and Materials Transactions A*, 29.1 (1998) 73-87.

[108] Y. Umakoshi, H. Y. Yasuda and T. Nakano. Plastic anisotropy and fatigue of TiAl PST crystals: A review. *Intermetallics*, 4 (1996) 65-75.

[109] S. Kim, J. K. Hong, Y. Na, J. Yeom and S. E. Kim. Development of TiAl alloys with excellent mechanical properties and oxidation resistance. *Materials & Design*, 54 (2014) 814-819.

[110] K. S. Chan and Y. W. Kim. Effects of lamellae spacing and colony size on the fracture resistance of a fully-lamellar TiAl alloy. *Acta Metallurgica Et Materialia*, 43.2 (1995) 439-451.

[111] H. Jiang, F. A. Garcia-Pastor, D. Hu, X. Wu, M. H. Loretto, M. Preuss and P. J. Withers. Characterization of microplasticity in TiAl-based alloys. *Acta Materialia*, 57.5 (2009) 1357-1366.

[112] H. Inui, M. H. Oh, A. Nakamura and M. Yamaguchi. Room-temperature tensile deformation of polysynthetically twinned (PST) crystals of TiAl. *Acta Metallurgica Et Materialia*, 40.11 (1992) 3095-3104.

[113] P. Wang, N. Bhate, K. S. Chan and K. S. Kumar. Colony boundary resistance to crack propagation in lamellar Ti–46Al. *Acta Materialia*, 51.6 (2003) 1573-1591.

[114] S. Yokoshima and M. Yamaguchi. Fracture behavior and toughness of PST crystals of TiAl. *Acta Materialia*, 44.3 (1996) 873-883.

[115] Z. W. Huang and P. Bowen. Localised cyclic plastic deformation on translamellar fracture surfaces in a P/M γ-TiAl-based alloy. *Acta Materialia*, 47.11 (1999) 3189-3203.

[116] N. Kamkar, F. Bridier, P. Jedrzejowski and P. Bocher. Water droplet impact erosion damage initiation in forged Ti-6Al-4V. *Wear*, 322-323 (2015) 192-202.

[117] Y. Umakoshi, H. Yasuda and Y. Nakano. The effect of orientation and lamellar structure on the fatigue behaviour of TiAl PST crystals. *International Journal of Fatigue*, 1.18 (1996) 65.

[118] Available online at: Nanoscaleworld.bruker-axs.com/nanoscaleworld/media/p/775.aspx.

[119] J. Zhang, X. Cheng and Z. Li. Total fatigue life prediction for Ti-alloys airframe structure based on durability and damage-tolerant design concept. *Materials & Design*, 31.9 (2010) 4329-4335.

[120] A. L. Dowson, M. D. Halliday and C. J. Beevers. In-situ SEM studies of short crack growth and crack closure in a near-alpha Ti alloy. *Materials & Design*, 14.1 (1993) 57-59.

[121] J. Yang, H. Li, D. Hu and M. Dixon. Microstructural characterisation of fatigue crack growth fracture surfaces of lamellar Ti45Al2Mn2Nb1B. *Intermetallics*, 45 (2014) 89-95.

[122] Z. W. Huang and P. Bowen. Persistent microslip bands in the lamellar TiAl structure subjected to room temperature fatigue. *Scripta materialia*, 45.8 (2001) 931-937.

[123] J. Polák and J. Man. Mechanisms of extrusion and intrusion formation in fatigued crystalline materials. *Materials Science and Engineering: A*, 596 (2014) 15-24.

[124] R. Wanhill and S. Barter. *Fatigue of Beta Processed and Beta Heat-Treated Titanium Alloys*, Springer Science & Business Media, Berlin, Germany, 2011.

[125] N. Kamkar Zahmatkesh. Water droplet erosion mechanisms of Ti-6Al-4V, PhD thesis, Ecole Technologie Superieure, Montreal (Canada) 2014.

[126] M. Nakai, M. Niinomi, T. Akahori, N. Ohtsu, H. Nishimura, H. Toda, H. Fukui and M. Ogawa. Surface hardening of biomedical Ti–29Nb–13Ta–4.6 zr and Ti–6Al–4V ELI by gas nitriding. *Materials Science and Engineering: A*, 486.1 (2008) 193-201.

[127] A. Zhecheva, W. Sha, S. Malinov and A. Long. Enhancing the microstructure and properties of titanium alloys through nitriding and other surface engineering methods. *Surface and Coatings Technology*. 200.7 (2005) 2192-2207.

[128] H. Shibata, K. Tokaji, T. Ogawa and C. Hori. The effect of gas nitriding on fatigue behaviour in titanium alloys. *International Journal of Fatigue*, 16.6 (1994) 370-376.

[129] I. Mitelea, E. Dimian, I. Bordeaşu and C. Crăciunescu. Ultrasonic cavitation erosion of gas nitrided Ti–6Al–4V alloys. *Ultrason. Sonochem*, 21.4 (2014) 1544-1548.

[130] H. C. Man, Z. D. Cui, T. M. Yue and F. T. Cheng, Cavitation erosion behavior of laser gas nitrided Ti and Ti6Al4V alloy, *Materials Science and Engineering: A*, 355.1 (2003) 167-173.

[131] A. Zhecheva, S. Malinov and W. Sha. Titanium alloys after surface gas nitriding. *Surface and Coatings Technology*, 201.6 (2006) 2467-2474.

[132] T. Bell, H. W. Bergmann, J. Lanagan, P. H. Morton and A. M. Staines. Surface engineering of titanium with nitrogen. *Surface Engineering*, 2.2 (1986) 133-143.

[133] S. Malinov, A. Zhecheva and W. Sha. Relation between the microstructure and properties of commercial titanium alloys and the parameters of gas nitriding. *Metal Science and Heat Treatment*, 46 (2004) 286-293.

[134] M. S. Mahdipoor, F. Mahboubi, S. Ahangarani, M. Raoufi and H. Elmkhah. The influence of plasma nitriding pre-treatment on tribological properties of TiN coatings deposited by PACVD. *Journal of Materials Engineering and Performance*, 21.6 (2012) 958-964.

[135] E. Mitchell and P. J. Brotherton. Surface treatments and lubricants for improving press-forming properties of titanium and its alloys. *Journal of Institute of Metals*, 93 (1965) 278-279.

[136] R. K. Nalla, B. L. Boyce, J. P. Campbell, J. O. Peters and R. O. Ritchie. Influence of microstructure on high-cycle fatigue of Ti-6Al-4V: Bimodal vs. lamellar structures. *Metallurgical and Materials Transactions A*, 33.13 (2002) 899-918.

[137] A. Zhecheva, S. Malinov and W. Sha. Surface gas nitriding of Ti-6Al-4V and Ti-6Al-2Sn-4Zr-2Mo-0.08 si alloys. *Zeitschrift Für Metallkunde*, 94.1 (2003) 19-24.

[138] I. M. Pohrelyuk, V. M. Fedirko and O. V. Tkachuk. Effect of the rarefaction of an oxygen-containing medium on the formation of titanium oxynitrides. *Journal of Materials Science*, 44.1 (2008) 64-69.

[139] M. D. Abràmoff, P. J. Magalhães and S. J. Ram. Image processing with ImageJ. *Biophotonics international*, 11.7 (2004) 36-42.

[140] M. Lee, W. W. Kim, C. K. Rhee and W. J. Lee. Liquid impact erosion mechanism and theoretical impact stress analysis in TiN-coated steam turbine blade materials. *Metallurgical and Materials Transactions A*, 30.4 (1999) 961-968.

[141] Y. He, I. Apachitei, J. Zhou, T. Walstock and J. Duszczyk. Effect of prior plasma nitriding applied to a hot-work tool steel on the scratch-resistant properties of PACVD TiBN and TiCN coatings. *Surface and Coatings Technology*, 201.6 (2006) 2534-2539.

[142] M. Raoufi, S. Mirdamadi, F. Mahboubi, S. Ahangarani, M. S. Mahdipoor and H. Elmkhah. Effect of active screen plasma nitriding pretreatment on wear behavior of TiN coating deposited by PACVD technique. *Applied Surface Science*, 258 (2012) 7820-7825.

[143] M. M. Lima, C. Godoy, P. J. Modenesi, J. C. Avelar-Batista, A. Davison and A. Matthews. Coating fracture toughness determined by Vickers indentation: An important parameter in cavitation erosion resistance of WC–Co thermally sprayed coatings. *Surface and Coatings Technology*, 177 (2004) 489-496.

[144] S. Dallaire, M. Dufour and B. Gauthier. Characterization of wear damage in coatings by optical profilometry. *Journal of Thermal Spray Technology*, 2.4 (1993) 363-368.

[145] C. Verdon, A. Karimi and J. Martin. A study of high velocity oxy-fuel thermally sprayed tungsten carbide based coatings. Part 1: Microstructures. *Materials Science and Engineering: A*, 246.1 (1998) 11-24.

[146] D. A. Stewart, P. Shipway and D. G. McCartney. Microstructural evolution in thermally sprayed WC–Co coatings: Comparison between nanocomposite and conventional starting powders. *Acta Materialia*, 48.7 (2000) 1593-1604.

[147] J. M. Guilemany, J. M. De Paco, J. R. Miguel and J. Nutting. Characterization of the W_2C phase formed during the high velocity oxygen fuel spraying of a WC 12 pct co powder. *Metallurgical and Materials Transactions A*, 30.8 (1999) 1913-1921.

[148] Y. Qiao, T. E. Fischer and A. Dent. The effects of fuel chemistry and feedstock powder structure on the mechanical and tribological properties of HVOF thermal-sprayed WC–Co coatings with very fine structures. *Surface and Coatings Technology*, 172.1 (2003) 24-41.

[149] B. R. Marple, J. Voyer, J. Bisson and C. Moreau. Thermal spraying of nanostructured cermet coatings. *Journal of Materials Processing Technology*, 117.3 (2001) 418-423.

[150] M. Jafari, M. H. Enayati, M. Salehi, S. M. Nahvi and C. G. Park. Microstructural and mechanical characterizations of a novel HVOF-sprayed WC-co coating deposited from electroless Ni–P coated WC-12Co powders. *Materials Science and Engineering: A*, 578 (2013) 46-53.

[151] S. Lathabai, M. Ottmüller and I. Fernandez. Solid particle erosion behaviour of thermal sprayed ceramic, metallic and polymer coatings. *Wear*, 221.2 (1998) 93-108.

[152] K. Niihara. A fracture mechanics analysis of indentation-induced palmqvist crack in ceramics. *Journal of Materials Science Letters*, 2.5 (1983) 221-223.

[153] B. R. Marple and R. S. Lima. Process temperature/velocity-hardness-wear relationships for high-velocity oxyfuel sprayed nanostructured and conventional cermet coatings. *Thermal Spray Technology*, 14.1 (2005) 67-76.

[154] A. G. Evans and T. R. Wilshaw. Quasi-static solid particle damage in brittle solids—I. observations analysis and implications. *Acta Metallurgica*, 24.10 (1976) 939-956.

Appendices

Appendix A

Appendix A contains additional information about water droplet erosion experiments

A.1. Water droplet erosion rig

The water droplet erosion experiments were performed using a state of art erosion rig with a rotating disk, which is available in TMG group. It was designed based on the ASTM G73 standard which can simulate the water droplet erosion damage observed in service conditions of turbine blades. A schematic of the water droplet erosion rig is presented in Figure A-1-a. There is a disk in the erosion chamber of this rig, which is able to rotate with very high speed, up to 20,000rpm. Erosion coupons are mounted on this disk. Drawing of the sample holder and the insert coupons used in this research are presented in Figure A-2. Water droplet generator system, which is highlighted in Figure A-1-a, inject water stream into the chamber. The water stream are shielded against the turbulence occurring inside the chamber to ensure the straightness of the stream with minimum aerodynamic distortion of the droplets till being impacted by rotating samples. The picture of this shield is presented in Figure A-1-b. After a certain distance from the nozzle, which is called breaking distance, water jet converts into droplets. Distance between the nozzle and coupons has been optimized to assure that only water droplets with desired diameters impact the rotating coupons, not water jet.

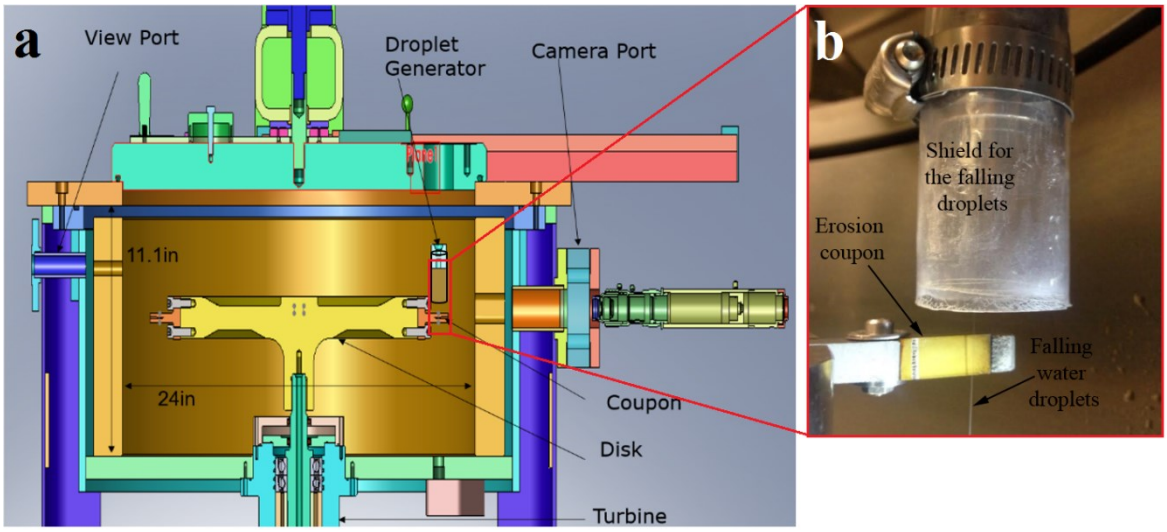

Figure A- 1: (a) Schematic of used water droplet erosion rig, (b) the used shield to protect water droplet from the turbulence

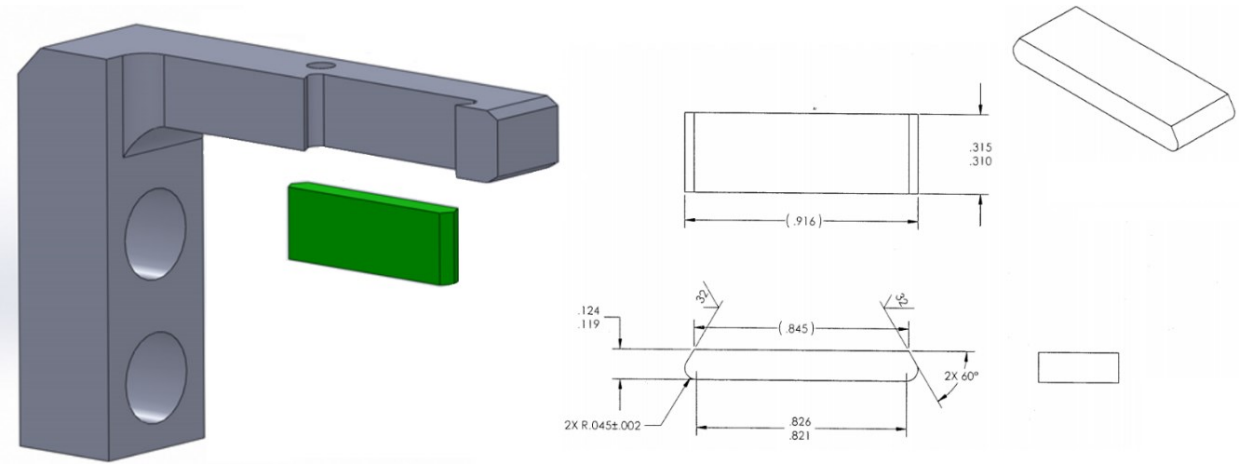

Figure A- 2: Schematic of the used sample holder and drawing of insert coupon

A.2. Measurement of droplet sizes and plotting their size distribution

Impacting water droplets has been studied in TMG group to provide accurate information for erosion investigations. An imaging setup was prepared using a transparent box which simulates the test chamber of erosion rig, Figure A-3. The water droplet generator of erosion rig was connected to this box. The same nozzle, back pressure and flow rate gauges were utilized. Falling droplets were monitored using a high speed camera. Using this setup, first the breaking distance of each nozzle was found and recorded. Then, the pressure and flow of sending water to the chamber were optimized to obtain the droplets with desired sizes. Typical images of water droplets, which are generated using 200, 400, 600µm nozzles, are shown in Figure A-3. It is noteworthy that these images were captured from the part of water stream, in which the distance from the nozzle is more than breaking distance. Obviously, not all of droplets are complete sphere and some distortion for the droplets can be seen. In these images, two diameters from each droplet were measured and their average was taken as the diameter of each droplet. Same approach was used to measure the diameter of 200 droplets for each nozzle and then their size distribution were plotted. These size distribution were shown in Figures 2-4 and 2-5.

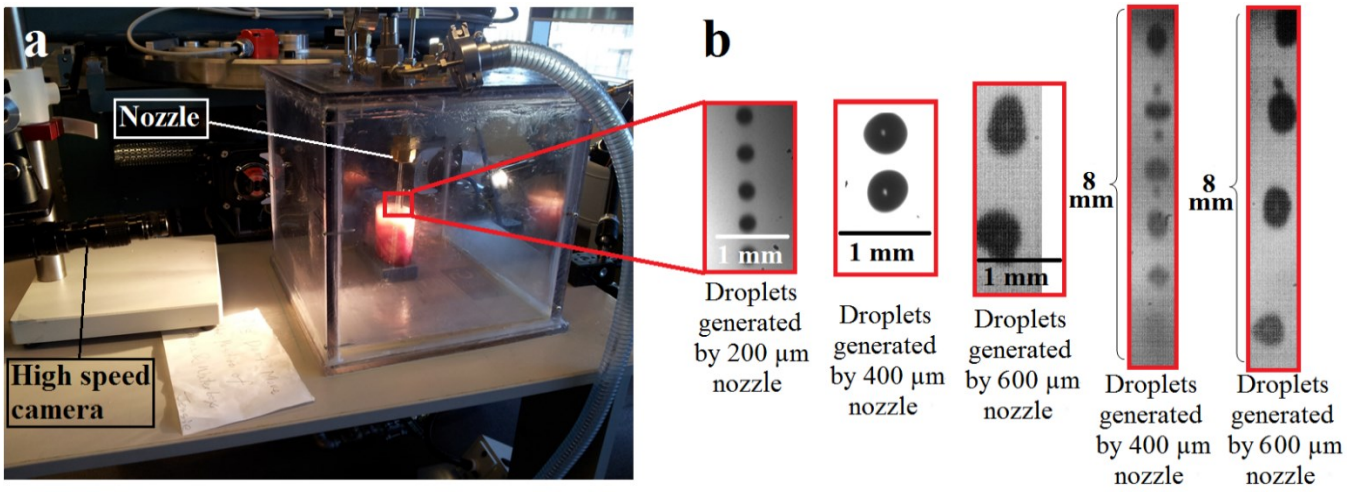

Figure A- 3: (a) Imaging setup to measure droplet sizes, (b) typical images of water droplets generated using different nozzles

A.3. Pattern of impacting droplets in each rotation

In order to find the number of droplet impacts, it is necessary to determine how many droplets hit the coupon in each rotation. Hence, the number of droplets in 8mm of the water stream, which is the width of the insert coupon, were counted in more than 10 images. To capture water droplets in larger area, the configuration of camera was changed and the quality of images were reduced. However, the droplets could be distinguished and counted. Typical images used for this counting are presented in Figure A-3. These images show that for 400 and 600 nozzles 6 and 4 droplets face and impact the coupon's surface in each rotation. These numbers would be questioned because of the air turbulence effect inside the erosion chamber, which is neglected in the transparent box setup. It is worthy to note that similar images from the falling droplets were captured inside the erosion rig while the disk was rotating with 12,000rpm. Very high speed camera (16,000fps) to catch the impact instants as well as special lighting source were prepared and several in situ images were captured. Figure A-4 shows that using 400 nozzle six droplets face the surface, impinge and then subdivide. These images verify that there is same number of droplets in 8mm of water stream, generated either in the transparent box or the erosion chamber. Indeed, the influence of air turbulence was notably suppressed using the protective shield. Therefore, knowing the rotational speed, time interval, average droplet size, and the exact number of impacting droplet in each rotation, the volume of impacting water was calculated for the erosion experiments and used to represent the results. These information are tabulated for the 400 and 600 nozzles in Table A-1.

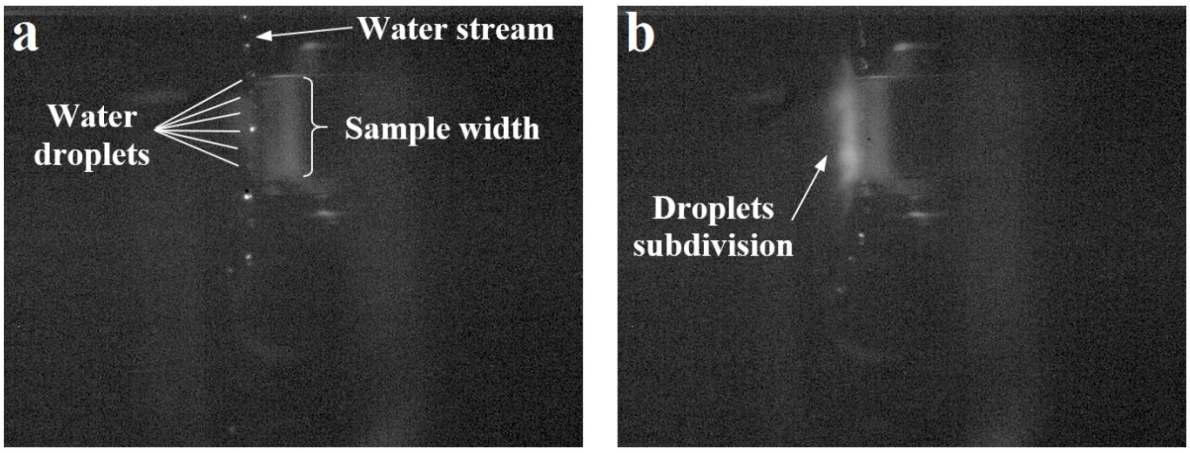

Figure A- 4: In situ images of water stream taken at 16,000fps for a test done at 300m/s using 464µm droplets: (a) before impingement, (b) after impingement

Table A- 1: Detailed information of used droplet generator nozzles

Nozzle	Breaking distance (cm)	Average droplet size (µm)	Number of droplet in each rotation	Volume of one water droplet (mm^3)	Volume of impacting water in each rotation (mm^3)	Area exposed to water droplets (mm^2)
400	4	464	6	0.0523	0.3138	4.8
600	3.5	603	4	0.1148	0.4592	6

A.4. Area exposed to water droplets

As mentioned earlier, it is recommended to use the rationalized and dimensionless values for the erosion rates and erosion exposures for the quantitative comparison among the experiments performed in different impingement conditions, Equations 2-5, 2-6, and 2-7. All parameters of the mentioned equations are known and only the area influenced by one droplet and total surface area exposed to water droplets must be defined. The area influenced by one droplet was defied in the standard as the projection of the droplet on the solid surface, which is a circle with droplet diameter. The total surface area exposed to water droplets in the erosion experiments depends on the used setup. Using available erosion rig in TMG group, the footprint of impacting droplets is in the form of a thick line on the coupon's surface, shown in Figure A-5. The area of this line was measured from the optical micrographs recorded at the end of the erosion incubation. The length of this line is known, 8mm as the width of the insert coupon; however, the width varies using different nozzles, as shown in Figure A-5. It was measured as 600 and 750µm for the 400 and 600

nozzles. Hence, 4.8 and 6mm^2 are total area exposed to the impact of water droplets. They are taken as the surface area exposed to droplet impacts.

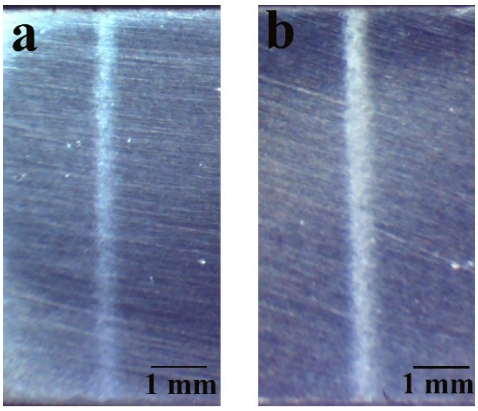

Figure A- 5: Surfaces of TiAl at the end of erosion incubation using (1) 464µm droplets , (2) 603µm droplets

In the case of treated coupons, the nature of top layers on the surface determines the performance. Despite the same area exposed to the impacting water droplets, different damaged surface areas were observed for the bulk materials and the surface treated coupons.